Computational Two Phase Marangoni Flow in a Microgravity Environment

A thesis submitted to The University of Manchester for the degree of Doctor of Philosophy in the Faculty of Engineering and Physical Sciences

2013

Yousuf Alhendal

School of Mechanical, Aerospace and Civil Engineering

Abstract

The lack of significant buoyancy effects in zero-gravity conditions poses an issue with fluid transfer in a stagnant liquid. In this thesis, the movement of a bubble or droplet in both stagnant and rotating liquids is analysed and presented numerically using computational fluid dynamics (CFD). The governing continuum conservation equations for two-phase flow are solved using the commercial software package (2011). The Volume of Fluid (VOF) method is used to track the liquid/gas interface in 2D and 3D domains. User-Defined Functions (UDFs) are employed in order to include the effect of surface tension gradient and fluid properties as a function of temperature, with a view to efficiently investigating temperature effects on the properties of the two phases. The flow is driven via Marangoni influence induced by the surface tension gradient, which in turn drives the bubble/droplet from the cold to the hot region. For stationary liquid, the results indicate that the scaled velocity of the bubble decreases with an increase in the Marangoni number, which agrees with the results of previous space experiments. An expression for predicting the scaled velocity of a bubble has been regressed based on the obtained data from the present numerical study for thermal Marangoni numbers up to 10,721. An expression for predicting the scaled velocity of a Fluorinert droplet migrating in oil has also been presented for an Ma_T range from 24.05 to 2771. The interactions of two droplets in thermocapillary motion have also been studied and compared with the results obtained for the isolated droplet. The results have shown that the leading droplet will not move faster than if it were isolated, as the trailing droplet has no influence on the velocity of the leading droplet. Three-dimensional results show that no bubbles broke in any of the cases observed and agglomeration could occur during thermocapillary migration for bubbles placed side by side. The results of the motion of a singular and multiple bubbles incorporating thermocapillary forces in a rotating liquid in a zero-gravity environment have been presented for the first time. When the Rossby number is 1, the effects of rotation are important. Furthermore, the deflection of the gas bubble motion increases towards the axis of rotation with a decrease in the Rossby number (Ro). Bubble population balance modelling has been investigated in normal gravity using Luo kernels for breakage and agglomeration and two different laminar kernels for zero-gravity conditions. The simulations covered a wide range of scenarios and results are presented as a bell and histogram shapes for number density and particle percentage distribution, respectively.

Declaration

I hereby declare that the dissertation entitled Computational Two Phase Marangoni Flow in a Microgravity Environment has been undertaken by me for the award of PhD degree in Mechanical engineering. I have completed this under the guidance of Prof. A. Turan, Postgraduate Programmes in Mechanical engineering, The University of Manchester, 2013. I also declare that this dissertation has not been submitted in support of an application for another degree or qualification of this or any other university or other institute of learning.

Copyright statement

Acknowledgements

This thesis is one of the results of my work and life in the student village B1,George Begg building, school of Mechanical Aerospace and Civil Engineering at the University of Manchester, during the last five years. This would not have been possible without the people who taught me so much and had such a profound impact on my professional and private life. For this, I will be always thankful and owe my deepest gratitude to my supervisor Prof. A. Turan for his support and supervision throughout all the stages of this PhD research study. It was a pleasure to get to know and work with him. Special thanks to everyone helped me to finish this PhD study. My special thanks go to all my colleagues. My heartfelt gratitude goes to my family for their support and understanding, especially my mother and dear daughter.

Contents

List of Figures

List of Tables

Chapter 1 Introduction

1.1 Overview

This thesis deals with two-phase flows, i.e. systems of different fluid phases, such as gas and liquid. A typical example of a two-phase flow is the motion of a bubble or droplet (the word droplet refers to a liquid phase; and the word bubble refers to a gas phase) in a stagnant fluid (liquid or gas). In many branches of engineering it is important to be able to describe the motion of gas bubbles in a liquid (Krishna and van Baten, 1999). In multiphase flow, the simultaneous flow strongly depends on the gravitational force. However, in zero-gravity conditions, buoyancy effects are negligible and as an alternative, three different surface tension effects were found to make the bubbles or droplet move in zero-gravity. A change in surface tension can be caused by a change of temperature (thermocapillary), a change of the concentration of surfactant or impurities (solutalcapillary), and also by the presence of an electrical charge or electrostatic potential on the surface (electrocapillary). However, for small geometries and/or zero-gravity environments, this is not the case and these capillary forces could become dominant (Alhendal and Turan, 2012). In a non-uniform temperature gradient field, the surface tension varies according to the local temperature conditions. Near cold regions, a greater surface tension force exists in comparison with the hotter regions. This causes a net imbalance in the force acting upon the fluid particles, thus leading to a general movement of fluid from the hot to the cold region (in the current case, from the upper to the lower surface). Surface tension generally decreases with increasing temperature and the non-uniform surface tension at the fluid interface leads to shear stresses that act on the outer fluid by viscous forces, thus inducing a motion of the fluid particle (a bubble or droplet) in the direction of the thermal gradient. Bubbles suspended in a fluid with a temperature gradient will move towards the hot regions due to thermocapillary forces (Nas and Tryggvason, 2003).

In space, where buoyancy forces are negligible, thermocapillary forces can be dominant and can lead to both desirable and undesirable motion of bubbles, drops, and particles moved up. Multi-phase flows are encountered in a variety of industrial processes and plants, in the petroleum industry and its equipment, and in the chemical industry. The transport phenomenon of bubbles/droplets in a liquid is a very important topic for both fundamental hydrodynamics and practical applications such as the production of pure materials in manufacturing. For example, glass is believed to have the potential of producing very pure materials (Uhlmann, 1981). Thermocapillary migration may provide a method of removing bubbles from the melt. The prevention of vapor bubbles forming in both the fuel systems of liquid-rockets (Ostrach, 1982) and the cooling system of space habitats may be achievable using thermocapillary migration. Thermocapillary migration may also lead to the accumulation of gas bubbles on the hot surface of heat exchangers, thus reducing their efficiency. Ostrach (1982) studied various types of fluid flows that could occur in low-gravity conditions and observed that Marangoni convection is significant. In practical applications, it is frequently necessary to deal with a large number of bubbles or droplets and their collective behaviour may differ from what one might expect based on the results for a single particle. An understanding of the behaviour of multiphase fluid flow in general and more specifically, bubbles/drops in specific in zero-gravity conditions, is important for designing useful experiments for the space shuttle and the international space station. In addition, such an understanding is important for the future design of thermo-fluid systems and machinery that might be employed in similar environments.

1.2 The need for CFD in zero-gravity investigation

The available experimental results are usually supposed to be the major source of information on the behaviour of the physical process of multiphase flow at zero gravity. However, very little is known of the behaviour of fluids in microgravity due to the relative difficulty of obtaining experimental results and the funds and time-involved in the design and fabrication of space experiment. Multiphase flow experiments generally require continuous observation of the moving fluid during a test, which makes the experimental setup extremely complicated. It is also a challenge for space researchers to design a space experiment to accommodate most of their objectives. On the other hand, computational fluid dynamics offers sensitivity and enables feasible studies to be carried out for different parameters and designs. It can help to understand the basic fluid physics and assist in designing the experiments or systems for the zero-gravity environment. Therefore, calculating these flow regimes by means of computational fluid dynamics (CFD) is very useful and desirable. For the above reasons and more, modelling the numerical methods in this ways is the ideal tool allowing the investigation of the behaviour of multiphase flow and the capture of the flow physics in reduced-frame and at a lower cost.

1.3 Description of this thesis and its objectives

This research specifically targets the use of computational techniques in order to simulate thermocapillary (Marangoni) bubble/droplet flow in zero-gravity conditions to better understand the physical processes behind many of the observed physical phenomena of zero-gravity environments. In this thesis we will use the ANSYS-Fluent (Release 13.0, 2011) code to analyse and design a bubble/droplet flow system in a zero-gravity environment and to investigate sensitivity studies for various parameters. This illustrates the importance of the CFD simulations and examines the effect of several external and internal forces on the bubble

flow in zero gravity. The finite volume method (FVM) with a fixed non-uniform spatial grid was used to computationally model 2D axisymmetric and 3D uniform grid domains. This work presents the importance of CFD in multiphase flow studies in zero gravity. Due to these challenges, many CFD models have been proposed to carry out appropriate numerical simulations for the behaviour of bubble/droplet flow in microgravity. The literature review in Chapter 2 examines the challenges facing fluid experiments aboard orbiting spacecraft and includes extensive discussion of the work on thermocapillary progression of recent years. The literature indicates the need for CFD for predicting bubble/droplet behaviour in zero gravity. Surprisingly, there is still no satisfactory approach for predicting thermocapillary particle flow, and this overview of the literature will outline the available correlations.

Chapter 3 provides an interesting opportunity to test the capability of the finite volume method (FVM) simulation and the volume of fluid (VOF) model along with the solution algorithm of Ansys-Fluent. In addition, several published articles concerning the use of the volume of fluid (VOF) method in bubble/droplet simulations are reviewed. The need to first substantiate the code validation and verification methods in order to have confidence that the simulation tool is actually generating correct solutions to the problems that motivate this study is the focus of Chapter 4. The model's solution algorithms, boundary conditions, source terms, and fluid properties used in the simulation are described in detail in Chapter 5, along with calculations. Throughout Chapter 5 the simulation was able to examine scenarios not covered experimentally in order to verify the effect of temperature gradient, column-particle aspect ratio, fluid properties and temperature on the behaviour of bubble/droplet flow. An expression for predicting the scaled velocity of a bubble has been derived based on the data obtained in this chapter between scaled velocity and Marangoni numbers. A Fluorinert droplet migrating in oil has also been investigated, and the interactions of two Fluorinert droplets in thermocapillary motion have also been discovered and compared with the results

obtained for the isolated droplet. Chapter 6 covered the thermocapillary flow and interaction of a single and multiple bubbles in a three-dimensional domain. The study in this chapter focuses on the interaction of a pair of bubbles migrating in a leading and trailing sequence in the first part and placed side by side in the second study. The behaviour of both a single bubble and a coalescence of bubbles under the effects of both fluid rotation and surface tension gradient is investigated in detail in Chapter 7. Transient trajectories for a single bubble and a group of bubbles are demonstrated in this chapter to illustrate the influence of external forces, such as rotation force, on the behaviour of particles. Though a huge amount of publications (textbooks, conference proceedings and journal articles) concern multiphase flow, publications on two-phase flow in microgravity is a very seldom studied field and information about bubble behaviour in a rotating column in particular is not so complete in comparison with other physical phenomena in normal gravity. These are the main reasons for carrying out simulation research in microgravity.

In Chapter 8, Population Balance Models (PBM) for bubble break-up and coalescence were implemented into two axisymmetric dimensional Eulerian/Eulerian simulations of two-phase (air/water) transient flow using a multiphase flow algorithm based on the finite-volume method for both stationary and rotating columns in normal and zero gravity. The study covered a wide range of scenarios and the interesting results were found to be of great help for future design of two-phase flows in general and of bubble columns in particular. In Chapter 9, conclusions and suggestions for future works and recommendations are given.

Chapter 2 Literature review

2.1 Overview

Research and experimentation on thermocapillary bubble and drop motion began in 1959 on the ground using a space laboratory and via drop towers some years later. A few on-board microgravity experiments on the thermocapillary migration of bubbles and drops have since been performed using spacecraft. With the advent of space flight, the study of flows under near-zero-gravity conditions was strongly motivated by practical considerations, (Ostrach, 1982). In recent years and with advances in numerical calculation, knowledge of thermocapillary flow has undergone a considerable change and new, calculated results can be used to support, modify, or change the previous results.

The first study recorded in the literature regarding gas bubble motion due to thermal gradient was investigated experimentally and theoretically by Young et al. (1959). In their ground based experiment where gravity force is presented, they succeeded in holding a small bubble stationary and moving it downwards against the buoyant rise of gas bubbles by applying a temperature gradient between the lower and upper sides. The liquid was heated from the lower side and the Rayleigh number (Ra) was kept small to avoid any natural convective flow during the experiment. They introduced a linear relation for small Marangoni (Ma) and Reynolds numbers (Re) to obtain the bubble/drop velocity as follows:

$$V_{YGB} = \frac{2\left|\frac{d\sigma}{dT}\right| r_b \lambda \frac{dT}{dx}}{(2\mu + 3\mu')(2\lambda + \lambda')} \qquad 2\text{-}1$$

where r_b is the radius of the bubble, $d\sigma/dT$ is the surface tension gradient, dT/dx is the temperature gradient, and μ and μ′ $\lambda and\ \lambda'$ are the dynamic viscosity, thermal conductivity of gas and continuous phase, respectively. In their study, no bubble velocity was recorded; the

objective was to calculate what temperature was needed to keep the bubble stationary or to move it against buoyancy.

Hardy (1979) used a closed rectangular cell to reduce the experimental error related to the free liquid surface in Young et al's model. He first repeated the ground experiment of Young et al. (1959) and used their theoretical prediction to compare his measured data. With the agreement in vertical temperature gradient amount required to render the bubble motionless, the bubble's velocity results were lower than the calculated results. He also found that the bubble increased in size during migration toward the hotter side.

The thermocapillary motion of bubbles in zero-gravity was first considered experimentally by Thompson et al. (1980) who used the drop tower at the NASA Lewis Research Centre for 5.2 s of free fall to eliminate buoyancy. Thompson et al. demonstrated the existence of the Marangoni phenomenon in zero-gravity. They succeeded in observing the existing of the Marangoni flow phenomena for nitrogen bubbles in ethylene glycol, Dow-Corning silicon oil, and ethanol. The nitrogen diameter was approximately 0.6 cm for ethanol and 0.8 cm for silicon oil and ethylene glycol. The cylindrical test container measured 12 cm in diameter and was 12 cm high. The liquid in the cylinder was heated from the upper side for a about 260 minutes before the bubble was injected from a nozzle located in the centre of the bottom of the cylinder. Thompson et al. (1980) related the failure to observe the movement of a nitrogen bubble in water to impurities concentrated at the bubble interface or to a molecular phenomenon. Thompson's et al.(1980) study focused on proving the reality of the Marangoni phenomena and confirming that the variation of surface tension with temperature is the driving force in the absence of gravity. Thompson et al. (1980) showed experimentally that the Marangoni phenomenon is a primary mechanism for the movement of a gas bubble in a non-isothermal liquid in a low-gravity environment. The maximum Re and Ma reached for ethylene glycol were 5.66 and 713, respectively. Thompson et al. (1980) suggested that the

use of a zero-gravity environment with sufficient time to undertake the investigation would help to improve the finding.

Merritt and Shankar Subramanian (1988) carried out experiments on bubbles with diameters ranging from 0.06 to 0.3 mm in three different test fluids, namely Dow-Corning 200 series silicone oils, in a downward temperature gradient, reversing the buoyant rise of the bubble. They were careful not to include buoyant convection cells by maintaining the Rayleigh number below the critical value. They observed that the bubble size doubled when migrating toward the hotter side, which was previously found by Hardy (1979). The authors deduced that this phenomenon is due to mass transfer. Their results were in good agreement with these obtained by Young et al., although they mentioned that the varying physical properties of a fluid with temperature should be considered at all times.

Subramanian (1981) discussed the influence of the convective transportation of energy on the migration of thermocapillary bubbles and its effect of reducing the bubble speed. He assumed the bubble size to be a non-deformable and nonzero convective heat transfer in order to present his expression to calculate the velocity of a gas bubble for 0 (Ma^2).

Shankar and Subramanian (1988) solved the energy equation numerically to compute the migration speed of a gas bubble in a liquid with a uniform temperature gradient. They noted the reduction in the gas bubble's scaled velocity with an increase in the Marangoni number and suggested two different equations to calculate the bubble velocity for different ranges of Marangoni numbers. They used streamlined figures to show the recirculation region around the bubble, and thermal line plots to display the extended thermal wake behind the moving bubble. They also suggested that future experimental works be conducted to confirm their numerical data, due to lack of existing data.

Siekmann and Szymczyk (1988) used numerical methods to solve the motion of a gas bubble under the action of a surface tension gradient for three different flows (creeping, creeping

with convection, and thermocapillary flow). They plotted the scaled migration speed versus Re values of up to 100 for different Prandtl number (Pr) = 0.01,0.1,10,100. They concluded that the bubble migration speed decreases with increasing Prandtl number and observed that the Marangoni number is an important parameter for the calculation of thermocapillary bubble migration. Balasubramaniam and Lavery (1989) investigated numerically the migration of a gas bubble in an infinite medium with a uniform temperature gradient under microgravity for Re and Ma values of up to 2000 and 1000, respectively, which only reduced the scaled bubble velocity from 0.5 to 0.16. They confirmed the earlier findings of Szymczyk and Siekmann (1988) concerning the central influence of the Marangoni number on the bubble velocity. They mentioned that further computational investigation was necessary to calculate the bubble velocity for higher Re and Ma numbers.

Balasubramaniam et al. (1996) reported experiments on the motion of drops and bubbles under the effects of surface tension gradient in reduced gravity conditions. They used a Dow-Corning silicon oil as the host liquid and air bubbles during their experiment aboard the NASA space shuttle in orbit. They used the YGB model to plot the scaled bubble velocity against Ma values of up to 810, which confirmed the trend predicted with quantitative difference.

Hadland et al. (1999) performed experiments aboard a NASA space shuttle mission and succeeded in increasing the Re and Ma values up to 87.2 and 5780, respectively. In their experiments on the thermocapillary migration of bubbles and drops, Dow-Corning silicon oil was used as a host liquid with air and Fluorinert for the bubbles and drops. Their results revealed the same trend of bubble migration scaled velocity of earlier work at higher Ma number. They also confirmed the reduction in scaled velocity as the Marangoni number was increased, and they noticed deformation of large bubbles to oblate spheroids. Their data on

bubbles and drops display complex transient behaviour due to variation in viscosity with temperature, which was also reported by Treuner et al. (1996).

Treuner et al. (1996) carried out experimental investigations for air bubbles in three paraffin liquids for Marangoni numbers of up to 2500 in the Bremen drop tower in Germany, which provided around 4.74 s of reduced gravity. Bubbles with a diameter from 0.2 to 5 mm were injected after two hours of preheating the host liquid in normal gravity and after 0.5 s of reduced gravity time to allow for bubble formation. Treuner et al. (1996) presented several plots for scaled velocity vs Marangoni number for three different Prandtl numbers (8.2, 12.1, and 25.5). The authors compared their experimental data with Thompson et al. (1980) and Szymczyk and Siekmann (1988). They also performed numerical calculations of the steady state and a good comparison with their experiment data was found. The short duration time of the experiments was considered to be a disadvantage by the authors. For better understanding of the thermocapillary bubble flow behaviour in reduced gravity, the authors suggested that a fully transient model was required to give better understanding and explanation of the bubble flow behaviour , which could not be covered theoretically or exponentially. Such a model would also serve to validate their experimental result.

Nas and Tryggvason (1993) and Nas (1995) presented numerical simulation results for two- and three-dimensional bubbles and drops migrating in temperature gradient by solving the full Navier-Stokes equation using a finite difference/front-tracking method. In their research, they began with the rise of a single bubble in different parameters before extending their work to a fully three-dimensional model in order to investigate in detail the interaction between two bubbles or drops and a group of bubbles. The authors plotted the behaviour and flow pattern of single and multiple bubbles moving under the action of the surface tension effect in zero-gravity and their tendency to line up side by side, across the channel, maintaining their spherical shape within the flow. Nas and Tryggvason (2003) later

investigated the thermocapillary motion of two particles toward the hotter side numerically. Their most important finding was that the deformation is very slight and the lower particle was moving faster toward the hotter wall until it caught up with the upper particle.

Arlabosse et al. (1999) investigated numerically the thermocapillary flow around a gas bubble when the two driving forces, surface tension gradient and gravity forces, were against each other, for different Pr. The results of velocity and temperature in a steady state obtained from the finite element model developed for this purpose have been validated against previous experimental data and small differences were shown. The authors analyzed and plotted the influence of the Rayleigh number (Ra), Ma and Pr on the flow pattern, which were then converted to an expression relating to the strength of the flow.

Wozniak et al. (2001) performed an experiment on the motion of bubbles and drops in stagnant liquid aboard the space shuttle in orbit. The buoyancy was reduced and thermocapillary flow dominated the flow of the bubble and the drop, air and Fluorinert FC-75, inside a Dow–Corning silicon oil. This result was composed of due to the surface tension gradient. The authors compared the experimental during the flight and the numerical calculations. The isothermal plots were similar; however, the authors mentioned the deviation of some other results due to the constant physical properties used during the numerical prediction. The authors also mentioned the complexity of performing similar experiments on the ground, due to the difficulty of eliminating buoyancy. The authors also mentioned the need for an optimized optical set-up and smaller tracers for quantitative measurement of the thermocapillary velocity fields.

In recent experiments on bubble thermocapillary migration by Kang et al. (2008), the results of the thermocapillary flow of one and two air bubbles injected in stagnant silicon oil of nominal viscosity 5cst on board the Chinese 22nd recoverable space satellite in 2005 were presented. The air bubbles were injected in the direction of the temperature gradient of the

stagnant heated liquid and the impact on the behaviour of the bubbles and their coalescence were presented in their research study. The maximum Marangoni number in this experiment was 9288, which was larger than any prior space experiment. The results showed that the minimum value of the scaled bubble velocity was 0.3076 as (Ma) goes to infinity. The trend of the thermocapillary scaled bubble velocity given by Kang et al. (2008) confirmed the previous results of Hadland et al. (1999) and Treuner et al. (1999, Treuner et al., 1996). The results of the interaction between two bubbles, leading and trailing, presented in this experiment plotted against time for different bubble diameters were similar in tendency to the earlier predictions for small Ma and Re numbers.

Meyyapan et al. (1983) studied theoretically the thermocapillary motion of two bubbles using an approximate method. The authors explained in detail the different reactions between two bubbles with different diameters. The authors found that the smaller bubble moved faster than the larger bubble and the velocity of the larger bubble moved slightly slower, unlike in the case of a single bubble. They also found that two bubbles of equal diameter will not affect each other's velocity for any separation distance.

Sun and Hu (2003) considered the interaction between two bubbles moving toward the hotter side in their theoretical work. Their results confirmed the previous findings by Meyyappan et al. (1983), in that the thermocapillary motion of two bubbles has a stronger influence on the smaller bubble than the larger bubble, and the velocity of the smaller bubble will change greatly as a result of this interaction.

Harper J. (2002) published a review of the book:The Motion of Bubbles and Drops in Reduced Gravity by Subramanian and Balasubramanian (2010). He gave a brief review of how important the text book is for researcher and those wishing to know about thermocapillary flow. Harper mentioned some important points related to the application of the topic, such as the fact that two bubbles will move at the same speed whatever the

separation distance if the Peclet and Reynolds numbers are both less than one, and if the flow is purely thermocapillary. The author found no mention of interfacial turbulence in this book, despite its significance.

Xie et al. (Xie et al., 1998) performed on-ground experiments on thermocapillary drop migration in the case of intermediate Reynolds numbers in a microgravity environment with a free fall of 4.5 s. The thermocapillary velocity of their experiment was smaller than that suggested by YGB linear theory. Results from their experiments show that the drop migration velocity depends on the temperature gradient and the drop size of the fixed host liquid. These findings agree with those of the ground-based experiment. Regarding their experimental time period (4.5 s of microgravity) the authors suggested that a longer microgravity period may give better results. The authors mentioned the need for numerical simulations with which to evaluate the experimental results.

Using the same methods as used for the ground-based experiment of Xie et al. (1996) and immiscible vegetable oil and 5cst silicone oil as experimental media for the matrix liquid and drop, respectively, Xie et al. (1998) studied experimentally the migration of drops for intermediate Reynolds numbers. The experiments were conducted using the drop with 4.5 s of freefall experiments in the Microgravity Laboratory of Japan. The experimental results showed that the thermocapillary drop velocities were smaller than those suggested by the YGB model, a finding which agrees with previous ground-based experiments (Xie et al., 1996). The author confirmed that a longer experimental time in microgravity conditions is necessary for a drop approaching its steady thermocapillary velocity and more experiments at larger Reynolds numbers are required.

Xie et al. (2005) carried out a space experiment on board the Chinese spacecraft ShenZhou-4 for isolated drops of Fluorinert liquid in a heated test cell of a 5cst silicone oil at two temperature gradients of 0.9 and 1.2 K/mm respectively. In these experiments, a decrease in

the scaled drop migration was recorded as the values of expanded Ma were increased to 5500. From all the experiments, the authors could not deduce whether the drop migration was consistent with the YGB model, or whether it could reach steady velocities. At large Marangoni numbers, the authors noticed complex behaviour for the thermocapillary drop migration and stated that further studies are still needed.

Recently, Cui et al (2008) used a single air bubble in a stagnant silicone oil of nominal viscosity 5cst to conduct, on board the Chinese 22nd recoverable satellite, an experiment complementary to that conducted previously by Kang et al. (2008). The curve obtained was comparable with the previous lower Balasubramaniam et al. (1996) Ma.et al. (1999) for scaled velocity vs. Marangoni numbers (Ma) up to 9288.

We can conclude from the historical review of thermocapillary bubble/drop flow in zero-gravity that a few microgravity experiments have been performed on board the microgravity sounding rocket and spacelab. Two-phase flow experiments generally require continuous observation of moving fluid during a test, which makes the experiment complicated. It is also a challenge for space researchers to design a space experiment to accommodate most of their objectives. The available results are limited to low Reynolds and Marangoni numbers because of the difficulties in obtaining experimental results in microgravity (Kang et al., 2008). Most experimental studies have noted that there are no theoretical or numerical results with which to compare their experiments. It is also difficult to obtain complete information about the behaviour of bubbles in space and a CFD study has been undertaken by many researchers to compare and analyse their experimental results (Treuner et al., 1996). Experiments under normal and microgravity conditions are too costly as well as being complicated (Bozzano and Dente, 2009). Numerical simulations consequently become an important tool in research studies of two-phase flows in a microgravity environment. For the above reasons and more it is necessary to carry out appropriate numerical simulations for the

behaviour of bubble/drop measurement in microgravity. Numerical simulations can also help to understand the basic fluid physics, as well as to assist in the design of experiments or systems for zero-gravity environments.

Chapter 3 Computational Fluid Dynamics

3.1 Overview

Two changes to the element in motion will most likely take place, which govern the evolution of fluid from one state to another. First, the translation of the fluid element, which is often referred to as convection, while the second process is called distortion is related to the presence of gradients in the velocity field. Sources and other phenomena can also contribute to the change of fluid with time. Convection, diffusion, and sources or sinks of the conserved or transported quantity can be tracked and defined by three principles: Conservation of mass, momentum and energy. The changes in one variable in these equations can give rise to changes in other variables. Analytically, these equations can only be solved for a limited number of flows. Numerically, with the arrival of modern computers with high process speed and large capacity, the solution of these partial differential equations has improved and led to new techniques in the field of computational fluid dynamics.

3.2 Conservation equations

3.2.1 Continuity (mass) equation

The continuity (mass) equation for a control volume of all the inlet and the outlet requires that the sum of the mass flow rates into the control volume equal the sum of the mass flow rates out of the control volume. The mass of fluid in this elemental volume depends on the amount of fluid entering and leaving through the faces.

For more general cases, the density can vary in time and in space, and the continuity equation takes on the more familiar form, when written in vector notation:

$$\frac{\partial \rho}{\partial t} + \nabla.(\rho \vec{\mathrm{v}}) = S_m \qquad 3\text{-}1$$

where $\frac{\partial \rho}{\partial t}$ is the change in density, and $\nabla.(\rho\vec{\mathrm{v}}) = 0$ is net flow of mass across boundaries (Convective term). The source S_m is the mass added to the continuous phase from the dispersed second phase. For incompressible fluids $\partial\rho/\partial t = 0$, and the equation becomes $\nabla.(\rho\vec{\mathrm{v}}) = 0$. For 2D axisymmetric geometries, the continuity equation is given by

$$\frac{\partial \rho}{\partial t} + \frac{\partial}{\partial x}(\rho \mathrm{v}_x) + \frac{\partial}{\partial r}(\rho \mathrm{v}_r) + \frac{\rho \mathrm{v}_r}{r} = S_m \quad 3\text{-}2$$

where *x* is axial coordinate, *r* is the radial coordinate, v_x, is the axial velocity and v_r is the radial velocity.

3.2.2 Momentum

The momentum equation, also called the Navier-Stokes equation, is a statement of conservation of momentum. Equation (3.3) present momentum transport by convection, diffusion, and several momentum sources (Batchelor, 2000).

$$\frac{\partial}{\partial t}(\rho\vec{\mathrm{v}}) + \nabla.(\rho\vec{\mathrm{v}}\vec{\mathrm{v}}) = -\nabla p + \nabla.(\bar{\bar{\tau}}) + \rho\vec{g} + \vec{F} \quad 3\text{-}3$$

In Eq. (3.3), the left hand side are the convection terms. The pressure gradient, a source term; the divergence of the stress tensor, the gravitational force, and other source terms are on the right hand side.

$$\bar{\bar{\tau}} = \mu\left[(\nabla\vec{\mathrm{v}} + \nabla\vec{\mathrm{v}}^T) - \frac{2}{3}\vec{\mathrm{v}}I\right] \quad 3\text{-}4$$

where μ is the molecular viscosity, *I* is the unit tensor.

For 2D axisymmetric geometries, the axial and radial momentum conservation equations are given by:

$$\frac{\partial}{\partial t}(\rho \mathrm{v}_x) + \frac{1}{r}\frac{\partial}{\partial x}(r\rho \mathrm{v}_x \mathrm{v}_x) + \frac{1}{r}\frac{\partial}{\partial r}(r\rho \mathrm{v}_r \mathrm{v}_x) = -\frac{\partial p}{\partial x} + \frac{1}{r}\frac{\partial}{\partial x}\left[r\mu\left(2\frac{\partial \mathrm{v}_x}{\partial x} - \frac{2}{3}(\nabla.\vec{\mathrm{v}})\right)\right] + \frac{1}{r}\frac{\partial}{\partial r}\left[r\mu\left(\frac{\partial \mathrm{v}_x}{\partial r} + \frac{\partial \mathrm{v}_r}{\partial x}\right)\right] + F_x \quad 3\text{-}5$$

and

$$\frac{\partial}{\partial t}(\rho \mathrm{v}_r)+\frac{1}{r}\frac{\partial}{\partial x}(r\rho \mathrm{v}_x \mathrm{v}_r)+\frac{1}{r}\frac{\partial}{\partial r}(r\rho \mathrm{v}_r \mathrm{v}_r)=$$
$$-\frac{\partial p}{\partial x}+\frac{1}{r}\frac{\partial}{\partial x}\left[r\mu\left(\frac{\partial \mathrm{v}_r}{\partial x}+\frac{\partial \mathrm{v}_x}{\partial r}\right)\right]+\frac{1}{r}\frac{\partial}{\partial r}\left[r\mu\left(2\frac{\partial \mathrm{v}_r}{\partial r}-\frac{2}{3}\frac{\mu}{r}(\nabla.\vec{\mathrm{v}})\right)\right]-2\mu\frac{\mathrm{v}_r}{r^2}+\frac{2}{3}\frac{\mu}{r}(\nabla.\vec{\mathrm{v}})+\rho\frac{\mathrm{v}_z^2}{r}+F_r$$

3-6

where

$$\nabla.\vec{\mathrm{v}}=\frac{\partial \mathrm{v}_x}{\partial x}+\frac{\partial \mathrm{v}_r}{\partial r}+\frac{\mathrm{v}_r}{r}$$

3.2.3 Energy

Heat transfer is often expressed as an equation for the conservation of energy. The equation for conservation of energy (total enthalpy) is:

$$\frac{\partial}{\partial t}(\rho E)+\nabla.(\vec{\mathrm{v}}(\rho E+p))=-\nabla.\left(\sum_j h_j J_j\right)+S_h \qquad 3\text{-}7$$

In this equation, the energy, E, is related to the static enthalpy, h_j, through the following relationship involving the pressure, P, and velocity magnitude, v:

$$E=h-\frac{p}{\rho}+\frac{\mathrm{v}^2}{2} \qquad 3\text{-}8$$

3.3 Computational Multiphase Flows Modelling

Computational fluid dynamics (CFD) is the name given to the solution of problems involving fluid flow, heat transfer, chemical species and turbulence models using computational and numerical techniques to convert the partial differential equation governing the flow with an algebraic equation. CFD can contribute to better understanding and analysis of problems that involve complex fluid flows, complex geometries and different boundary conditions, and has the ability to change the design parameters without the need for alterations to hardware. The time required to run CFD cases is usually favourable in comparison with the effort required to conduct experiments in zero-gravity. In the area where measurements are unfeasible or

difficult to obtain, CFD can guide the researchers to the cause of problems and provide full information about a flow field. The main stages in a CFD study are:

- Pre-processing step, involving the establishment of governing equations and boundary conditions, followed by the construction of a computational mesh
- Numerical solution of the governing equations
- Post-processing of the solution by way of the plotting and analysis of results.

3.4 Overview of Multiphase Flows Solvers

A multiphase model can only be used when multiple fluids are involved in a flow field. When a multiphase model is used, each of the fluids is assigned a separate set of properties, including the different densities and forces of different magnitude that may act on the fluids. The selection of the appropriate model for solving multiphase problems numerically depends on the flow regime in question. For the numerical calculation of multiphase flows there are two approaches: the Euler-Lagrange approach and the Euler-Euler approach (Ansys-Fluent, 2011). In the Euler-Lagrange approach, the fluid phase is treated as a continuum by solving the time averaged Navier-Stokes equations in the same manner as for a continuous fluid phase, while the Lagrangian particle tracking method is solved by tracking a large number of particles, bubbles or droplets through the calculated flow field using Newtonian equation of motion. Heat, mass, and momentum exchange is permitted between the dispersed and fluid phases. The model is widely used for coal and liquid fuel combustion, bubble columns, and gas spargers in stirred tanks. The Euler-Lagrange Model is inappropriate in any application where the volume fraction of the second phase is not negligible (Ansys-Fluent, 2011), for example modelling of liquid-liquid mixtures, fluidized beds. In the Euler-Euler approach, the volume fraction of each phase is introduced and assumed to be continuous functions of space and time. The volume fraction of each phase cannot be occupied by the other phases, and

their sum must equal to one. In Euler-Euler methods three different multiphase model are available in the ANSYS-Fluent CFD program: the volume of fluid (VOF) model, the mixture model, and the Eulerian model, and each model is developed for its own specific flow type. For the liquid and solid phases, an Eulerian granular multiphase model is recommended and separate sets of momentum equations are used. Gas sparging can be modelled using the Eulerian or mixture multiphase models. In this research study, the governing continuum conservation equations for bubble/drop flow were solved using the Volume of Fluid (VOF) method. The VOF model is a surface-tracking technique designed for two or more immiscible fluids where the position of the interface between the fluids is of interest (Ansys-Fluent, 2011). The VOF method is designed for flows with completely separated phases; the phases do not diffuse into each other (Ansys-Fluent, 2011). In the Euler-Euler approach, the different phases are treated mathematically as interpenetrating continua. Since the volume of a phase cannot be occupied by the other phases, the concept of phase volume fraction is introduced. These volume fractions are assumed to be continuous functions of space and time and their sum is equal to one. Conservation equations for each phase are derived to obtain a set of equations, which have similar structure for all phases. These equations are closed by providing constitutive relations that are obtained from empirical information, or, in the case of granular flows, by application of kinetic theory. In the Eulerian model a set of n momentum and continuity equations is derived by ensemble averaging the local instantaneous balance for each phase. Coupling is achieved through the pressure and interphase exchange coefficients. The manner in which this coupling is handled depends upon the type of phases involved; granular (fluid-solid) flows are handled differently than nongranular (fluid-fluid) flows. Momentum exchange between the phases is also dependent upon the type of mixture being modelled. FLUENT's user-defined functions (UDF-Manual, 2011) are used for the momentum exchange calculations.

3.5 The volume of fluid (VOF) model and background

In the VOF model, the motion of all phases is modelled by solving a single set of transport equations with appropriate jump boundary conditions at the interface (Krishna and van Baten, 1999). This model has been successfully employed in a wide range of multiphase flow cases, including stratified flows, free-surface flows, the steady or transient tracking of any liquid gas interface and the effects of surface tension (Ansys-Fluent, 2011). The work of Tomiyama et al. (1993) illustrated the capability of VOF to accurately simulate bubble shapes, which were shown to agree with the experimental published data of Bhaga and Weber (1981). Kawaji et al. (1997) noted a new result which was not observed experimentally when they compared the numerical simulation results of the VOF model of a two dimensional simulation of a Taylor bubble rising in a stagnant liquid filled tube to the results given by experimental analysis. The VOF simulations with gas-liquid systems could be used as an investigative tool for studying bubble rise and bubble-bubble interactions in gas-liquid bubble columns (Alhendal et al., 2010). The VOF model has been used to simulate a bubble's motion in bubbly flows (Cook and Behnia, 2001); (Essemiani et al., 2001); (Lörstad et al., 2004) and slug flow (Taha and Cui, 2006); (Kang et al., 2004). The VOF model is also suitable for the simulation of sharp fluid-fluid interfaces using a finite volume approach (Akhtar et al., 2007). One of the major drawback of the volume of fluid model is the so-called artificial coalescence of bubbles which occurs when their mutual distances is not larger than the size of the computational cell (Ranade, 2002).

3.5.1 The VOF Model Governing Equations

The concept of the VOF model was originally proposed by Hirt and Nichols (1981) in order to reduce the excessive computer memory required by the marker particle interface tracking method. Hirt and Nichols defined a volume fraction function (α) whose average value was

unity at any cell fully occupied by fluid and zero at any cell containing no fluid, and between zero and one in the cells where an interface was present.

This volume fraction function is then tracked through the domain by solving its transport equation, as well as a single set of conservation equations common to both phases, and the motion of the interface is then deduced indirectly from these results. The VOF model can also be used in problems consisting of more than two phases, as the volume fraction variables of the additional phases will be added in the computational domain. The model can have a steady or time-dependent (transient) implementation in order to track the motion of the bubble/drop. The movement of the gas–liquid interface is tracked based on the distribution of α_G, the volume fraction of gas in a computational cell, where $\alpha_G = 0$ in the liquid phase and $\alpha_G = 1$ in the gas phase. Therefore, the gas–liquid interface exists in the cell where α_G lies between 0 and 1. A single momentum equation, which is solved throughout the domain and shared by all of the phases, is given by Batchelor (2000):

$$\frac{\partial}{\partial t}(\rho\vec{\mathrm{v}}) + \nabla.(\rho\vec{\mathrm{v}}\vec{\mathrm{v}}) = -\nabla p + \nabla.[\mu(\nabla\vec{\mathrm{v}} + \nabla\vec{\mathrm{v}}^{T})] + \vec{F} \qquad 3\text{-}9$$

where v is treated as the mass-averaged variable:

$$\mathrm{v_m} = \frac{\alpha_G\rho_G\mathrm{v}_G + \alpha_L\rho_L\mathrm{v}_L}{\rho} \qquad 3\text{-}10$$

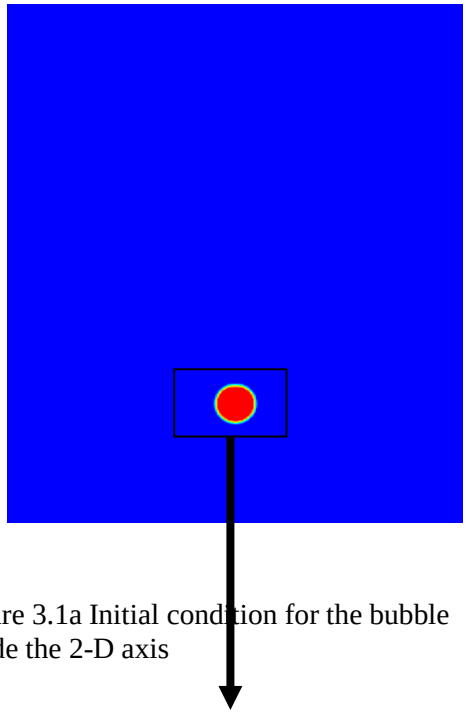

Figure 3.1a Initial condition for the bubble inside the 2-D axis

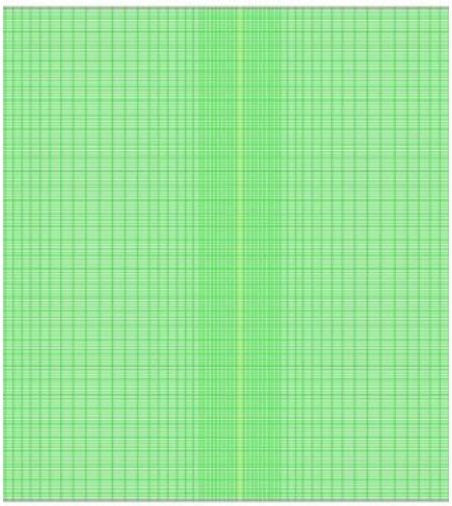

3-1b Typical mesh used for Marangoni cases

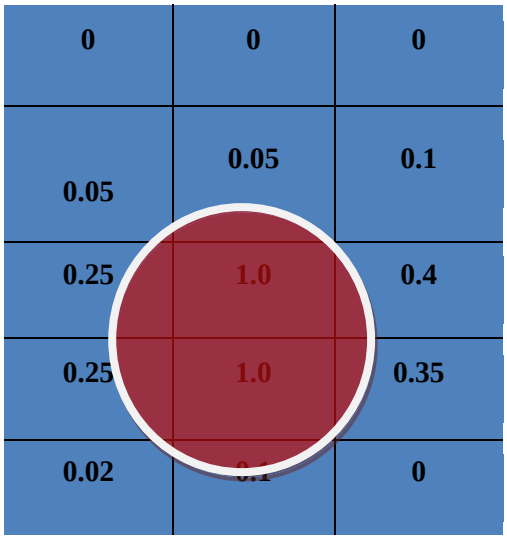

3-1c Volume of fluid (VOF) interface reconstruction

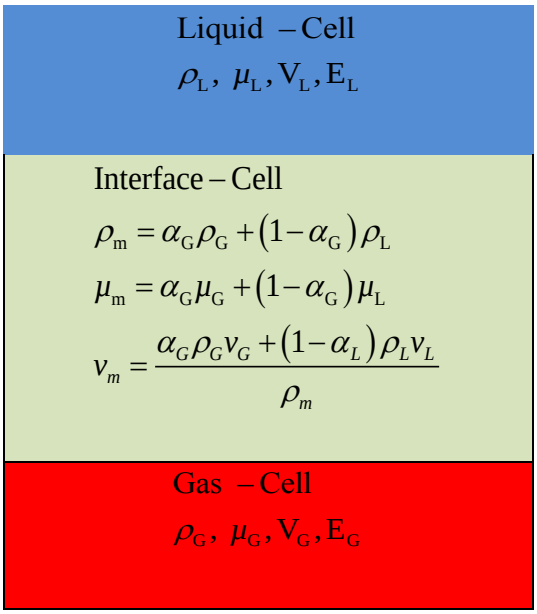

3-1d Volume fraction and properties in each cell in the bubble

Figure 3-1 Show volume fraction equation method employed in the simulations

The following three conditions are therefore possible for representation of, for example, the q_{th} fluid's volume fraction (α_G):

$\alpha_G = 0$: the cell does not contain the α_{th} fluid;

$\alpha_G = 1$: the cell is full of the q_{th} fluid;

$0 < \alpha_G < 1$: the cell contains the interface between the q_{th} fluid and one or more other fluids.

Based on the local value of α_G the appropriate properties and variables will be assigned to each control volume within the domain. The values for all variables and properties are calculated as volume-averaged values based on the weighted average of the values for the individual fluids. The variables and properties in any given cell are therefore either purely representative of one of the phases, or representative of a mixture of the phases, determined by the volume fraction contributions.

The VOF model includes the effects of surface tension along the interface between each pair of phases. The CSF model was used to compute the surface tension force for the cells containing the gas–liquid interface. With this model, the addition of surface tension to the VOF calculation results in a source term in the momentum equation, $\vec{F}$, (Brackbill et al., 1992):

$$\vec{F} = \sigma \frac{\rho k n}{\frac{1}{2}(\rho_L + \rho_G)} \qquad 3\text{-}11$$

Where σ is the coefficient of surface tension, *n* is the surface normal which is estimated from the gradient of the volume fraction and κ is the local surface curvature, calculated as follows (Brackbill et al., 1992):

$$k = -(\nabla \hat{n}) = \frac{1}{n}\left[\frac{n}{|n|}\nabla|n| - (\nabla . n)\right] \qquad 3\text{-}12$$

The tracking of the interface between the gas and liquid is accomplished by the solution of a continuity equation for the volume fraction of gas, which is:

$$\frac{\partial}{\partial t}(\alpha_G \rho_G) + \nabla \cdot (\alpha_G \rho_G \vec{v}_G) = 0 \qquad 3\text{-}13$$

The volume fraction equation will not be solved for the primary phase; the primary-phase volume fraction will instead be computed based on the following constraint:

$$\alpha_G + \alpha_L = 1 \qquad 3\text{-}14$$

where α_G and α_L are the volume fraction of the gas and liquid phases respectively. The properties appearing in the transport equations are determined by the presence of the component phases in each control volume. In a two-phase system, for example, if the phases are represented by the subscripts G and L, and the mixture density in each cell is given. The density and viscosity in each cell at the interface were computed by the application of the following equations:

$$\rho = \alpha_G \rho_G + (1-\alpha_G)\rho_L \qquad 3\text{-}15$$

$$\mu = \alpha_G \mu_G + (1-\alpha_G)\mu_L \qquad 3\text{-}16$$

where ρ_G, ρ_L, μ_G, and μ_L are the density and viscosity of the gas and liquid phases respectively, while α_G is the volume fraction of gas. In general, for the *n* phase system, the volume-fraction-averaged density takes on the following form:

$$\sum_{p=1}^{n} \alpha_q = 1 \qquad 3\text{-}17$$

All other properties (e.g. viscosity) are also computed in this manner. The energy equation is also shared among the phases:

$$\frac{\partial}{\partial t}(\rho E) + \nabla.[\vec{v}(\rho E) + p)] = \nabla.(\kappa_{eff} \nabla T) \qquad 3\text{-}18$$

The VOF model treats energy, E, and temperature, T, as mass-averaged variables:

$$E = \frac{\sum_{q=1}^{n} \alpha_q \rho_q E_q}{\sum_{q=1}^{n} \alpha_q \rho_q} \qquad 3\text{-}19$$

where E_q for each phase is based on the specific heat of that phase and the shared temperature. The effective thermal conductivity k_{eff} is also shared by the phases.

3.6 The Eulerian Model

In comparison to the previous models the Eulerian model is a more complicated and computationally expensive model, but potentially more accurate for general use. The Eulerian multiphase model available in the CFD code provides the ability to simulate multiple separate phases, and their interactions, in any combinations (i.e. liquids, gases and solids). However, the overview of this model will be limited to fluid-fluid flows. This model can handle any number of phases, and is only limited by memory requirements and convergence behaviour. The Eulerian model is based on solving continuity and momentum equations for each phase, and a single pressure is shared among them. Additionally, several interface drag coefficient functions are available to include in the model, as well as turbulence models which can be applied to all phases separately or to the mixture.

3.6.1 The Eulerian Model Governing Equations

In general, the mass conservation equation of the Eulerian model for phase q takes the following form:

$$\frac{\partial}{\partial t}\left(\alpha_q \rho_q\right) + \nabla.\left(\alpha_q \rho_q \vec{v}_q\right) = \sum_{p=1}^{n}\left(\dot{m}_{pq} - \dot{m}_{qp}\right) + S_q \qquad 3\text{-}20$$

where $\overrightarrow{v_q}$ is the velocity of phase q, the source term S_q on the right-hand side is zero by default, but can be specified by the user. The volume fractions are obtained from the phase continuity equations, ensuring the condition that the volume fractions sum to one within a control volume.

The momentum balance for the phase q can be generally written as:

$$\frac{\partial}{\partial t}\left(\alpha_q \rho_q \vec{v}_q\right) + \nabla.\left(\alpha_q \rho_q \vec{v}_q \vec{v}_q\right) = -\alpha_q \nabla P + \nabla.\overline{\overline{\tau}}_q + \alpha_q \rho_q \vec{g} + \sum_{p=1}^{n}\left(\vec{R}_{pq} + \dot{m}_{pq}\vec{v}_{pq} - \dot{m}_{qp}\vec{v}_{qp}\right) + \left(\vec{F}_q + \vec{F}_{lift,q} + \vec{F}_{vm,q}\right)$$

3-21

where P is the pressure, shared by all phases, and $\bar{\bar{\tau}}_q$ represents the stress-strain tensor of phase qth which is given as:

$$\bar{\bar{\tau}}_q = \alpha_q \mu_q \left(\nabla \vec{v}_q + \nabla \vec{v}_q^T \right) + \alpha_q \left(\lambda_q - \frac{2}{3} \mu_q \right) \nabla . \vec{v}_q \bar{\bar{I}} \qquad 3\text{-}22$$

μ_q and λ_q are the shear and bulk viscosity of phase q. The term $\vec{v}_{pq}$ is the interface velocity, which can be defined as follows:

If $\dot{m}_{pq} > 0 : \vec{v}_{pq} = \vec{v}_p$ (i.e. phase p mass is being transferred to phase q)

If $\dot{m}_{pq} < 0 : \vec{v}_{pq} = \vec{v}_q$ (i.e. phase q mass is being transferred to phase p)

$\vec{R}_{pq}$ is an interaction force between phases, $\vec{F}_q$ represents any external body force, $\vec{F}_{lift,q}$ is a lift force, and $\vec{F}_{vm,q}$ represents a virtual mass force. The momentum conservation equation must be closed with appropriate expressions for the interface force $\vec{R}_{pq}$. This force is subject to the following conditions:

$\vec{R}_{pq} = -\vec{R}_{qp}$ and $\vec{R}_{qq} = 0$

and depends on the friction, pressure, cohesion and other effects. ANSYS FLUENT uses a simple interaction model of the following form:

$$\sum_{p=1}^{n} \vec{R}_{pq} = \sum_{p=1}^{n} K_{pq} \left(\vec{v}_p - \vec{v}_q \right) \qquad 3\text{-}23$$

where K_{pq} is the interface momentum exchange coefficient which depends on a drag function that is based on a relative Reynolds number.

The lift forces acting on a particle (particle here can mean either a droplet or bubble in fluid-fluid flows) are mainly due to velocity gradients in the primary-phase flow field. In the ANSYS FLUENT model the inclusion of lift is not appropriate for closely packed particles or for very small particles, as the model is based on the assumption that the particle diameter is much smaller than the interparticle spacing. On the other hand, it must be kept in mind that the lift force will be more significant for larger particles. The lift force is added to the right-

hand side of the momentum equation for both phases. The lift force acting on a secondary phase p in a primary phase q is calculated from:

$$\vec{F}_{lift} = -C_l \rho_q \alpha_p \left(\vec{v}_q - \vec{v}_p\right) \times \left(\nabla \times \vec{v}_q\right) \qquad 3\text{-}24$$

where C_l is the lift coefficient, which typically takes a value of 0.5 for inviscid flow. In most cases, the lift force is insignificant compared to the drag force and can thus be ignored. In the ANSYS FLUENT model, by default, it is not included, but it can be specified if it is significant.

Another force term in the ANSYS FLUENT model is the virtual mass force, which is also added to the right-hand side for both phases. The virtual mass force effect occurs when a secondary phase p accelerates relative to the primary phase q. The inertia of the primary phase mass encountered by the accelerating particles exerts a virtual mass force on the particles:

$$\vec{F}_{vm} = 0.5\alpha_p \rho_q \left(\frac{d_q \vec{v}_q}{dt} - \frac{d_p \vec{v}_p}{dt} \right) \qquad 3\text{-}25$$

where $\frac{d_q}{dt}$ denotes the phase material time derivative of the form,

$$\frac{d_q(\phi)}{dt} = \frac{\partial(\phi)}{\partial t} + \left(\vec{v}_q . \nabla\right)\phi \qquad 3\text{-}26$$

The virtual mass effect is significant when the secondary phase density is much smaller than the primary phase density. In the ANSYS FLUENT model the virtual mass force is not included, by default, but it can be modelled when desired.

3.7 Solution algorithm of ANSYS-FLUENT

To solve the governing (transport) equations for the conservation equations, a pressure-based solver and a coupled-based solver are available in the ANSYS-FLUENT code, which for both methods the velocity field is obtained from the momentum equations. In the density-based

approach, the continuity equation is used to obtain the density field while the pressure field is determined from the equation of state. On the other hand, in the pressure-based approach, the pressure field is extracted by solving a pressure or pressure correction equation which is obtained by manipulating continuity and momentum equations. Only pressure-based solver algorithms is available in FLUENT for multiphase flow.

3.7.1 The Pressure-Based Segregated Algorithm

In the segregated algorithm the individual governing equations are solved one after another, and each variable is therefore updated in turn. Each solution loop in the segregated algorithm is made up of the following steps and describe in figure 3.2:

1. Updating flow properties including turbulent viscosity based on the current solution.
2. Solving the momentum equations, in a segregated manner, using the currently estimated values of pressure and face mass fluxes.
3. Solving the pressure correction equation using the velocity field, from the previous step, and the corresponding mass-fluxes.
4. Correcting the pressure, velocity field and face mass fluxes using the pressure correction obtained from the previous step.
5. Solving the equations for additional scalars such as turbulent quantities using the current values of the solution variables.
6. Updating the source terms arising from the interactions among different phases.
7. Checking for the convergence of the equations.

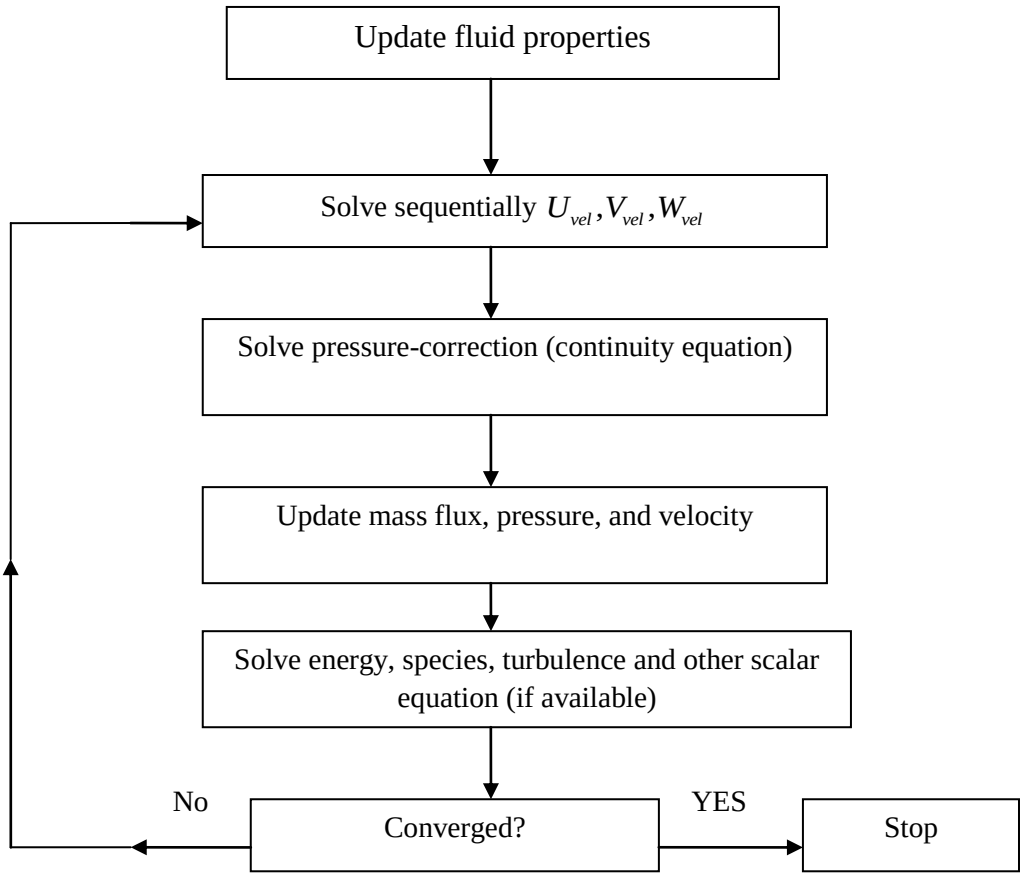

Figure 3-2 Overview of the Pressure-based solution methods

These steps are continued until the convergence criteria are satisfied. The segregated algorithm is efficient in terms of the required memory as the discretized equations need only be stored one at a time. On the other hand, the solution convergence can be relatively slow.

3.7.2 General Scalar Transport Equation: Discretization and Solution

The control volume technique consists of integrating the transport equations over each control volume. These integrations, and associated approximations, result in a set of discrete equations that express the conservation laws on a control-volume basis. Illustration of this procedure can be given by starting with writing the unsteady conservation equation for transport of a scalar quantity (ϕ), as follows:

$$\frac{\partial(\rho\phi)}{\partial t}+\nabla\cdot(\rho\boldsymbol{V}\phi)=\nabla\cdot(\Gamma_{\phi}\nabla\phi)+S_{\phi} \qquad 3\text{-}27$$

Equation (3.27) can be integrated over an arbitrary control volume V. This yield:

$$\int_{V}\frac{\partial\rho\phi}{\partial t}dV+\oint\rho\phi\vec{v}\cdot d\vec{A}=\oint\Gamma_{\phi}\nabla\phi\cdot d\vec{A}+\int_{V}S_{\phi}dV \qquad 3\text{-}28$$

where $\vec{A}$ is surface area vector, Γ_{ϕ} is diffusion coefficient for ϕ, $\nabla\phi$ is the gradient of ϕ, and S_{ϕ} is any source term of ϕ per unit volume. Equation 3.28 is applied to each cell in the computational domain. These integrals can be approximated by writing the cell face values of the unknown ϕ and relating them to the cell centre values of these unknowns, and for a given cell this discretization yields:

$$\frac{\partial\rho\phi}{\partial t}V+\sum_{f}^{N_{faces}}\rho_{f}\vec{v}_{f}\phi_{f}\cdot\vec{A}_{f}=\sum_{f}^{N_{faces}}\Gamma_{\phi}\nabla\phi_{f}\cdot\vec{A}_{f}+S_{\phi}V \qquad 3\text{-}29$$

where N_{faces} is the number of faces enclosing the cell, ϕ_f is value of ϕ at the centre of face *f*, $\vec{A}_f$ is the area of this face, $\rho_f\vec{v}_f\cdot\vec{A}_f$ is mass flux through the face, $\nabla\phi_f$ is the gradient of ϕ at the centre of face f, and V is cell volume. The discretized equation obtained is, in general, non-linear and contains the unknowns (ϕ) at the cell centre and in the surrounding neighbouring cells. A linearized form of equation (3.29) can be written as follows;

$$a_{P}\phi=\sum_{nb}a_{nb}\phi_{nb}+b \qquad 3\text{-}30$$

where a_P and a_{nb} are the linearized coefficients for the scalar quantities (ϕ and ϕ_{nb}) at the cell centre and surrounding neighbouring cells respectively. The number of the surrounding cells is equal to the number of faces enclosing the cell. A similar procedure can be conducted for the other cells in the computational domain, which results in a set of algebraic equations. ANSYS-FLUENT solves the resultant linear system using a point implicit (Gauss-Seidel) linear equation solver in conjunction with an algebraic multigrid (AMG) method.

3.8 Discretization of the Domain: Grid Generation

Because of the nonlinearity of the equation set, it is difficult to solve the governing equation analytically and the sets of equations have to be discretized before the systems can be solved. Discretization means approximating the transport equations by a system of algebraic equations for flow variables at some set of discrete locations in space and time. Gambit (2005) is a pre-processor used to great the geometry which describes the computational domain of the problem to be analyzed. In Gambit, the whole computational domain has to be divided into small control volumes in order to solve the discretized transport equation. A grid (also called a mesh and shown in figures 3-3) is the first step in designing and building the computational domain of flow model and is used to break the domain into a set of discrete sub-domains, or cells, or control volumes. The success of the CFD analysis is highly depends on how dense the cells of the computational domain is, which needs to be fine enough to capture the flow details; on the other hand, the larger the numbers of cells the more time it will take to converge and a CFD user should consider the computer capability and simulation time when simulating. The grid cells are usually tetrahedral, prisms, pyramids, or hexahedral in 3D domains or quadrilaterals and triangles in 2D domains. Quadrilateral for the 2D or hexahedral for the 3D are always structured. In 2D axissymmetry, non-uniform grids can be used to cluster a larger number of mesh cells in regions where there is needed and fewer mesh cells in other part to increase the simulation accuracy and reduce the simulation time.

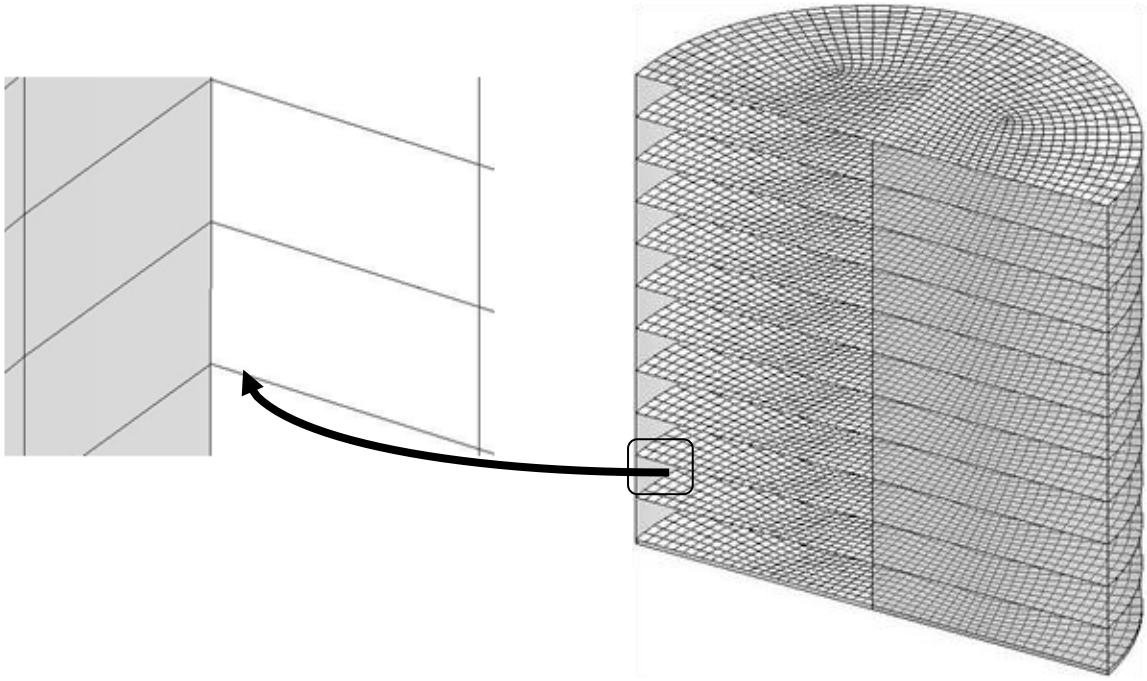

Figure 3-3a Control volume

Figure 3.3b The computational domain is discretized into a finite set of control volumes.

3.9 Spatial Discretization

Since FLUENT stores discrete values of the scalar ϕ at the cell centers, the face values ϕ_f are required to be interpolated from the cell centre values using one of the upwind scheme. FLUENT has several upwind schemes: first-order upwind, second-order upwind, power law, and QUICK. To do this, consider a steady-state conservation equation:

$$\frac{\partial}{\partial x}(\rho U \phi) = \frac{\partial}{\partial x}\left(\Gamma \frac{\partial \phi}{\partial x}\right) \qquad 3\text{-}31$$

where Γ and ρu are constant across the interval ∂x . Equation (3.31) can be integrated to yield the following solution describing how ϕ varies with x :

$$\phi = \phi_0 + (\phi_L - \phi_0)\frac{\exp\left(Pe\frac{x}{L} - 1\right)}{\exp(Pe - 1)} \qquad 3\text{-}32$$

where

$$\phi_0 = \phi\big|_{x=0}$$
$$\phi_L = \phi\big|_{x=L}$$

Depending on the value of the Peclet number, Pe,

$$Pe = \frac{\rho UL}{\Gamma} \qquad 3\text{-}33$$

which represent the ratio of the influence of convection to that of diffusion on the flow field, different limiting behaviour exists for the variation of between x = 0 and x = L, and according to these limiting, more differencing schemes cases are discussed below along with some more rigorous discretization,

3.9.1 Central-Differencing Scheme

For Pe = 0, the solution is purely diffusive, and there is no convection. The second-order central-differencing scheme calculates the face value for a variable (ϕ_f)as follows:

$$\phi_{f,CD} = \frac{1}{2}(\phi_0 + \phi_1) + \frac{1}{2}(\nabla\phi_0.\vec{r}_0 + \nabla\phi_1.\vec{r}_1) \qquad 3\text{-}34$$

where the indices 0 *and* 1 refer to the cells that share face f and $\vec{r}$ is the vector directed from the cell centroid toward the face centroid. In this approach, the upwind part is treated implicitly while the difference between the central-difference and upwind values is treated explicitly and the face value is calculated as follows:

$$\phi_f = \underbrace{\phi_{f,UP}}_{implicit\_part} + \underbrace{(\phi_{f,CD} - \phi_{f,UP})}_{Explicit\_part} \qquad 3\text{-}35$$

where UP stands for upwind. As indicated, the upwind part is treated implicitly while the difference between the central-difference and upwind values is treated explicitly. Provided that the numerical solution converges, this approach leads to pure second-order differencing.

3.9.2 First-Order Upwind Scheme

For Pe >>1, convection dominates, and also called Upwind Differencing Scheme. When first-order accuracy is desired, the value at the cell face can be assumed to be identical to the upstream value, i.e. $\phi_f = \phi$. First-order upwind is available in the pressure-based and density-based solvers.

3.9.3 Second-Order Upwind Scheme

In a modified version of first order upwind differencing, quantities at cell faces are computed using a multidimensional linear reconstruction approach based on the upwind neighbour and its neighbours. In this second order upwind differencing scheme, which makes use of a Taylor series expansion to describe the upwind gradients, the face value ϕ_f is computed using the following expression:

$$\phi_{f,SOU} = \phi + \nabla\phi.\vec{r} \qquad 3\text{-}36$$

where $\vec{r}$ is the displacement vector from the upstream cell centroid to the face centroid and ϕ and $\nabla\phi$ are the cell-centered value and its gradient in the upstream cell. This formulation requires the determination of the gradient ϕ_f in each cell, which is limited. It requires additional computational effort than the first order upwind method, but offers greater accuracy.

3.9.4 Power-Law Scheme

For intermediate values of the Peclet number, 0 < Pe < 10, The power-law discretization scheme interpolates the face value of a variable, ϕ , using the exact solution to a one-dimensional convection-diffusion as shown in eq. (3.31) and can be approximated by one that does not use exponentials, involving the Peclet number raised to an integral power. It is identical to the first order upwind differencing scheme in the limit of strong convection but offers slightly improved accuracy for the range of Peclet numbers mentioned above.

3.9.5 QUICK Scheme

FLUENT also provides the QUICK scheme for computing a higher-order value of the convected variable ϕ at a face. The QUICK scheme (Leonard and Mokhtari, 1990) is similar to the second order upwind differencing scheme, with modifications that restrict its use to quadrilateral or hexahedral meshes (Edward L. Paul et al., 2004). For the face e in Figure 3.4, if the flow is from left to right, such a value can be written as:

$$\phi_e = \theta\left[\frac{S_d}{S_d+S_c}\phi_P + \frac{S_c}{S_d+S_c}\phi_E\right] + (1-\theta)\left[\frac{S_u+2S_c}{S_u+S_c}\phi_P - \frac{S_c}{S_u+S_c}\phi_W\right] \qquad 3\text{-}37$$

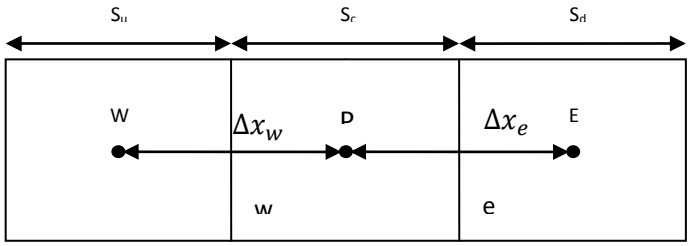

Figure 3-4 One-dimensional control volume

In this scheme, a quadratic function is fitted to the variable at three points, upwind cell centre and next upwind neighbour along with the value at the node *P*, and use to compute the face value. This scheme can offer improvements over the second order upwind differencing scheme for some flows with high swirl.

3.9.6 Third-Order MUSCL Scheme

Is available for all transport equations and most significantly for complex three-dimensional flows. Comparing to the second-order upwind scheme, the third-order MUSCL has a potential to improve spatial accuracy for all types of meshes by reducing numerical diffusion (Ansys-Fluent, 2011). This third-order convection scheme was conceived from the original

MUSCL by combination a central differencing scheme and second-order upwind scheme (van Leer, 1979) as:

$$\phi_f = \theta\phi_{f,CD} + (1-\theta)\phi_{f,SOU} \qquad 3\text{-}38$$

where $\theta_{f,CD}$ defined in Equation (3-34), and $\theta_{f,sou}$is computed using the second-order upwind scheme as described above in Equation (3-36). Compared to the second-order upwind scheme, the third-order MUSCL has a potential to improve spatial accuracy for all types of meshes by reducing numerical diffusion, most significantly for complex three-dimensional flows, and it is available for all transport equations.

3.9.7 Geometric Reconstruction Scheme

In the VOF, the geometric reconstruction scheme represents the interface between fluids using a piecewise-linear approach. It assumes that the interface between two fluids has a linear slope within each cell, and uses this linear shape for calculation of the advection of fluid through the cell faces using the standard interpolation schemes that are used in ANSYS FLUENT. The first step in this Geometric Reconstruction Scheme is calculating the position of the linear interface relative to the centre of each partially-filled cell based on information about the volume fraction and its derivatives in the cell. Then calculating the advecting amount of fluid through each face using the computed linear interface representation and information about the normal and tangential velocity distribution on the face. Finally, using the balance of fluxes calculated during the previous step, the volume fraction in each cell is obtaining.

Table 3-1 : Summary of spatial discretization scheme (Marshall and Bakker, 2003)	
Discretization Scheme	**Description, Advantages, and Disadvantages**
Central	Good when diffusion dominates. Assumes there is no convection, and that variables vary linearly from cell center to cell center. For convective flows, errors can be reduced by the use of a refined grid. This scheme is recommended for LES simulations.
First order upwind	Good when convection dominates and the flow is aligned with the grid. Assumes the face value for each variable is equal to the upstream cell center value. Stable, and a good way to start off a calculation. A switch to a higher order scheme is usually recommended once the solution has partially converged.
Second order upwind	Good for full range of Peclet numbers. Computes the face value for each variable from gradients involving the upwind neighbour and its neighbour s.
Power law	Good for intermediate values of Peclet number. Computes the face value for each variable from gradients expressed in the form of a power law function. For high Peclet numbers, results are equivalent to first order upwind.
QUICK	Good for full range of Peclet numbers. Similar to second order upwind, but restricted to quadrilateral and hexahedral meshes.
Third-Order MUSCL Scheme	Is available for all transport equations and most significantly for complex three-dimensional flows. Comparing to the second-order upwind scheme, the third-order MUSCL has a potential to improve spatial accuracy for all types of meshes by reducing numerical diffusion.

3.10 Temporal Discretization

The discrete location in time means that an unsteady flow will be divided in small time steps. A discretization scheme gives for flow variables like pressure or velocity a relation between a particular cell and its neighbours, and relates information of the previous time step with the

current time step. The relations for space and time form an equation for every cell, which yields to a system of equations with a size equal the number of cells. Temporal discretization involves the integration of every term in the differential equations over a time step Δt to solve a time-dependent problem. The time derivative is discretized using backward differences, the time derivative can be approximated to first order as:

$$\frac{\partial \phi}{\partial t} = F(\phi) \qquad 3\text{-}39$$

where the function F incorporates any spatial discretization. If the time derivative is discretized using backward differences, the first-order accurate temporal discretization is given by:

$$\frac{\phi^{n+1} - \phi^{n}}{\Delta t} = F(\phi) \qquad 3\text{-}40$$

and the second-order discretization is given by:

$$\frac{3\phi^{n+1} - 4\phi^{n} + \phi^{n-1}}{2\Delta t} = F(\phi) \qquad 3\text{-}41$$

where ϕ is a scalar quantity, $n+1$ is the value at the next time level, $t + \Delta t$ is the value at the current time level, t, and $n-1$ is the value at the previous time level, $t - \Delta t$.

3.10.1 Implicit and Explicit time integration

Explicit methods are best suited to certain flow conditions, such as compressible flow, while an implicit method is usually the most robust and stable choice for a wide variety of applications. The major difference between the explicit and implicit methods is whether $f(\phi)$ in Eq. (3-43) is evaluated at the current time (Explicit), $f(\phi) = f(\phi^n)$, or at the new time (Implicit): $f(\phi) = f(\phi^{n+1})$, since ϕ^{n+1} in a given cell is related to in neighbouring cells through $f(\phi^{n+1})$,:

$$\phi^{n+1} = \phi^{n} + \Delta t F(\phi^{n+1}) \qquad 3\text{-}42$$

This implicit equation can be solved iteratively at each time level before moving to the next time step. The advantage of the fully implicit scheme is that it is unconditionally stable with respect to time step size. Here, the time step Δt is limited by the Courant-Friedrich-Lewy condition (CFL). In order to be time-accurate, all cells in the domain must use the same time step, and must be the minimum of all the local time steps in the domain for stability.

3.10.2 Time Schemes in Multiphase Flow

In many multiphase applications, the process can vary spatially as well as temporally. In order to accurately model multiphase flow, both higher-order spatial and time discretization schemes are necessary. In addition to the first-order time scheme, the second-order time scheme is available in the Eulerian multiphase model and with the VOF Implicit Scheme. In multiphase flow, a general transport equation (3-39) may be written as:

$$\frac{\partial(\alpha\rho\phi)}{\partial t} + \nabla.(\alpha\rho\bar{u}\phi) = \nabla.\overline{\overline{\tau}} + S_\phi \qquad 3\text{-}43$$

where ϕ is either a mixture or a phase variable, α is the phase volume fraction (unity for the mixture equation), ρ is the mixture phase density, $\bar{u}$ is the mixture or phase velocity (depending on the equations), $\overline{\overline{\tau}}$ is the diffusion term, and S_ϕ is the source term. As a fully implicit scheme, this second-order time-accurate scheme achieves its accuracy by using an Euler backward approximation in time (see eq. 3-41). The general transport equation, Equation (3-43) is discretized as:

$$\frac{2(\alpha_P\rho_P\phi_P V)^{n+1} - 4(\alpha_P\rho_P\phi_P V)^{n} + (\alpha_P\rho_P\phi_P V)^{n-1}}{2\Delta t} = \sum\left[A_{nP}(\phi_{nP} - \phi_p)\right]^{n+1} + S_U^{n+1} - S_P^{n+1}\phi_P^{n+1} \qquad 3\text{-}44$$

Equation (3-44) can be written in simpler form:

$$A_P\phi_P = \sum A_n b\phi_n b + S_\phi \qquad 3\text{-}45$$

where

$$A_P = \sum A_{nP}^{n+1} + S_P^{n+1} + \frac{1.5(\alpha_P \rho_P V)^{n+1}}{\Delta t} \qquad 3\text{-}46$$

$$S_\phi = S_U^{n+1} + \frac{2(\alpha_P \rho_P \phi_P V)^n - 0.5(\alpha_P \rho_P \phi_P V)^{n-1}}{\Delta t} \qquad 3\text{-}47$$

This scheme is unconditionally stable; however, the negative coefficient at the time level t_{n-1}, of the three-time level method, may produce oscillatory solutions if the time steps are large. This problem can be eliminated if a bounded second-order scheme is introduced. However, oscillating solutions are most likely seen in compressible liquid flows. Therefore, a bounded second-order time scheme has been implemented for compressible liquid flows only. For single phase and multiphase compressible liquid flows, the second-order time scheme is, by default, the bounded scheme.

3.10.3 Volume-of-Fluid Model Time Schemes

In the Volume-of-Fluid model, the volume fraction equation may be solved either through implicit or explicit time discretization.

When the implicit scheme is used for time discretization, FLUENT's standard finite-difference interpolation schemes, QUICK, Second Order Upwind and First Order Upwind, and the Modified HRIC schemes, are used to obtain the face fluxes for all cells, including those near the interface.

$$\frac{\alpha_L^{n+1}\rho_L^{n+1} - \alpha_L^n \alpha_L^n}{\Delta t} V + \sum_f (\rho_L U_f^{n+1} \alpha_{L,f}^{n+1}) = \left[S_{\alpha_L} + \sum_{G=1}^{n} (\dot{m}_{GL} - \dot{m}_{LG}) \right] V \qquad 3\text{-}48$$

where $n+1$ and n represents the index for the new and previous time step, respectively. $\alpha_{q,f}$ is the face value of the q^{th} volume fraction, computed from the first- or second-order upwind, Quadratic Upwind Interpolation for Convective Kinematics (QUICK), Compressive Interface Capturing Scheme for Arbitrary Meshes (CICSAM) and High Resolution Interface Capturing (HRIC) schemes. V is the volume of cell and U_f is the volume flux through the face, based on normal velocity. The face fluxes were interpolated either using interface

reconstruction or using a finite volume discretization scheme. The reconstruction based scheme investigated was Geometric Reconstruction (GR) method given by Donor-Acceptor scheme can be used only with quadrilateral or hexahedral meshes. For the computations of interpolation near the interface, the control-volume formulation required that convection and diffusion fluxes through the control volume faces be computed and balanced with source terms within the control volume itself. In the geometric reconstruction and donor-acceptor schemes, an interpolation treatment was applied to the cells that lie near the interface between two phases.

Since Equation (3-48) requires the volume fraction values at the current time step (rather than at the previous step, as for the explicit scheme), a standard scalar transport equation is solved iteratively for each of the secondary-phase volume fractions at each time step.

The implicit scheme can be used for both time-dependent and steady-state calculations. In the explicit approach, FLUENT's standard finite-difference interpolation schemes are applied to the volume fraction values that were computed at the previous time step.

$$\frac{\alpha_L^{n+1}\rho_L^{n+1}-\alpha_L^n\alpha_L^n}{\Delta t}V+\sum_f(\rho_L U_f^n \alpha_{L,f}^n)=\left[S_{\alpha_L}+\sum_{G=1}^{n}(\dot{m}_{GL}-\dot{m}_{LG})\right]V \qquad 3\text{-}49$$

This formulation does not require iterative solution of the transport equation during each time step, as is needed for the implicit scheme. When the explicit scheme is used for time discretization, the face fluxes can be interpolated either using interface reconstruction or using a finite volume discretization scheme.

3.10.4 Evaluation of Gradients and Derivatives

Gradients are needed not only for constructing values of a scalar at the cell faces, but also for computing secondary diffusion terms and velocity derivatives. The gradient $\nabla\phi$ of a given variable ϕ is used to discretize the convection and diffusion terms in the flow conservation

equations. The gradients are computed in according to the following methods: Green-Gauss Cell-, Green-Gauss Node- or Least Squares Cell-based methods.

3.10.5 Green-Gauss Theorem

When the Green-Gauss theorem is used to compute the gradient of the scalar ϕ at the cell center c_0 , the following discrete form is written as:

$$(\nabla\phi)_{c0} = \frac{1}{v}\sum_f \overline{\phi_f}\vec{A}_f \qquad 3\text{-}50$$

where ϕ_f is the value of ϕ at the cell face centroid, computed as shown in the sections below. The summation is over all the faces enclosing the cell.

3.10.6 Green-Gauss Cell-Based Gradient Evaluation

By default, the face value $\overline{\phi_f}$, in Equation (3-50) is taken from the arithmetic average of the values at the neighbouring cell centers, i.e.,

$$\overline{\phi_f} = \frac{\phi_{c0} + \phi_{c1}}{2} \qquad 3\text{-}51$$

3.10.7 Green-Gauss Node-Based Gradient Evaluation

Alternatively, $\overline{\phi_f}$, can be computed by the arithmetic average of the nodal values on the face:

$$\overline{\phi_f} = \frac{1}{N_f}\sum_n^{Nf} \overline{\phi_n} \qquad 3\text{-}52$$

where N_f is the number of nodes on the face.
The nodal values,$\overline{\phi_n}$, Equation (3-52), are constructed from the weighted average of the cell values surrounding the nodes. This scheme reconstructs exact values of a linear function at a node from surrounding cell-centered values on arbitrary unstructured meshes by solving a constrained minimization problem, preserving a second-order spatial accuracy. The node-based averaging scheme is known to be more accurate than the default cell-based scheme for unstructured meshes.

3.10.8 Least Squares Cell-Based Gradient Evaluation

In this method the solution is assumed to vary linearly. In Figure 3-5, the change in cell values between cell c_0 and c_i along the vector δr_i from the centroid of cell c_0 to cell c_i, can be expressed as:

$$(\nabla\phi)_{co}.\Delta r_i = (\phi_{ci} - \phi_{c0}) \qquad 3\text{-}53$$

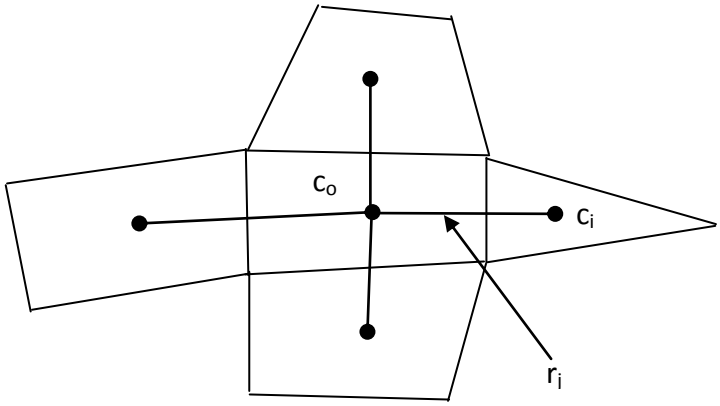

Figure 3-5 Cell centroid evaluation

If we write similar equations for each cell surrounding the cell c_0, we obtain the following system written in compact form:

$$[J](\nabla\phi)_{co} = (\Delta\phi) \qquad 3\text{-}54$$

where $[J]$ is the coefficient matrix which is purely a function of geometry. The objective here is to determine the cell gradient, $\nabla\phi_o = \phi_x\hat{i} + \phi_y\hat{j} + \phi_z\hat{k}$, by solving the minimization problem for the system of the non-square coefficient matrix in a least-squares sense. The above linear-system of equation is over-determined and can be solved by decomposing the coefficient matrix using the Gram-Schmidt process. This decomposition yields a matrix of weights for each cell. Thus for our cell-centered scheme this means that the three components of the weights $(W^x_{i0,}W^y_{i0,}W^z_{i0,})$ are produced for each of the faces of cell c_0. Therefore, the gradient at

the cell center can then be computed by multiplying the weight factors by the difference vector $\Delta\phi = (\phi_{ci} - \phi_{c0})$:

$$(\phi_x)_{c0} = \sum_{i=1}^{n} W_{i0}^{x}(\phi_{ci} - \phi_{c0})$$
$$(\phi_y)_{c0} = \sum_{i=1}^{n} W_{i0}^{y}(\phi_{ci} - \phi_{c0}) \qquad 3\text{-}55$$
$$(\phi_z)_{c0} = \sum_{i=1}^{n} W_{i0}^{z}(\phi_{ci} - \phi_{c0})$$

3.11 Pressure-Based Solver

Discretization of the momentum and continuity equations and their solution by means of the pressure-based solver are addressed by considering the steady-state continuity and momentum equations in integral form:

$$\oint \rho\vec{u}.d\vec{A} = 0 \qquad 3\text{-}56$$

$$\oint pI.d\vec{A} + \oint \bar{\bar{\tau}}.d\vec{A} + \int_V \vec{F}dV \qquad 3\text{-}57$$

where I is the identity matrix, $\bar{\bar{\tau}}$ is the stress tensor, and $\vec{F}$ *is* the force vector.

3.11.1 Discretization of the Continuity and Momentum Equations

The discretized form of the *x*-momentum equation, for example, can be obtained by setting:

$\phi = u$

$$a_P u = \sum_{nb} a_{nb} u_{nb} + \sum p_f A.\hat{i} + S \qquad 3\text{-}58$$

where the subscript nb refers to neighbour cells, and $a_p$and a_{nb} are the linearized coefficients for the velocity component (u and u_{nb}) at the cell centre and surrounding neighbour cells respectively. P_f is the pressure value at the faces enclosing the cell in question and S is any other momentum source term contributions. The number of surrounding cells is equal to the number of faces enclosing the cell. A similar discretization procedure can

be conducted for the other cells in the computational domain, which results in a set of algebraic equations. If the pressure field and face mass fluxes are known, Equation (3.58) can be solved directly and a velocity field obtained. However, the pressure field and face mass fluxes are not known a priori and must be obtained as a part of the solution. Equation (3.58) requires particularly the value of the pressure at the face between two cells c_0 and c_1 shown in Figure (3.7), as an example. The face pressure value can be obtained from interpolating between cell centre values employing an interpolation scheme, as ANSYS-FLUENT stores both pressure and velocity at cell centres using a co-located scheme. There are different methods of pressure interpolation available in ANSYS FLUENT, which will be addressed next.

In the default pressure interpolation scheme the cell-face pressure values are interpolated using the discretized momentum equation coefficients:

$$p_f = \frac{\frac{p_{c0}}{a_{p,c0}} + \frac{p_{c1}}{a_{p,c1}}}{\frac{1}{a_{p,c0}} + \frac{1}{a_{p,c1}}} \qquad 3\text{-}59$$

This formulation gives a good estimation to the pressure field as long as the pressure variation between cell centres is smooth. However, in some cases, include two-phase problems, there may be large gradients in the momentum source terms that result in high pressure gradients across the cells.

A simpler alternative for obtaining cell-face pressures is a standard linear interpolation between adjacent cell-centre values. However, for multiphase problems this linear pressure interpolation scheme is only available with the mixture model. Another scheme is the body-force-weighted scheme in which the face pressure is computed by assuming that the normal gradient of the difference between pressure and body forces is constant. This scheme works well for both the VOF and mixture models. However, the recommended, and default, scheme

for use with the VOF in ANSYS-FLUENT is the PRESTO! (Pressure Staggering Option) scheme. The PRESTO! scheme uses the discrete continuity balance for a staggered control volume about the face to compute the staggered (i.e. face) pressure.

Cell-face mass fluxes are also required in equation (3.58), since they appear in the a_{nb} and a_P coefficients arising from discretization of the convection terms. They are also required for a discretized form of the continuity equation. The steady-state continuity equation may be written in integral form as follows:

$$\oint \rho \vec{v}.d\vec{A} = 0 \qquad 3\text{-}60$$

and applying this to the control volume illustrated in figure (3-7) leads to the following discrete equation:

$$\sum_{f}^{N_{faces}} J_f A_f = 0 \qquad 3\text{-}61$$

where J_f represents the mass flux (ρv_n) through face *f*.

To evaluate the cell-face mass fluxes again requires some interpolation since the velocity values are stored at the cell centres. In ANSYS-FLUENT the velocity face values are not interpolated linearly, as this may lead to unphysical checker-boarding of pressure; instead, a momentum-weighted averaging procedure is employed. The momentum-weighted averaging procedure is based on the use of weighting factors that utilize the a_P coefficient from equation (3.31). Thus, the face mass flux (J_f) can be written as:

$$J_f = \rho_f \frac{a_{p,c0}u_{n,c0} + a_{p,c1}u_{n,c1}}{a_{p,c0} + a_{p,c1}} + d_f((p_{c0} + (\nabla p)_{c0}.\vec{r}_0) - (p_{c1} + (\nabla p)_{c1}.\vec{r}_1)) = \hat{J}_f + d_f(p_{c0} + p_{c1}) \qquad 3\text{-}62$$

where the term d_f is a function of $\bar{a}_P$, the average of the momentum equation a_P coefficients for the cells on either side of face *f*, and P_{c_0}, P_{c_1} and v_{n,c_0}, v_{n,c_1} are the pressure and face normal velocities, respectively, within the two cells on either side of the face.

3.11.2 Pressure-Velocity Coupling

The momentum equations, for example Eq. (3.62) for the *x*-momentum, can be solved to obtain the velocity field if the pressure field is known a prior. The continuity equation cannot be used directly to obtain the pressure field. However, an iterative procedure is usually used to correct the pressure field in order to ensure that the velocity field satisfies the continuity equation. Such iterative procedure is generally referred to as pressure correction scheme. There are several pressure-velocity coupling algorithms available in ANSYS FLUENT, including: SIMPLE, SIMPLEC, PISO, COUPLED, and Fractional Step (FSM). For Eulerian multiphase calculations, ANSYS FLUENT uses the phase coupled SIMPLE (PC-SIMPLE) algorithm for the pressure-velocity coupling. PC-SIMPLE is an extension of the SIMPLE algorithm to multiphase flows. The velocities are solved coupled by phases, but in a segregated fashion. Pressure and velocities are then corrected so as to satisfy the continuity constraint.

In the SIMPLE algorithm, a guessed pressure field is used in the solution of the momentum equations in the segregated algorithms. The new computed velocities will not, in general, satisfy the continuity equation, so corrections to the velocities will need to be determined. A pressure correction is computed then based on the velocity corrections, which then add to update the original guessed pressure. Following the solution of the remaining problem variables, the iteration is complete and the entire process repeated. All iterative algorithms have the same general structure: they start with a guessed pressure field (P^*). With a known pressure field it is possible to solve the momentum equations and determine a temporal velocity field. Then a pressure correction (p') is calculated based on these temporal velocities. With these pressure corrections the final velocities and pressures, then the resulting face mass fluxes (J_f^*) can be obtained:

$$J^*_f = \hat{J}^*_f + d_f(p^*_{c0} - p^*_{c1}) \quad 3\text{-}63$$

Corrections ($\acute{J}_f$) are then added to these face fluxes (J_f^*) in order to ensure they satisfy the discretized continuity equation. Therefore, the corrected face flux (J_f) can be written as:

$$J_f = J^*_f + J'_f \quad 3\text{-}64$$

ANSYS-FLUENT defines the correction value ($\acute{J}_f$) as following:

$$J'_f = d_f(p'_{c0} - p'_{c1}) \quad 3\text{-}65$$

where p' represent the cell pressure correction. The corrected mass fluxes equation (3.61) is substituted into the discrete continuity equation (3.64), and equation (3.65) used to express the flux corrections in terms of pressure corrections. This leads to a discrete equation for the pressure corrections:

$$a_p p' = \sum a_{nb} p'_{nb} + b \quad 3\text{-}66$$

where the source term *b* represents the net flow rate into the cell:

$$b = \sum_{f}^{N\ faces} J^*_f A_f \quad 3\text{-}67$$

The pressure corrections ($\acute{P}$) obtained from solving equation (3.66) can then be used to correct the cell pressure and the face mass fluxes as follows:

$$p = p^* + a_f p' \quad 3\text{-}68$$

and

$$J_f = J^*_f + d_f(p'_{c0} - p'_{c1}) \quad 3\text{-}69$$

where α_P is the under-relaxation factor for pressure.

The SIMPLEC procedure is similar to the SIMPLE procedure. The only difference between SIMPLEC and SIMPLE lies in the expression used for the face flux correction, J'_f. As in SIMPLE, the correction equation may be written as shown in Equation (3-70):

$$J_f = J^*_f + d_f(p'_{c0} - p'_{c1}) \quad 3\text{-}70$$

However, the coefficient d_f is redefined as a function of $\overline{\left(a_p - \sum_{nb} a_{nb}\right)}$. The use of this modified correction equation has been shown to accelerate convergence in problems where pressure-velocity coupling is the main deterrent to obtaining a solution (Van Doormaal and Raithby, 1984).

One of the limitations of the SIMPLE and SIMPLEC algorithms is that new velocities and corresponding fluxes do not satisfy the momentum balance after the pressure-correction equation is solved. As a result, the calculation must be repeated until the balance is satisfied. To improve the efficiency of this calculation, the PISO algorithm performs two additional corrections: neighbour correction and skewness correction.

The main idea of the PISO algorithm is to move the repeated calculations required by SIMPLE and SIMPLEC inside the solution stage of the pressure-correction equation. After one or more additional PISO loops, the corrected velocities satisfy the continuity and momentum equations more closely. This iterative process is called a momentum correction or "neighbour correction". The PISO algorithm takes a little more CPU time per solver iteration, but it can dramatically decrease the number of iterations required for convergence, especially for transient problems. For the flow problem on hand it is chosen to use the PISO algorithm; The PISO algorithm is highly recommended for all transient flow calculations, especially when the use of a large time step is intended. Due to the second pressure correction it is possible to enlarge the time step, which means a considerable decrease in demanded CPU-time. It is also possible to increase the Under-Relaxation-Factor of the velocities, which means faster convergence and thus also decreased CPU-time.

3.11.3 Under-Relaxation of Variables

Because of the nonlinearity of the equation set being solved by FLUENT, it is necessary to control the change of ϕ. If ϕ_{old} is the value of the variable from the previous iteration and ϕ

is the new value, then some small difference or change in the variable brings the variable from the old value to the new one:

$$\phi = \phi_{old} + \Delta\phi \qquad 3\text{-}71$$

underrelaxation factors, α, typically range from 0.1 to 1.0 is used in all cases for some material properties and in the pressure-based coupled algorithm. This process is called underrelaxation, and α is used to reduces the change of ϕ produced during each iteration at the expense of slowing the rate of convergence as follows:

$$\phi = \phi_{\text{old}} + \alpha\Delta\phi \qquad 3\text{-}72$$

Then the under-relaxation of equations is used in the pressure-based solver to stabilize the convergence behaviour of the outer nonlinear iterations:

$$\frac{\alpha_p \phi}{\alpha} = \sum_{nb} \alpha_{nb}\phi_{nb} + b + \frac{1-\alpha}{\alpha}\alpha_p \phi_{old} \qquad 3\text{-}73$$

The Courant-Friedrichs-Lewy (CFL) number is a solution parameter in the pressure-based coupled algorithm and can be written in terms of α:

$$\frac{1-\alpha}{\alpha} = \frac{1}{CFL} \qquad 3\text{-}74$$

3.11.3 General approach - convergence

The iterative process is repeated until the change in the variable from one iteration to the next becomes so small that the solution can be considered converged and all discrete conservation equations (momentum, energy, etc.) are obeyed in all cells to a specified tolerance. In addition the solution no longer changes with additional iterations, and mass, momentum, energy and scalar balances are obtained.

3.11.4 Residuals

Residuals measure imbalance (or error) in conservation equations. The absolute residual at point P is defined as:

$$R_p = \left| \frac{a_b \phi_b - \sum_{nb} a_{nb} \phi_{nb}}{a_b \phi_b} \right| \qquad 3\text{-}75$$

Residuals are usually scaled relative to the local value of the property *f* in order to obtain a relative error:

$$R_{p,scaled} = \left| \frac{a_b \phi_b - \sum_{nb} a_{nb} \phi_{nb} - b}{a_b \phi_b} \right| \qquad 3\text{-}76$$

They can also be normalized, by dividing them by the maximum residual that was found at any time during the iterative process. An overall measure of the residual in the domain is:

$$R^{\phi} = \frac{\sum_{all\ cells} \left| a_p \phi_p - \sum_{nb} a_{nb} \phi_{nb} - b \right|}{\sum_{all\ cells} a_b \phi_p} \qquad 3\text{-}77$$

It is common to require the scaled residuals to be on the order of 10^{-3} to 10^{-4} or less for convergence.

3.11.5 Time-Advancement Algorithm

For steady-state flows, the governing equations do not contain time-dependent terms. For time-dependent flows, the discretized form of the generic transport equations is of the following form:

$$\int_V \frac{\partial \rho \phi}{\partial t} dV + \oint \rho^{n+1} \phi^{n+1} \bar{u}^{n+1} . d\vec{A} = \oint \Gamma_{\phi}^{n+1} \nabla \phi^{n+1} . d\vec{A} + \int_V S_{\phi}^{n+1} dV \qquad 3\text{-}78$$

As a standard default approach, all convective, diffusive, and source terms are evaluated from the fields for time level $n+1$. In the pressure-based solver, the overall time-discretization error is determined by both the choice of temporal discretization (e.g., first-order, second-order) and the manner in which the solutions are advanced to the next time step (time-advancement scheme). Temporal discretization introduces the corresponding truncation error; $O(\Delta t), O[(\Delta t)^2]$, for first-order and second-order, respectively. The segregated solution process by which the equations are solved one by one introduces splitting error. There are

two approaches to the time-advancement scheme depending on how we want to control the splitting error.

3.11.6 Iterative and Non-Iterative Time-Advancement Scheme

The iterative scheme is the default in FLUENT. In the iterative scheme, all the equations are solved iteratively, for a given time-step, until the convergence criteria are met. With this iterative scheme, non-linearity of the individual equations and inter-equation couplings are fully accounted for, eliminating the splitting error, but requires a considerable amount of computational effort due to a large number of outer iterations performed for each time-step. In the non-iterative time-advancement (NITA) scheme, one does not really need to reduce the splitting error to zero, but only have to make it the same order as the truncation error. The NITA scheme does not need the outer iterations, performing only a single outer iteration per time-step, which significantly speeds up transient simulations.

Chapter 4 Benchmark test cases for bubble dynamics in zero-gravity condition

4.1 Introduction

One of the issues associated with the numerical predictions of flow regimes in zero gravity is their validation against available data. Before proceeding to examine and investigate in detail the impact of changing the boundary conditions and parameters, the very challenging and often overlooked task of multiphase code validation and verification must be performed before beginning any multiphase simulations, especially in zero gravity. Predicting surface tension-dominated flows numerically is a challenging task, since numerical errors caused by the discretisation of this singular term can lead to large errors: so-called spurious currents (Herrmann et al., 2008). If the correct model is used and if the results obtained are verified against results available from the literature, code validation and verification can help to solve multiphase flow. With regard to the verification process, the relationship between the simulation and the correct mathematics and method being used is the primary concern; however, in the validation process, the comparison between computational and experimental data is the issue. Verification is primarily a mathematics issue; validation is primarily a physics issue (Roache, 1998).

4.2 Numerical model, boundary and operating conditions

The objective of this chapter is to simulate the behaviour of a single bubble under the influence of a linear temperature gradient in a zero-gravity environment using CFD code. The results obtained are then be validated against an existing experimental method from the literature before proceeding to the main topic. For the verification and validation process, the thermocapillary flow of an isolated N_2 bubble in ethanol (Pr 16.2) in a two-dimensional axisymmetrical cylinder was first investigated.

A description of the geometry in question is shown in Figure 4.1, and the following assumptions are made for all numerical simulations:

1. The width of the domain is 20D and the height of the domain is 20D.
2. The thermocapillary velocity is small and the flow is laminar.
3. The upper and lower surfaces are flat and non-deformable; adiabatic and non-slip wall conditions are applied to all surfaces.
4. A steady-state temperature distribution is established as an initial condition before releasing the bubble into the unsteady motion, where the top and bottom walls are maintained at constant temperatures: $T_{Top} > T_{Bottom}$
5. The host liquid is an incompressible Newtonian fluid and an assumption of constant properties is applicable, except for surface tension.
6. The driving force for the flow is the variation of surface tension according to temperature, which is modelled by a linear function shown in Equation 4.1 below:

$$\sigma = \sigma_0 + \sigma_T (T_0 - T) \qquad 4\text{-}1$$

where σ_o is the coefficient of surface tension at reference temperature *To* and σ_T is the rate of change of surface tension with fluid temperature *T* (usually negative). Table 4.1 presents the physical properties of the host liquid and gas bubble used for the simulations at 300K.

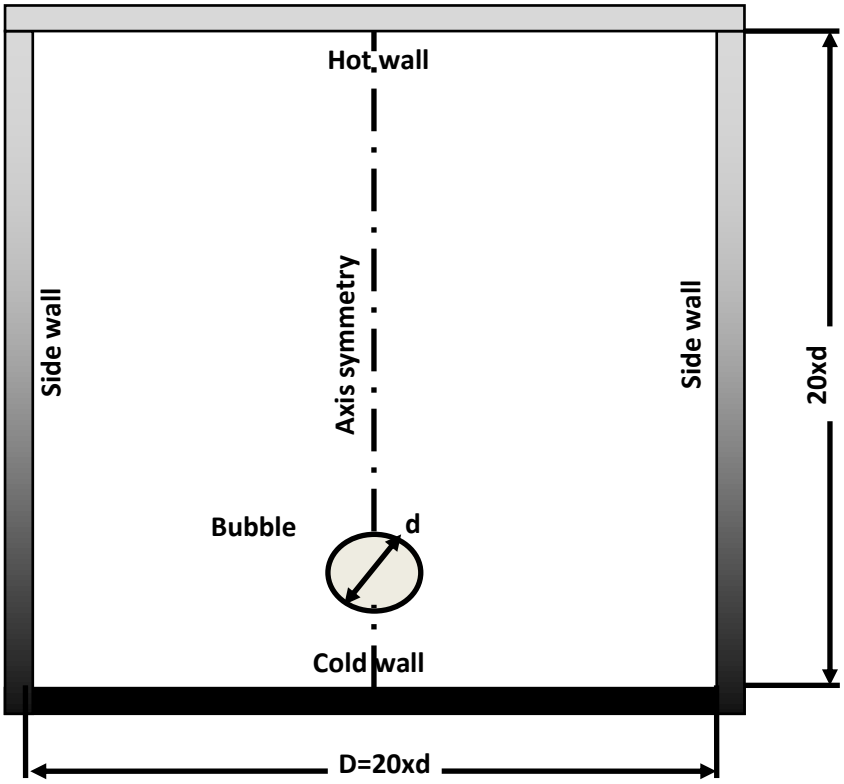

Figure 4-1 Schematic of solution domain for bubble migration in a uniform temperature gradient.

Table 4-1 Physical properties of the liquids employed in the simulation at 300K for Silicone oil (Pr=138) , ethanol (Pr=16.3) and Nitrogen (Pr=0.79).

Properties	Unit	Silicone oil	Ethanol	Nitrogen (N_2)
Density (ρ)	kg/m^3	940	790	1.138
Specific Heat (Cp)	j/kg-K	1800	2470	1040.7
Thermal Conductivity (k)	w/m-K	0.134	0.182	0.0242
Viscosity (μ)	kg/m-s	0.0103	0.0012	1.66e-5
Surface Tension (σ_0)	N/m	0.0201	0.0275	------
Surface Tension Coefficient (σ_T)	N/m-K	0.00007	0.00009	------
Temperature Gradient (∇T)	K/mm	0.208	-	------
Prandtl Number (Pr)	-------	138	16.28	0.79

Once the geometry and the grid were formulated, they were read into the fluid simulation code. The boundary conditions and source terms must be specified in the momentum equations. The calculations were performed using a pressure-based, segregated, implicit solver. The two-phase problems were computed within the VOF framework in which one

single set of conservation equations is solved for both phases, together with the volume fraction equation for the gas phase, as detailed in Chapter 3. The walls of the cylinder had non-slip boundary conditions applied for the three sides and one axis side. Pressure–velocity coupling was accomplished by the pressure-implicit with the splitting of the operators (PISO), which performs two corrections: one for neighbour and the other for skewness. The pressure-staggering option (PRESTO) scheme is used for the pressure interpolation, and the momentum and the energy equations were discretised using a second-order upwind differencing scheme. Other algorithms were also attempted, such as QUICK, instead of a second-order upwind scheme. No difference was observed in the simulation results using these alternative methods; however, simulations using non-iterative methods were considerably computationally faster than when the iterative method was used.

The geometric reconstruction scheme, based on the piece-wise linear interface calculation (PLIC) method of Youngs (1982), is applied to reconstruct the gas–liquid interface. According to many different operational conditions, non-iterative time advancements with time steps of 2.5×10^{-3} s are used to obtain convergence. Since mass transfer at the interface is not important in this situation, no mass sources were involved. Only the surface tension source was considered in the momentum. As previously described, the CSF method represents the surface tension force as a source term for cells with fractional liquid volumes. This method has been incorporated into the solver in such a way that the only input required is the surface tension coefficient force, written by a user-defined function (UDF) and called by the code simulation for each control volume at each time step. No gravitational force was imposed on the simulation, and all cases were run in double precision mode in the FLUENT software.

4.3 Bubble dynamics in a 2D axisymmetrical simulation

The thermocapillary motion of a bubble in a confined apparatus was the first multiphase test case, which will serve as a stringent test for our treatment (explain) of surface tension.

A single bubble with a diameter of 6 mm for ethanol and 8 mm for oil was placed 10 mm from the lower (cold) wall using the region adaptation setting on Ansys-Fluent. The size of the computational wall-bounded domain was chosen as 120 x 60 mm^2 with impermeable sides. The properties for ethanol used in the simulation shown in Table 4.1 were taken from the study by Thompson et al. (1980). The initial velocity for the bubble was set to zero. The upper surface (upper wall) of the domain was hotter than the lower surface (lower wall); (see Fig. 4.1).

Figure 4.2 shows the temperature contours for a thermocapillary isolated bubble migrating in microgravity. The figure shows the moves towards the warmer side when subjected to a temperature gradient in a microgravitational environment. Such a phenomenon is known as the Marangoni problem or the thermocapillary migration problem. Surface tension generally decreases with increasing temperature and the non-uniform surface tension at the fluid interface leads to shear stresses that act on the outer fluid by viscous forces. This causes bubbles in the fluid to move in the direction of the thermal gradient. Temperature gradients cause surface tension gradients at the liquid-gas interface (meniscus), and the variation of surface or interfacial tension along the meniscus gives rise to convection. The flow from a region of low surface tension to a region of higher surface tension is referred to as Marangoni flow. This phenomenon is clearest in Figures 4.4 & 4.5. The motion of the bubble triggers motion of the liquid around it. This motion of the ethanol reflects off the bottom of our domain and then rebounds into the back of the bubble.

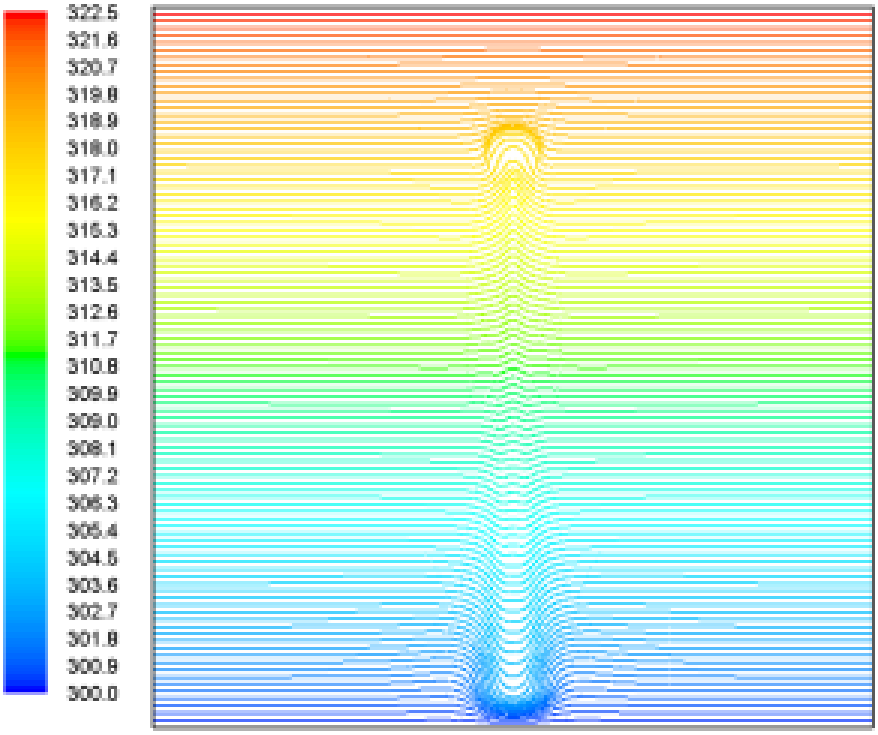

Figure 4-2 A nitrogen bubble rising in a stationary fluid with an imposed stratified temperature gradient for ethanol with Pr=16, Re_T= 148.2, and Ma_T=2412.3 at t=9 s from the start of the bubble migration.

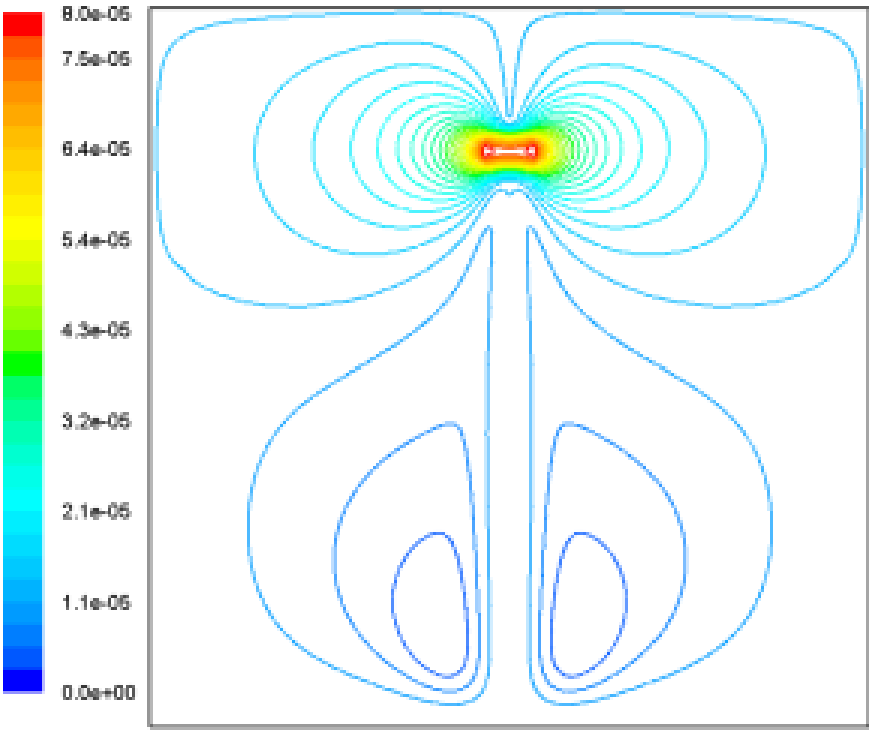

Figure 4-3 streamlines (Kg/s) for a bubble rising in a stationary fluid for ethanol with Pr=16, Re_T= 148.2, and Ma_T=2412.3 at t=9 s from the start of the bubble migration.

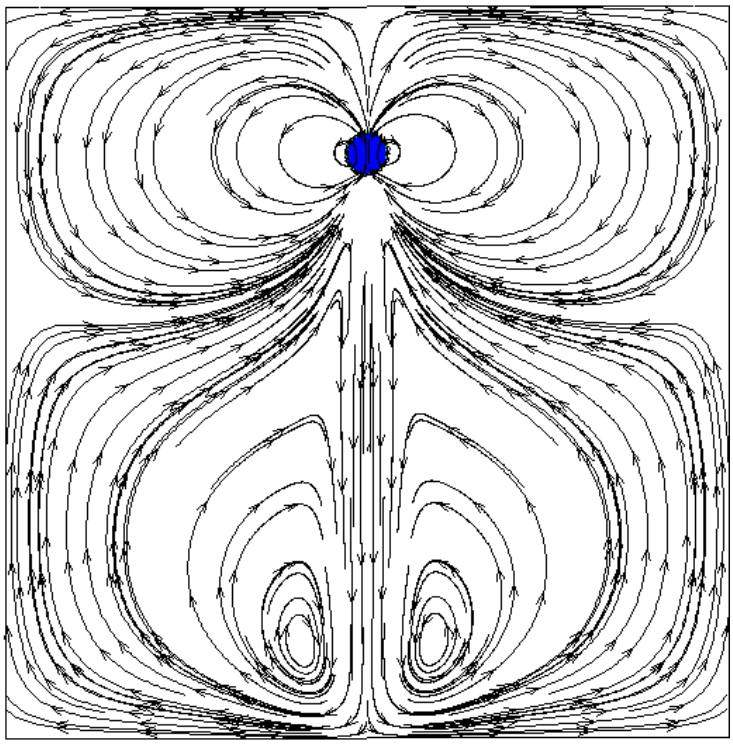

Figure 4-4 A bubble rising in a stationary fluid with an imposed temperature gradient for ethanol with Pr=16, Re_T= 148.2, and Ma_T=2412.3 at t=9 s from the start of the bubble migration.

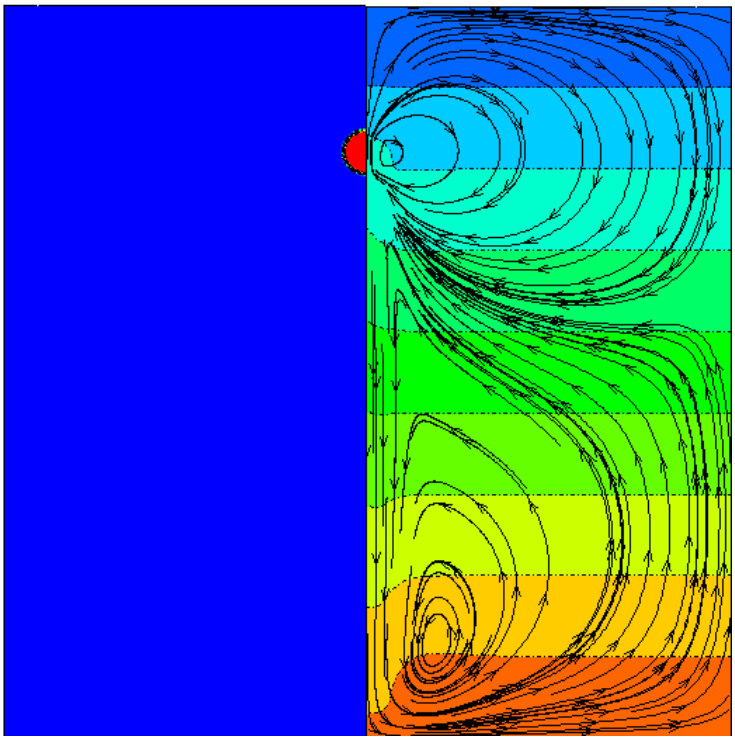

Figure 4-5 streamlines (Kg/s) for a bubble rising in ethanol with Pr=16.3, Re_T= 148.2, Ma_T=2412.3 at t=9 s from the start of the bubble migration.

The final numerical results were then compared with the experimental measurements of Thompson et al (1980), as shown in Figure 4.6. The Fluent solver over-predicts bubble motion early in the process, and the steady velocity predicted by the current model does not agree well with the steady velocity measured by Thompson et al. (1980) for Pr = 16.3; however, the predictions improved later in the process, as seen in Figure 4.6. The reason for this variation is that the bubble is placed in the domain by 'patching' the shape of a sphere at the initial boundary condition and numerically duplicating the initial bubble injection process is almost impossible, whereas for simulations a stagnant bubble is assumed. The exact experimental initial conditions are often difficult or impossible to determine and this leads to slight differences in the bubble trajectory early on the bubble motion. However, the predictions are quite close to the experimental results in the latter stages. From Figure 4.6 one can see the similarity between the obtained results and experimental data for Nitrogen bubble migrating in Silicon oil. This match in result is due to the low migration speed of the bubble inside high Prandtl number (Pr=138) and the easy for the CFD results to catch up with the experimental from the early stage. Based on the results shown in Figure 4.6 and discussed in this section, it was also found that CFD predictions with the VOF model agreed better with the experimental data, due to the fact that it is based on the Geo-Reconstruct algorithm. The VOF model with the UDF were examined properly and results show that the surface tension coefficient was well coded, suggesting that it is an appropriate choice to solve thermocapillary problems.

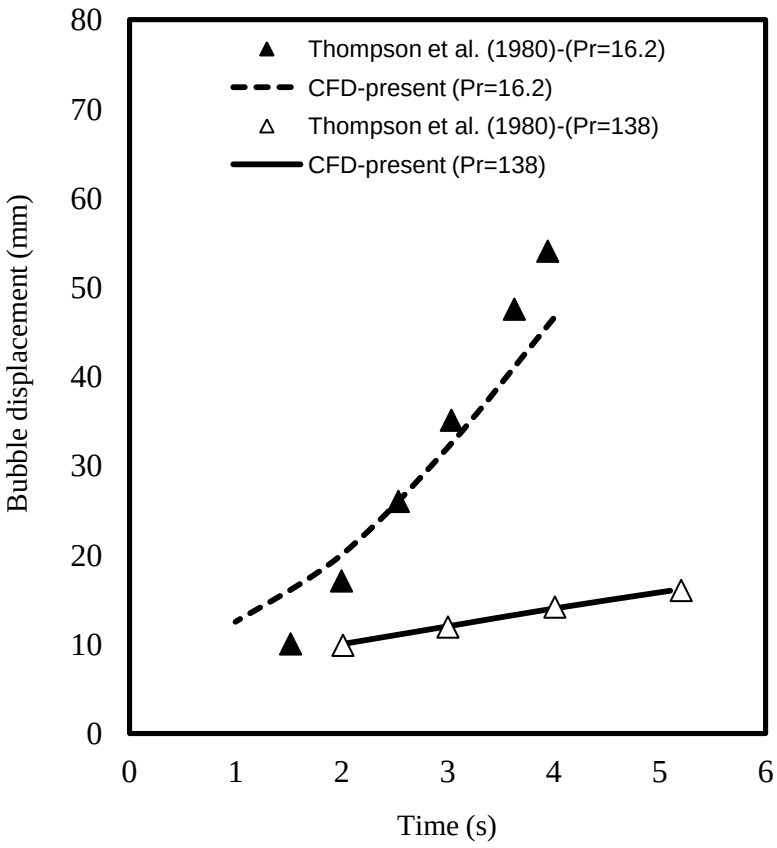

Figure 4-6 Validation of VOF-model with previous experimental data for bubble diameters, d=6 and 8 mm in ethanol (Pr=16.3) and silicon oil (Pr=138) respectively.

4.4 Grid resolution study for a two-dimensional axisymmetry

The objective of a grid independence study is to ensure that the simulation result are independent of the grid density. Grid independence was achieved by increasing the number of region adaption cells from 72 to 406 per bubble radius by increasing the grid cells in both the X and Y directions, and plotting the convergence of certain parameters of interest such as bubble migration time towards the hotter side and migration distance to ensure that the solution remains independent of grid size. Concerning the number of cells in the present study, a non-uniform grid with grid lines clustered towards the centre was used in order to keep cell count down and to avoid the drawback of increasing memory and CPU time. The grid sensitivity test is shown in Table 4.2 and was simulated with the parameters outlined in Table 4.1. Another important point is that, when using an axisymmetric solver, a mesh need only be created for half of the domain, thus drastically reducing the number of cells used and consequently the time of calculation.

Table 4-2. Grid sensitivity check for a gas bubble diameter=8 mm in ethanol (Pr=16.3) for the 2D-axis models.

Grid	(Δx,Δy)	Number of cells	Cells per radius	Migration time (s)	Bubble speed (cm/s)
(1)	0.6x0.6	8400	72	9.5	1.12
(2)	0.5x0.5	9600	104	9.5	1.08
(3)	0.4x0.4	17760	158	9.75	1.05
(4)	0.3x0.3	23200	278	10	1.04
(5)	0.25x0.25	31200	406	10	1.024

Five different grids were used to study the grid size dependency. Each of the grids was used to simulate the thermocapillary bubble migration under zero-gravity conditions. Since the bubble translation behaviour is of interest to this study, five simulations using each of the five grids developed in Table 4.2 are presented in Figure 4.7 and the mesh size with streamline

resolutions was tested using Tecplot software to simulate the 2D representation of the domain, as seen in Figure 4.8. Note that due to the difficulty obtaining the experimental initial condition for each 3D case; it was assumed that the previous validation results with Thompson et al. (1980) in Figure 4.6 is in accepted agreement with the 2D axis simulation results for Pr=16.3 and 138. Therefore the coming 3D grid dependency figures are excluded from Thompson et al.'s (1980) results and replaced with the results from the 2D axis simulation only.

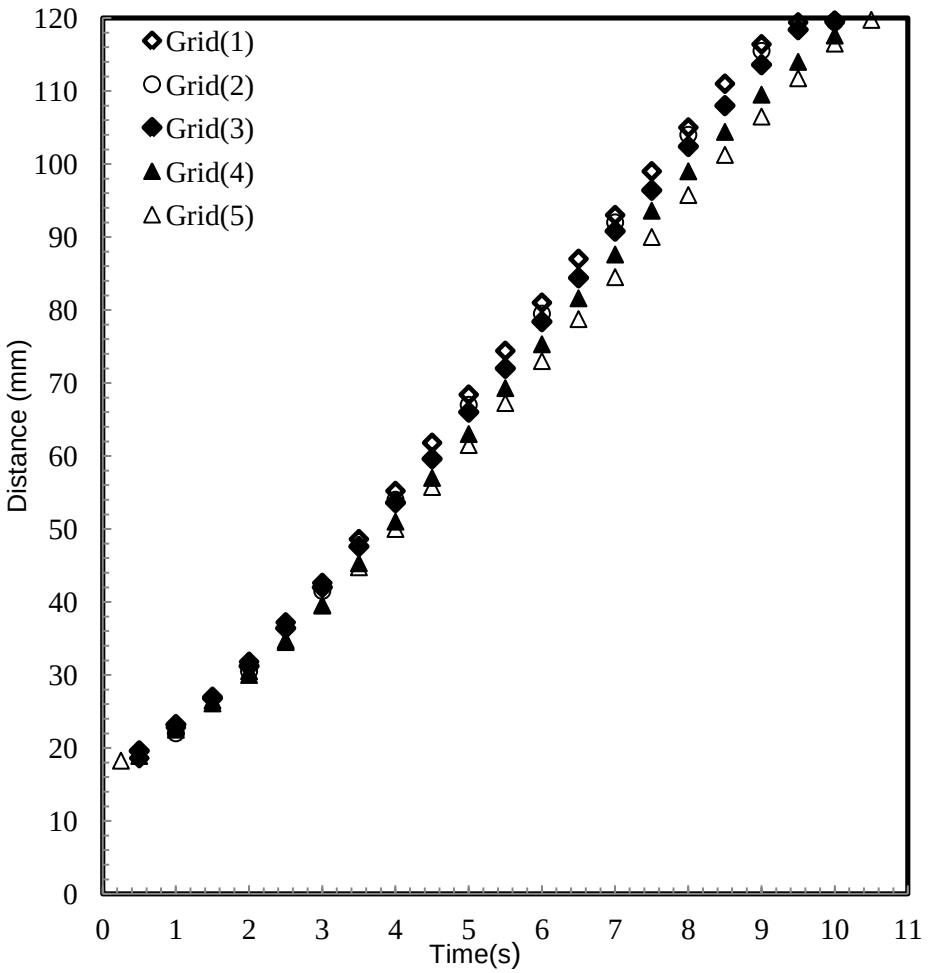

Figure 4-7 The predicted rising distance of a bubble, for five different grid sizes, vs. time (s)

The profiles of bubbles with diameter of 8 mm were extracted across half of the 2D axis domain at a time = 9s at different distances from the cold lower side. These figures show only

a very small difference in the calculated bubble motion profiles using the 23200 mesh (grid-4) and the 31200 mesh (grid-5) of the domain, which give 278 and 406 cells per bubble radius respectively. As seen from the results, it was expected that the greater grid density would give more accurate simulation results as finer grids reduce the distance over which variables in the computation are interpolated. However, as the 31200 mesh is computationally expensive, it is desirable to use the 23200 mesh to produce the desired results. In this grid study, the number of computational cells in the horizontal and vertical directions was increased while maintaining a square computational cell. This is achieved by changing the grid to uniform control volume ($\Delta x/\Delta y=1$), which is more satiable for accurate schemes at higher orders, avoiding numerical aliasing errors.

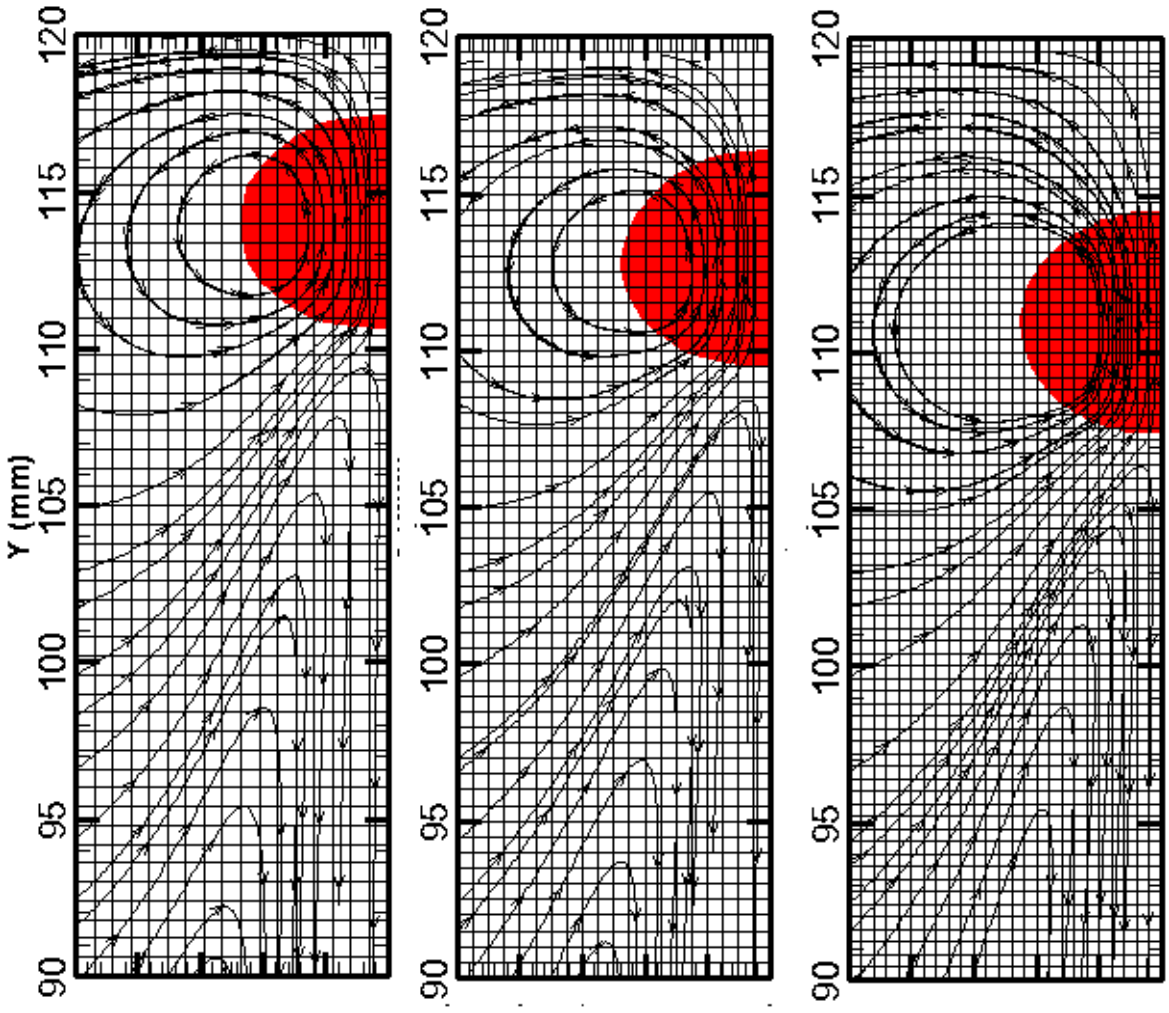

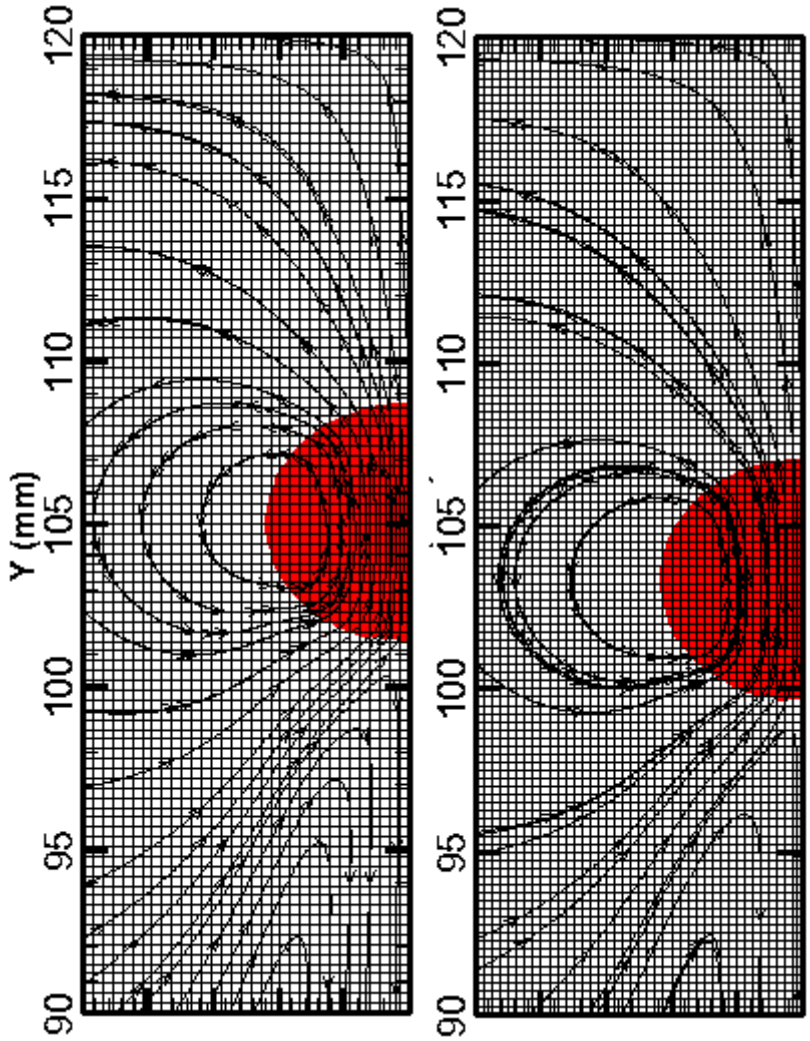

Figure 4-8 The rising distance of a bubble for five different grid sizes at t=9 s from the start of the bubble migration.

4.5 Bubble dynamics in a three-dimensional domain (periodic boundary and complete cylinder)

If an axisymmetric model could be assumed to simulate the thermocapillary flow of a bubble, then a 2D-axis geometry would suffice; conversely, to model a bubble placed off-centre, then a 3D model simulation (using x, y and z co-ordinates) is necessary and a 2D axis will no longer be valid to model such flow. On the other hand, 3D models are more complicated and require more computational resource, i.e. running time and memory, while simultaneously conferring a loss of accuracy or creating difficulties with convergence by reducing the mesh size. Alternatively, periodic geometry could be used to reduce the computational effort required for some simulations. Periodic geometry is a very important step in the 3D simulation of bubble dynamics and is recommended for bubbles located in the centre and off-centre area of the domain. When using the periodic flow solver, a mesh is only created for a quarter, half, three quarters or any other suitable fraction of the domain, as seen in Figure 4.10. This method therefore reduces the number of cells used, and consequently the calculation time required.

Four different grid densities were generated using Gambit (2005) software, one of which was used for each quarter of the cylinder. All grids used in this investigation were structured meshes. These refinements were adopted specifically to investigate the effect of using different cell sizes on the simulation of Marangoni flow, as shown in Figure 4.9. The results of the grid sizes and bubble speed are listed in Table 4.3. When creating a mesh for a quarter of the cylinder, as seen in these figures, the cells required to model the cylinder is reduced by a factor of 4, i.e., the total cells required for quarter 4 (shown in Figure 4.9 and Table 4.3) are equal to 375,000, which is equivalent to 1,500,000 cells if the case were to be simulated in a full 3D geometry.

Table 4-3 Grid sensitivity check for a nitrogen bubble of 11mm diameter migrating in ethanol (Pr=16.3) in quarterly periodic boundaries

Grid	(Δx,Δy,Δz)	Quarter hexahedral cells	Cells per bubble quarter	Bubble speed (mm/s)
Quarter 1	25x25x100	50700	26	10.7
Quarter 2	30x30x120	81000	46	10.9
Quarter 3	40x40x160	192000	106	10.92
Quarter 4	50x50x200	375000	206	10.3

The use of periodic boundaries can be of great assistance to ensure the validity of the previous 2D axisymmetric simulation results, leading to better justification of the full 3D geometry. For example, some benefits of this method may be greater simplicity of building and meshing the 3D geometry, ability to check the 3D grid dependency resolution, insight into the flow physics expected from fully three-dimensional flow, and help in predicting the results of the 3D flow. However, although using periodic geometries offers considerable benefits, they cannot be employed in the case of bubble/droplet motion in a rotating cylinder, as will be seen in Chapter 7; alternatively, a full 3D geometry will be used to calculate thermocapillary bubble migration in a rotating cylinder.

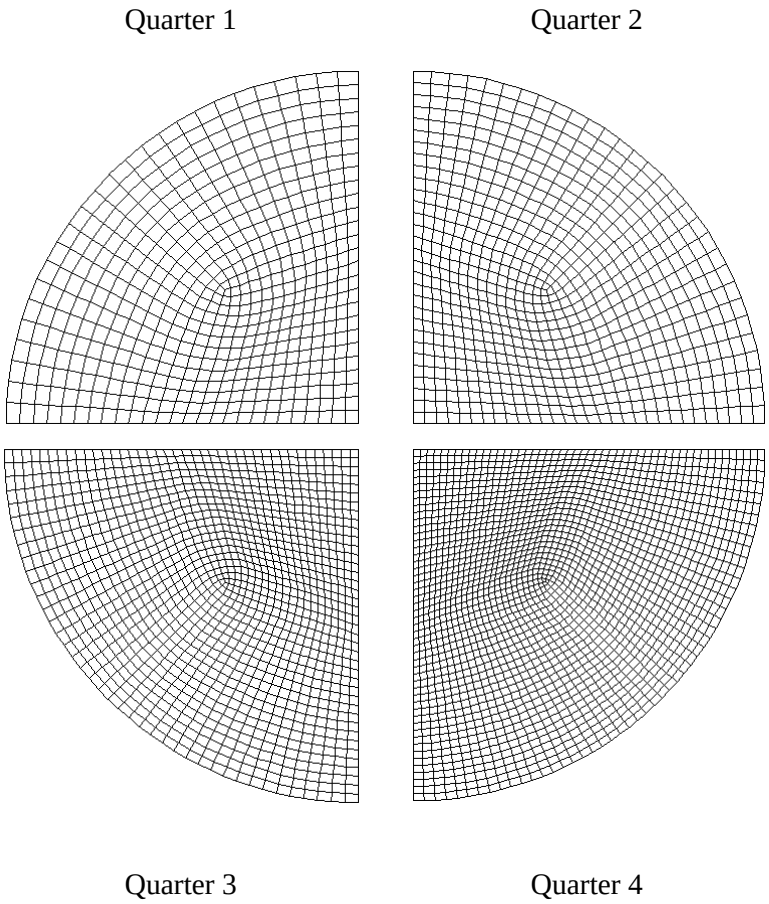

Figure 4-9 Grid sensitivity check for quarterly periodic boundaries

In order to study Marangoni bubble motion phenomena in a 3D geometry and as a result of computational requirements, the thermocapillary motion of a bubble in a confined apparatus was first performed in periodic domains measuring a quarter, half and three quarters of a circle before the experimental locus was extended into a more complex, fully 3D domain. Half and three-quarter geometries can also be utilised to reduce the computational time and memory, but can only be used for particles that do not flow across the periodic boundary when migrating toward the hotter surface. Subsequently, the results obtained were subject to grid dependency tests before being extended to three dimensions, as seen in Figure 4.11.

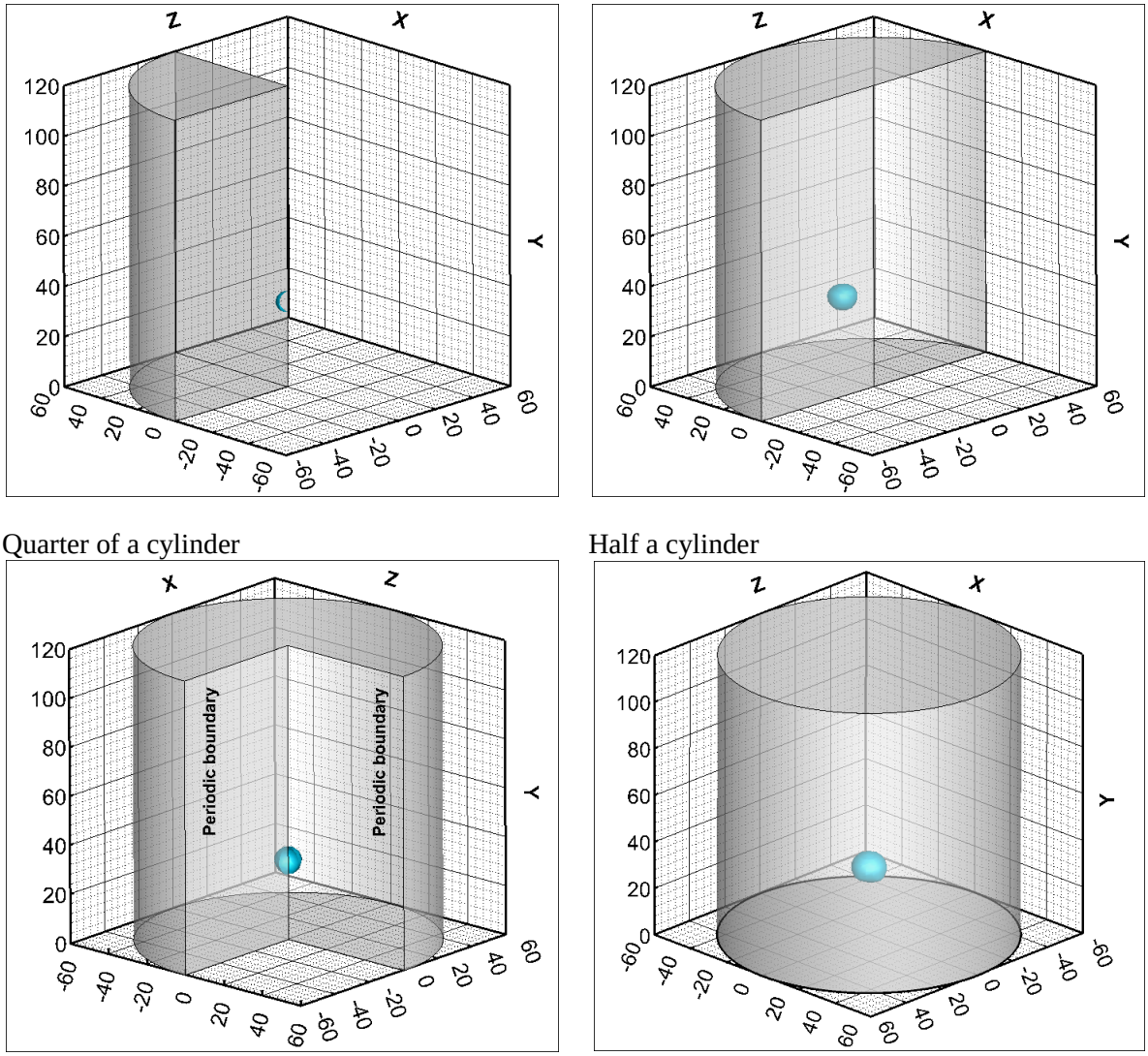

Quarter of a cylinder

Half a cylinder

Three quarters of a cylinder

Full 3D cylinder

Figure 4-10 Rotational periodic/full geometry used to calculate bubble migration toward the hotter side, with bubble initial position equal 1.5d

The effects of grid resolution on the numerical predictions of thermocapillary bubble flow in zero gravity show the same behaviour as seen in Figure 4.9. In the same figure, the three-dimensional periodic data for varying grid resolutions and a full 3D geometry confirmed the results with the 2D axisymmetric configurations, which were validated with results from the experiments of (Thompson et al., 1980). The simulations were plotted in terms of bubble displacement versus time .

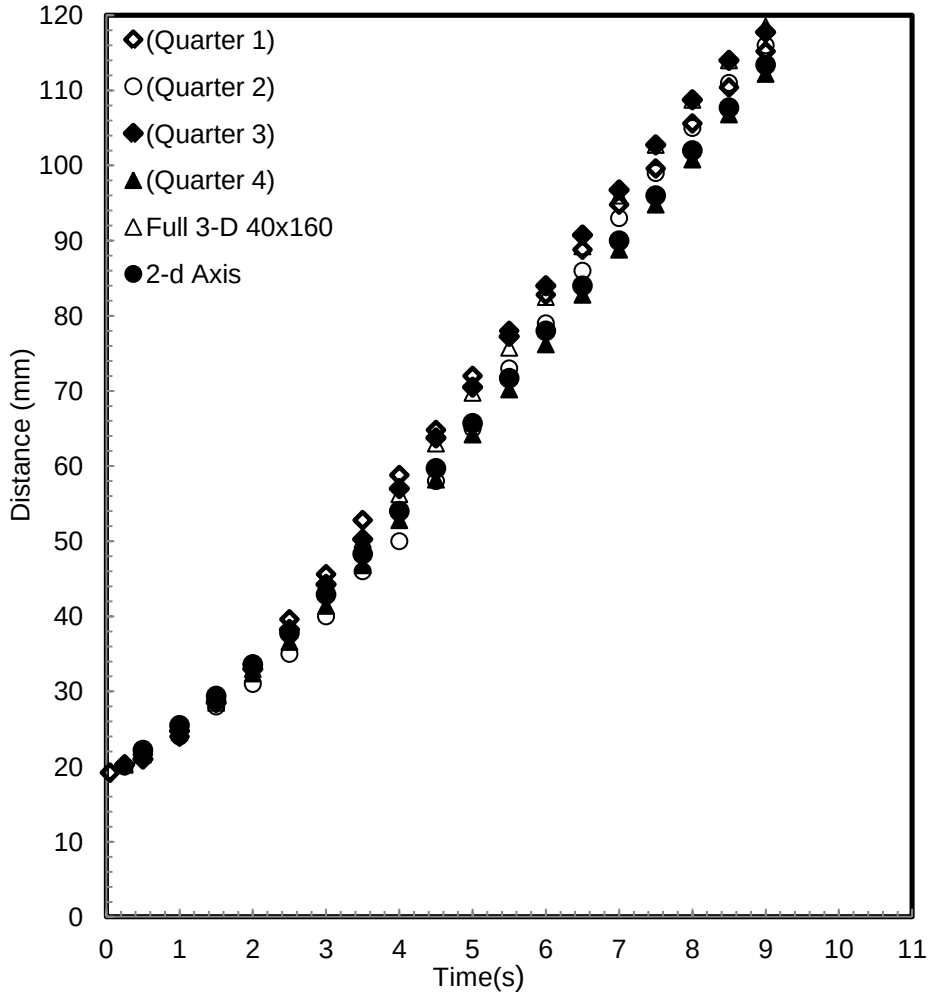

Figure 4-11 Grid sensitivity check for a bubble diameter of 11mm in quarterly periodic boundaries

Further validation of the present VOF model was achieved by producing a series of increasingly refined grid densities using Gambit (2005) software. The reason for creating grids of different densities is to analyse how the grid density affects simulation characteristics of particular interest. It is very important to understand which grid will produce the desired effect with the least requirements of computational time and memory. Three different grid densities were created for meshing the full 3D cylinder with structured grids. These refinements were particularly adopted to investigate the effect of using different cell sizes on the simulation of thermocapillary bubble motion in zero gravity. The number of these cells and their data are listed in Table 4.4. (A, B, and C) and shown in Figure 4-12.

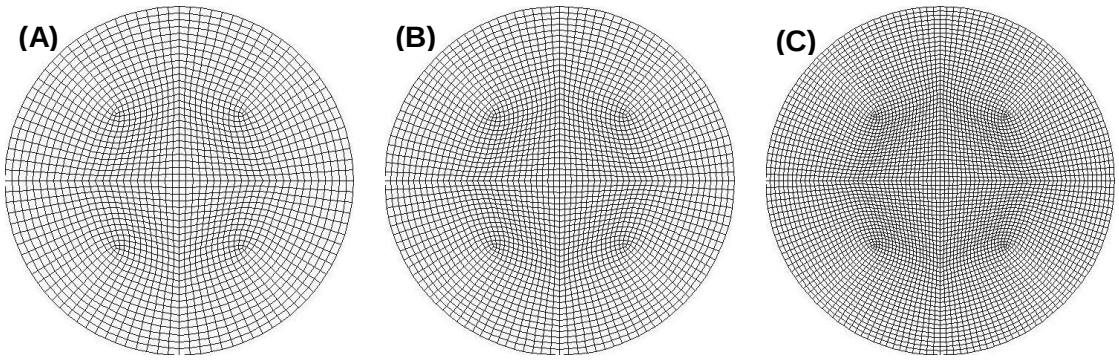

Figure 4-12 Grid sensitivity check for full 3D models related to Table 4-4

Grid	(X, Y, Z)	Number of hexahedral cells	Cells per bubble radius	Migration time (s)	Bubble speed (cm/s)
(A)	25x100x25	192400	100	9.5	1.09
(B)	30x120x30	324000	184	9.5	1.09
(C)	40x160x40	768000	424	9.75	1.10

Table 4-4 Grid sensitivity check for a bubble diameter of 11mm for full 3D models

Figure 4.13 shows a cross-sectional view of the 3D grid. The 3D model geometry has both a diameter and height of 120 mm with zero permeability (no "inflow" or "outflow" through the side boundaries). For the simulations, ethanol properties were taken as given in Table 4.1 and the calculations were performed using Re_T=111, Pr=16.2 and Ma_T 1809.2. Bubble movement was observed from the colder to the hotter region. For bubbles with a diameter of 7 mm, finer mesh (FM) was utilised for the purpose of validation, using the results published by Thompson et al. (1980), as illustrated in Figures 4.13a-d. These figures show that the bubble staggers along the vertical line, maintaining a spherical shape due to the asymmetric distribution of the pressure in its wake.

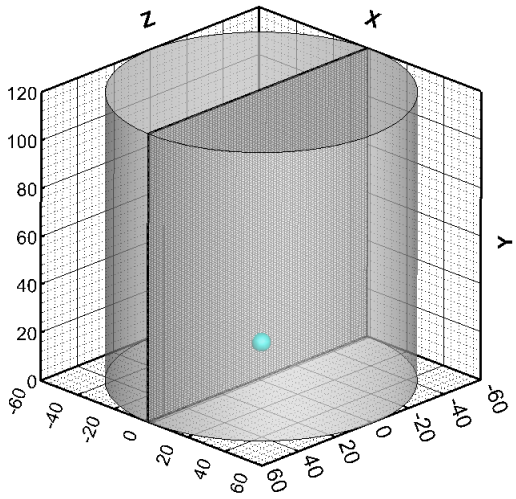

Figure 4.13a Diagram of the solution, t=0 s

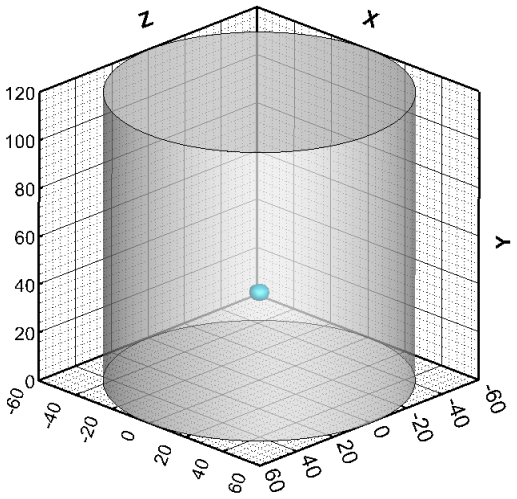

Figure 4.13b Migration t=2 s

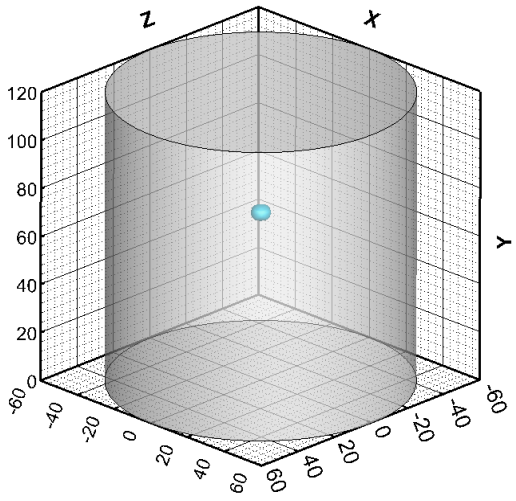

Figure 4.13c Migration t=4 s

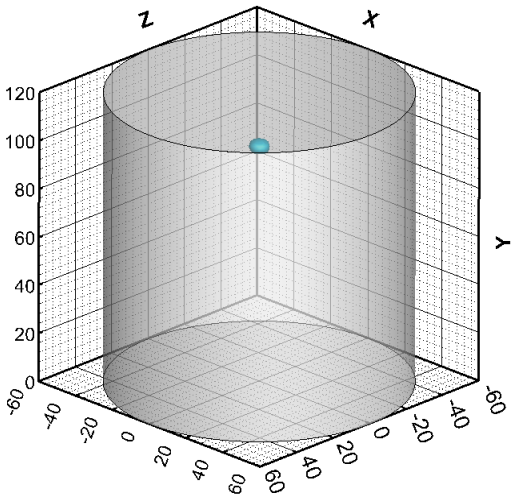

Figure 4.13d Migration t=6 s

Figure 4-13a, b, c and d represent 3D code validation for the thermocapillary motion of N2=6 mm diameter in ethanol (Pr=16.2) at zero gravity for different time steps

Grid independence was achieved for parameters such as bubble migration time and velocity by increasing the number of region adaption cells from 100 to 424 per bubble; this was achieved by increasing the grid size in the X, Y, and Z directions. Figures 4.14 show the migration distance of the bubble in the Y direction, towards the hotter side, versus time for the three tested meshes of dimensions CM (25 x 100 x 25, 192,400 cells), MM (30 x 120 x 30, 324,000 cells) and FM (40 x 160 x 40, 768,000 cells). Only a minor difference in the results was seen between the MM and FM dimensions, whereas the computational cost almost doubled.

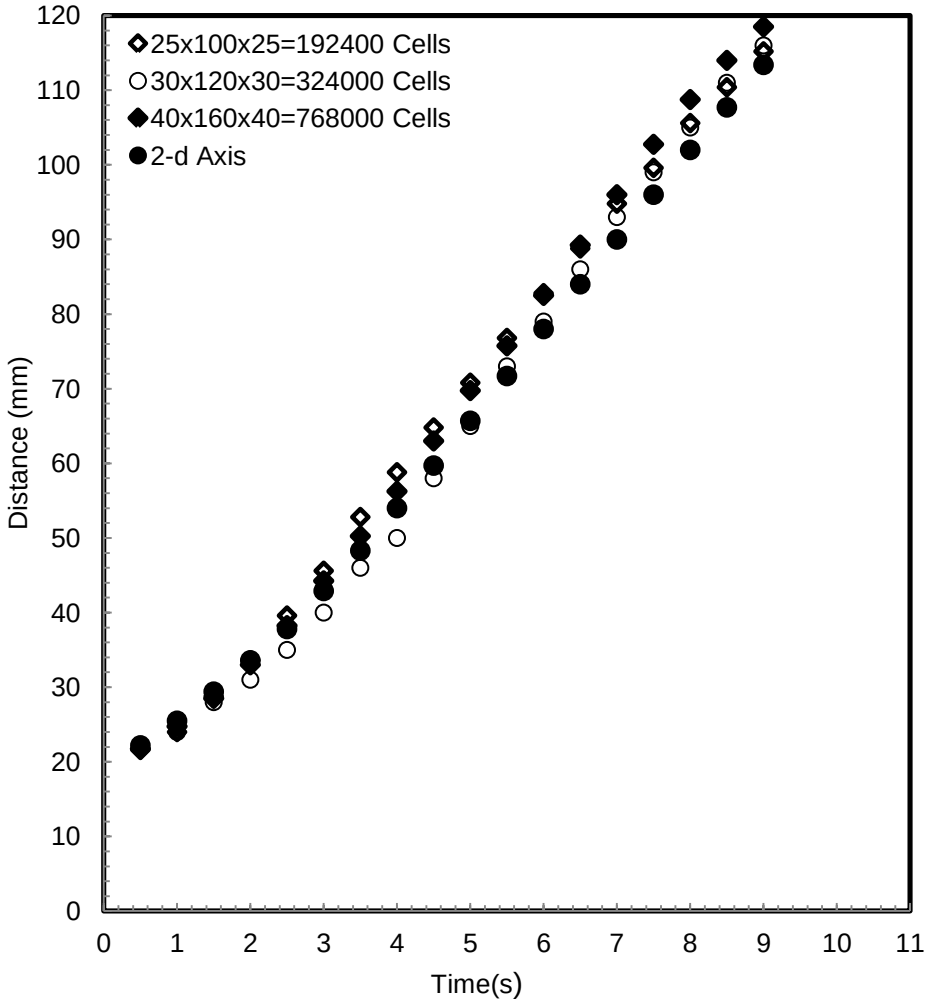

Figure 4-14 Migration distance of the bubble (11mm) inside ethanol (Pr=16.2) towards the hotter side (Y-direction), versus time for the three tested meshes

4.6 Conclusion

At the beginning of this research study and for the verification and validation process, investigations based on the computational fluid dynamics (CFD) concept have been carried out in detail and a reasonable agreement was found with (Thompson et al., 1980). The work documented in this chapter is very important in terms of an initial attempt to test the VOF solver capabilities of Fluent and its ability to predict surface tension-dominated flows numerically. The data and figures in this chapter have proven the existence of Marangoni bubble flow phenomena in zero-gravity conditions in a confined apparatus of axisymmetric, periodic, and fully three-dimensional geometries. The results were then validated with previous data from zero-gravity experiments. With regard to the VOF solver of Fluent, the CFD predictions of the VOF model exhibited better agreement with the experimental data due to the fact that they were based on the Geo-Reconstruct algorithm. Close examination of the VOF model with UDF showed that the surface tension coefficient was well coded, suggesting that this model is an appropriate choice to solve this problem. Further validation of the present VOF data was achieved by performing a series of calculations, as numerical errors due to the discretisation of this singular term can lead to large errors. Further to this, the numerical results of the surface tension gradient will serve as a base for the rest of this study. As the accuracy of the simulation is mostly dependent on mesh density, the process of using different mesh sizes, time steps, convergence criteria and discretisation schemes, grid tests and extending the geometry from periodic boundaries to a fully three-dimensional model was checked and validated with previous experimental work and the 2D axisymmetric data. Nonetheless, the numerical simulation facilities available nowadays should encourage researchers to make use of high-density grids and complex three-dimensional models to obtain results of the highest possible accuracy.

Chapter 5 Numerical results and discussion

5.1 Thermocapillary Simulation of Single Bubble Dynamics in Zero Gravity

The CFD tools used in this chapter are employed to simulate the flow of thermocapillary (Marangoni) bubbles/droplets along a 2D axis in zero-gravity conditions. These simulations were carried out in order to better understand the physical processes behind many of the observed physical phenomena of zero-gravity environments. The CFD method also allows sensitivity and feasible studies to be carried out for different parameters and designs. The thermocapillary motion of a bubble was observed in a confined 2D axis apparatus, as described in Chapter 4. Figure 4.1 is the first multiphase test case, which will serve as a base test when solving for Marangoni bubble flow in this section. All simulations were run at time t=0 with an initial stationary liquid and gas, with an applicable surface tension between those of ethanol and nitrogen (σ) = 27.5 (dyn/cm), and surface tension gradient (σt) = -0.09 (dyn/cm ^{o}C), (Kuhlmann, 1999). The domain was defined as a cavity with bounded walls. For all simulations the initial state will be set with no velocity at the inlet or the outlet, and the pressure will be taken to equal atmospheric pressure. The axisymmetric solver will be used in Fluent to model the effect of different parameters on the ascension of a bubble in a column of liquid; for instance, the effect of temperature, geometry aspect ratio, changing bubble position in the x direction on the bubble's migration behaviour in weightless conditions will be examined.

5.1.1 Effect of liquid temperature upon bubble migration

In order to investigate what happens to the thermocapillary bubbles when a linear temperature distribution is prescribed between the upper and lower walls, four different temperature differences were tested. The lower wall temperature was kept constant at 300 K, and the temperature of the upper wall was varied from 317.5 to 325 K in increments of 2.5 K. Figures 5.1a-c show the temperature contours (right) and streamlines (left) for a single gas bubble N_2 (d_p=8mm) migrating in Ethanol (Pr=16.2) at t=9 sec. The volume fraction contours for the same condition are shown in Figure 5.2a-c at t=9 s. The flow pattern in these figures show that bubbles in an immiscible fluid will move toward the warmer side when subjected to a temperature gradient in a zero-gravity environment. The effect of the temperature gradient is clear in these figures; for example, as the temperature gradient increases, the migration velocity increases. Figure 5.3 presents the relationship between migration time and migration distance for different upper wall temperatures. As seen from the figures, increasing the temperature gradient (upper wall temperature) simultaneously increases the bubble displacement.

In this test section regarding the effect of temperature gradient on the bubble migration and by analysing the simulation results from in Figures 5.1-5.4, the results shown that different temperature gradients lead to different bubble migration velocities, indicating a direct relationship between temperature gradient and bubble speed. It also reveals that the bubble velocity decreases if the temperature gradient between the upper and the lower walls decreases, and vice versa.

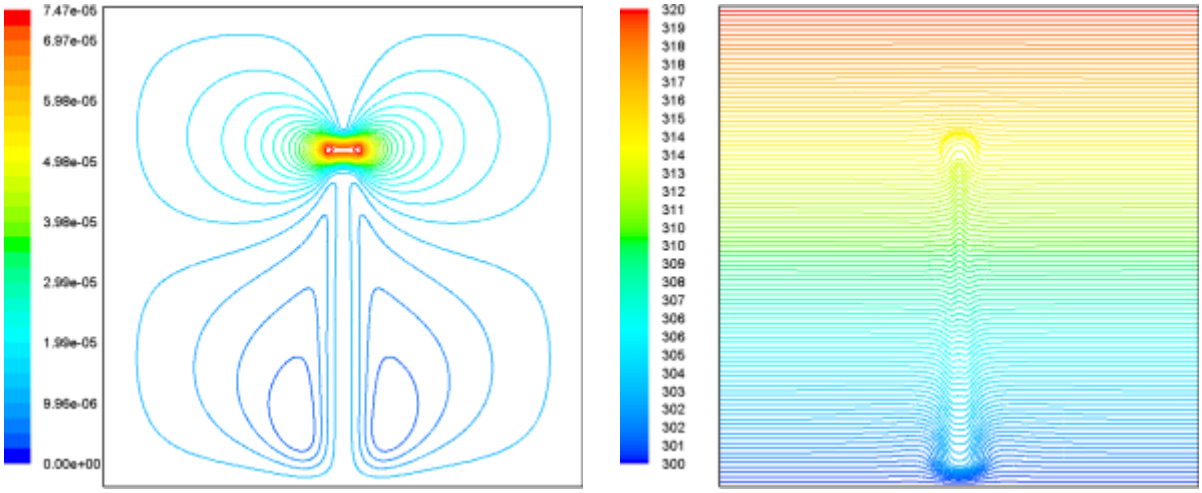

Figure 5.1a Temperature contours (right-K) and streamlines (left-Kg/s) for N_2=8 mm diameter at t=9 s, with a lower wall temperature of 300K and upper wall temperature of 320K

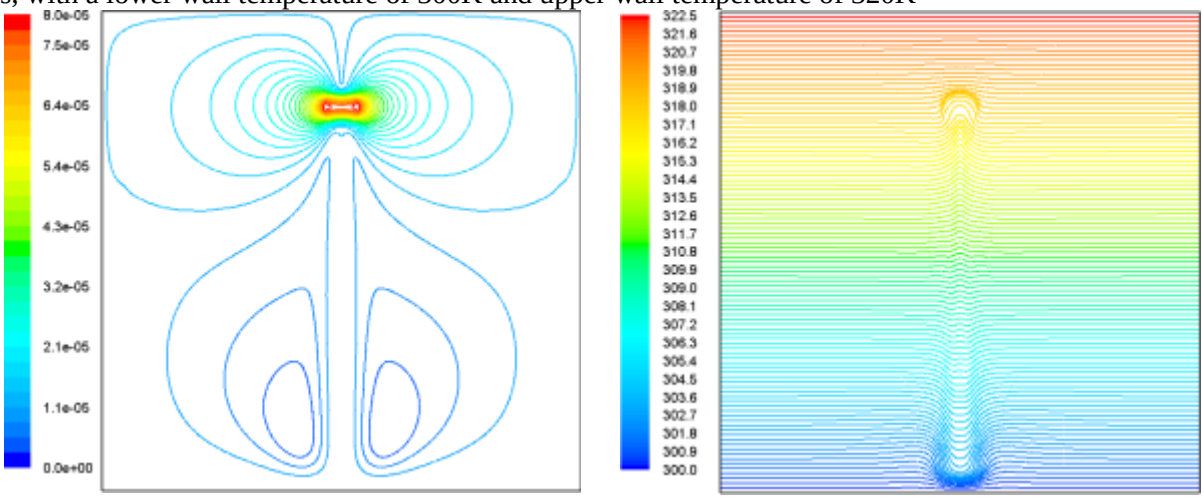

Figure 5.1b Temperature contours (left) and streamlines (right-Kg/s) for N_2 =8 mm diameter at t=9 s, with a lower wall temperature of 300K and upper wall temperature of 322.5K

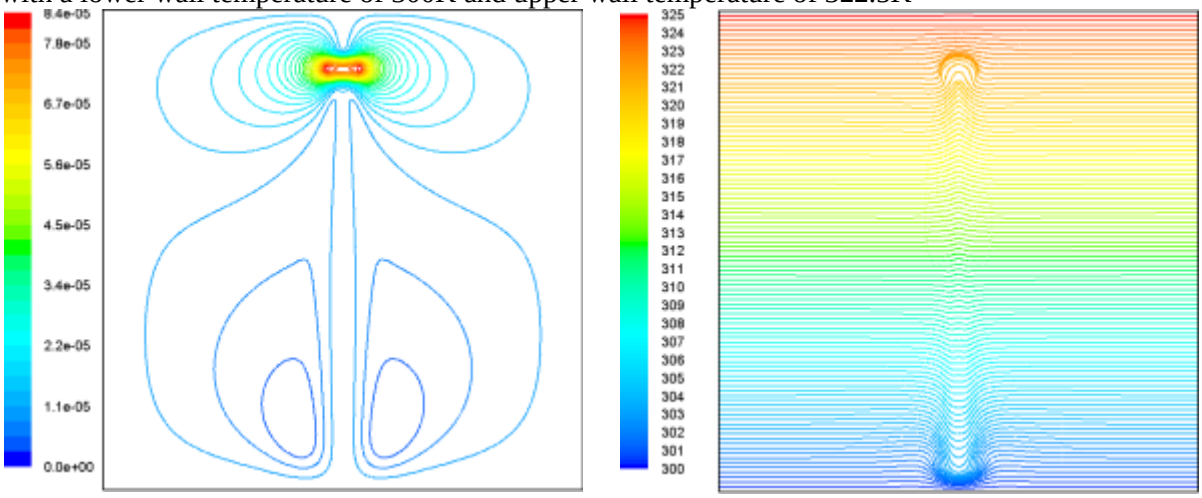

Figure 5.1c Temperature contours (left) and streamlines (right-Kg/s) for N_2=8 mm diameter at t=9 s, with a lower wall temperature of 300K and upper wall temperature of 325K

Figure 5-1 (a-c) Temperature contours and streamlines at t=9 s

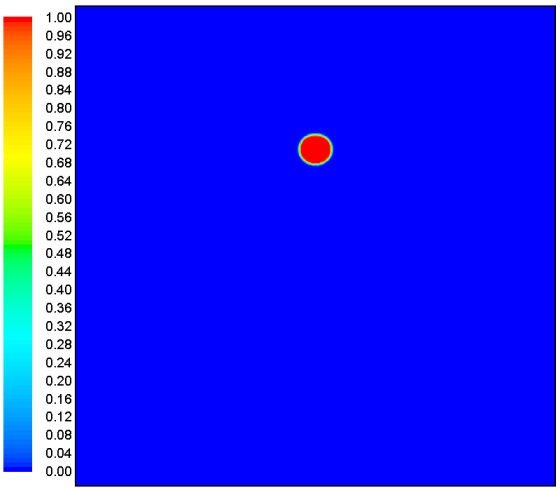

Figure 5.2a phase fraction contours for N_2=8 mm diameter at t=9 s, with a lower wall temperature of 300K and upper wall temperature of 320 K

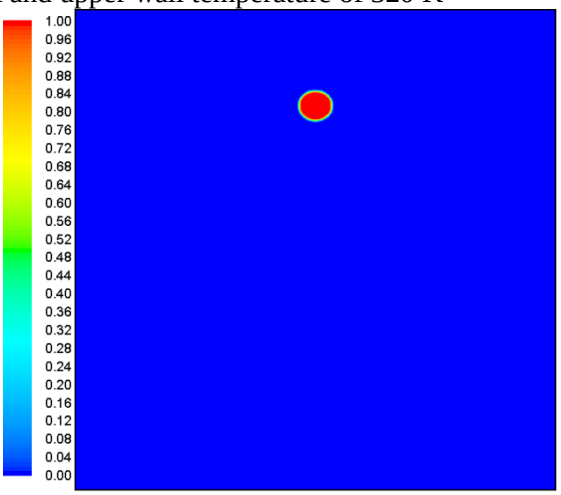

Figure 5.2b volume fraction contours for N_2=8 mm diameter at t=9 s, with a lower wall temperature of 300K and upper wall temperature of 322.5 K

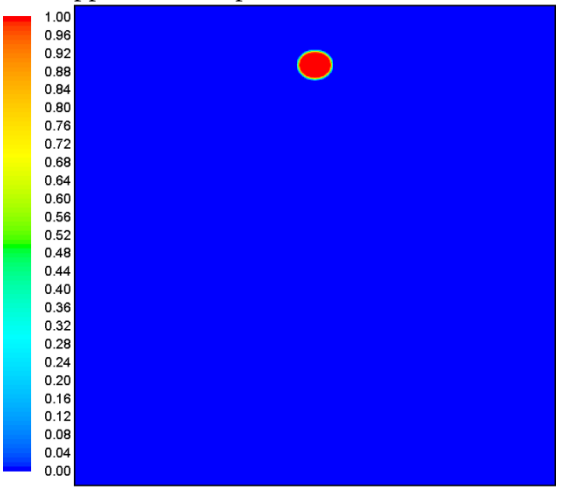

Figure 5.2c volume fraction contours for N_2=8 mm diameter at t=9 s, with a lower wall temperature of 300K and upper wall temperature of 325 K

Figure 5-2 (a-c) volume fraction at t=9 s

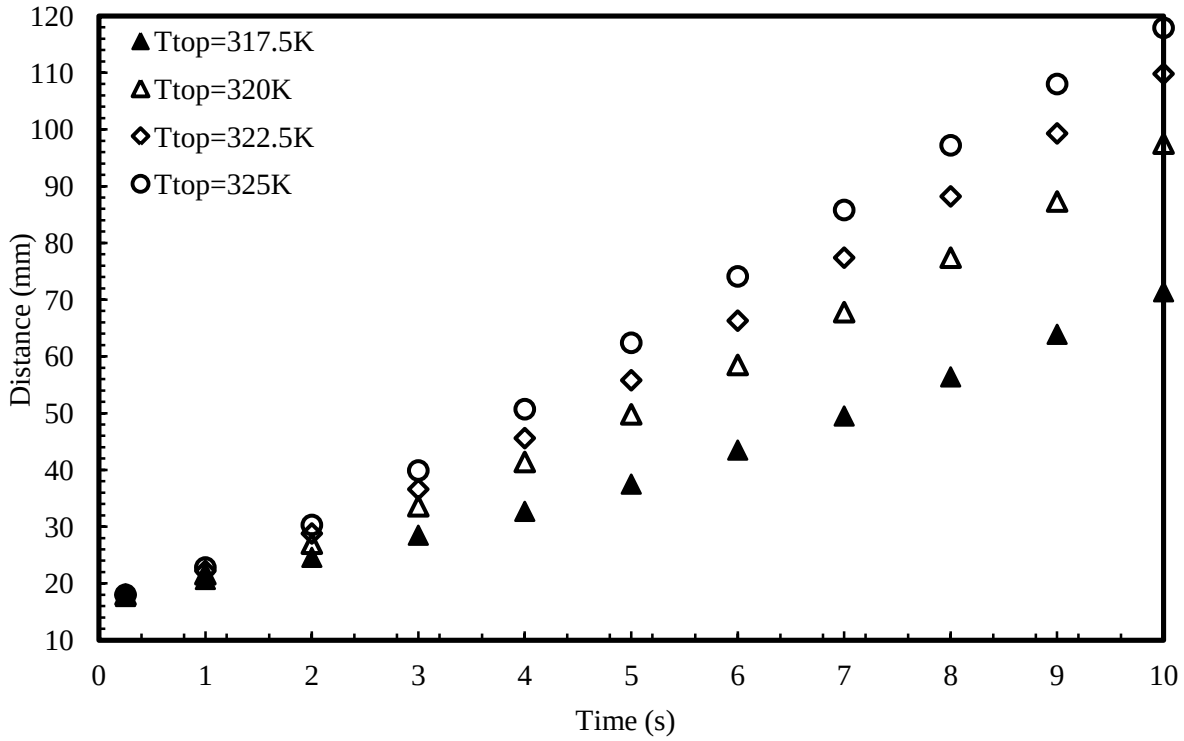

Figure 5-3 Relationship of displacement versus time for a bubble of N_2=8 mm diameter to migrate in ethanol (Pr =16.2) for different temperature gradients, T_{Bottom}=300 K.

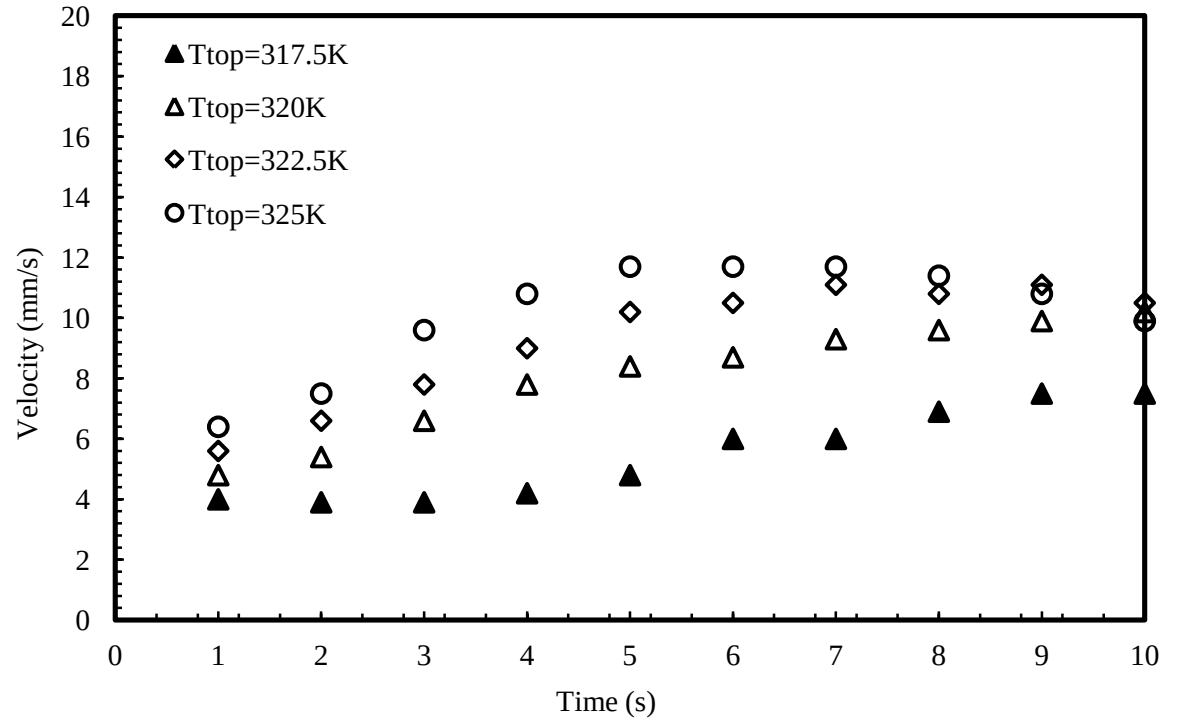

Figure 5-4 Relationship of migration speed versus time for a bubble of =8 mm diameter to migrate in ethanol (Pr =16.3) for different temperature gradients, T_{Bottom}=300 K.

5.1.2 Effect of changing the width of the cylinder on bubble migration

This section presents the results of an extensive numerical investigation of the thermocapillary flow of a bubble with a diameter (d) equal to 6 and 8 mm rising in stagnant ethanol liquid. The size and aspect ratios of the cylinders were varied by using four different columns with diameters of 20, 40, 60, and 80 mm to test the effect of column width on the time and speed of the bubble migration while keeping heights fixed. The results of the migration time and speed for each aspect ratio (AR), the ratio of the bubble diameter to the column diameter, are summarised in Table 5.1 and Figure 5.5, which show the effect of the column width on the ascension speed of the bubble.

Table 5-1 Numerical results for eight different aspect ratio

Bubble diameter (mm)	Column width (mm)	Aspect Ratio (Ar)	Migration time (s)	Bubble speed (mm\s)
4	15	0.53	16.2	6.8
4	20	0.4	11.5	9.88
3	20	0.3	12.5	9.66
4	30	0.267	10.65	9.93
4	40	0.2	10.5	10.0
4	60	0.13	10.5	10.0
4	80	0.1	10.5	10.0
4	100	0.08	10.5	10.0
4	120	0.067	10.5	10.0

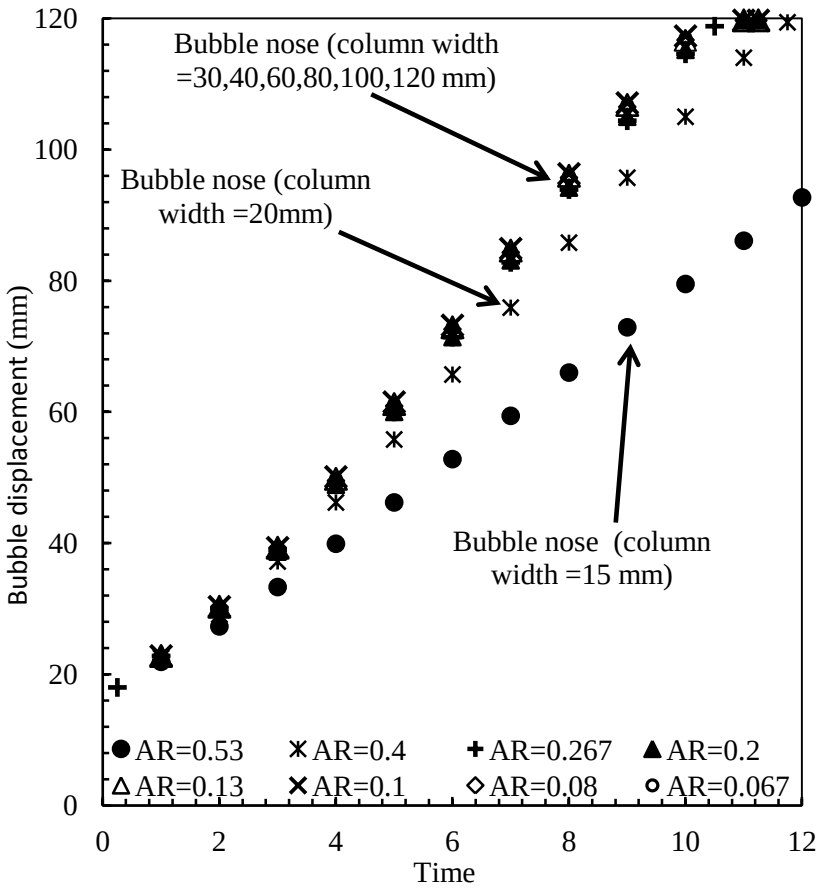

Figure 5-5 Compares the x-coordinates of the nose of 8 mm bubbles

The liquid phase streamlines profiles for four aspect ratios (AR = 0.53, 0.4, 0.267, and 0.2), illustrated in Figures 5.6a-d. These results show that when the ratio of the bubble diameter to the column diameter is less than 0.267, the influence of the column diameter on the ascension velocity is negligible; however, as the AR increases, there is a significant reduction in the bubble's velocity. When calculating the bubble speed in the next section, the results obtained here were considered as a factor having crucial effect on the bubble speed; consequently, the wall effect was removed from the calculations. Note that in all thermocapillary bubble flow calculations, the migration velocity is taken as the bubble migration in the axial direction, as seen in Figure 5.7; moreover, the bubble remained spherical in shape and no deformation was noticed for any of the ARs (see Figures 5.6a-d).

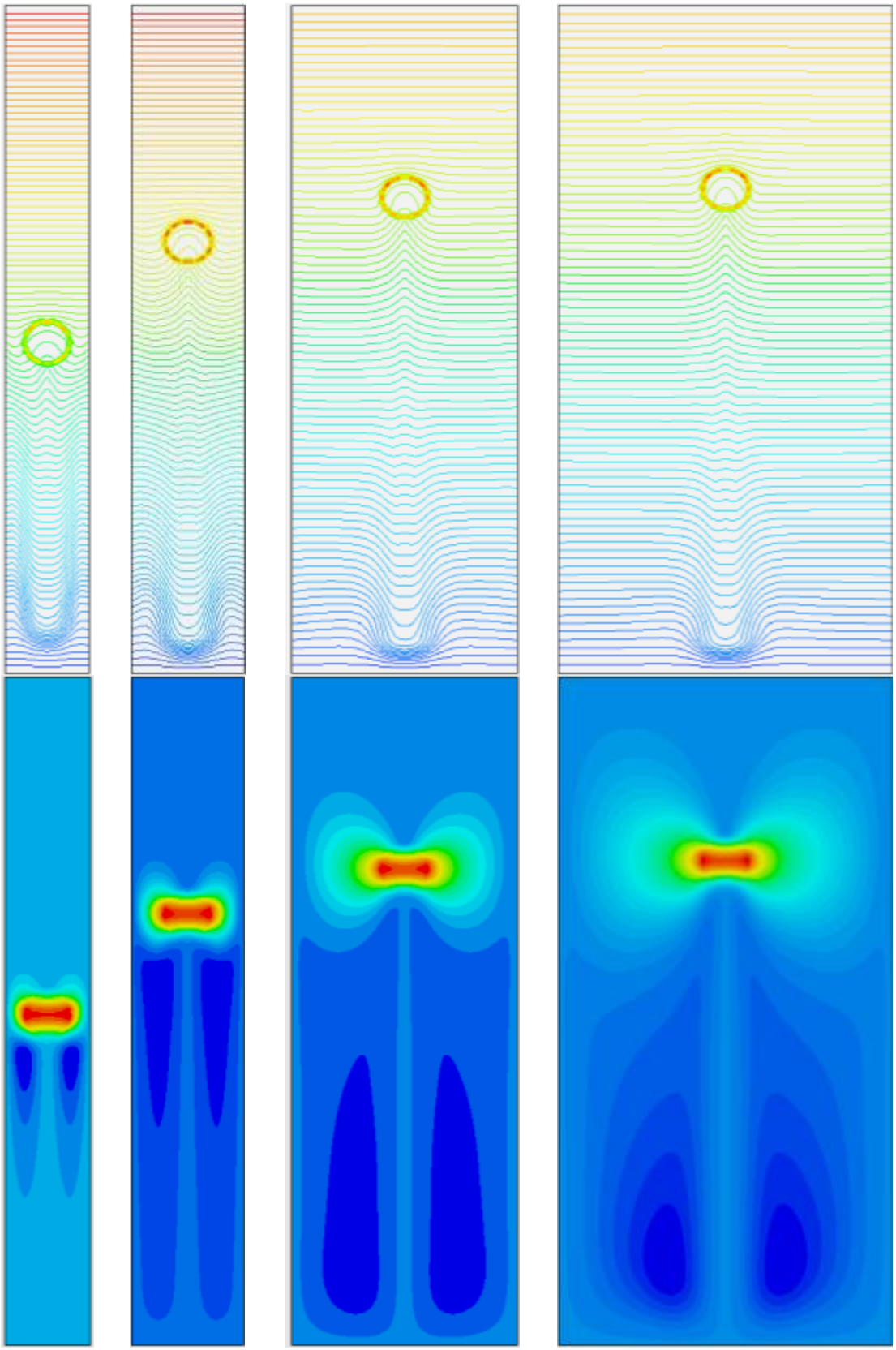

a)AR=0.5 b) AR=0.4 c) AR=0.2 d) AR=0.133

Figure 5-6a-d Contours of temperature (top) and streamlines (bottom) illustrate the effect of four different (AR) upon bubble migration at time =7.5 sec

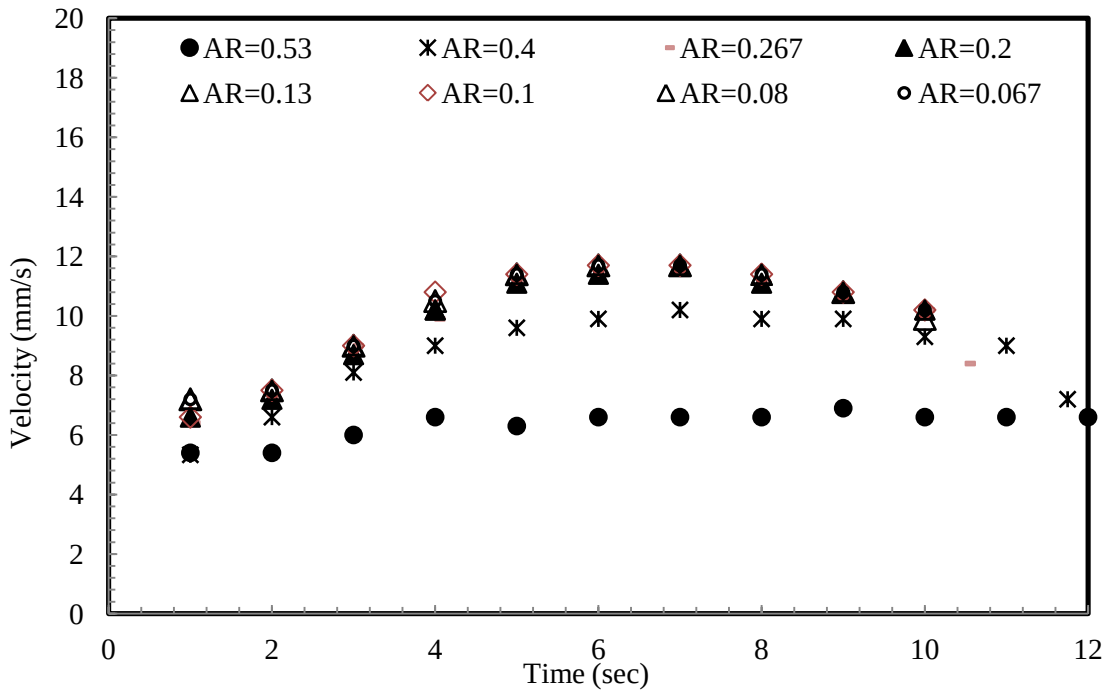

Figure 5-7 Bubble velocity in columns with widths of 15, 20, 30, 40, 60, 80, 100, and 120 mm diameters

5.1.3 Effect of changing a bubble's initial position upon its migration velocity

In addition to the temperature gradient and width of the cylinder, another important factor that may influence bubble migration and is worthy of investigation is the starting position of the bubble in relation to the bottom of the cylinder. In this subsection this effect is investigated numerically. The idea is to place the bubble at various starting positions, starting at a distance of 1d from the lower wall and then increase the distance by 1d in each run, up to a distance of 4d. Figures 5.8 and 5.9 illustrate the effect of changing the initial bubble position on bubble migration. In all of these simulations, the diameter of the bubble is 10mm, the height of the domain is 120mm, and the temperature gradient is 0.25 K/mm. Clearly, the lower wall has no direct influence on bubble migration, and a distance of up to 1d shows no attractive force from the lower wall to the bubble. What is more, the further the bubble's starting position from the upper, warmer wall, the more likely it is to reach the steady state, as seen in Figure 5.9 for a position of 1d, which shows that the bubble approaches the steady

state at a time between 5 and 7s. Therefore, the initial bubble-wall distance is an important factor for the effect of the wall on the bubble. Thus, a bubble placed far away from the warmer side will reach a steady state migration velocity. The motion induced in the x direction in zero gravity for all four position distances shows that the bubble migrates toward the warmer region. This observation is in line with the Marangoni phenomena, which asserts that the surface tension gradient effect is dominant.

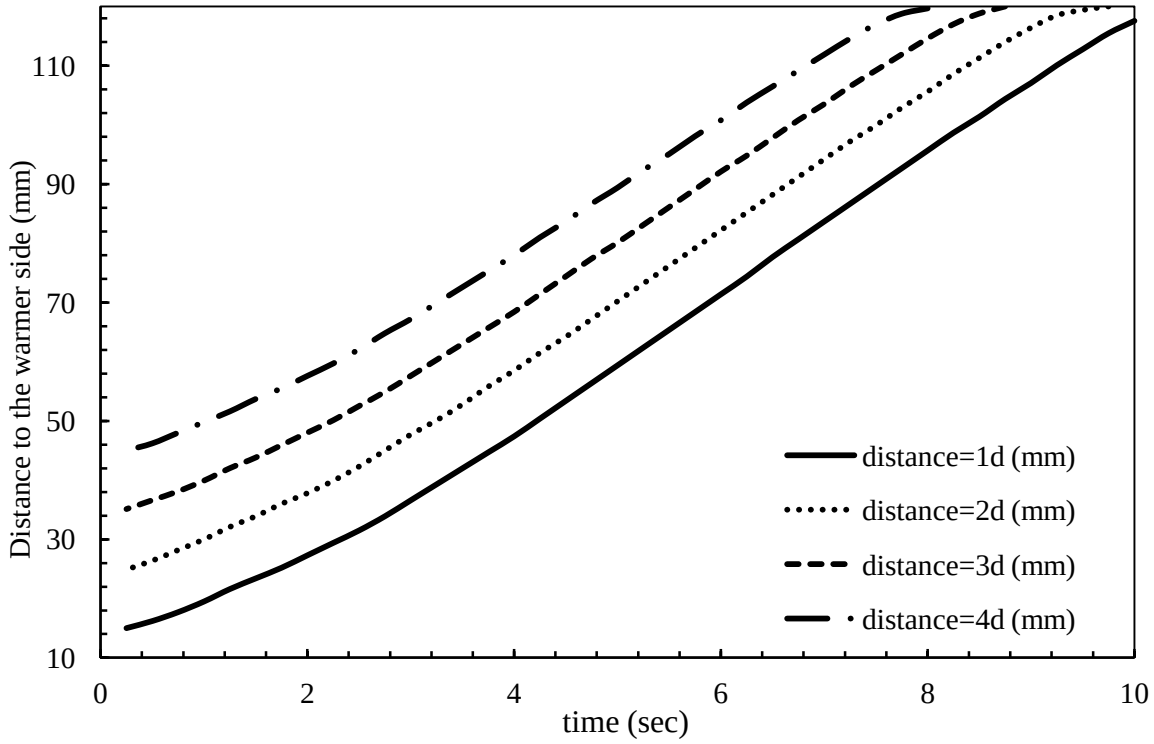

Figure 5-8 A 10 mm-diameter bubble rising from a position equal to 1d, 2d, 3d, and 4d from the lower wall.

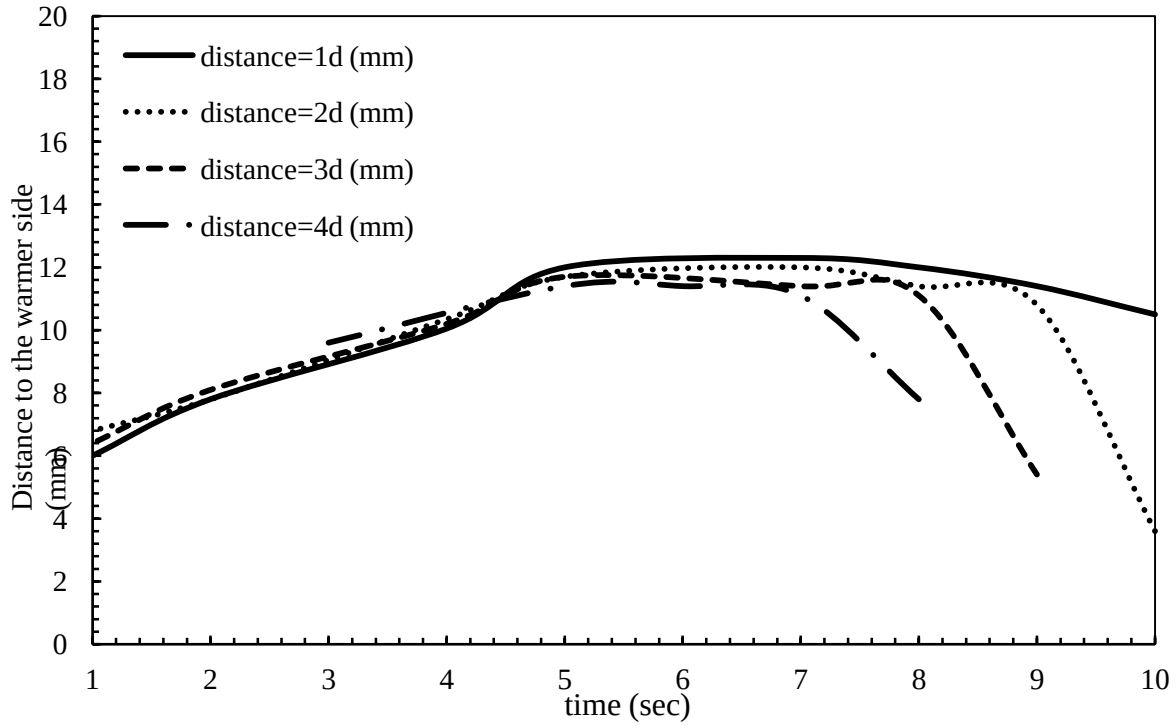

Figure 5-9 Velocity of a 10 mm-diameter bubble rising from a position equal to 1d, 2d, 3d, and 4d from the lower wall

5.1.4 Correlation for the thermocapillary bubble migration velocity

Young, Block, and Goldstein (1959) first investigated the thermocapillary migration of bubbles and droplets with a linear model, as previously stated in Eq. (2.1) from chapter 2:

$$V_{YGB} = \frac{2\left|\frac{d\sigma}{dT}\right| r_b \lambda \frac{dT}{dx}}{(2\mu + 3\mu')(2\lambda + \lambda')}$$

commonly called the YGB model, which is suitable for small Reynolds and Marangoni numbers:

$$\mathrm{Re_T} = \frac{r_b V_T}{\mathrm{v}} \qquad 5\text{-}1$$

$$Ma_T = \frac{r_b V_T}{\alpha} = \mathrm{Re}_T . \mathrm{Pr} \qquad 5\text{-}2$$

where Prandtl number is the ratio of kinematic viscosity to thermal diffusivity:

$$\Pr = \frac{\nu}{\alpha} \quad 5\text{-}3$$

and ν is the kinematic viscosity in m²/s:

$$\nu = \frac{\mu}{\rho} \quad 5\text{-}4$$

The velocity V_T, derived from the tangential stress balance at the free surface, is used for scaling the migration velocity (m/s) in Eq.s (5.2) and (5.3):

$$V_T = \frac{\frac{d\sigma}{dT}.\frac{dT}{dx}.r_b}{\mu} \quad 5\text{-}5$$

where $\mu, and\ \mu', \lambda\ and\ \lambda'$ are the dynamic viscosity and thermal conductivity of continuous phase and gas, respectively. ρ is the density and, r_b is the radius of the bubble. The constant $d\sigma/_{dT}$ or σ_t is the rate of change of interfacial tension and $dT/_{dx}$ is the temperature gradient imposed in the continuous phase fluid. The bubble velocity is obtained from the ratio of the monitored displacement of a small Δx (2D axis) or Δy (3D) and the short time interval Δt. This definition implies that:

$$V_{CFD} = \frac{\Delta x}{\Delta t} \quad 5\text{-}6$$

where V_{CFD} is the bubble's velocity at time t and Δx is the change in displacement of the bubble between times t and $t + \Delta t$. In this situation Δt must be kept small so that the bubble velocity does not change appreciably between times t and $t + \Delta t$. If Δt is too large then formula (5.6) becomes invalid.

The current numerical tool allows for the use of different gravity values. However, the current chapter only presents the zero gravity results, specifically flow movement due to surface tension rather than buoyancy effects. In a non-uniform temperature gradient field, the surface tension varies according to the local temperature conditions. Near cold regions, a greater surface tension exists than in the warmer regions. This causes a net imbalance of force acting upon the fluid particles, leading to a general motion of fluid from the warm region to

the cold region (in the current case, from the upper to the lower surface). Upon closely observing the bubble movement (see Figs 5.1 & 5.6) it is noted that the bubble absorbs heat at the hot end and rejects heat at the cold end, as observed by (Nas and Tryggvason, 1993): "Whenever surface is created, heat is absorbed, and whenever surface is destroyed heat is given off. Therefore a swimming bubble absorbs heat at its hot end and rejects heat at its cold end". In Figure 5-10 a single bubble migration velocity correlation was obtained numerically in a differentially heated fluid cell. A spherical bubble shape is then assumed to find the relation for the scaled rise velocity of the bubble (V_{CFD}/V_{YGB}). This is given as:

$$\frac{V_{CFD}}{V_{YGB}} = 1.35Ma^{-0.16} \qquad 5\text{-}7$$

V_{YGB} was used for scaling the calculated bubble velocity in Equation (5-7). Figure 5.10 presents the relationship between the present results for the simulated scaled rise velocity (V_{CFD}/V_{YGB}) and previous experimental results for Kang et al. (2008) and Treuner et al. (1996). It is clear from the figure that, the) present numerical simulations, for (V_{CFD}/V_{YGB}) agree well with the previous experimental results, also shown in the same figure is the correlation given by Eq. 5.7 which predicts the scaled velocity with a maximum standard deviation of 5.2% for the simulation range of the present study. For the current simulations, the selection of temperature gradient between the walls was kept low to avoid fluid property changes due to thermodynamics. It was observed that as Ma increases, the bubble's scaled migration velocity tends to approach an asymptotic behaviour ($V_{CFD}/V_{YGB} \approx 0.3$). In the current case, the migration velocity of a single bubble is smaller than that predicted by the YGB model, as can be seen from the curve fit in Figure 5.10. In fact, the current results seem to better agree with other predictions of Kang et al. (2008) and Treuner et al. (1996). Figure 5.11 show a percentage error between simulated and predicted scaled velocity.

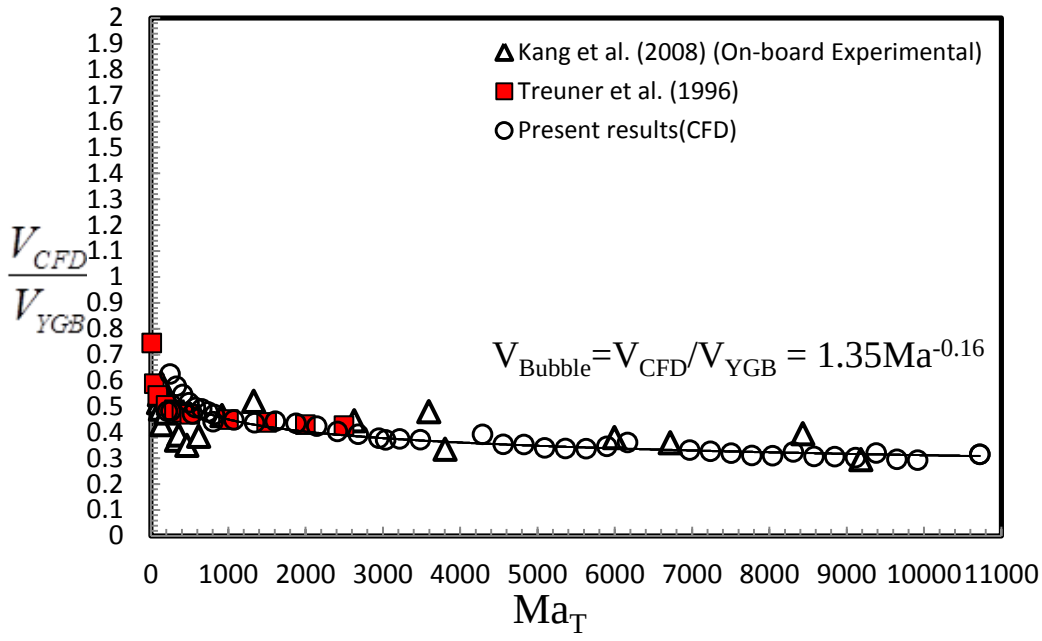

Figure 5-10 Scaled velocity plotted against Marangoni number; earlier experimental data also shown

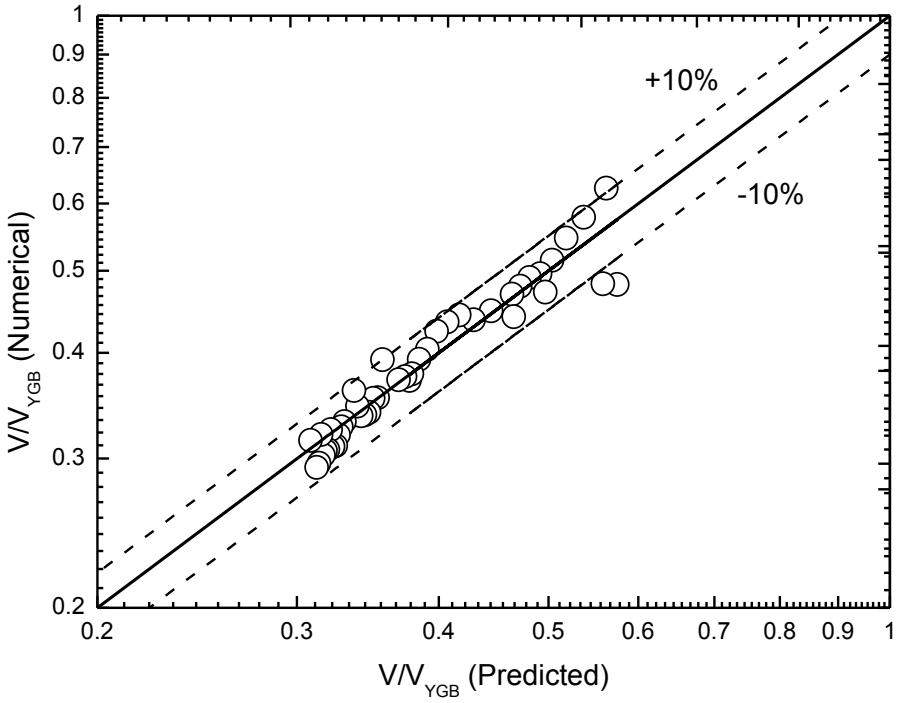

Figure 5-11 Relationship between simulated and predicted scaled velocity

5.2 Thermocapillary migration of an isolated droplet in zero gravity

5.2.1 Over view

In a non-uniform temperature gradient field, the surface tension varies according to the local temperature conditions. Near cold regions, a greater surface tension exists than that observed in the hotter regions. This causes a net imbalance of force acting upon the fluid particles, thus leading to a general motion of fluid from the hot region to the cold region. Such a phenomenon is known as the Marangoni problem or the thermocapillary migration problem. Research and experimentation on thermocapillary bubble and droplet motion began in 1959 on the ground using a space laboratory by Young, Goldstein and Blocks. In their ground-based experiment where gravitational force was presented, they succeeded in holding a small bubble stationary and moving it downwards against the buoyant rise of gas bubbles by applying a temperature gradient between the lower and upper sides. A few years later, on-board microgravity experiments on the thermocapillary migration of bubbles and droplets have since been performed using spacecraft. Two-phase flow experiments generally require continuous observation of moving fluid during a test, which makes the experiment complicated, and it is also a challenge for space researchers to design a space experiment to accommodate most of their objectives. Furthermore, experiments under microgravity conditions are limited to low Reynolds and Marangoni numbers because of the difficulties in obtaining experimental results in microgravity (Kang et al., 2008). A few microgravity experiments on the thermocapillary droplet flow in zero gravity have been performed on board the microgravity sounding rocket and Spacelab, and noted that there are no numerical results with which to evaluate their data. Xie et al. (2005) mentioned the complex behaviour of thermocapillary droplet migration, confirming that further studies were still needed. They also confirmed that a longer experimental time in microgravity conditions is necessary for a droplet approaching its steady thermocapillary velocity. It is also difficult to obtain complete

information about the behaviour of bubbles/droplets in space, and CFD studies have been undertaken by many researchers in order to compare and analyse their experimental results (Treuner et al., 1996). In recent years and with advances in numerical calculation, knowledge of thermocapillary flow has undergone a considerable change and new calculated results could be used to revise and adjust some previous results. On the other hand, numerical simulations have consequently become an important tool in studies of two-phase flows in a microgravity environment and can help to clarify the basic fluid physics, as well as to assist in the design of the experiments or systems for the zero-gravity environment.

Xie et al. (2005) presented results from aboard China's spacecraft ShenZhou-4 space experiment, which show decreases in the droplet scale velocity with increasing Marangoni number. These results are in contrast with the work of the theoretical predictions from a numerical solution made by Ma et al. (1999) and the theoretical predictions of Balasubramaniam and Subramanian (2000), which show a decrease and subsequent increase in the droplet scale speed with Marangoni number. These three research works used the same liquid media of Fluorinert liquid FC-75 and silicone oil for the drop liquid and matrix phase respectively. From the above comparison, it can be seen that the behaviour of a droplet's thermocapillary migration at large Marangoni numbers appears complex, and further studies are needed to observe the developing trend of droplet migration velocity with an increase in the values of Ma_T. There is also a conflict in the results of some authors on the subject of the interaction between two droplets, which will be discussed in detail later in this chapter. For the above reasons and more, it is necessary to carry out appropriate numerical simulations for the measurement of the behaviour of droplets in microgravity (Subramanian et al., 2009). Flow patterns are key to the understanding and prediction of the physics behind flow systems. The shape and the area of the varying interfaces are very complex and often a numerical simulation study is required. Furthermore, the flow patterns of some regimes remain largely

undiscovered; consequently, accurate predictions of flow patterns are highly desirable (Wölk et al., 2000). This subsection is a step in this direction; some aspects of the thermocapillary two-phase flow in zero gravity will be numerically investigated and discussed. In this chapter, the results from the Ansys-Fluent CFD are reported and the data are compared with the numerical results of Ma et al. (1999) and Balasubramaniam and Subramanian (2000) as well as the space experiment results of Xie et al. (2005).

5.2.2 Simulation method for migration of a droplet in liquid

The objective of this CFD work is to simulate and observe the behaviour of a single and multiple droplets under the influence of a linear temperature gradient in a zero-gravity environment and to validate the present CFD work with an existing experiment from the literature, before proceeding to find an expression for the relationship between the droplet scale velocity and the Marangoni number. The behaviour of leading and trailing droplets is a central topic in research and engineering applications and the results of these tests will be included in detail in this section as well.

A description of the geometry is shown in Fig.5.12, and the following assumptions are made for all numerical simulations:

7. The diameter and height of the domain are 12d.
8. The thermocapillary velocity is small and the flow is laminar.
9. The upper and lower surfaces are flat and non-deformable; adiabatic non-slip wall conditions are applied to all surfaces.
10. A steady-state temperature distribution is established as an initial condition before releasing the drop in the unsteady motion, where the top and bottom walls are maintained at constant temperatures: $T_{top} > T_{bottom}$
11. The host liquid is an incompressible Newtonian fluid and an assumption of constant properties is applicable, except for density, viscosity, and surface tension.
12. The driving force for the flow is the variation of surface tension according to temperature, which is modelled by a linear function shown in Equation 4-1 below:

$$\sigma = \sigma_0 + \sigma_T (T_0 - T)$$

where or σ_0 is the coefficient of surface tension at reference temperature T_0 and σ_T is the rate of change of surface tension with temperature T. Table 5.2 presents the physical properties of the host liquid and liquid droplet used for the simulations at 300K. The calculation was carried out for FC-75 Fluorinert droplets migrating in DOW-Corning DC-200 series of nominal viscosity 10 cst at different temperature gradients (∇T) K/mm, in order to investigate what happens to the thermocapillary drop when a linear temperature distribution is prescribed between the upper and lower walls. A stationary cylindrical domain with an isolated spherical droplet inside was considered by the initial locations of its centre at (1d, 0d) mm from the lower wall, at the cylindrical coordinates of (X,Y) so that the droplet is close to the bottom of the cylinder.

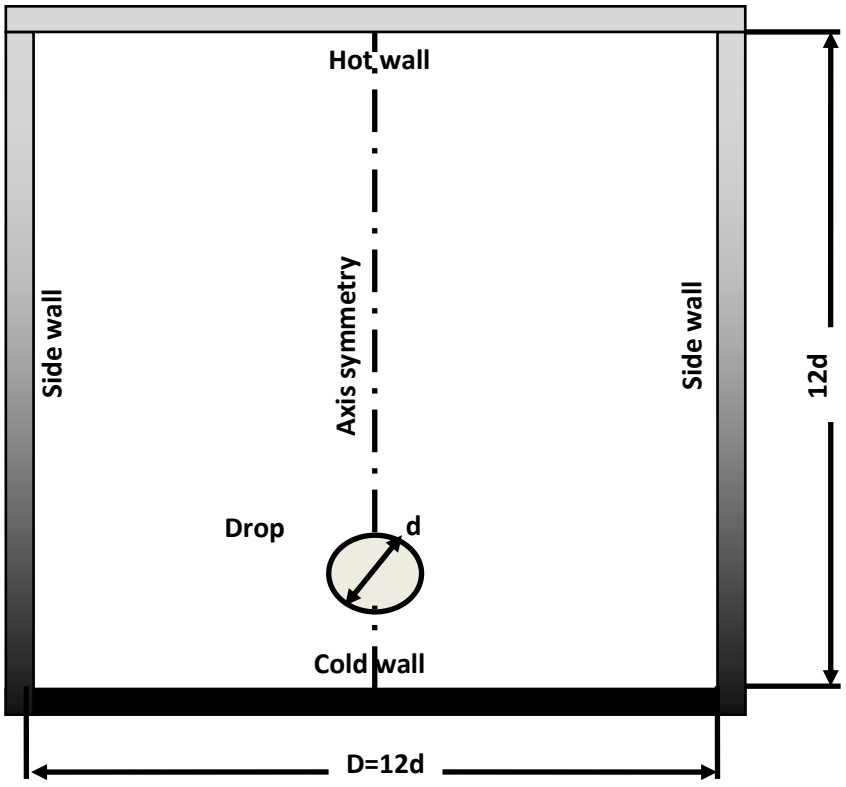

Figure 5-12 Schematic of drop migration in a uniform temperature gradient.

Numerical calculations were carried out to simulate the droplet's Marangoni migration in a 2D axisymmetrical column in a zero-gravity environment, to investigate in detail the

behaviour of a single and multiple droplets under thermocapillary force in a column of liquid. The domain was defined as a cavity with abounded walls (described in Chapter 4 and Figure 5.12) and was used for all simulation. All simulations were run at time t=0 with initially stationary liquid and droplet. For all simulations the initial state will be set with no velocity at the inlet or at the outlet. Before patching the droplet using Fluent's "region" function, the matrix liquid was preheated to obtain the steady state against temperature gradient. The surface tension coefficient between the host liquid and the droplet, density, and viscosity were considered to be dependent on temperature and were computed via UDF.

Table 5-2 Physical properties of the liquids employed in the simulation of silicone oil (DOW-Corning DC-200 series of nominal viscosity 10 cst) and Fluorinert FC-75.

Properties	Unit	Silicone oil	Fluorinert	Fluorinert FC-75/10 cst silicone oil (ratio)
Density (ρ) =A+BT	kg/m^3	A=1200 B=-0.9	A=2504 B=-2.48	1.89
Viscosity (μ)= exp (C+D/T)	kg/m-s	C=-10.17 D=1643	C=-11.76 D=1540	0.147
Initial Prandtl Number (Pr)	-------	121.6	22	22/121.6
Specific Heat (Cp)	j/kg.K	1778.2	1047	0.589
Thermal Conductivity (k)	w/m.K	0.13389	0.063	0.47
Surface tension gradient	N/m-K	0.000086		

The thermophysical properties for density, viscosity and surface tension gradient for silicone oil (DOW-Corning DC-200 series of nominal viscosity 10 cSt) and Fluorinert FC-75 were taken to be the same as those used by Hadland et al. (1999), as follows:

The density variation with temperature of the two liquids is assumed to be of the form:

$$\rho = A + BT \qquad 5\text{-}8$$

and the viscosity variation with temperature of the two liquids is assumed to be of the form

$$\mu = \exp(C + D/T) \qquad 5\text{-}9$$

The major properties of the liquid system used in the present simulation are summarised in Table 5.2.

5.2.3 Grid size dependency

The objective of the grid independence study was to ensure that the results of the simulation were independent of the grid density. Grid independence was achieved by increasing the number of regional adaption cells from 111 to 632 per droplet radius by increasing the grid cells along the X and Y axes and plotting the convergence of certain parameters of interest, such as the time taken for droplets to migrate towards the warmer side and their migration distance, to ensure that the result remained independent of the grid size. In terms of the number of cells in the present study, a non-uniform grid with grid lines clustered towards the centre was developed in order to keep cell count down and to avoid the potential negative consequences of increased memory usage and CPU time. Another key consideration is that, when using an axisymmetric solver, you create a mesh only for half of your domain, thus drastically reducing the number of cells used, and consequently the calculation time. These cases were simulated with the parameters outlined in Table 5.2. A study of the grid size dependency is described in Table 5.3.

Table 5-3 Grid sensitivity check for a droplet with diameter of 10 mm for 2D-axis models				
Grid	(Δx,Δy)	Number of cells	Cells per drop radius	Droplet speed (mm/s)
(1)	0.6x0.6	8400	111	1.90
(2)	0.5x0.5	9600	158	1.90
(3)	0.4x0.4	17760	242	1.83
(4)	0.3x0.3	23200	430	1.70
(5)	0.25x0.25	31200	632	1.7
(6)	0.2x0.2	45000	988	1.7

Figure 5.13 shows the migration distance of the droplet versus time for these 6 cases. Note that, in all the results presented in this study, the migration velocity is simply taken as the droplet's velocity in the X direction. In the present study, a non-uniform grid of 23,200 cells with grid lines clustered towards the centre (grid 4), giving 430 cells per droplet radius, has been used in all calculations.

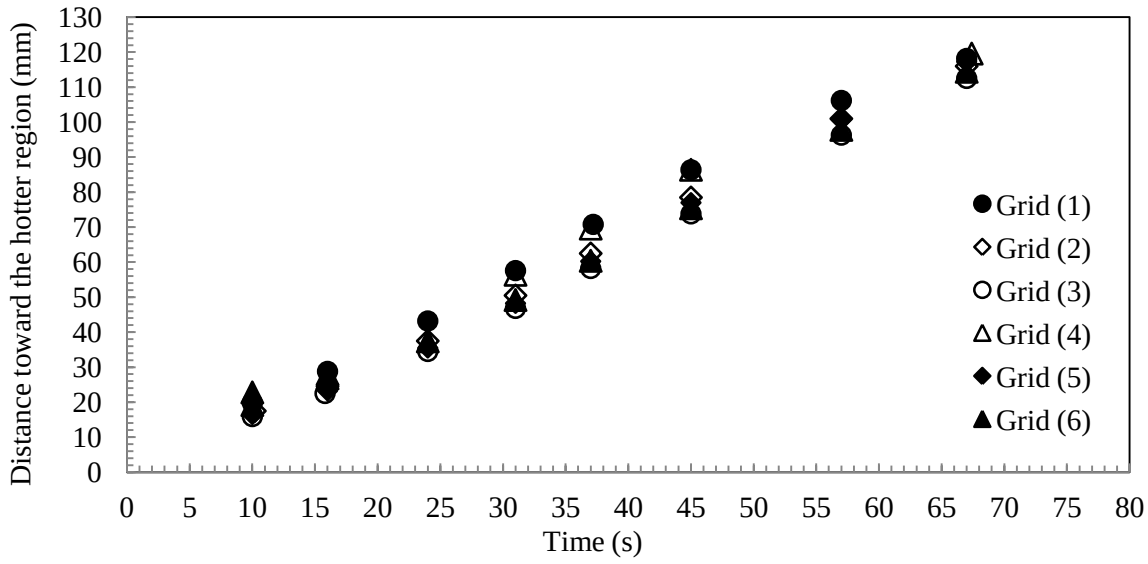

Figure 5-13 Ascension distance of a droplet nose for five different grid sizes vs. time (s)

Figure 5.14 shows the result of four different grid densities used in this simulation to give the isothermal contour of an isolated droplet at a time equal to 66 sec for all five grid studies.

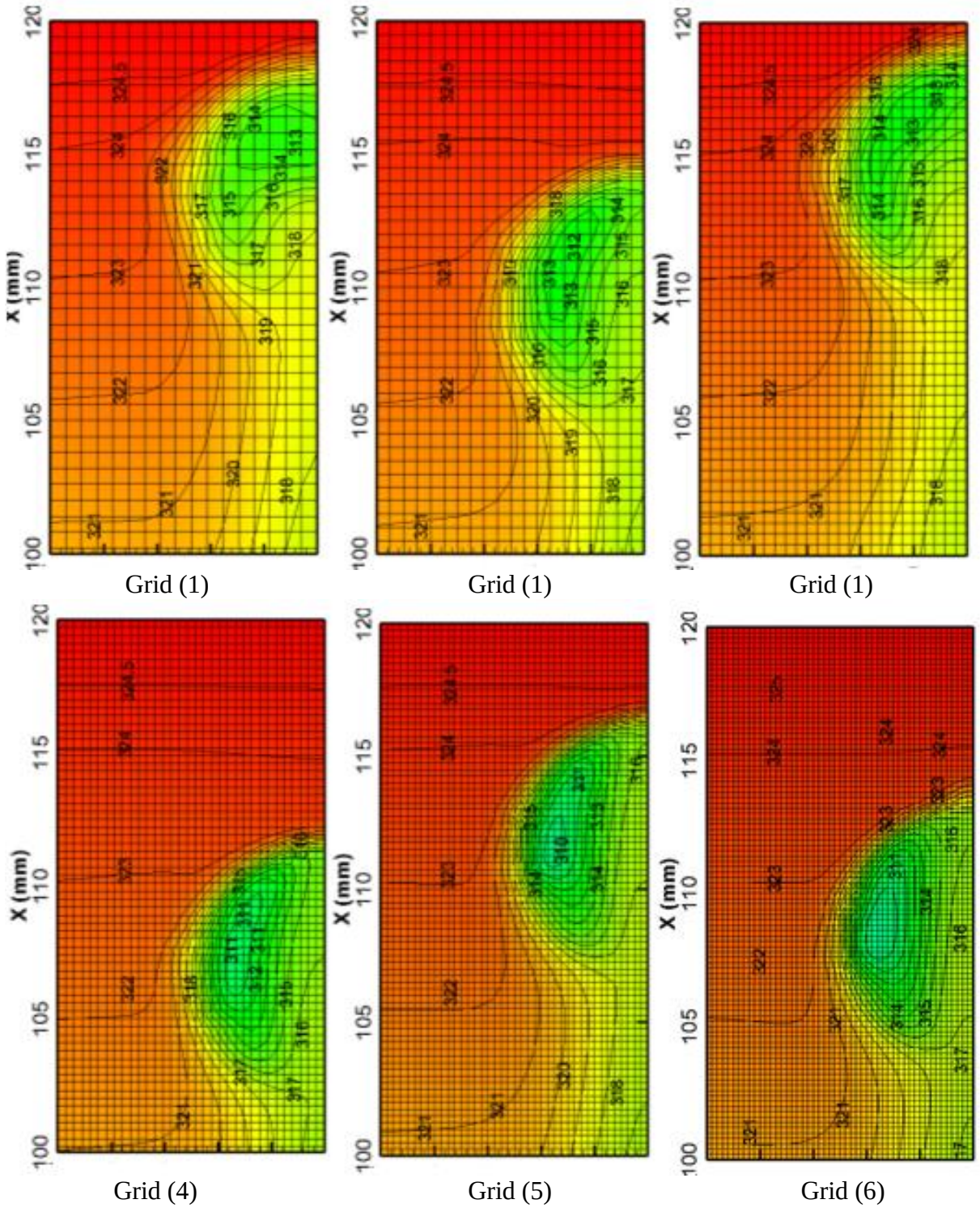

Figure 5-14 Distance (mm) towards the warmer region of the droplet for five different grid sizes at time = 66 sec

5.2.3 Results and discussion

In this subsection, the migration of a droplet with a diameter of 10 mm was observed in a container with lower and upper surfaces at temperatures of 300 and 325 K respectively. At a given temperature and from the physical properties of the liquids employed in the simulation of silicone oil (DOW-Corning DC-200 series of nominal viscosity 10 cst) and Fluorinert FC-75 given in Table 5.2, the corresponding average thermal Reynolds (Re_T) and Marangoni numbers (Ma_T) were 7.80 and 769.8 respectively. The droplet was released from the colder region (lower wall) and reached the warmer region (upper wall) within about 75 sec. The contours of the isotherms which developed near the interface and within the droplet for axisymmetric simulations at the indicated time from 25 sec to 70 sec in increments of 5 sec are shown in Figure 5.15. The results show that the droplet in an immiscible fluid will move towards the warmer side when subjected to a temperature gradient in a zero-gravity environment. Such a phenomenon is known as the Marangoni problem or thermocapillary migration.

Upon closely observing the temperature contours in these figures, two types of heat transfer can be perceived that are both responsible for the droplet's movement towards the hotter side. These forms of transfer are conduction heat transfer between the surrounding liquid and the droplet, and convection within the droplet itself. It was also noted that the temperature inside the droplet was different from that of the surrounding liquid, due to insufficient time for the temperature gradient inside the droplet to reach a steady distribution. The second significant effect is that which the outside temperate gradient had on the heat transfer rate between the droplet and the matrix liquid, which provides an explanation for the observed movement of the Fluorinert droplet in the silicon oil and the inside droplet, as will be seen in the following subsection.

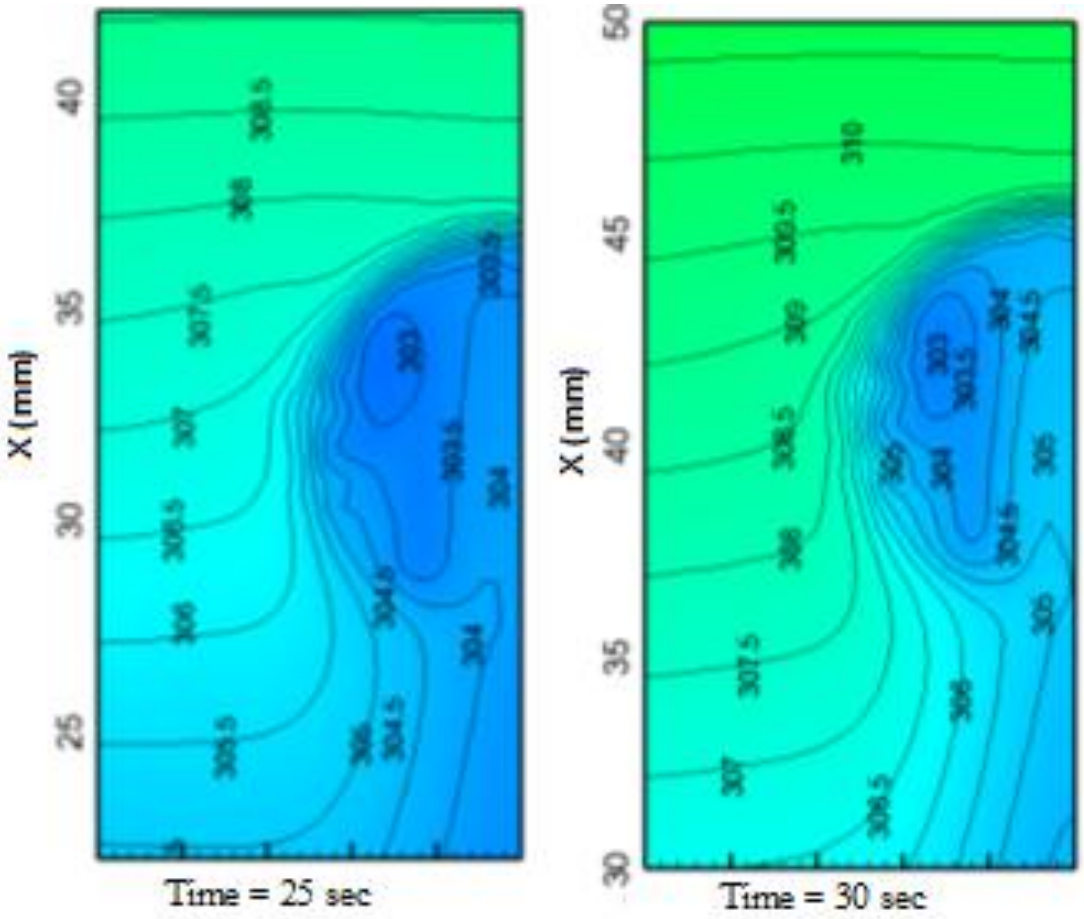
X (mm)
40
35
30
25
Time = 25 sec
X (mm)
50
45
40
35
30
Time = 30 sec

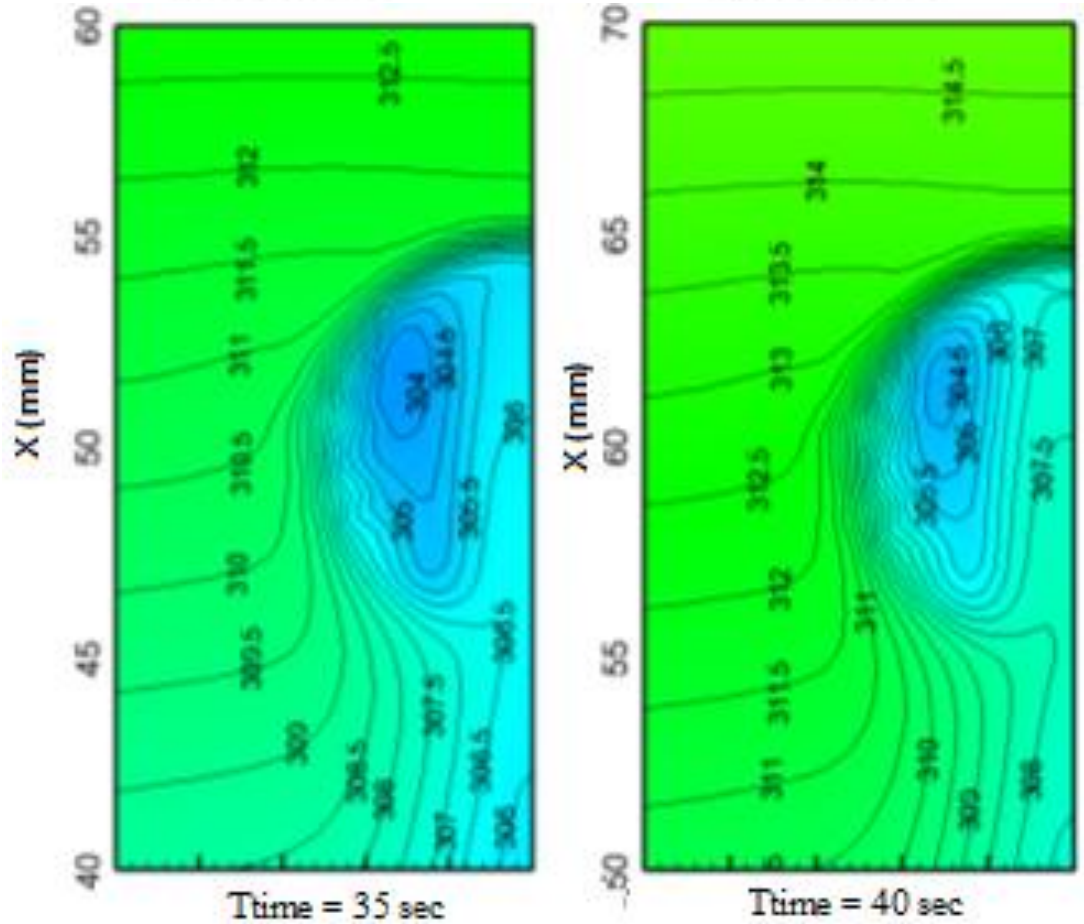
X (mm)
60
55
50
45
40
Ttime = 35 sec
X (mm)
70
65
60
55
50
Ttime = 40 sec

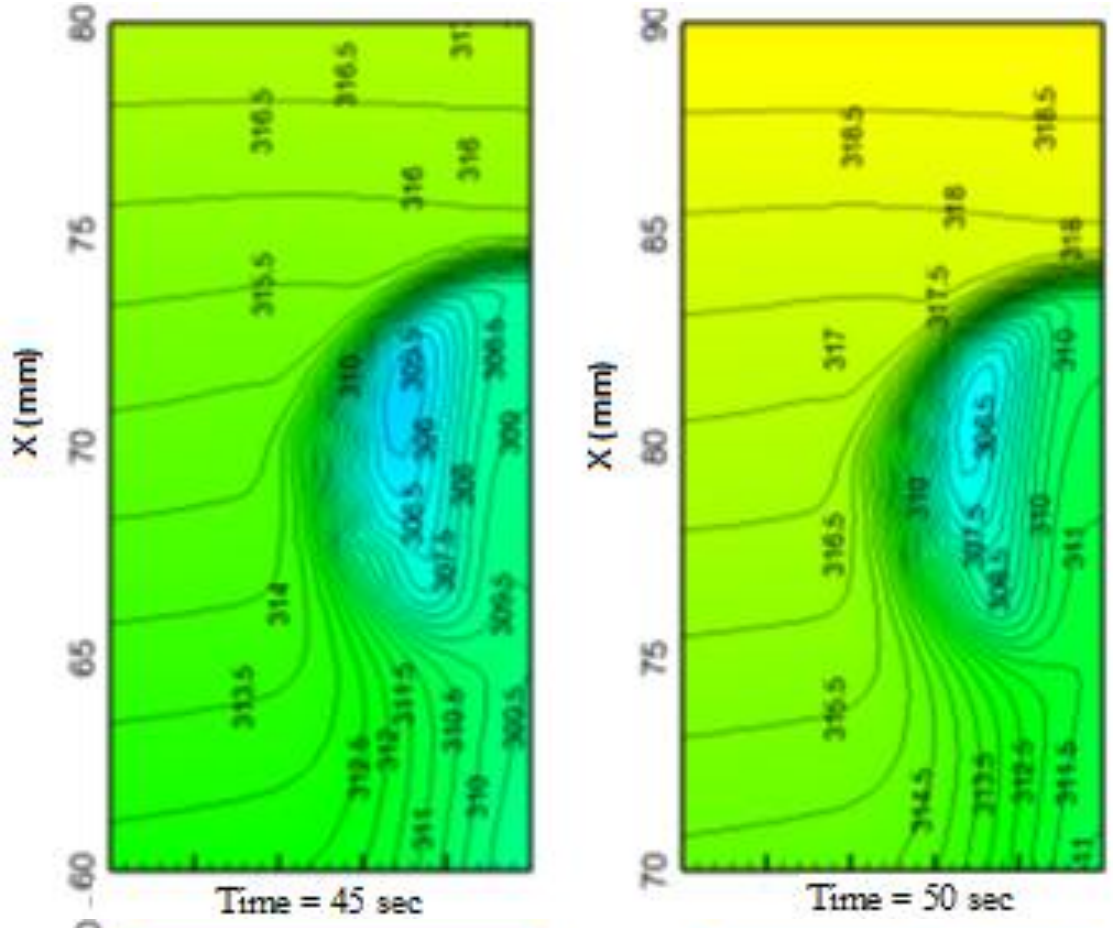
X (mm)
Time = 45 sec

X (mm)
Time = 50 sec

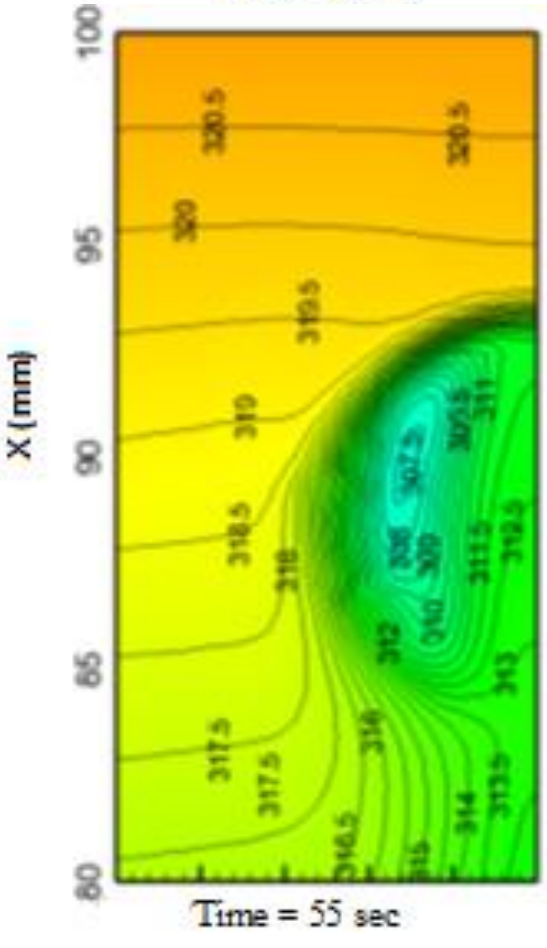
X (mm)
Time = 55 sec

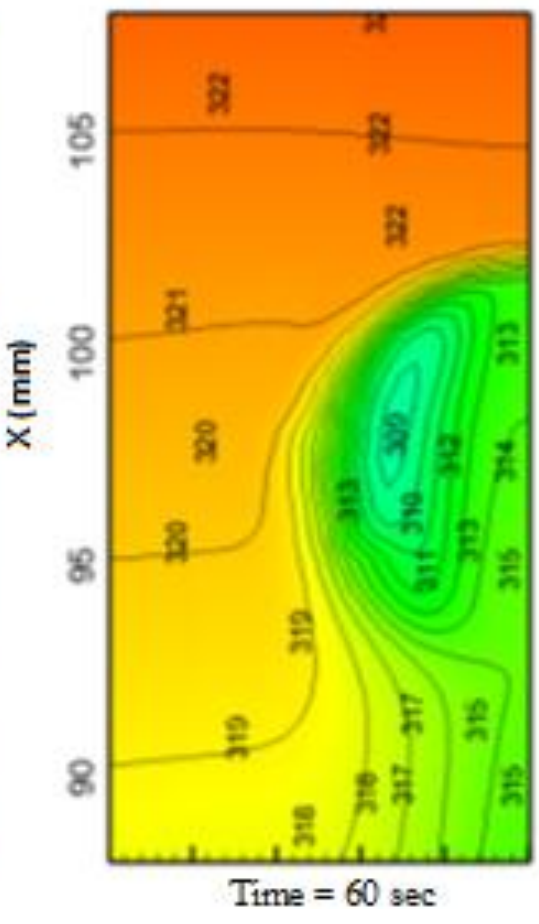
X (mm)
Time = 60 sec

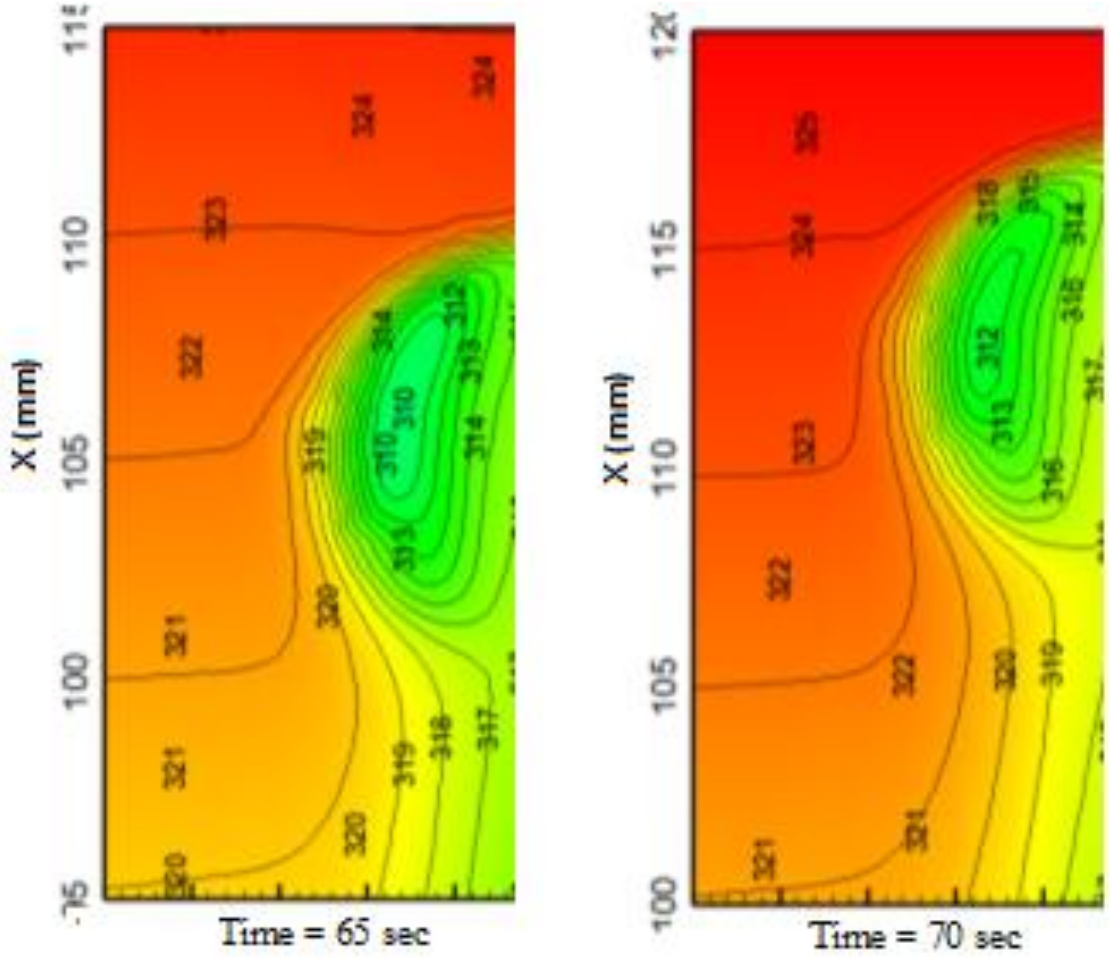

Figure 5-15 Contour of isotherms, showing the development of the cold region inside the droplet at ReT=7.8 and MaT=769.8 for different time steps.

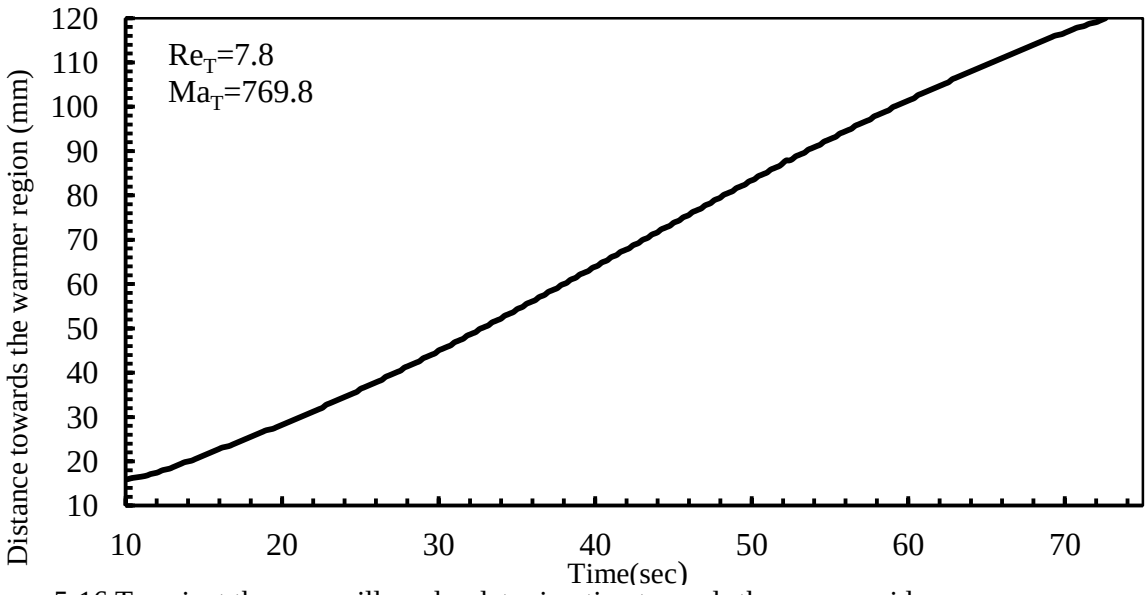

Figure 5-16 Transient thermocapillary droplet migration towards the warmer side

Note that so far the numerical analysis has been restricted to a given temperature gradient ∇T=0.25 K/mm. Intuitively, decreasing or increasing the temperature gradient of the liquid medium could affect the rate of conduction heat transfer across the droplet, thus increasing or decreasing the convection heat transfer within the droplet. This in turn affects the migration velocity of the droplet, causing it to move towards the warmer region. The next section will investigate numerically the effect that varying the temperature gradient has on the conduction rate while keeping V_T, and V_{YGB} constant, as shown in Table 5.4.

5.2.4 Effect of varying the temperature gradient on the thermocapillary flow

Table 5.4 summarises the droplet migration speed observed for different temperature gradients between the upper and lower walls. The thermal Reynolds and Marangoni numbers varied, depending on the diameter of the droplet and the temperature gradient, from 0.24 to 15.6 and from 24.06 to 1540 for the Re_T and Ma_T respectively. The specific value of the Prandtl number is constant at 98.7 for all calculations. The thermal velocity $V_{T,}$ caused by tangential stress, and the Young model velocity ($Y_{YGB)}$ are also constant at 12.62 mm/s and 4.2 mm/s, respectively. In the first example from the table and for Ma=24.06, the temperature gradient applied is equal to 6.66 K/mm, and the droplet CFD migration speed V_{CFD} was found to be equal to 2.38 mm/sec, which is higher than in the rest of the simulations. The lowest value of V_{CFD} was equal to 1.49 mm/s at an Ma of 1540. This shows that the CFD-calculated velocity (V_{CFD}) of the droplet decreases as the Marangoni number increases, becoming almost constant at Marangoni numbers of 750 and higher. In the same table one can see a variation in the calculated droplet speed, V_{CFD}, due to the varying temperature gradient of the host liquid; a direct relation between temperature gradient and droplet speed is thus observed. It can therefore be concluded that different temperature gradients lead to different droplet migration velocities.

Table 5-4 Calculation of the average non-dimensional numbers and velocities corresponding to the fluid properties given in Table 5.2 and the results of CFD test for Fluorinert droplet migrating in Oil

∇ T (K/mm)	Pr (FC75)	Pr (oil)	Re_T	Ma_T	V_T (mm/s)	V_{YGB} (mm/s)	V_{CFD} (mm/s)	V
6.66	18.1	98.7	0.24	24.06	12.62	4.2	2.38	0.57
3.33	18.1	98.7	0.49	48.11	12.62	4.2	2.03	0.48
1.67	18.1	98.7	0.98	96.22	12.62	4.2	1.83	0.44
0.83	18.1	98.7	1.95	192.4	12.62	4.2	1.85	0.44
0.42	18.1	98.7	3.90	384.9	12.62	4.2	1.82	0.43
0.28	18.1	98.7	5.85	577.3	12.62	4.2	1.88	0.45
0.21	18.1	98.7	7.80	769.8	12.62	4.2	1.69	0.40
0.17	18.1	98.7	9.75	962.2	12.62	4.2	1.68	0.40
0.14	18.1	98.7	11.7	1155	12.62	4.2	1.69	0.40
0.12	18.1	98.7	13.7	1347	12.62	4.2	1.66	0.40
0.10	18.1	98.7	15.6	1540	12.62	4.2	1.49	0.36

The flow pattern shown in Figures 5.17a-j for the dynamic of a droplet in a host liquid with a ∇T of between 0.1 and 6.66 K/mm is in good agreement with the transient movement of the isolated droplet presented in Figure 5.15 for ∇T=0.25 K/mm. Initially in Figure 5.17a, the thermal Marangoni number (Ma_T) is small, and the droplet is subjected to a large temperature gradient at its surface (6.66 K/mm), resulting in strong thermocapillary flow. Interestingly, the isotherms in the continuous phase around a Fluorinert FC-75 droplet migrating in 10 cs silicone oil for Ma_T= 24.06 are almost straight, excluding the thermal wake behind the droplet. Moreover, the recirculation flow within the droplet is located in the upper section, and the temperature difference of the fluid inside and outside the droplet is almost identical for this low Ma_T and high temperature gradient. This is because the higher heat transfer rate across the droplet forces the isothermal layers to detach from the droplet more quickly than in the case of the droplet with lower heat transfer across it, resulting in a high migration speed. As the $Ma_T \rightarrow 0$, one can conclude that the flow pattern will corroborate the theory of Young et al. (1959). As the temperature gradient between the top and the bottom decreases and Ma_T increases, as shown in Figures 5.17b to 5.17j, the heat transfer by conduction across the streamlines to the interior of the droplet decreases. As a result, increasing the temperature difference between the interior and the surface of the droplet, i.e. causing the inside region of

the droplet to become colder than the surrounding liquid, results in the development of a clearly visible longer thermal wake behind the isolated droplet. Thus, the droplet speed begins to decrease and the recirculation expands inside the droplet. Using the relationships between the various temperature gradients summarised in Table 5.3 and the flow pattern presented in Figures 5.17a-j, it is evident that the heat transfer between the outside and inside of the droplet becomes constant for Ma>750; consequently, the inside colder region and the thermal wake become constant too. It is worth noting that in this study, the results confirmed that the thermocapillary droplet's migration velocity depends largely on the applied temperature gradient.

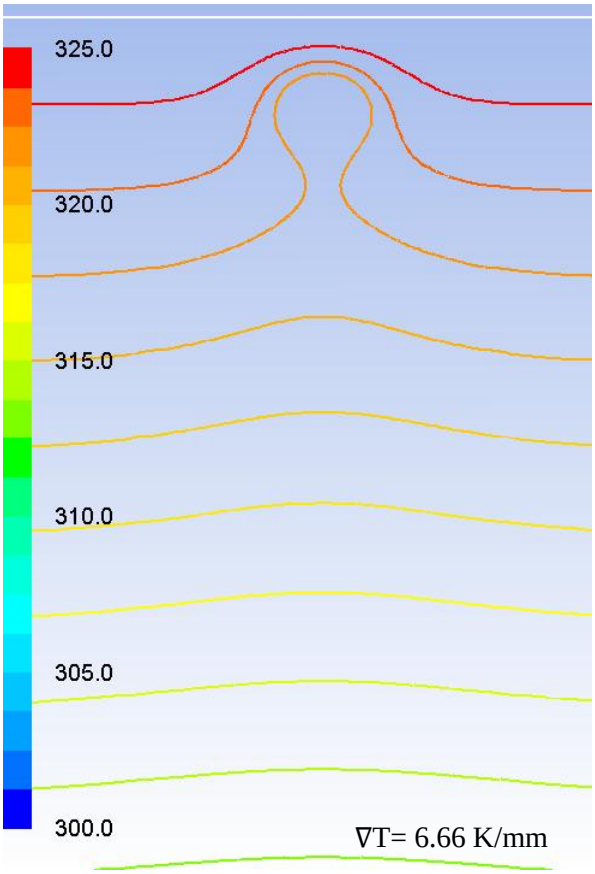

Figure 5.17a Ma_T =24.05

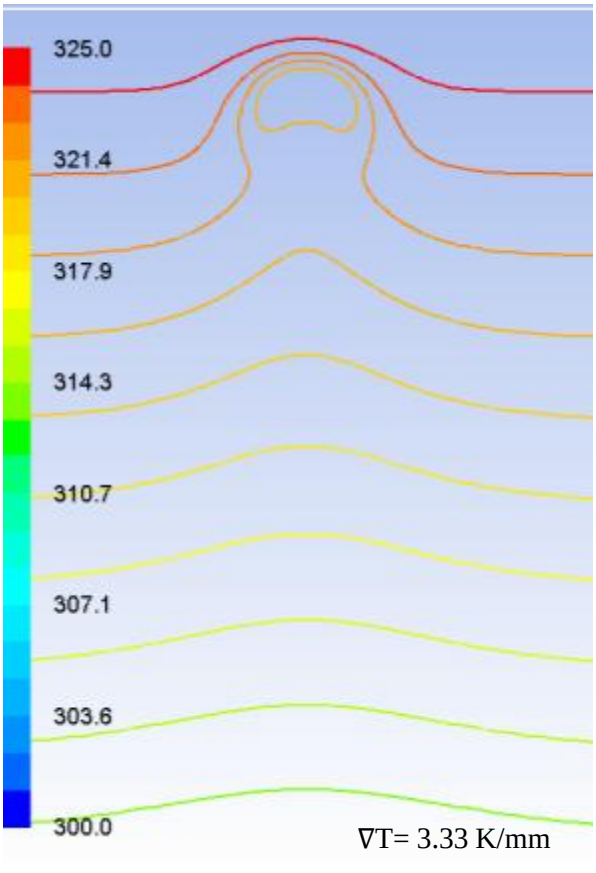

Figure 5.17b Ma_T =48.11

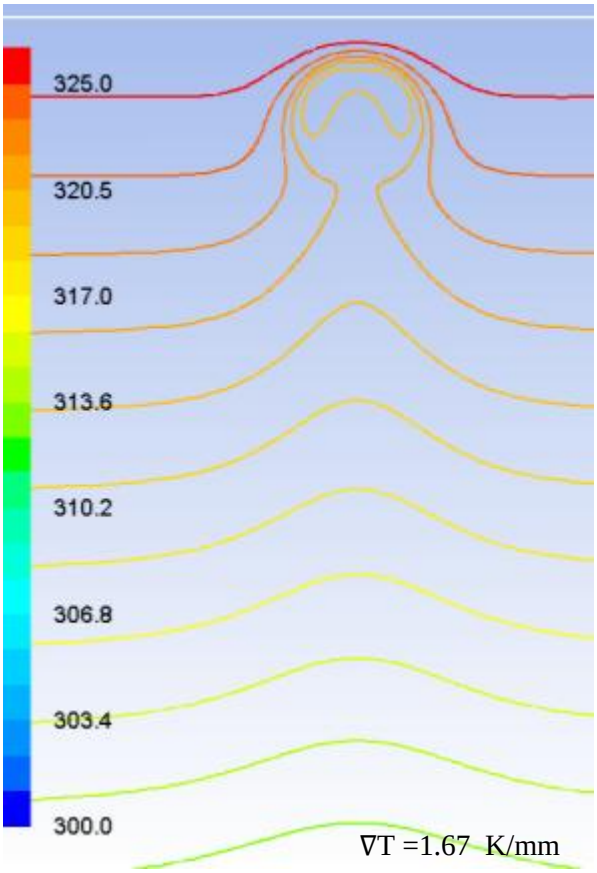

Figure 5.17c Ma_T =96.22

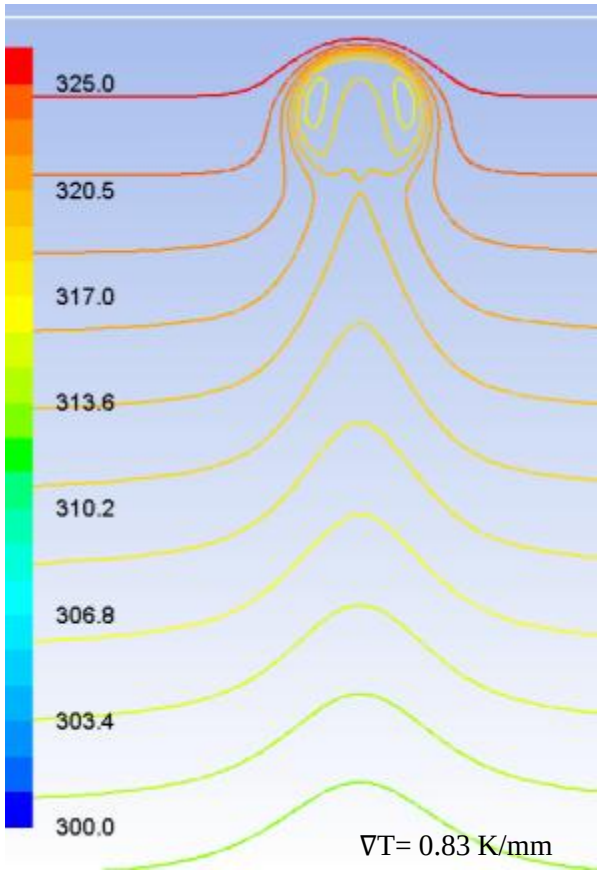

Figure 5.17d Ma_T =192.4

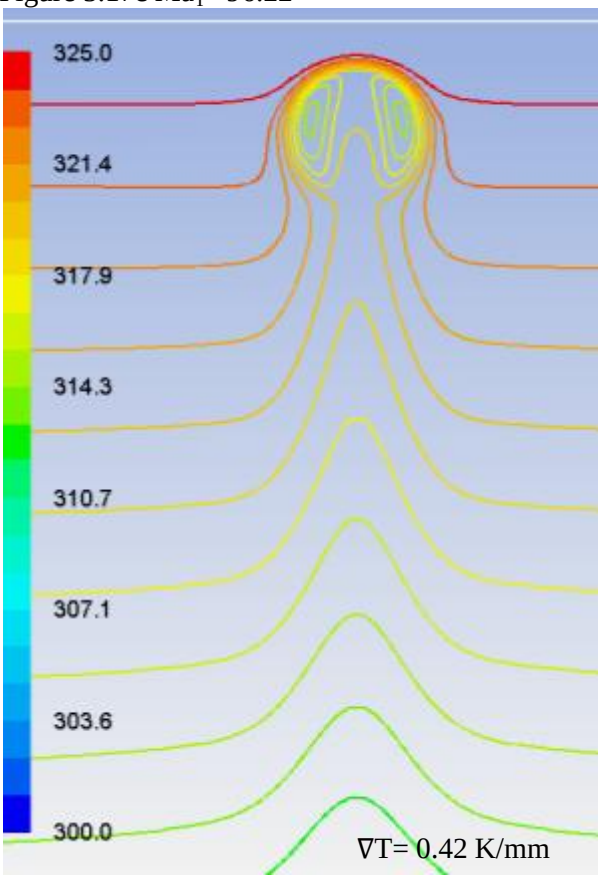

Figure 5.17e Ma_T =384.9

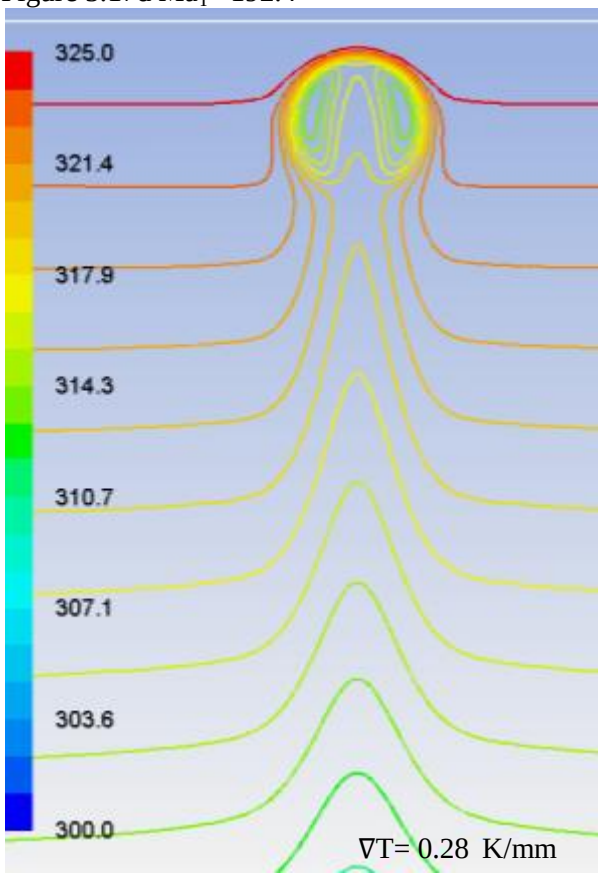

Figure 5.17f Ma_T = 577.3

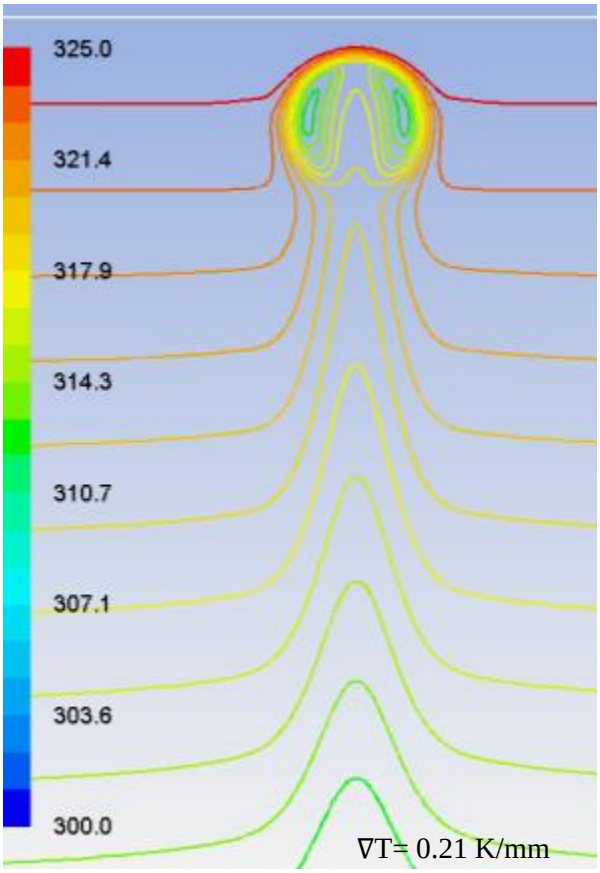

Figure 5.17g Ma_T =769.8

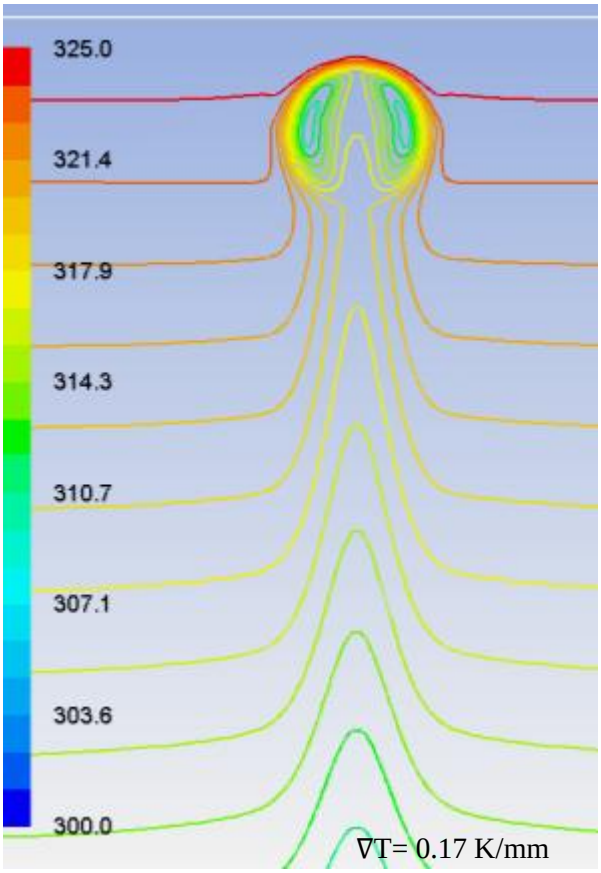

Figure 5.17h Ma_T =962.2

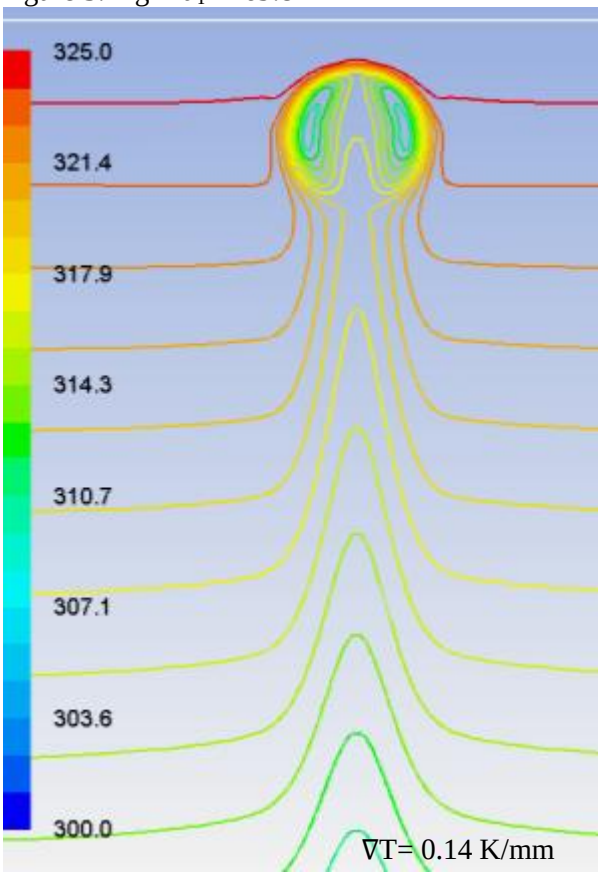

Figure 5.17i Ma_T = 1155

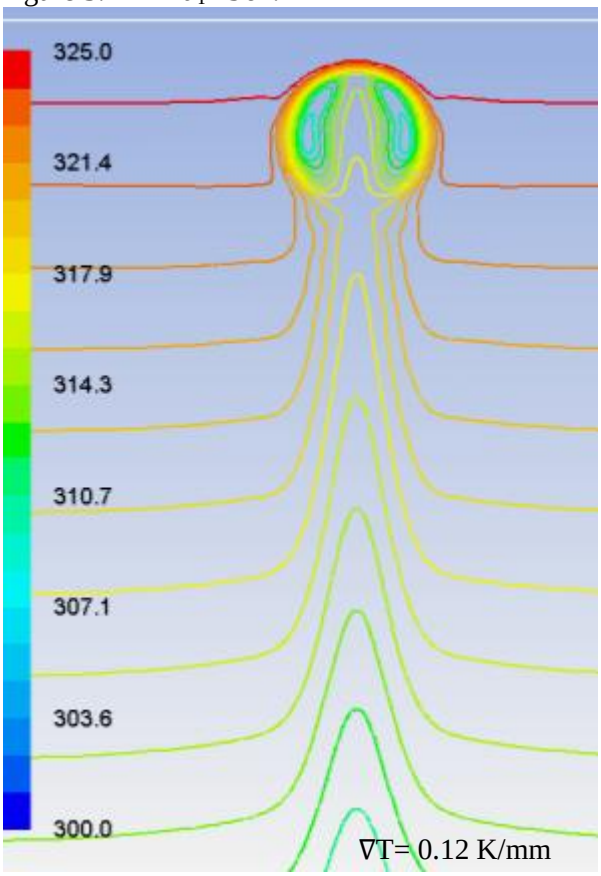

Figure 5.17j Ma_T =1347

Figure 5-17 a-j Isolated droplet migration for different temperature gradients

5.2.4 Comparison with previous numerical and space experimental results

All of the data shown in figure 5.18 present a droplet's scaled velocity versus Marangoni number for a droplet of DOW-Corning DC-200 series fluid of nominal viscosity 10cst and Fluorinert (FC-75) as a host liquid. Thermal Reynolds and Marangoni numbers and average calculated velocity V_{CFD} vary due to differences in temperature gradients (∇T) for each simulation, as summarised in Table 5.4. The Prandtl number, reference velocity V_T and the V_{YGB} theory model were taken as average and constant for all cases in this study. For the current simulations, the temperature gradients between the walls were kept low to avoid fluid property changes caused by thermodynamics.

The numerical results show that for the smaller and larger Ma_T, 24.06 and 2771 in the present simulations, the scaled droplet velocities (V_{drop}) are 0.57 and 0.35 respectively. Both values of V_{drop} are smaller than that given by the linear prediction of the YGB model.

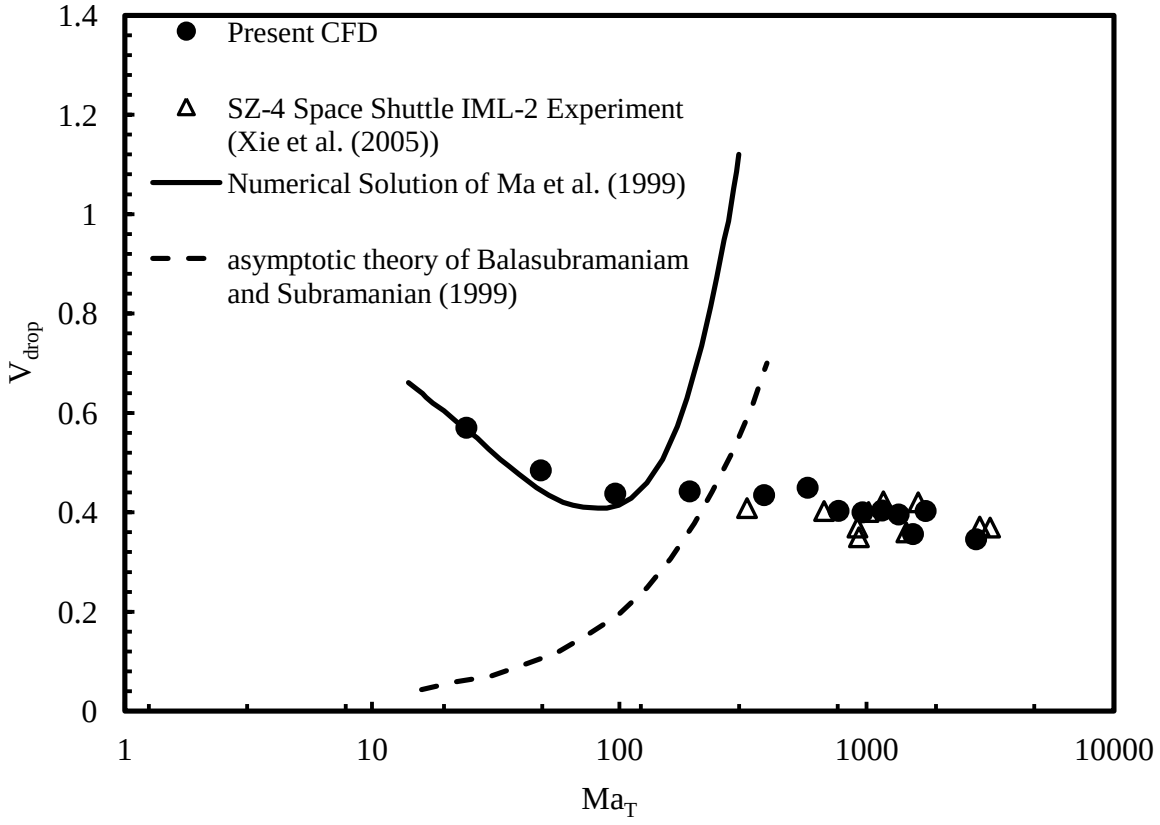

Figure 5-18 Comparison and validation of scaled velocity plotted against Marangoni number

The CFD results in this graph, Figures5-19, show a decrease in the scaled droplet speed with increasing Ma_T, which contrasts with the trends of the asymptotic theory of Balasubramaniam and Subramanian (2000) and the numerical results of Ma et al. (1999). In fact, the current results seem to better agree with the other predictions of the space experimental results of Xie et al. (2005). Some important parameters numerical users should be mindful of when conducting simulations include grid sensitivity, droplet diameter, and the number of mesh cells used inside the droplet, as these factors could affect the droplet's motion in zero gravity. It is also very important to have all the physiochemical properties for the host liquid and droplet as a function of temperature or the exact value of each parameter at a given temperature.

Figure 5.19 displays the details more clearly for Marangoni number versus scaled droplet velocities, (V_{drop}), up to 2771. In the same figure, the migration velocity correlation of a single droplet was obtained numerically in a differentially heated fluid cell. A spherical droplet shape is then assumed in order to find the relationship of the scaled rise in velocity of the droplet (V_{drop}). This is given as:

$$V_{drop} = 0.7Ma^{-0.08} \quad \text{5-10}$$

where V_{drop} is the droplet's scaled migration velocity and V_{YGB} was used for scaling the calculated droplet velocity in Eq. 5-10.

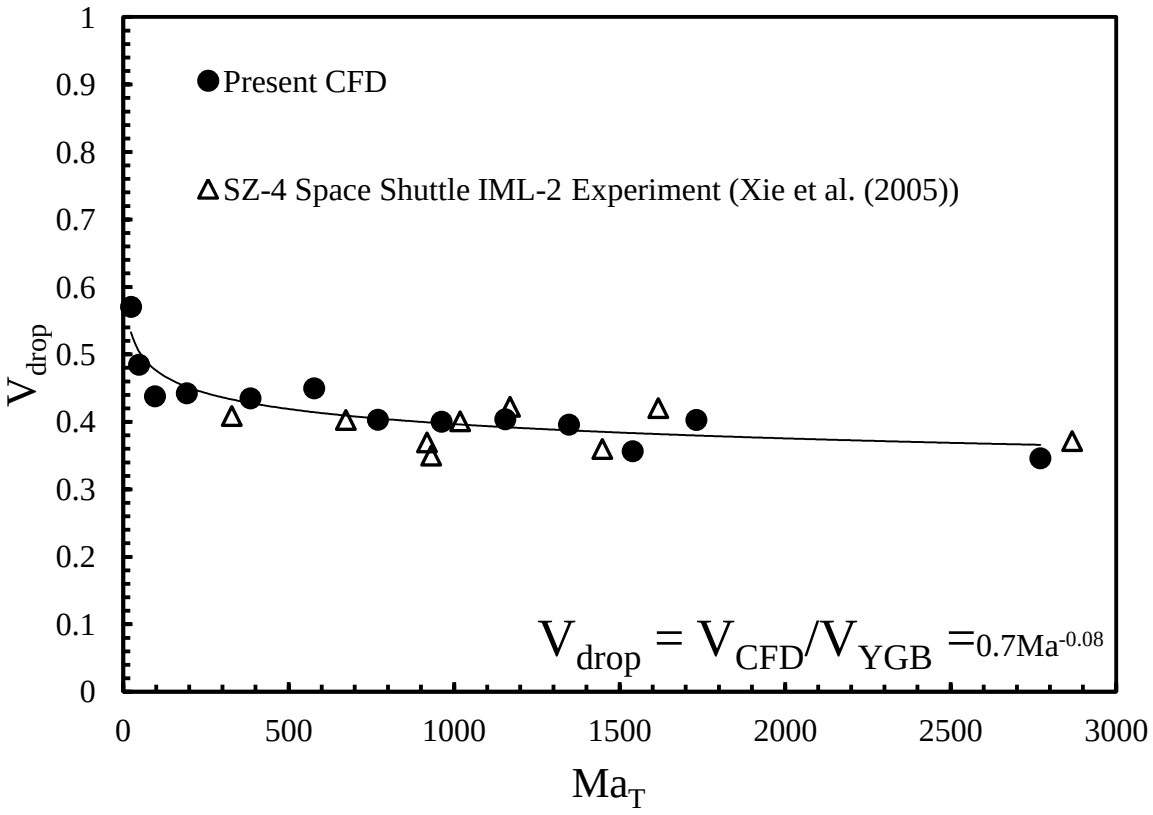

Figure 5-19 Scaled velocity plotted against Marangoni number; earlier experimental data also shown

Figure 5.19 presents the relationship between the present results for the simulated scaled rise velocity (V_{CFD}/V_{YGB}) and the experimental results obtained by Xie et al. (2005). Figure 5.20 show a percentage error between simulated and predicted scaled velocity.

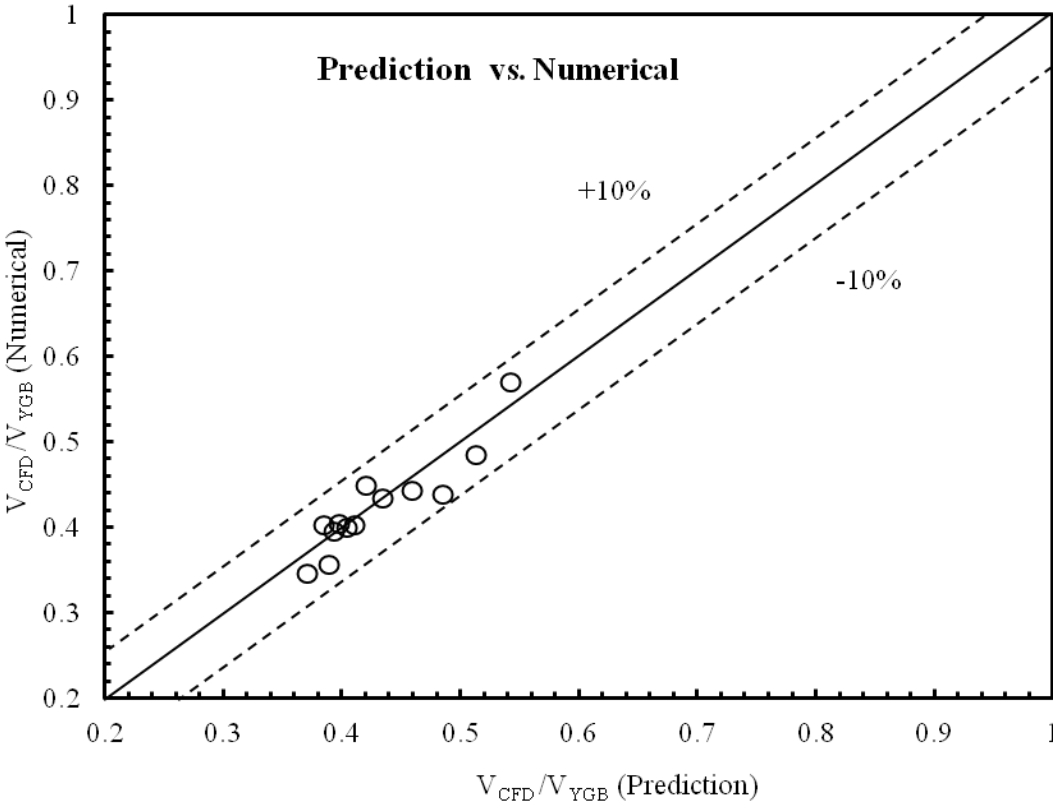

Figure 5-20 Relationship between simulated and predicted scaled velocity

5.2.5 Thermocapillary migration of leading and trailing droplets in zero gravity

The thermocapillary migration and interaction of two droplets are very important areas of study and are topics that have not been extensively covered, especially in zero gravity. A bubble or droplet is not usually found in isolation, and studying the interaction of a pair or multiple particles, or, more specifically, a column of bubbles or droplets, is of great benefit to numerous industrial processes. In practice, it is common to have two or more bubbles or droplets in the continuous phase; as such, it is necessary to study their interactions (Yin et al., 2011). This study will continue to examine the conditions used in the previous section, as well as inserting a leading droplet at a distance (h) equal to 3d from the centre of the isolated droplet, located 1d from the lower wall in the x direction. The density, specific heat, thermal diffusivity, and kinematic viscosity are constant for all cases, as tabulated in Table 5.1. The droplet diameter and temperature gradient vary with the domain size ratio. The two droplets are of equal diameter and migrate under the same temperature gradient and physical properties.

From Figure 5.21, one can note that the trailing droplet has no effect on the leading droplet, and both droplets migrate towards the warmer side. Note that neither the leading nor the trailing droplet has a higher migration speed than an isolated droplet.

Throughout all of the simulations shown in these figures, the initial position of the lower droplet is comparable to that of the isolated droplet in Figure 5.17 for different Reynolds and Marangoni numbers. The comparison shows that the higher the temperature gradient, the smaller the distance between the leading and the trailing droplets. As the temperature is decreased, the distance between the two droplets will increase. Furthermore, the distance between the two droplets is expected to be constant for a very low Ma (<1). On the other hand, a reduction in the trailing migrating speed is visible as the Ma_T increases. As the temperature difference reduces between the two walls, the inner region of the leading droplet

remains at a low temperature and thrusts downward, causing a thermal fluctuation toward the trailing droplet. This thermal variation in local temperature can have a significant impact on the dynamics of the trailing droplet, due to the strong dependency of the surface tension gradient on the local temperature. Generally speaking, in the x direction and for leading and trailing droplets for the range of Marangoni numbers shown in Figure 5.21, the trailing droplet moves as slowly as decreasing the temperature gradient due to thrusting colder liquid by the leading droplet, while the leading droplet appears unaffected by the droplet following it.

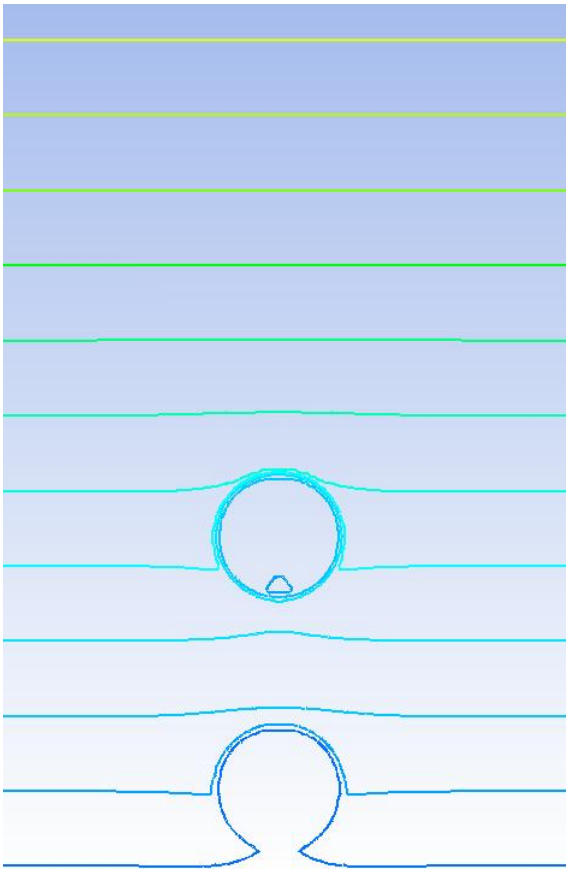

Iinitial bounbery of two droplets

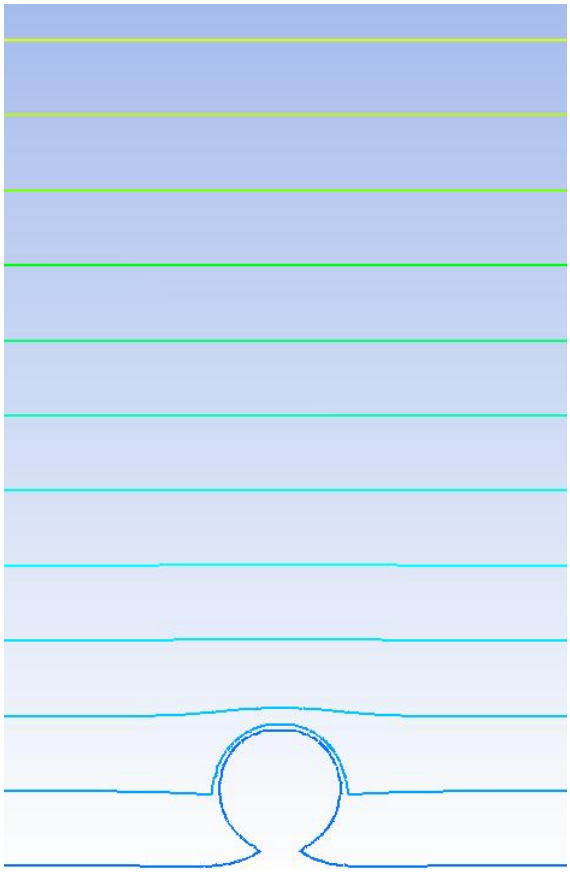

Initial of isolated droplet

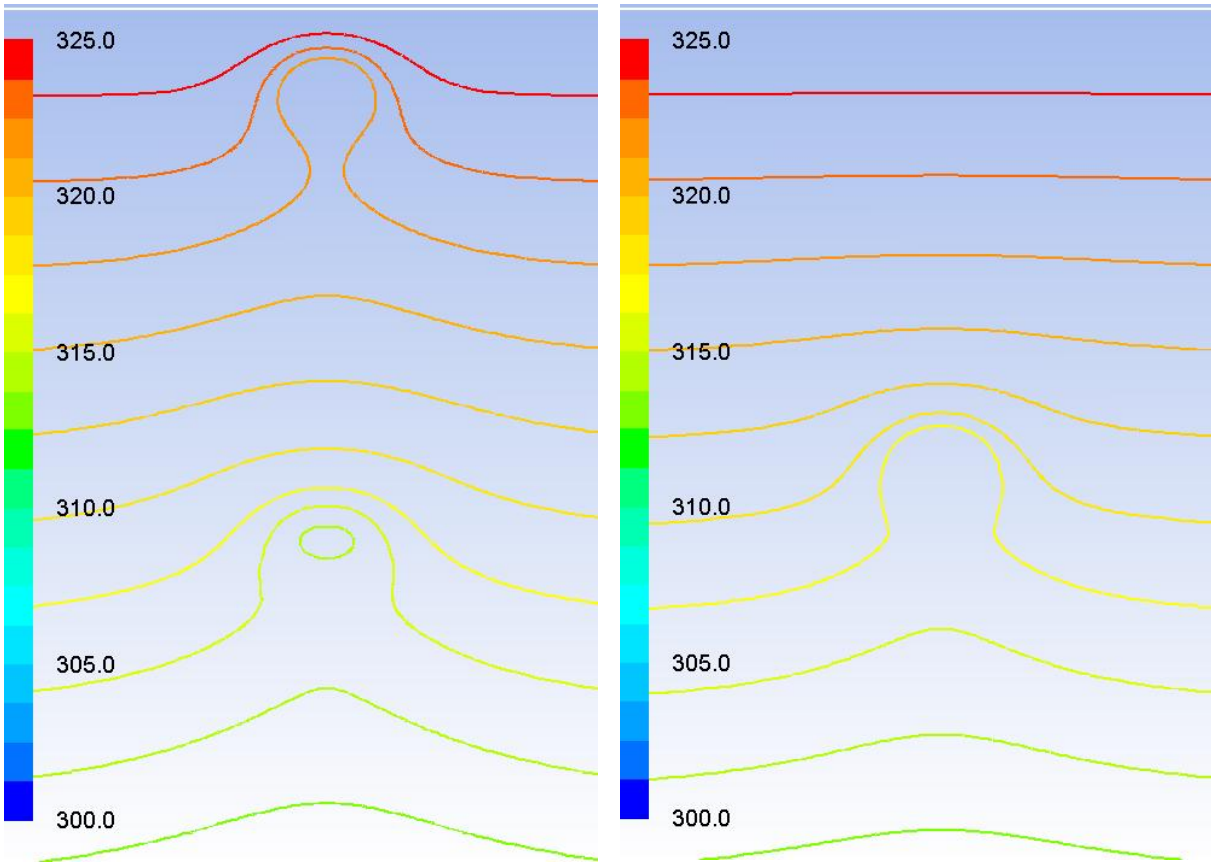

The isotherms around the two droplets and the isolated droplet for ReT=0.24, MaT=24.06 at t=1 sec, both the trailing and the isolated droplet has same inital distance =1d from the bottom wall, ∇T= 6.66 K/mm

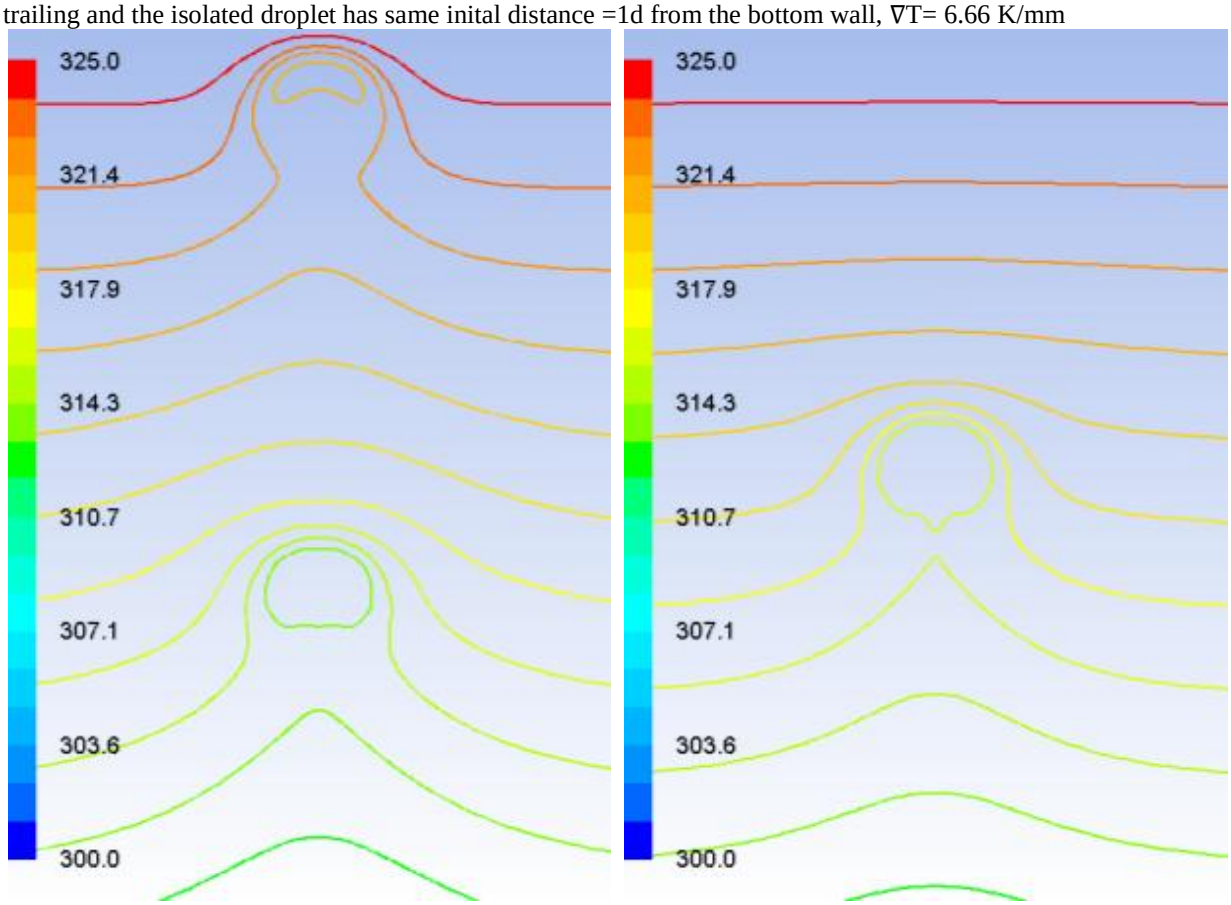

The isotherms around the two droplets and the isolated droplet for Re_T=0.48, Ma_T=48.11 at t=2.4 sec; both the trailing and the isolated droplets have the same initial distance =1d from the lower wall, ∇T =3.33 K/mm

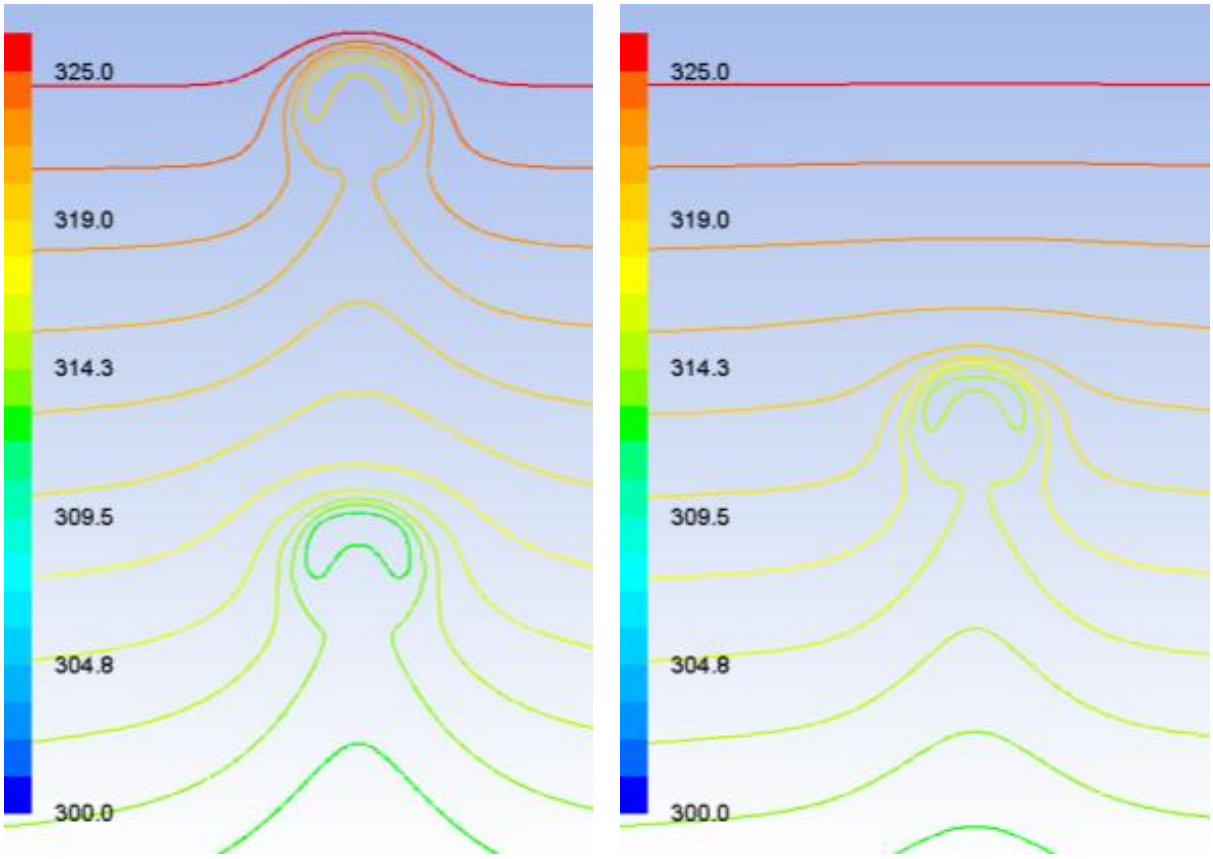

The isotherms around the two droplets and the isolated droplet for Re_T=0.975, Ma_T=96.2 at t=5.5 sec; both the trailing and the isolated droplets have the same initial distance =1d from the lower wall, ∇T =1.67 K/mm

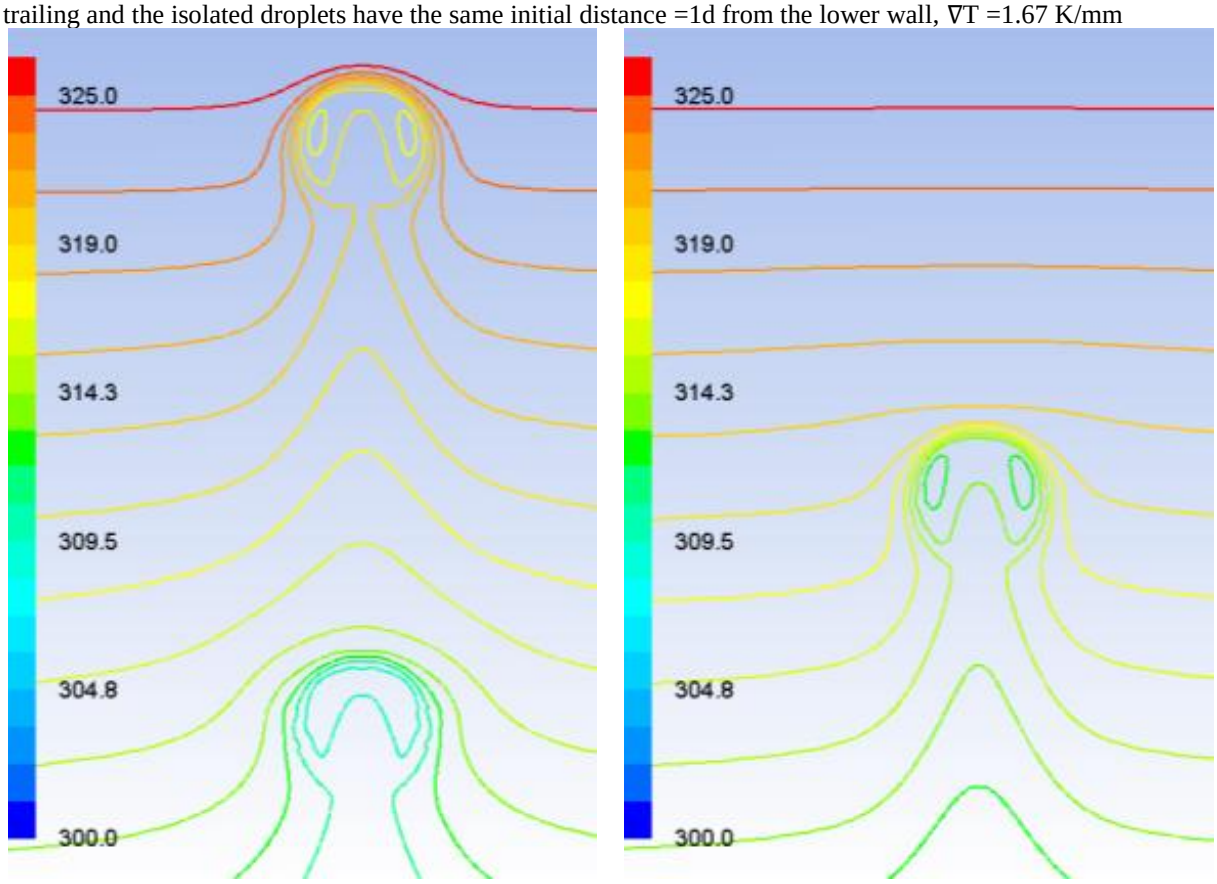

The isotherms around the two droplets and the isolated droplet for Re_T =1.95, Ma=192.4 at t=12 s; both the trailing and the isolated droplets have the same initial distance =1d from the lower wall, ∇T= 0.83 K/mm

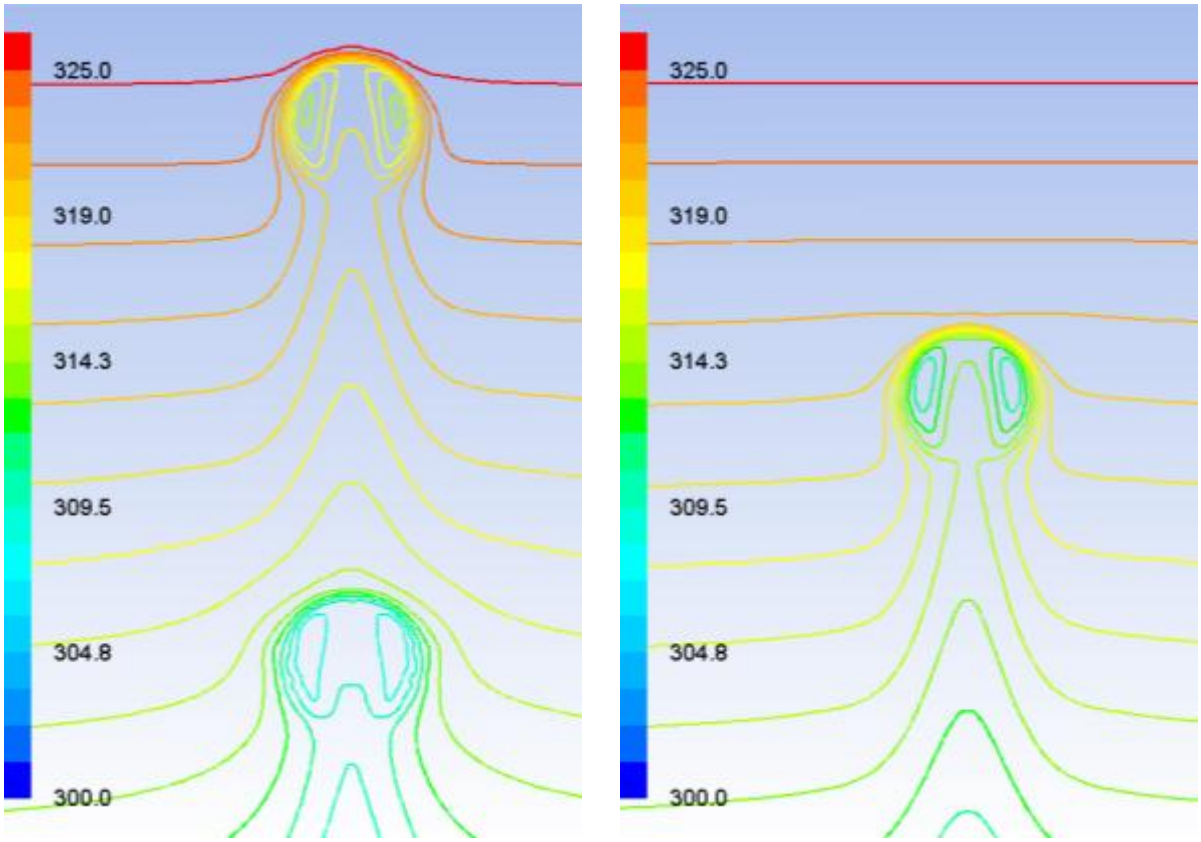

The isotherms around the two droplets and the isolated droplet for Re_T =3.9, Ma_T=384.9 at t=31 sec; both the trailing and the isolated droplets have the same initial distance =1d from the lower wall, ∇T= 0.42 K/mm

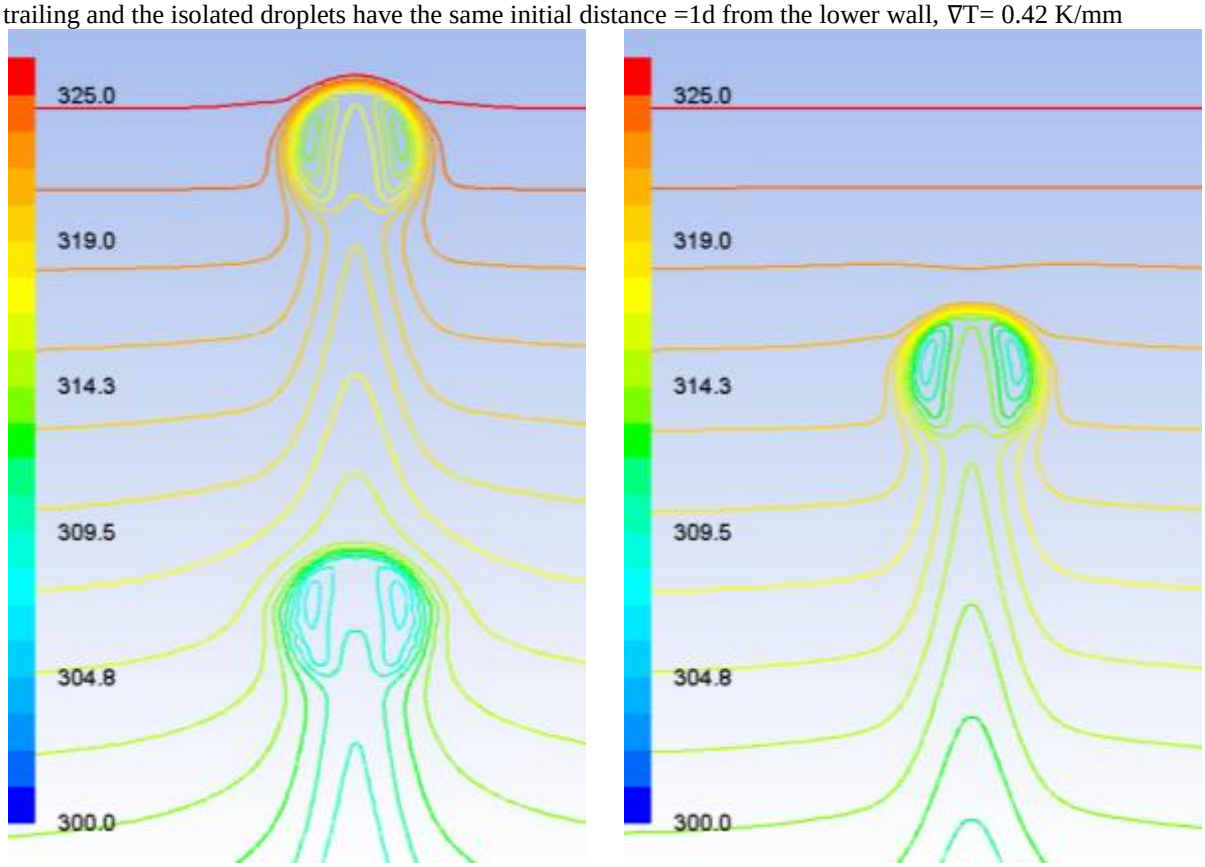

The isotherms around the two droplets and the isolated droplet for Re_T =5.85, Ma_T=577.3 at t=41 sec, both the trailing and the isolated droplet droplets have the same initial distance =1d from the lower wall, ∇T= 0.28 K/mm

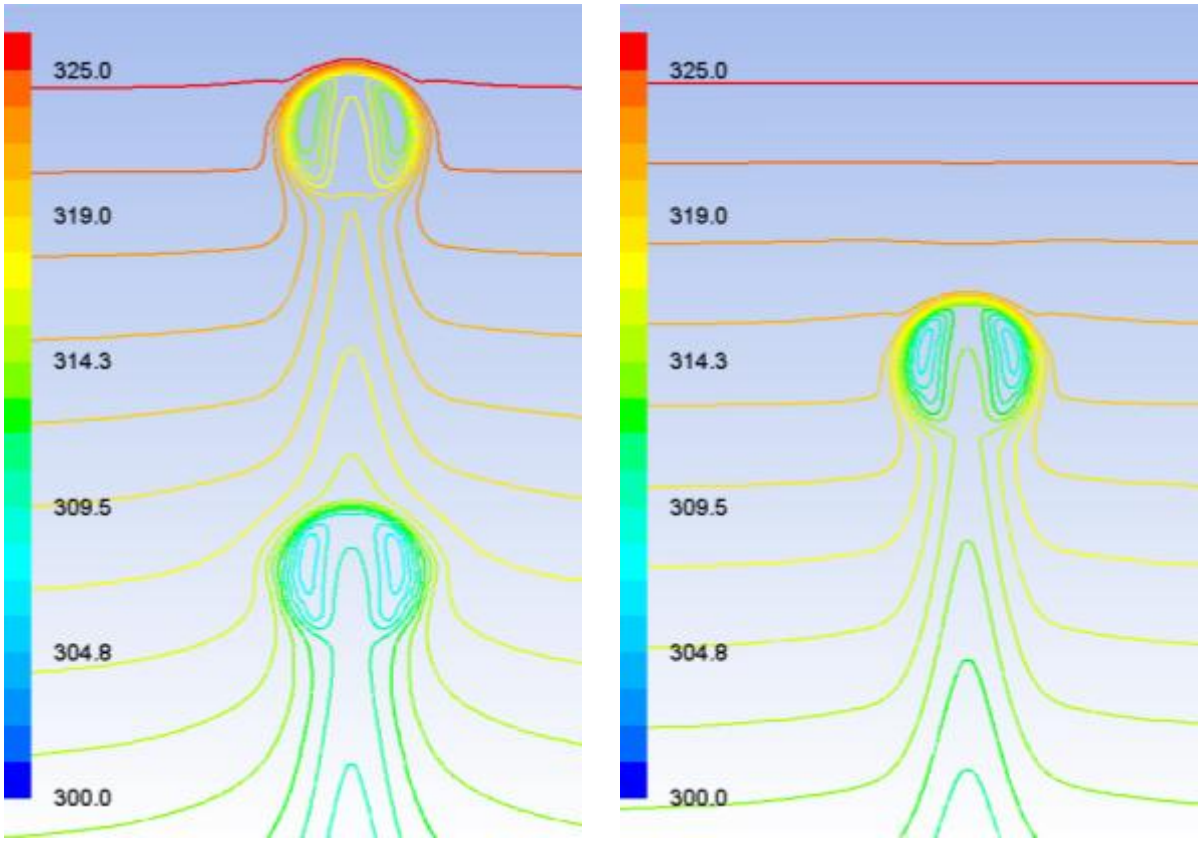

The isotherms around the two droplets and the isolated droplet for with Re_T=7.8 Ma_T=769.8 at t=56 sec; both the trailing and the isolated droplets have the same initial distance =1d from the lower wall, ∇T= 0.21 K/mm

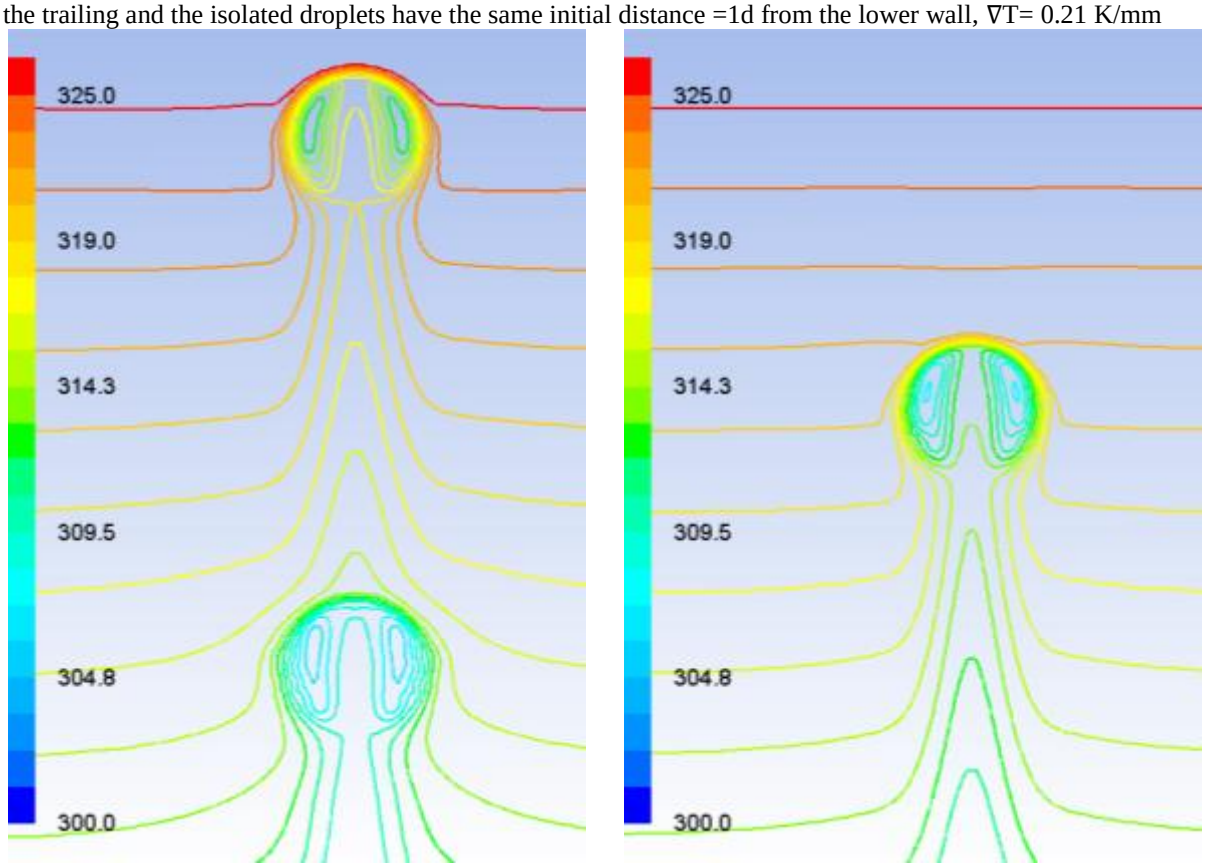

The isotherms around the two droplets and the isolated droplet for Re_T =9.75 Ma_T=962.2 at t=70 sec; both the trailing and the isolated droplets have the same initial distance =1d from the lower wall, ∇T= 0.17 K/mm

Figure 5-21 Interaction and comparison of leading and trailing droplets with an isolated drolpet

5.2.6 Conclusions

This section utilises a computational approach to calculate the transient thermocapillary migration of an isolated droplet in a zero-gravity environment. The work has shown conclusively that the current VOF technique is a robust numerical method for the simulation of liquid–liquid flow.

The present methodology has the ability to simulate surface tension as a function of temperature (thermocapillary flow), using a UDF for routine design and development engineering. The current results show conclusive existence of Marangoni droplet flow phenomena in a zero-gravity environment. The droplet velocity is scaled and compared with the measurements of (Xie et al., 2005) for Marangoni numbers from 24.05 to 1540. This study shows that, generally speaking, as Ma_T increases, the scaled velocity of a single droplet decreases and steadily approaches its asymptotic value.

The present CFD results show that different temperature gradients lead to different droplet migration velocities, and it was proven that droplet migration velocity varies linearly with the temperature gradient for the given condition. This phenomenon is expected due to an increase or decrease in the movement source - in this case, temperature difference. At low Ma_T the droplet is cooler than the surrounding liquid, and with increasing Ma_T the interior of the droplet cools, leaving a long thermal wake behind it. The interactions of two droplets in thermocapillary motion have also been studied and compared with the results obtained for the isolated droplet. The results have shown that the leading droplet will not move faster than the isolated droplet, as the trailing droplet has no influence on the velocity of the leading droplet. In addition, the trailing droplet translates more slowly than the isolated droplet due to the thermal wake of the leading droplet. Moreover, the results indicate that as $Ma_T \rightarrow 0$, the trailing droplet will move at the same velocity as the isolated droplet.

Most experiments in microgravity have constraints such as time limitations; computer simulations, on the other hand, are not restricted in such a way, and can simulate any arbitrary geometry. Thus, numerical simulations prove to be a valuable tool to study such complex problems under the conditions of zero and reduced gravity. A wider range of parameters and deeper physical explanations could be included in future work, such as the impact of the distance between the two droplets on their interaction. The droplet behaviour is fundamentally different from that of the bubble in thermocapillary flow and further attention should be paid to this observation in future research.

5.3 Thermocapillary bubble dynamics in a 2D axis swirl domain

5.3.1 Overview

As mentioned previously (Chapter 1), there is still much to be understood about two-phase flows in general and especially in zero-gravity conditions. As a result, this section will investigate the sensitivity of various parameters and/or scenarios that could not be investigated or fully covered previously, i.e. thermocapillary bubble migration in a rotating cylinder. The investigation of both rotational and surface tension-driven motion on the shape and trajectory of a bubble is a new area of study and aims to support research into space applications. Swirl flow is a technique that involves a rotational flow around an axis. This flow can be found in a wide range of engineering applications, such as turbomachinery, chemical and mechanical mixing devices and separation devices. Swirling flows appear in spray drying towers, burners, cyclone separators, and a wide variety of other process systems, and are among the most common and most complex in the process industry. "Water droplets in petroleum lines and vapor bubbles in cryogenic fluids in microgravity conditions are some other applications in which the two phases need to be separated from the mixture" (Gupta and Kumar, 2007). This simulation will show the effect of a rotating cylinder on a single bubble under the effect of surface tension gradient in zero gravity. To understand the flow structure in such thermocapillary flows, it is necessary to pay attention to the behaviour of each individual bubble and their interaction with external forces – rotation, in this study. The aim of the numerical simulation in this section is to simulate and observe the Marangoni bubble migrating along the cylindrical axis of a rotation. Two-dimensional axisymmetric and full three-dimensional computational domains could both be used to simulate such flows; however, due to the complexity of modelling this process in 3D, starting with a simple 2D model will enable different parameters and scenarios to be investigated in order to simplify and clarify the flow process, before extending the study to 3D flows. It should be noted that

when using a VOF model to simulate bubbles placed off-centre, as will be seen in the coming chapters, the swirl in the flow contains a large degree of three-dimensionality, invaliding two-dimensional simulations and therefore requiring a fully three-dimensional approach.

5.3.2 Numerical Method

Thermocapillary single bubble migration in swirling flow was simulated by placing the bubble 1.5d from the lower (cold) wall by using the region adaptation function (Ansys-Fluent, 2011). A 2D swirl axisymmetric interface is available in VOF-Fluent, where the flow in the rotational direction is incorporated in the equation:

$$\frac{\partial}{\partial t}(\rho\omega)+\frac{1}{R}\frac{\partial}{\partial x}(R\rho u\omega)+\frac{1}{R}\frac{\partial}{\partial R}(R\rho\upsilon\omega)=\frac{1}{R}\frac{\partial}{\partial x}\left[R\mu\frac{\partial\omega}{\partial x}\right]+\frac{1}{R^2}\frac{\partial}{\partial R}\left[R^3\mu\frac{\partial}{\partial R}\left(\frac{\omega}{R}\right)\right]-\rho\frac{\upsilon\omega}{R}+\vec{F} \quad 5\text{-}11$$

where x is the axial coordinate, R is the radial coordinate, u is the axial velocity, v is the radial velocity, and ω is the swirl velocity. All simulations were run at time $t = 0$ with an initial velocity for the bubble of zero and different angular rotational speeds for the liquid phase. For all simulations the initial conditions were set with no velocity at the inlet or at the outlet, and the pressure was set to atmospheric. The size of the computational wall-bounded domain was chosen as 120x60 mm^2 with impermeable sides. The properties of the ethanol used in the simulation are shown in Table 5.5. The upper surface (upper wall) of the domain was at a higher temperature than the lower surface (lower wall); both top and bottom walls were defined as no-slip solid walls (see Fig. 5.22). The material properties of the bubble and the ambient fluids are different and the interfacial tension depends on the temperature. The numerical scheme for the variation of surface tension with temperature was implemented with user-defined functions (UDFs). A grid dependency study is described in Chapter 4.

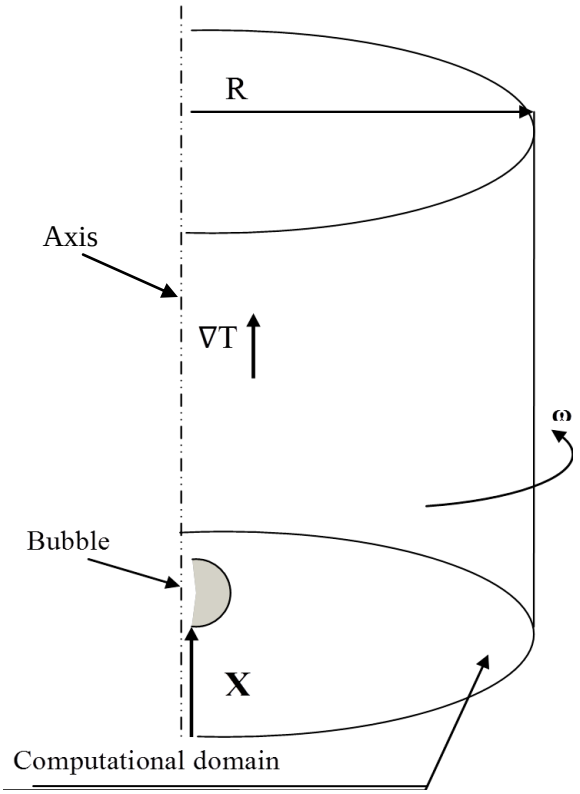

Figure 5-22 Schematic diagram of the swirl axisymmetric model for Marangoni bubble migration.

Fluent requires that the horizontal x-axis be the axis of rotation for axisymmetric flows; this is described for axisymmetric swirling flows (Ansys-Fluent, 2011).

5.3.2 Distribution of tangential velocity component, pressure, and temperature of the surrounding liquid

Ethanol is used as the working fluid for the present case, with no bubble present in the domain. The properties of ethanol are given in Table 5.5, and the cylinder is set to be working under zero-gravity condition. The cylinder has varying angular velocities at the walls, with the lower and upper surfaces having the temperatures of 300 K and 330 K respectively.

Table 5-5 Physical properties of the liquids employed in the simulation at 300K for (Pr=16.28)

Properties	Unit	Ethanol	Nitrogen (N_2)
Density (ρ)	kg/m^3	790	1.138
Specific heat (Cp)	j/kg-K	2470	1040.7
Thermal conductivity (k)	w/m-K	0.182	0.0242
Viscosity (μ)	kg/m-s	0.0012	1.66e-5
Surface tension (σ_0)	N/m	0.0275	------
Surface tension coefficient (σ_T)	N/m-K	0.00009	------
Temperature gradient (∇T)	K/mm	0.250	------
Prandtl number (Pr)	-------	16.28	0.79

To confirm the accuracy of the simulation after the steady state had been reached, the tangential velocity component, pressure, and temperature gradient of the host liquid were measured and results are given in Figure 5-23. The steady state result shows that the tangential velocity is increased linearly from the cylinder axis of rotation to the wall of the cylinder and the measured values agreed with the $v = r\omega$ relationship at every axial measurement position for ω=0.5 rad/sec and cylinder radius R=60 mm, and the pressure change from the centre to any point in the radial direction is given as $P = \rho \frac{r^2 \omega^2}{2}$ where r is the distance from the axis of rotation. Furthermore, the total pressure is highest at the wall and lowest in the centre. The temperature has also shown a linear behaviour from the lower to the upper surface of the cylinder, and the overall results for the three figures show that the steady state CFD measurements for the present study validating the theoretical study.

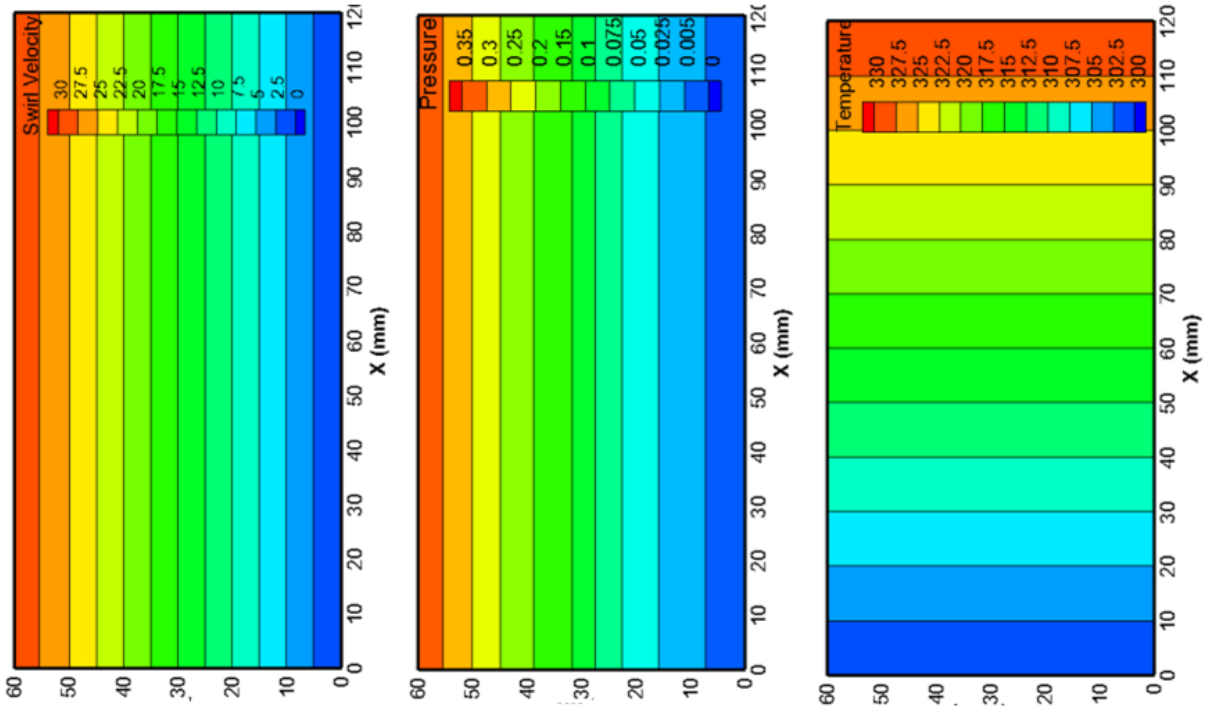

Figure 5-23 Tangential velocity (mm/s) between the centre and the outside wall (left), distribution of static pressure (Pascal) between the centre and the wall (middle), distribution of temperature (K) between the lower and upper walls (right).

The steady state pressure gradient is presented in Figure 5.24 and shows the radial pressure distribution results of eight simulations for the dynamics of a bubble inside a cylinder with angular velocities of 0.25, 0.5, 0.6, 0.75, 1, 1.25, 1.5, 1.75 and 2 rad/sec. The figure shows that the pressure remains constant at a radial rotation speed of zero, while for cases with rotational speed the pressure is at its lowest at the closest point to the axis of rotation, i.e. at the point of minimum radial direction. Conversely, the pressure increases steadily as the radial distance from the axis increases. The gradient of the static pressure depends upon the value of rotational speed, i.e. the radial pressure gradient increases with an increase in rotational velocity and reaches its maximum value at the wall of the cylinder at 2 rad/sec. These findings are in agreement with the pressure gradient term given in the tangential momentum transfer term in Eq. 5.11.

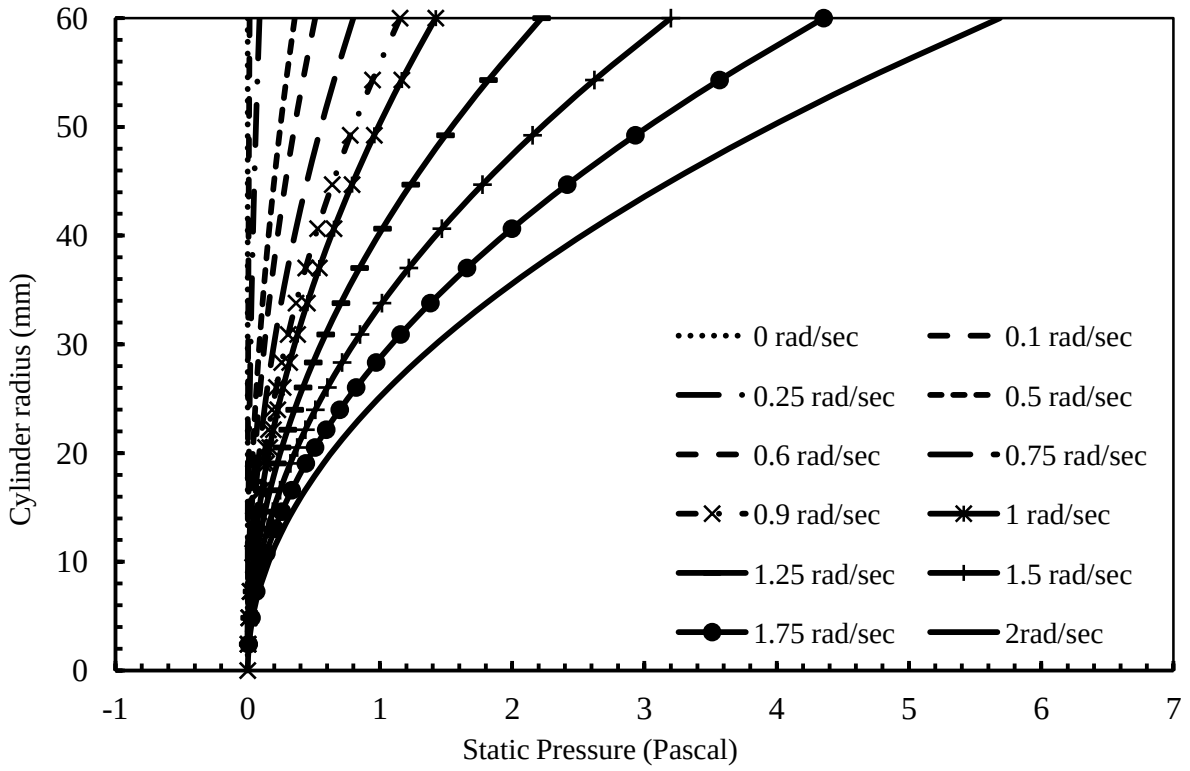

Figure 5-24 Steady state pressure distribution (Pascal)

5.3.4 Results of the investigation of bubble dynamic in thermocapillary flow including swirling flow

The results obtained for the steady state simulation of the rotating cylinder shown in Figures 5.22 to 5.24 for angular velocity, pressure gradient and temperature gradient will now be used to predict the effect of different rotational speeds (centrifugal force) on the dynamics of a single bubble migrating under the dominant surface tension gradient force. After obtaining the steady state for each rotational speed, a bubble diameter of 8 mm with zero velocity fields at the initial moment for each rotational speed was then patched and its centre placed at the locations of 1.5d and 0d in the X and Y directions respectively, where "d" is the diameter of the bubble. The temperature gradient was kept at a constant value of 0.25 K/mm for each simulation. The corresponding thermal Reynolds (Re_T) and Marangoni (Ma_T) numbers for the given temperature gradient, diameter and thermal properties shown in Table 5.5 are 257 and 4188 respectively. At the same time, the bubble was subjected to a constant angular speed (ω)

applied to the walls of the cylinder, ranging from 0.25 rad/sec to 2.0 rad/sec for each simulation. This speed was then evaluated at tangential velocities of the cylinder ranging from 15-120 mm/s. Figures 5.25 show the pressure distribution around the bubble at different angular velocities after 5 sec of flow time from the start of the transient flow. At lower angular velocities the bubble moves faster and its speed decreases as the angular velocity increases. Moreover, the radial pressure gradient increases steadily along the radial direction with increasing rotational speed. It can be deduced from the figures that at lower angular velocities the dominant force affecting the bubble motion is the thermocapillary force acting within the domain; this is due to the application of a temperature gradient between the upper and lower walls of the cylinder. As the angular velocity increases the pressure gradient between the cylinder's outer wall and the axis of rotation increases, forcing the lowest pressure region to shift from the sides of the bubble to the axis of rotation (front and back of the bubble), as evident in the same figure. In other words, the pressure close to the outer edge of the cylinder has the higher positive region than that close to the axis of rotation, which has a lower, and in some cases negative, pressure region, causing a reduction in the bubble's migration speed and high angular velocity, trapping the bubble within this region.

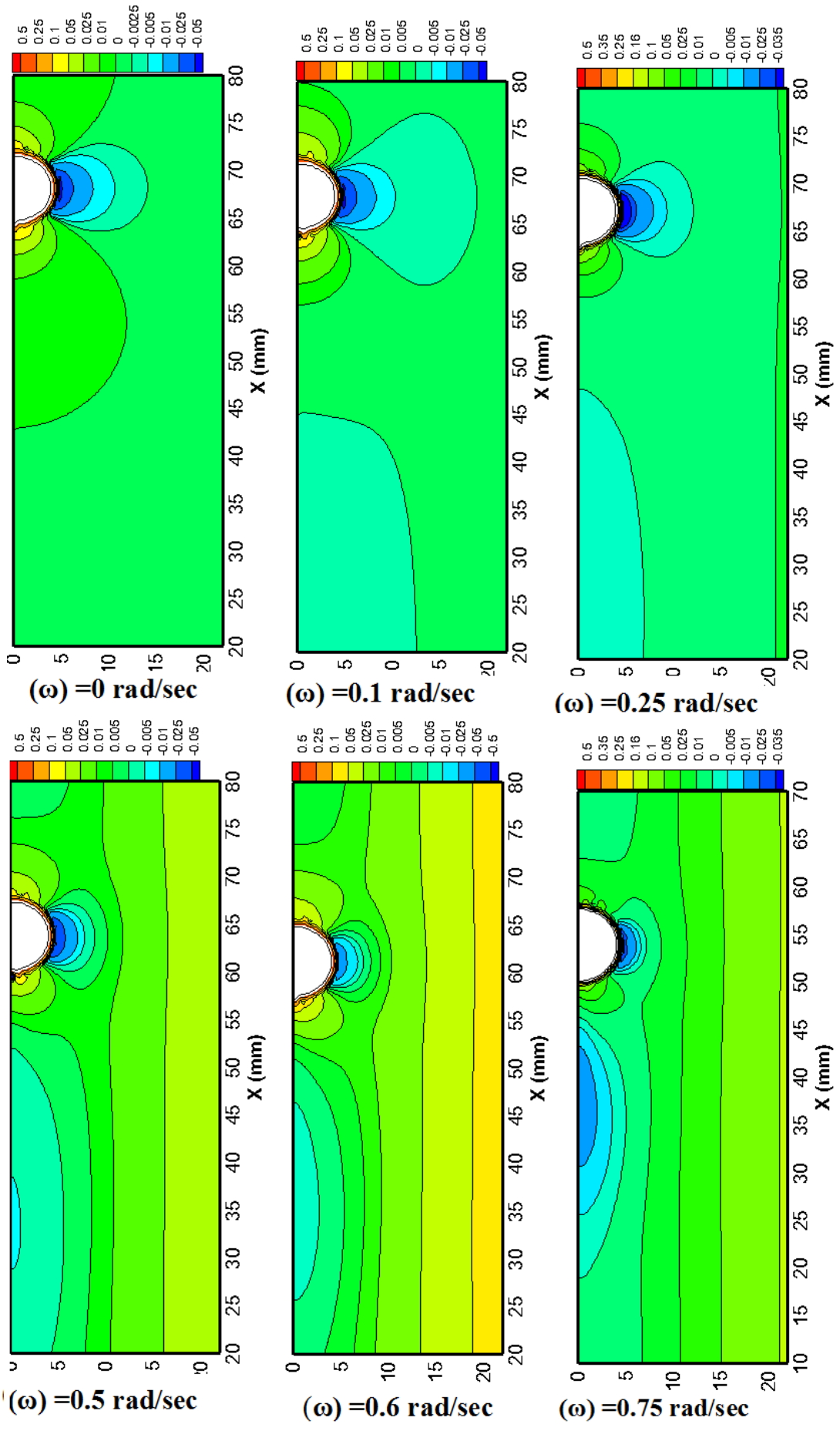
(ω) =0 rad/sec
(ω) =0.1 rad/sec
(ω) =0.25 rad/sec
(ω) =0.5 rad/sec
(ω) =0.6 rad/sec
(ω) =0.75 rad/sec
X (mm)

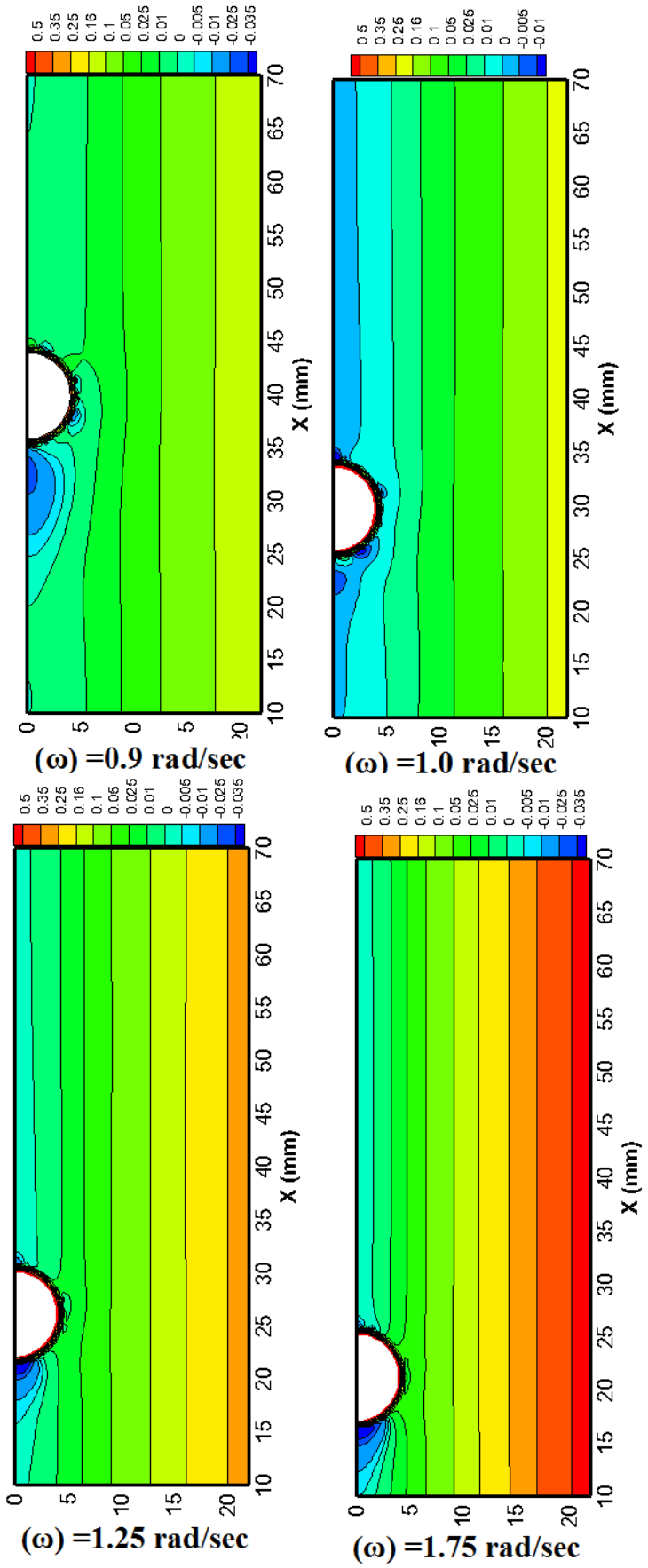

Figure 5-25 present the effect of the static pressure gradient (Pascal) on the bubble dynamics for different angular velocities at t=5s

It can ultimately be deduced from these figures that the rotational speed of the wall imparts extra radial forced vortex motion to the adjacent fluid layer, subsequently toward the centre of the cylinder, causing an increase in the fluid radial velocity towards the axis of rotation. Here, the application of rotation in thermocapillary flow imparts an additional downward force on the gas bubble, resulting in a reduction in the bubble rise velocity and preventing its migration towards hotter wall. The location of the bubble along the axis of symmetry is shown in Figure 5.26, which demonstrates that the effect of rotational speed is minimal up to 0.75 rad/sec, and the thermocapillary force dominates the bubble's motion. Above this level the bubble shows a large decrease in its velocity, as the larger radial pressure gradient produces a negative pressure region on the lower section of the bubble, slowing the bubble's motion in the positive axial direction. It can also be noticed from the same figure that the remarkable change in this calculation began in the case of 1rad/sec and up to 2 rad/s, but that there are no major changes in the final bubble position after 10 sec of flow time. The trend shows an overall decrease in migration distance with increasing rotational rate and gradually approaches its asymptotic value. This phenomenon occurs because the bubble becomes trapped in the region where the thermocapillary force due to temperature gradient and the pressure gradient force due to rotational speed balance out, causing the bubble to cease to move in the axial direction.

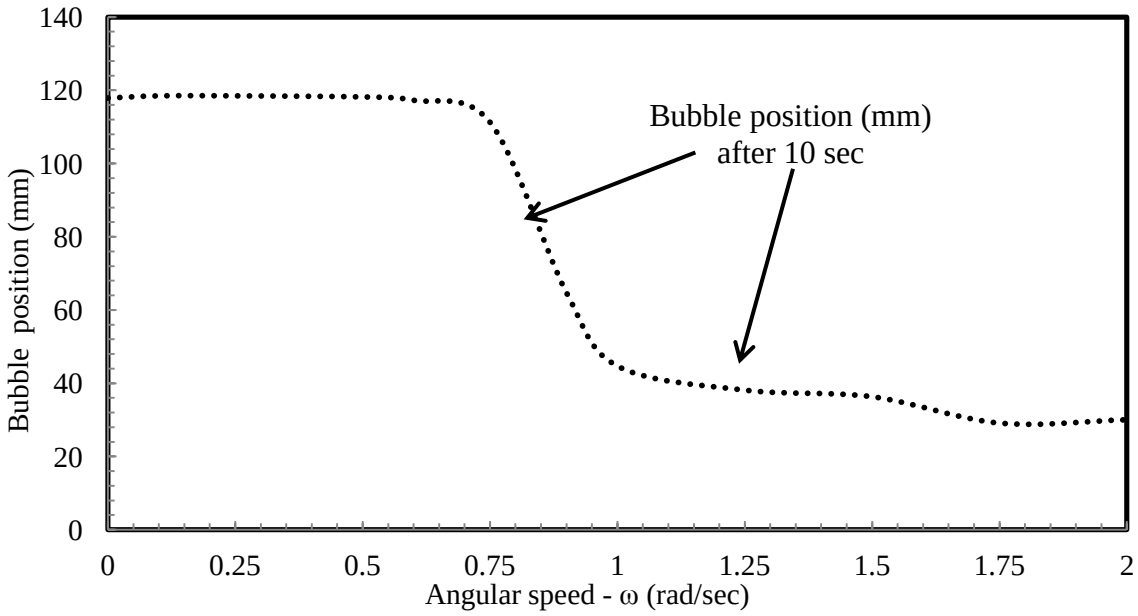

Figure 5-26 Reduction in bubble distance from the bottom with higher rotational speeds for Re_T and Ma_T equal 257 and 4188, respectively.

The velocity field inside the bubble may also have been affected by the mobility of the flow around the interface. This is shown in Figures 5.27a-d, where the velocity field inside and outside the bubble respectively exhibit increasing thermocapillary flow (top) and higher rotational rate (bottom).

For low rotational speeds of up to 0.75 rad/sec in the present condition, no vortex was formed inside the bubble, whereas two vortices were formed when the angular speed was increased to 0.9 rad/sec and above. The formation of the two vortices inside the bubble is due to the reverse flow at the front of the bubble acting against the direction of the bubble's movement. Furthermore, the bubble is more compressed in these cases than at lower rotational speeds because of the higher pressure gradient between the wall and the axis of rotation.

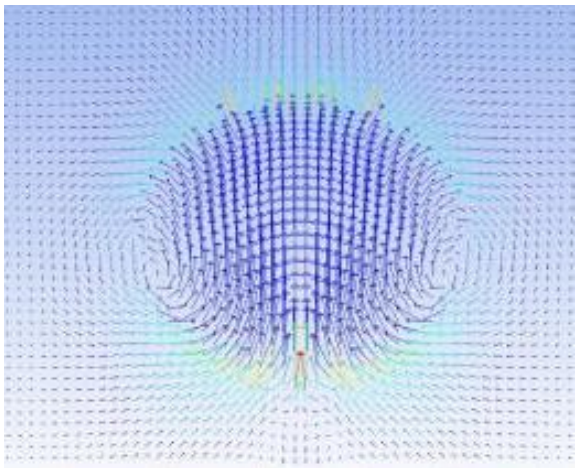

Figure 5.27a Angular velocity (ω) =0.1 rad/sec

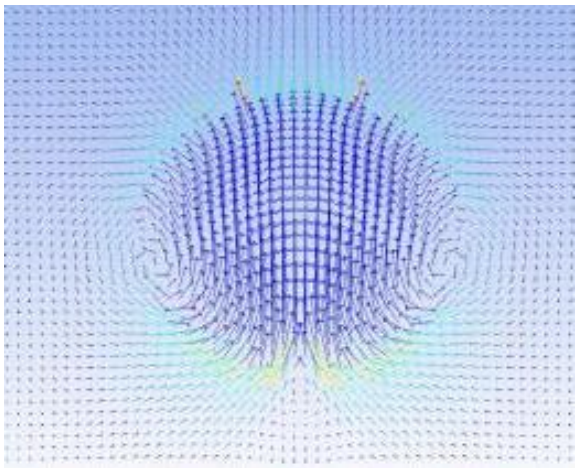

Figure 5.27b Angular velocity (ω) =0.5 rad/sec

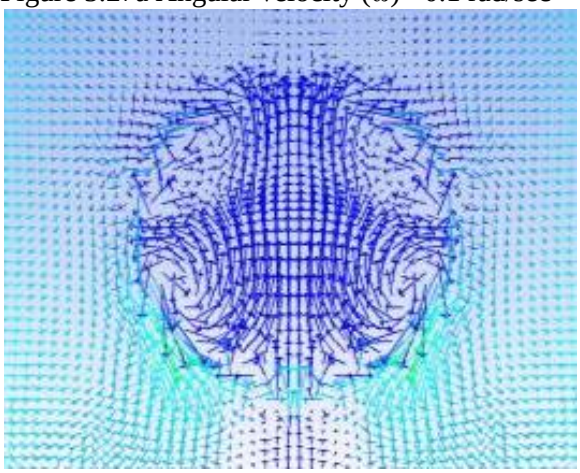

Figure 5.27c Angular velocity (ω) =1 rad/sec

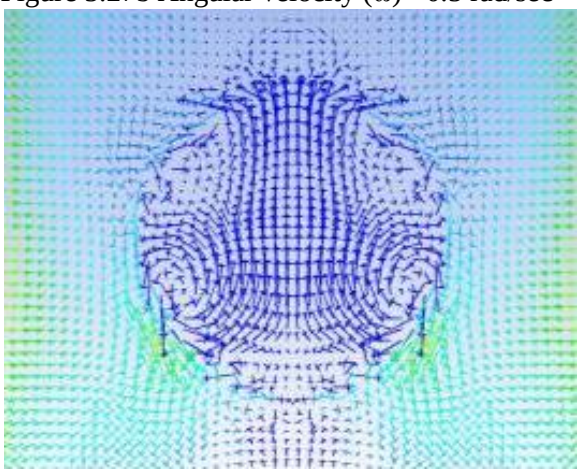

Figure 5.27d Angular velocity (ω) =1.5 rad/sec

Figure 5-27 Velocity field inside and outside the thermocapillary bubble migration at low rotational rate (top) and at higher rotational rate (bottom) for time = 6 sec.

Figures 5.28a-h present the streamline results of the liquid phase for different rotational speeds. From Figures 5.28a to 5.28f one can see that the streamlines of the liquid phase are clearly dominated by thermocapillary force. One large convection roll can be seen in the first two figures for a stationary case and for small angular velocities of 0.1 rad/sec in Figures 5.28a and 5.28b. A second vortex begins to form at the bottom of the cylinder (cold region), which is induced by increasing the radial pressure gradient, as seen in Figure 5.28c for an angular velocity of 0.25 rad/sec. Increasing the angular speed to 0.75 rad/sec will show very similar results, but with more circulation and a slight decrease in the bubble migration speed, which does not have a major impact on the bubble speed due to its direction in relation to the

bubble's motion. However, due to increasing angular velocity caused by the pressure gradient moving inwards towards the axis of rotation, small vortices are formed at the front and back of the bubble, as seen in Fig. 5.28g and 5.28h. These vortices are created to account for the opposing flow directions. At the front of the bubble, another smaller recirculation zone vortex is formed through rotation due to the negative pressure layer, causing the bubble to move backwards. However, as a result of increasing the rotational speed, the shape of the vortices does not coincide exactly with the present results obtained for the small recirculation zone. As mentioned in Figure 5.27, the reason for the formation of the two internal vortices is the negative pressure generated due to increasing pressure gradient.

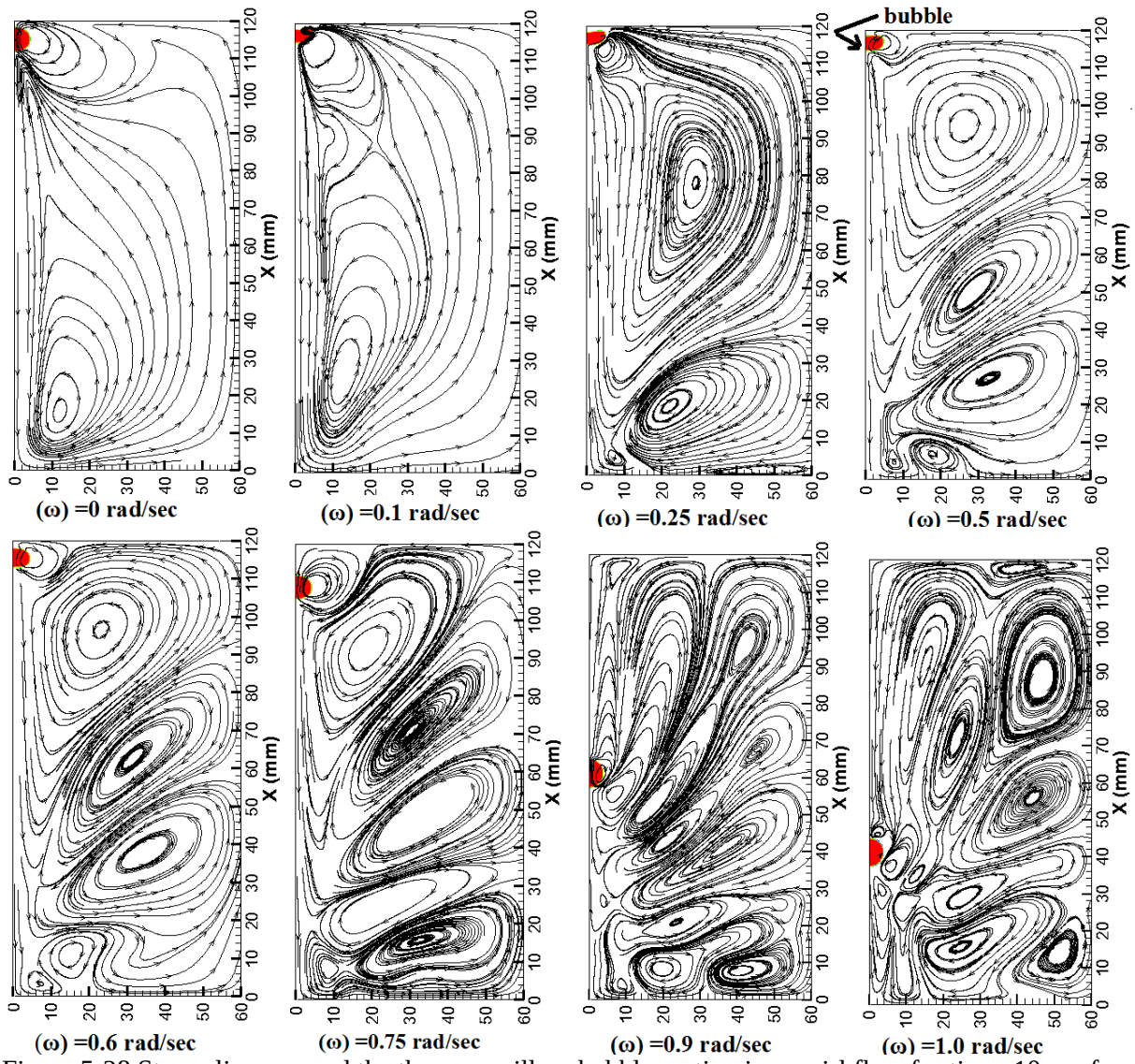

Figure 5-28 Streamlines around the thermocapillary bubble motion in a swirl flow for time=10 sec for different angular speeds and for Re_T and Ma_T equal 257 and 4188, respectively.

5.3.4 Conclusion

Numerical results were presented to show the trajectory and shape of the bubbles in a rotating liquid under zero-gravity conditions. The conclusive existence of Marangoni bubble flow phenomena in a zero-gravity environment was demonstrated in figures. The bubble trajectories reported in this study show that as the rotational speed is increased, the time taken for a bubble to migrate towards the hotter side also increased. It was shown that by adjusting the rotational speed it is possible to change a bubble's behaviour in a thermocapillary flow, which can help to determine the new migration time and speed in the rotating cylinder.

For the present calculations, the bubble was located at the axis of rotation and under the present numerical conditions and for angular velocities up to 2 rad/s there was no deformation and the bubble was spherical in shape.

No previous similar work was used to compare the obtained results; this could be used in future in order to validate newer results. In order to test the behaviour of bubbles located off-centre, a 3D simulation is necessary and a 2D swirl axis will no longer be sufficient to model such flows.

Chapter 6 Thermocapillary Bubbles Flow and Coalescence in a Static Cylinder: 3D Study

6.1 Overview

This study will investigate bubble dynamics and coalescence in two- and three-dimensional simulations to give a better understanding of the dynamics and coalescence of thermocapillary bubbles in a weightless environment. In general, it is common to have a group of bubbles in a continuous liquid and it is very important to understand their interaction. "In fact, the interactions between bubbles or droplets are more common than the migration of a single bubble" (Kang et al., 2008).

Some examples of bubble coagulation in which this research is interested include chemical flow processes, the removal of gas bubbles from glass, melt, and gaseous flow. "Bubbles have also advantageous effects since they are responsible for the gas–solids mixing and gas circulation and thus they play an important role in chemical reactions in fluidized beds" (Sobrino et al., 2009). Understanding thermocapillary bubble flow and the interaction between bubbles is very important for future research and for designing useful experiments; indeed, an understanding of these phenomena is highly desirable for the future design of space shuttles and equipment that might be employed in zero-gravity environments. "In reality, the interactions of the bubbles with one another and with the boundaries of the melt are likely to play important roles in determining the rate of gas removal" (Satrape, 1992). Very little is known about bubble collision and agglomeration in zero-gravity conditions, due to the relative complexity of conducting experiments under such conditions. In addition, the literature reveals the complexity of modelling three-dimensional geometries to simulate the thermocapillary flow of a group of bubbles in cylindrical coordinates. "The question of whether two bubbles will coalesce in a particular situation is obviously a complicated issue" (Satrape, 1992).

The objective of this chapter is therefore to investigate numerically the thermocapillary bubbles' trajectory and the merging process of two and a group of bubbles inside a cylinder in zero-gravity conditions. The first step of this study will investigate in detail the movement of a single bubble rising in a complex flow field under the effect of surface tension gradient (Marangoni force). Under such conditions, the study will be expanded further in order to investigate in detail the effect of temperature gradient and bubble size diameter on both the dynamic and collision between bubbles during their migration toward the hotter region. Due to the lack of information available on the interaction of two and a group of bubbles/droplets, the main focus of this section will extend the previous study of this thesis to multiple bubbles and will investigate in detail the coalescence process between two and a group of bubbles under the effect of surface tension gradient alone. Previous studies have shown that there is much still to be understood about thermocapillary flows and the interaction of two and a group of bubbles.

6.2 Fluids and Initial Conditions: Description of Parameters and Domain

A cylindrical vessel measuring 120 mm high (H) x 120 mm diameter (D) was filled with liquid Ethanol (Pr=16.28). The origin of the cylindrical coordinate system was placed on the centre of the lower plate, and the vertical axis, y, was directed upward. Nitrogen bubbles were patched into liquid contained in a cylinder and subjected to a vertical temperature gradient, ∇T (K/mm). The velocity is set to zero, with a no-slip boundary used for the walls of the vessel. This signifies that no flow passes across the wall boundary and the flow does not slip along the wall, as well as meaning that no heat is lost or gained from the wall. The physical parameters used for the three-dimensional simulation are similar to the two-dimensional simulations in Section 5.1of Chapter 5, except that the initial locations of the bubble are slightly different. The domain boundary conditions for the scenarios that were simulated are better understood with the visual representation of the domain represented in

Figure 6.1. Once the geometry and the grid were formulated, they were coded using CFD software. The calculations were performed using a pressure-based, segregated, implicit solver. Pressure–velocity coupling was accomplished using the pressure-implicit with splitting of operators (PISO), which performs two corrections for neighbour and skewness. The pressure-staggering option (PRESTO) scheme is used for pressure interpolation, and the momentum and energy equations were discretised using a second-order upwind differencing scheme. Other algorithms such as QUICK were also tried instead of a second-order upwind scheme. No difference was observed in the simulation results using these alternative methods; however, simulations using non-iterative methods were considerably faster than iterative methods from a computational perspective. According to several different operational conditions, the non-iterative time advancement in time steps of 2.5×10^{-3} s is used to obtain convergence. No gravitational force was imposed on the simulation and all cases were run in double-precision mode.

6.3 Thermocapillary flow and interaction of two vertically-placed spherical bubbles

To serve as a control case and indicator, the motion of an isolated bubble immersed in liquid Ethanol placed at the centre of the cylinder and 1.5d from the bottom wall (colder region) was first computed. The simulation was conducted with the set of parameters shown in Table 6.1, with Re_T and Ma_T equal to 308.6 and 5025.7, respectively, for a bubble with a diameter equal to 8 mm and a temperature gradient of ∇T =0.25K/mm. The final results, shown in Figure 6.1a, present the motion of the isolated bubble from the colder to the hotter region over 10 time steps. Besides the existence of Marangoni phenomena (as seen in Figure 6.1a), the results from the same figure show good agreement with the earlier 2D axis study and the experimental results of Thompson et al. (1980).

Table 6-1 Physical properties of the liquid and gas employed in the simulation at T_o=298.2K and sample results of a bubble with a diameter equal to 10 mm.

Properties	Unit	Ethanol	Nitrogen (N_2)
Density (ρ)	kg/m^3	790	1.138
Specific Heat (Cp)	j/kg-k	2470	1040.7
Thermal Conductivity (λ)	w/m-k	0.182	0.0242
Viscosity (μ)	kg/m-s	0.0012	1.66e-5
Surface Tension (σ_0)	N/m	0.0275	------
Surface Tension Coefficient (σ_t)	N/m-k	0.00009	------
Temperature Gradient (∇T)	K/mm	0.208	------
Prandtl Number (Pr), Eq. (4)	-------	16.28	0.79
Thermal Reynolds Number(Re_T), Eq. (2)	-------	257.2	-------
Thermal Marangoni Number(Ma_T), Eq. (3)	-------	4188	-------

Three different studies for three different bubble diameter sizes were carried out to investigate the effect of bubble diameter size on thermocapillary migration and interaction of leading and trailing bubbles located at the centre of the cylinder and perpendicular to the hotter region. Identical boundary conditions and physical properties of the isolated bubble were used; the only variable was the bubble's diameter. In the first case, presented in Figure 6.1b, two bubbles of equal diameter (10 mm) were aligned perpendicular to the hotter surface. The lower bubble was located at a distance of 1.5d above the lower wall (cold surface) and at a distance of 2d below the centre of the upper bubble. In the second case, presented in Figure 6.1c, two bubbles with different diameters were placed one above the other. The smaller and larger bubbles had diameters of 8 and 10 mm and were located at 1.5d and 3d from the bottom wall, respectively. In the third case, presented in Figure 6.1d, two bubbles with different diameters were used, with the larger bubble positioned below the smaller one. The centre of the lower bubble was positioned 1.5d from the colder wall and the upper bubble at 2.5d from the centre of the lower bubble. The final and critical result found from the three simulations is that in a zero-gravity environment, the thermocapillary

migration of a pair of bubbles immersed in a surrounding liquid with a temperature gradient, both bubbles will migrate toward the hotter side. The motion of these two bubbles depends on the temperature difference, their position, and the length of their diameters. The results recorded in Figures 6.1a-d show the final results for the three cases at two time steps (0.25 to 7.25s). As expected, the trailing bubble has no influence on the migration of the leading bubble, which moves as if it were an isolated bubble. Contrary to the behaviour of the upper bubble, the lower bubble was found to be significantly affected by the dynamics of the leading bubble. The lower bubble always moves more slowly than an isolated bubble, due to the back flow produced by the leading bubble. Balasubramaniam and Subramanian (2000) studied two bubbles migrating in large Reynolds (Re_T) and Marangoni numbers (Ma_T) and found that the thermal wake of the leading bubble disturbed the temperature field around the trailing bubble and reduced its velocity, in contrast to the findings of Meyyappan et al. (1983) who studied theoretically the different reactions between two bubbles with different diameters along their line of centres and found that the smaller of the two bubbles always moves faster and the larger bubble moves slightly more slowly, unlike in the case of a single bubble. All the theoretical work on the interaction between bubbles or droplets mentioned above was restricted to small Re and Ma values.

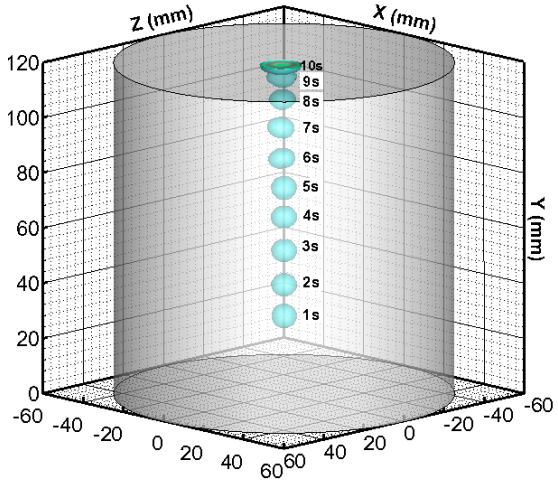

Figure 6.1a Isolated bubble migration at 10 time steps (d=8 mm).

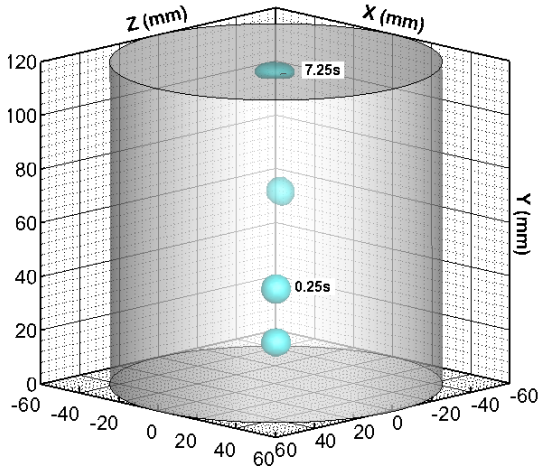

Figure 6.1b Two equal bubbles migrating at two time steps (d=8 mm).

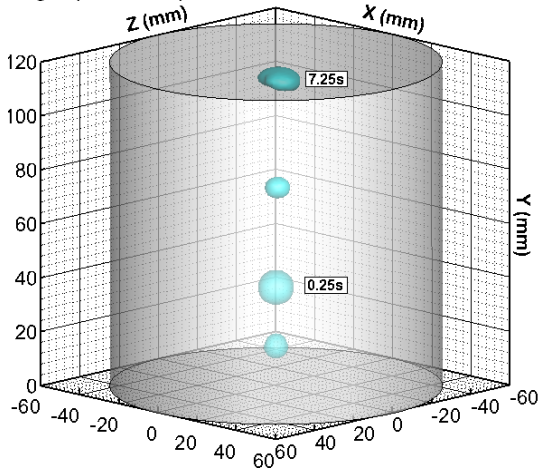

Figure 6.1c Two unequal bubbles migrating at two time steps (d_{top}=12 and d_{bottom}=8 mm)

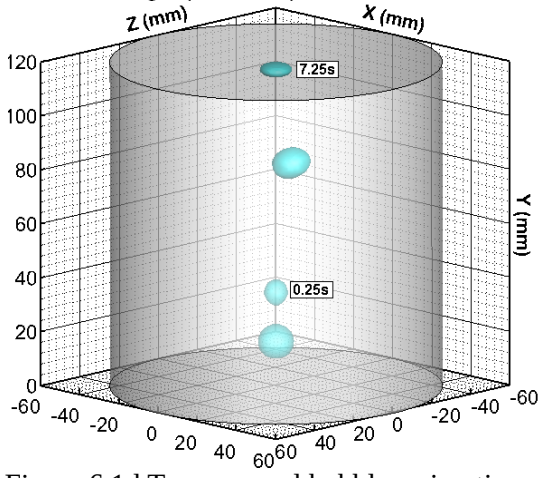

Figure 6.1d Two unequal bubbles migrating at two time steps (d_{top}=8 and d_{bottom}=12 mm)

Figure 6-1a-d Final position of single and two bubbles aligned vertically in ∇T=0.25K/mm. The bubbles are shown at different times along with their path.

6.5 Thermocapillary flow and interaction of two horizontally-placed spherical bubbles

The thermocapillary flow of two and a group of bubbles located side by side in a zero-gravity environment may be considerably different from the flow observed in normal gravity. In this section, several fundamental aspects of multi-bubble behaviour are presented, which include thermocapillary bubble merging and coalescence (small bubbles merging into a large bubble) and bubble size distribution due to bubble coalescence.

This numerical study observed the behaviour of two spherical bubbles inside a stationary cylindrical domain. The two bubbles had zero-velocity fields and were prescribed

horizontally with a distance of h = 2d between their central points. The bubbles were placed at initial locations of -1d, 1.5d, 0d and 1d, 1.5d. 0d mm on the coordinate system X, Y, Z for the left and right bubble respectively, so that both of the bubbles were close to the centre of the cylinder. Two simulations were conducted with two different temperature gradients; the corresponding thermal Reynolds and Marangoni numbers for the two different temperature gradient were Re_T= 257.2 and Ma_T= 4188 for ∇T = 0.208 K/mm and Re_T= 308.6 and Ma_T= 5025.7for ∇T = 0.25 K/mm. For the first temperature gradient of 0.25 K/mm, the numerical simulations of stationary cylinder systems show that the two bubbles move from the cooler to the hotter side in an almost linear motion, as seen in Figure 6.2a and 6.3. The bubbles maintain the same distance from each other and travel to the hotter side without colliding, rising separately and developing almost spherical shapes. The final configuration can be explained by the fact that, in addition to the motion towards the warmer surface, the bubbles migrate with equal space between them at a steady state velocity. The results of the case with two bubbles are similar to what is seen for the isolated bubble in a stationary cylinder (as reported in the previous section; see Fig. 6.1). Another simulation was carried out in the same conditions, except with a higher temperature gradient between the bottom and the top wall, equal to 0.25 K/mm. It is evident from Figure 6.2b that when the temperature gradient between the lower and the upper wall is increased to 0.25 K/mm, a collision and agglomeration into a single bubble occurred in the upper region of the Y-axis at time t=8.0 s. Here, the increase in shear stress force caused by the increase in temperature is seen to advance the motion of the bubbles towards the centre of the cylinder. This shows that as the bubbles move more consistently, their trajectory and agglomeration are dominated by the temperature gradient. The critical result of this is that, in zero gravity, two bubbles immersed in a surrounding liquid with a temperature gradient will migrate towards the hotter side. The

dynamic and agglomeration of the two bubbles depends on the temperature difference of the liquid (∇T), their position (h), and their diameter (d).

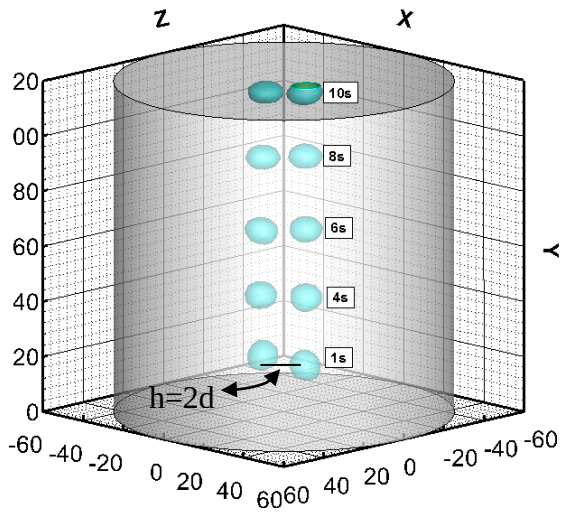

Figure 6.2a Final results of two bubbles (d_b=10 mm) migrating at ∇T =0.208 K/mm

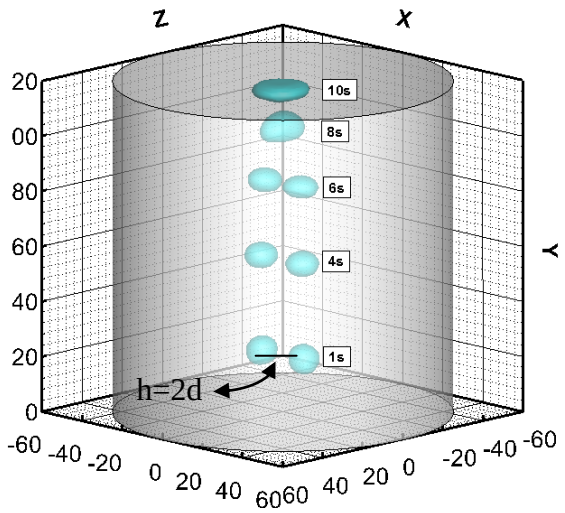

Figure 6.2b Final results of two bubbles (d_b=10 mm) migrating at ∇T =0.25 K/mm

Figure 6-2 Rise of a pair of bubbles aligned horizontally and migrating towards the hotter side. The bubbles are shown at four times along with their path.

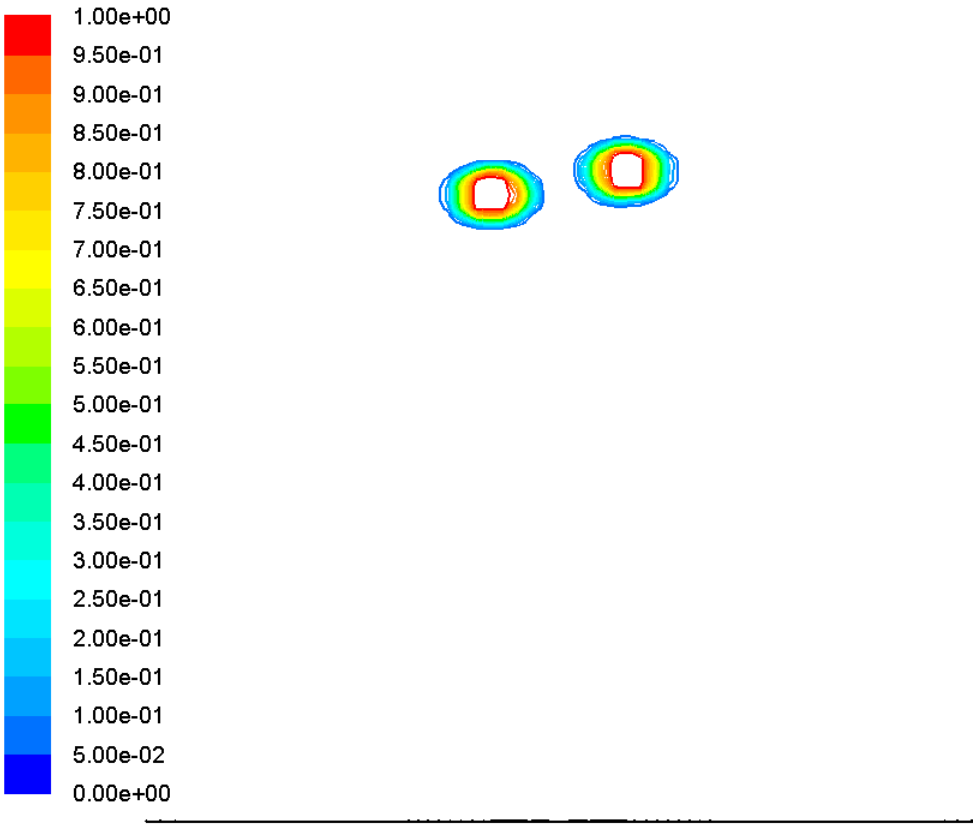

Figure 6-3 A plane of a pair of bubbles aligned horizontally and migrating towards the hotter side

6.6 Thermocapillary flow and coalescence of a group of bubbles in zero gravity

In the same conditions and using similar fluid properties to those selected in the previous section, two simulations were performed to evaluate the transition time for bubble-bubble collision and agglomeration in zero gravity due to change in bubble diameter. Figures 6.4 and 6.5 show eight equally-sized bubbles placed 1.5d above the bottom wall and aligned horizontally in the Y and Z directions at a distance of 2d from the centre of the cylinder for the first row and 4d for the second row. The temperature gradient between the lower and the upper walls was 0.25 K/mm, and the corresponding thermal Reynolds (Re_T) and thermal Marangoni (Ma_T) numbers for a bubble diameter of 8 mm (as seen in Figure 6.4) were equal to 197.5 and 3216.4. For the 10 mm diameter bubble, shown in Figure 6.5, these numbers were equal to 308.6 and 5025.7. The four different time in these two figures present the bubble trajectory between time, t = 0.25 to t = 10.0 sec. The final results in these two figures show that in both cases the eight bubbles merged into four bubbles and reached the top of the cylinder at a time of t = 10 sec. It is evident from the comparison between these two figures that the collision and agglomeration occur at different times due to the difference in the diameters of the bubbles. In the case of the bubble with a diameter of 8 mm, the coalescence occurred at around t = 4.25 sec. On the other hand, for the 10 mm diameter bubble, the coalescence happened at around t = 6 sec. The two figures also display a shift in the bubble position towards the right of the centre due to the relatively high-speed motion of the bubbles on the outer side. This result strongly suggests that thermocapillary bubble-bubble collision and agglomeration can take place in zero gravity, and there is a clear dependence of bubble-bubble interaction on their diameter, i.e. with greater diameter the bubble coalescence mechanism could occur at a higher point in the Y direction. In general, the present results show similarities with experimental results and differences with other numerical findings. For instance, the current results contrast with the results of Nas and Tryggvason (1993) in their

three-dimensional numerical study, which reported that no collision could occur in zero gravity and that bubbles repel each other due to cold liquid carried between the particles during migration. Their results contrast with both the present results and those recorded onboard the Chinese 22nd recoverable satellite experiment by (Kang et al., 2007), who observed a total of 19 coalescences between air bubbles injected in the direction of the temperature gradient of the stagnant heated liquid, where the bubbles were found to stay at the upper side of the test cell.

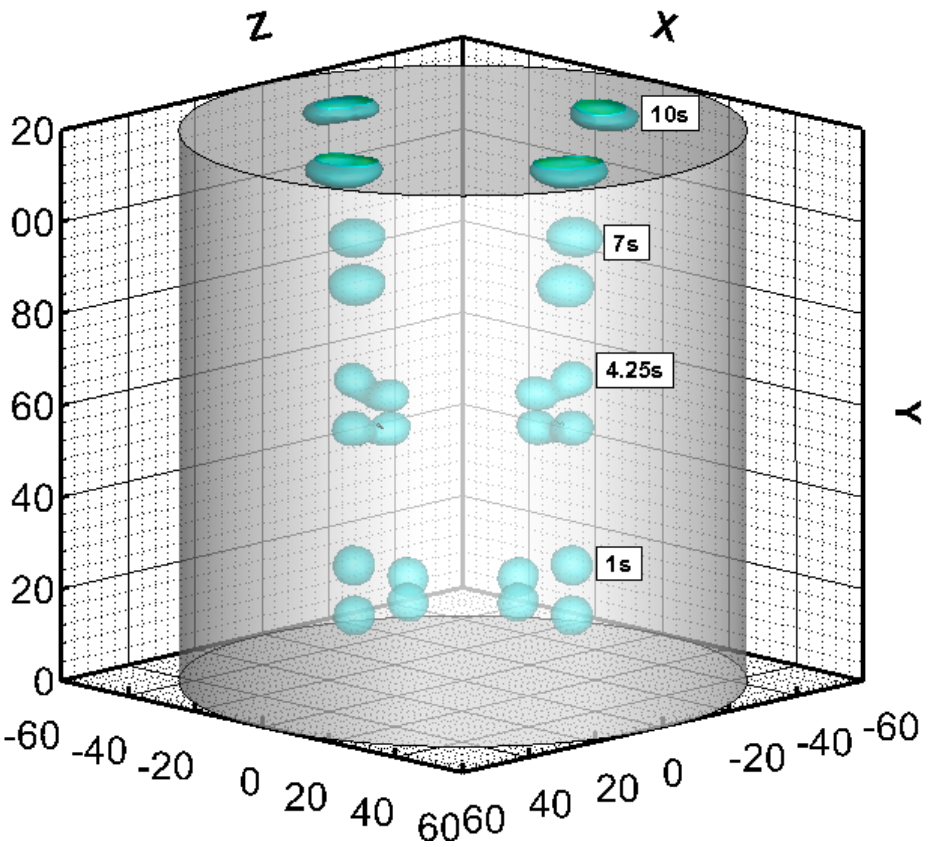

Figure 6-4 Bubble coalescence into four bubbles at ∇T=0.25K/mm (d_b=8 mm). The bubbles are shown at four times along with their path.

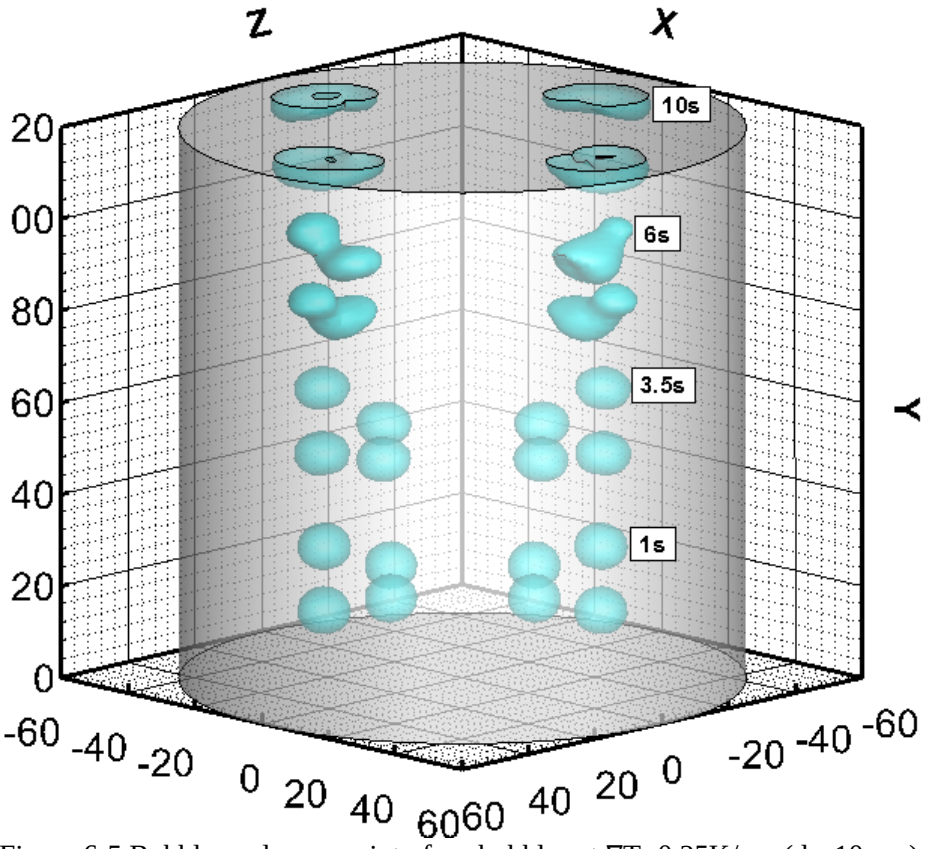

Figure 6-5 Bubble coalescence into four bubbles at ∇T=0.25K/mm(d_b=10mm). The bubbles are shown at four times along with their path.

6.7 Coalescence of a group of bubbles

In continuous flow such as is found in a bubble column, it is common to have many bubbles. In this subsection, the VOF method was used to simulate thermocapillary flow and the interaction of 13 bubbles equal in diameter (8 mm) in a fully three-dimensional geometry. A constant temperature gradient of 0.25 K/mm was applied between the top and bottom walls, and the corresponding Re_T and Ma_T for the given conditions were equal to 197.5 and 3216.4, respectively. All of the bubbles were placed at 1.5d from the bottom of the cylinder (colder region) with one bubble at the centre; the remaining twelve bubbles were distributed regularly in the Y and Z directions. Figure 6.6 presents the final result of the thermocapillary flow and coalescence of these bubbles at four different time steps. The results show that the bubbles' behaviour is similar in tendency to the earlier predictions for smaller numbers of

bubbles with a slight difference in coalescence time. The observation worth noting is that the bubbles tend to flow away from the centre of the cylinder during their migration. The final results show the tendency for the 8 bubbles in the core to coalesce into 4 larger bubbles. The outer bubbles were found not to collide, due to their relatively high speed.

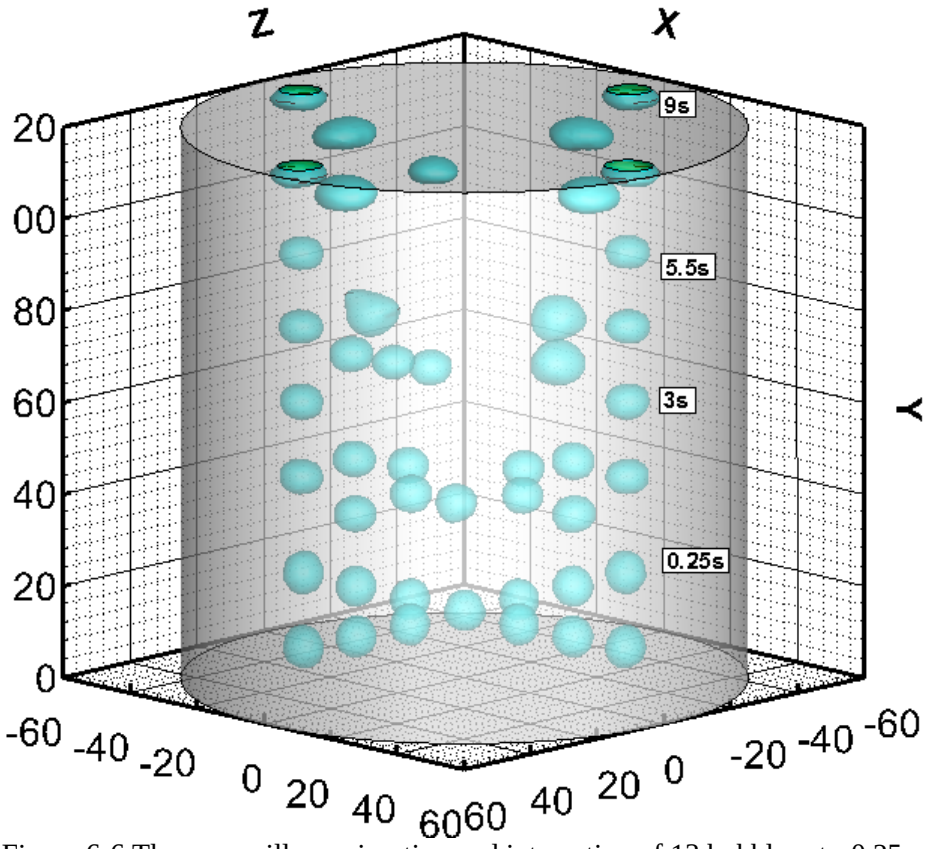

Figure 6-6 Thermocapillary migration and interaction of 13 bubbles at =0.25 K/mm and d_b=8 mm. The bubbles are shown at four times along with their path.

6.8 Conclusion

This section has covered the thermocapillary flow and interaction of single and multiple bubbles in a three-dimensional domain. The results show that the trailing bubble migrates more slowly than the isolated bubble, due to the disturbed temperature caused by the leading bubble. The interaction and disturbance increases as the gap between the two vertically aligned bubbles decreases, and vice versa. With a centre-to-centre (h) distance equal to 2d between two horizontal bubbles, the results show that the bubbles aggregated when the temperature gradient (∇T) was 0.25 K/mm. The final results show that the dynamic and agglomeration of the two bubbles depends on the temperature difference (∇T), the distance of the bubbles from each other (h), and the size of their diameter (d). Other fundamental aspects of bubbles placed side by side were also presented, which included the size distribution of smaller bubbles and their agglomeration to form a larger bubble. The results show that collision and agglomeration could occur at a higher distance and longer time if larger bubbles were used. No bubbles broke in any of the cases observed and agglomeration only occurred during thermocapillary migration for a given range of thermal Reynolds and Marangoni numbers.

Chapter 7 Thermocapillary Bubbles Flow and Coalescence in a Rotating Cylinder: 3D study

7.1 Overview

This work aims to provide a better understanding of the dynamics of single and multiple bubbles in confined rotating flows subject to thermocapillary forces in zero-gravity conditions. In an actual rotating cylinder, the momentum of the rotating cylinder often causes gas bubbles to merge as they move to the axis of the rotation. This increases the bubble size and can lead to a reduction in the gas holdup. Furthermore, it can also affect the momentum exchange (drag) between the different phases. However, even with the advent of modern science, the motion of a single bubble in a rotating flow field is yet to be fully understood; "In particular, the spin force acting on a small bubble is not clearly identified, and it is not easy to predict optimum conditions for bubble removal" (Yamaguchi et al., 2004). The results of a three-dimensional rotating cylinder can complement the previous published 2D studies thereby explaining not only the motion of small bubbles but also their coalescence into one large bubble. "A rotating fluid provides a gyrostatic pressure field which causes less dense material such as bubbles to move inward toward the rotation axis"(Subramanian and Cole, 1979). In a rotating field, fluid particles which are less dense compared to the surrounding media migrate inwards, i.e. towards the axis of rotation (Annamalai et al., 1982). This technique of adding an additional force, such as centrifugal force, is one way to enhance bubble-bubble interaction and has potential applications in micro gravitational science and technology. The same method can be used in the glass-manufacturing process by controlling bubble coalescence, which may improve gas bubble distribution. "Rotation of the melt followed by thermocapillary migration of the coalesced bubbles results in a “centrifugal fining” operation for bubble removal (Annamalai et al., 1982)". This method is also applicable to removing non-metallic inclusions and is useful in microgravity" (Yamaguchi et

al., 2004). Thus, the objective of this chapter is first to confirm the existence of the centrifugal force on the bubbles inside a cylinder under zero-gravity conditions subjected to Marangoni force, and secondly to investigate numerically the rising and merging process of a group of bubbles affected by both these forces. The numerical study will investigate in detail the behaviour of a single bubble rising in such a complex flow field. Under such conditions, the study will be expanded further to investigate in detail the effect of two important parameters: the temperature gradient and the angular velocity. The study will also provide a relation ratio for the bubbles' trajectory under the action of both Marangoni and centrifugal forces. Young, Block, and Goldstein (Young et al., 1959) first investigated the thermocapillary migration of bubbles and drops with a linear model:

Thus, the objective of this chapter is first to confirm the existence of the centrifugal force on the bubbles inside a cylinder in zero-gravity conditions subjected to Marangoni force, and secondly to investigate numerically the rising and merging process of a group of bubbles affected by both forces. The numerical study will investigate in detail the behaviour of a single bubble rising in such complex flow fields. Under such conditions, the study will be expanded further to investigate in detail the effect of two important parameters: the temperature gradient and the angular velocity, and to provide a relation ratio for the bubbles' trajectory under the action of both forces.

7.2 Problem description

A cylindrical vessel measuring 120 mm high x 120 mm diameter and filled with liquid (Pr=16.28) was rotated around its vertical axis at a constant angular speed (ω). The origin of the cylindrical coordinate system was placed on the centre of the bottom plate and the vertical axis, y, was directed upward. Nitrogen bubbles in the diameter d=10 mm were patched into liquid contained in a cylinder and subjected to a vertical temperature gradient (∇T). The velocity was set to zero. A non-slip boundary was used for the walls; this refers to the lack of

flow across the boundary wall and the inability of the flow to slip along the wall, as well as indicating that no heat was lost or gained from the wall.

7.3 Theory

The three-dimensional Navier-Stokes equation for incompressible fluid flow in a system rotating about a vertical axis reads as seen from chapter 3, Eq. 3-3:

$$\frac{\partial}{\partial t}(\rho\vec{v}) + \nabla.(\rho\vec{v}\vec{v}) = -\nabla P - 2\omega.\vec{v} + \nabla.[\mu(\nabla\vec{v} + \nabla\vec{v}^{T})] + \vec{F}$$

where, ω is the angular velocity of the system and P is the modified pressure accounting for centrifugal force: $P = p - \frac{1}{2}\rho\omega^2 R^2$. Here the coriolis force $(-2\omega.v)$ results from a combination of fluid velocity and the angular velocity of the system (Detzel et al., 2009). Other important dimensionless numbers when dealing with the thermocapillary bubble flow in a rotation system are Taylor number $Ta = \frac{R^2\omega}{\upsilon}$, the swirl Rossby number $Ro = \frac{V_{YGB}}{R\omega}$ (which characterises the relative importance of inertial force (thermocapillary force in this study) to Coriolis forces and the Ekman number, $E_k = \frac{\upsilon}{R^2\omega}$ (which indicates that of viscous to Coriolis forces (Bush et al., 1995)). We consider situations where the bulk external fluid motion is geostrophic, i.e. the Coriolis forces are balanced by pressure gradients: $2\rho\omega v(R) = \frac{dp}{dR}$, where R is the radial distance measured from the centreline of the vessel and ω is the angular velocity of the rotation of the cylinder measured in rad/sec.

To check the procedure, we first examine the simple problem of ω= 0.5 rad/sec as the baseline case. To confirm the accuracy of the simulation, after a steady state was established, the tangential velocity component, pressure and temperature gradient of the host liquid were measured. Figures 7.1a-d show the distributions of the tangential velocity component, v, along with the temperature and pressure within the computational domain after reaching the

steady state condition. Here, the cylinder has a rotational velocity of 0.5 rad/sec and a temperature differential of 25 K between the lower and the upper faces. Ethanol is used as the working fluid with its properties given in Table 7.1. The results given in figure 7.1a, show that the radial distributions of the tangential velocity component measured on the horizontal planes (R=60 mm) obeyes $v = R\omega$ relationship at every axial measurement position.

Table 7-1 Physical properties of the liquids employed in the simulation at300K for (Pr=16.28)

Properties	Unit	Ethanol	Nitrogen (N_2)
Density (ρ)	kg/m^3	790	1.138
Specific Heat (Cp)	j/kg-K	2470	1040.7
Thermal Conductivity (k)	w/m-K	0.182	0.0242
Viscosity (μ)	kg/m-s	0.0012	1.66e-5
Surface tension (σ_0)	N/m	0.0275	------
Surface tension coefficient (σ_T)	N/m-K	0.00009	------
Temperature gradient (∇T)	K/mm	0.208	------
Prandtl Number (Pr)	-------	16.28	0.79

The steady state result approximated in figures 7.1a show that the tangential velocity increases linearly from the cylinder's axis of rotation to the walls of the cylinder. It also indicates that the total pressure has its minimum and maximum value at the centre and the outside walls of the cylinder, respectively. The temperature also shows a linear behaviour from the lower to the upper face of the cylinder. Thus the steady state result shown in figures 7.1a-d verifies that the present CFD measurements are accurate.

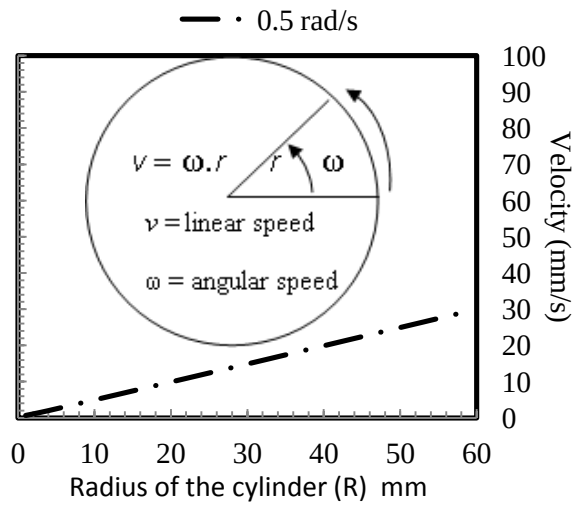

Figure7.1a Tangential velocity along the radius

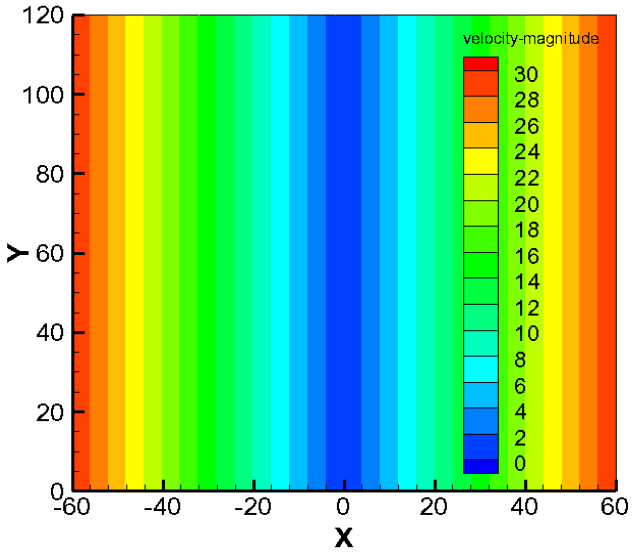

Figure7.1b Tangential velocity (mm/s)

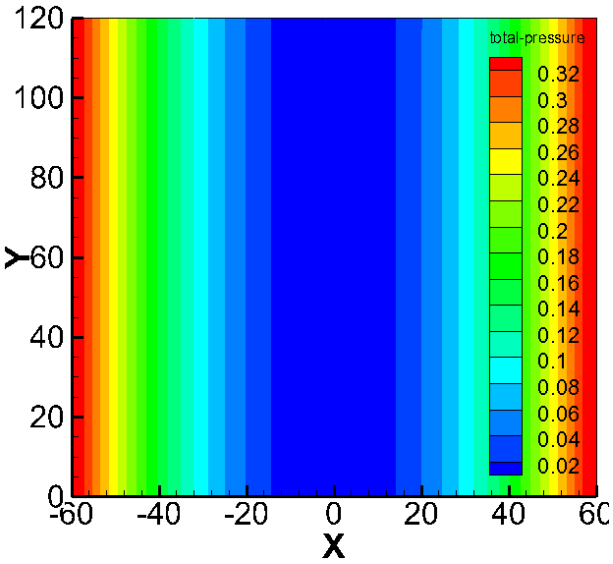

Figure7.1c Distribution of static pressure (Pascal)

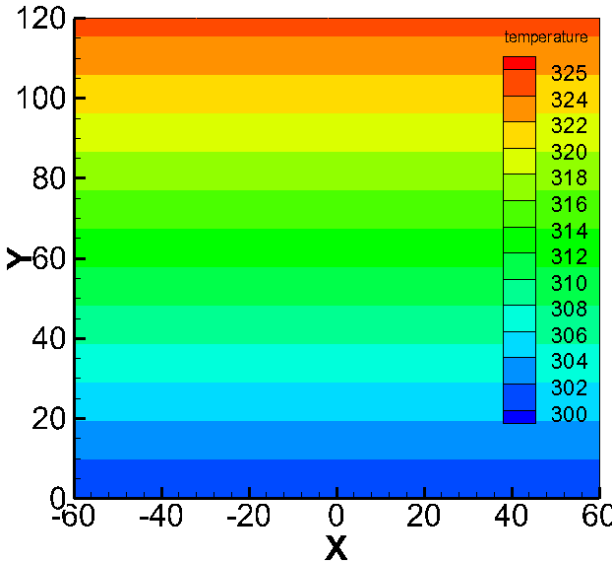

Figure7.1d Distribution of temperature (K) between the lower and upper walls

Figures 7-1a-d Tangential velocity, static pressure, and temperature gradient along X, and Y axis.

7.4 Singular bubble dynamics in a rotating cylinder

The results obtained from the steady state simulation of the rotating cylinder will now be used to predict the behaviour of a single bubble within such a cylinder. A bubble was placed at the location of (5d,1.5d,0d) in the (X,Y,Z) directions respectively, where "d" is the diameter of the bubble.

Table 7-2 A simple calculation for the dynamic of a single bubble using the physical properties from Table 7.1

Radius of the Cylinder (R)	60	[mm]
Bubble diameter (d)	10	[mm]
Bubble position at X-axis	50	[mm]
ω	0.5	[rad/s]
V_{YGB}	35.8	[mm/s]
Re_{T}	257	
Ma_T	4188	
Ro	1.37	
E_k	0.00122	
Ta	822.9	

The transient simulation result in figure 7.2 presents the location profiles of the bubble in the x, y and z directions at different time intervals. It is evident from the figure that two important forces affect the thermocapillary bubble dynamics. This induces Marangoni flow in the surrounding liquid, which may affect the bubble migration by subjecting it to additional forces. Since the applied thermal gradient (and hence the thermocapillary motion) is parallel to the rotational axis, i.e. the y-axis, the bubble dynamics can be simplified into motion along the transverse plane (x-z plane) and motion in the axial direction, where the bubble can be expected to be asymmetrically placed. Since the transverse plane motion for a bubble is an inward-spiralling trajectory and the vertical thermocapillary motion is a straight line (from the cooler to the warmer region), qualitatively, the bubble trajectory should follow a helical path, as is observed from figure curves in figures 7.3 to 7.5 and 7.6 for the non-dimensional numerical solution of a bubble dynamic for ω= 0.5 rad/sec. The radius and the pitch of the

helix will depend on the relative magnitude of the temperature gradient that causes the vertical motion and the rotation rate that governs that rate of inward-spiralling motion, which will be studied in detail in the coming sections of this chapter. From the same figures, it can also be concluded that the gas bubble trajectory under the current rotating conditions is significantly different from that of a non-rotating case. That is, the Coriolis force due to the rotation of the cylinder is the more dominant factor than the inertial force caused by the Marangoni flow where the deflection is strongly influenced by the rotation rates.

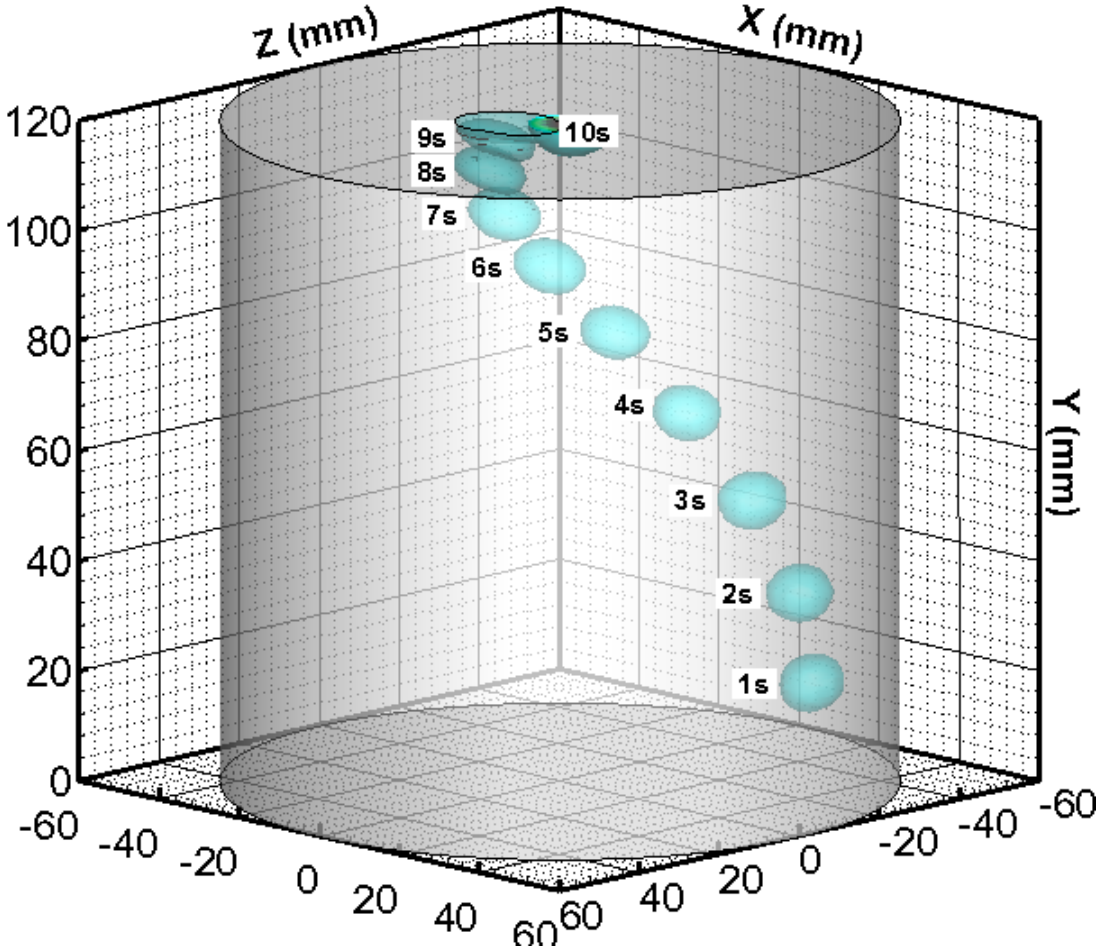

Figure 7-2 Three-dimensional numerical solution of a bubble trajectory in XYZ when ω = 0.5 rad/sec, d_b=10mm, ∇T=0.208 K/mm.

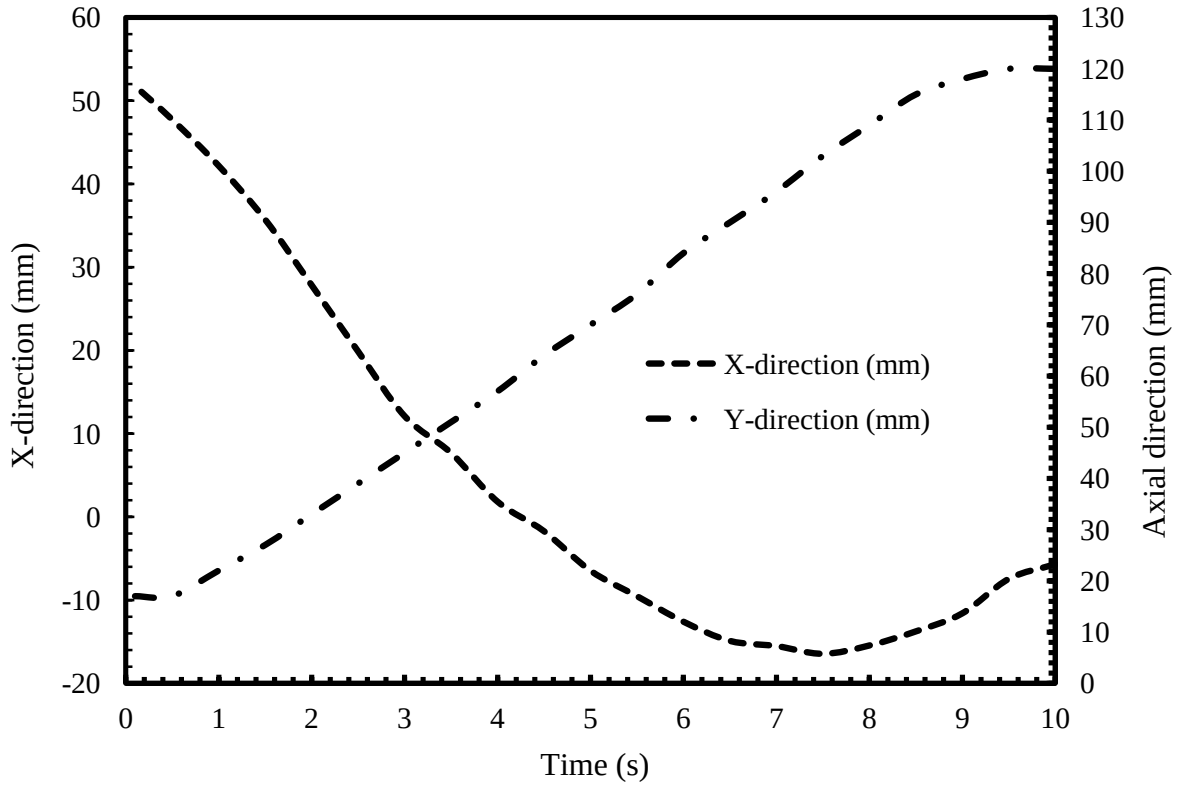

Figure 7-3 The X and Y directions of a single bubble vs. time (s)

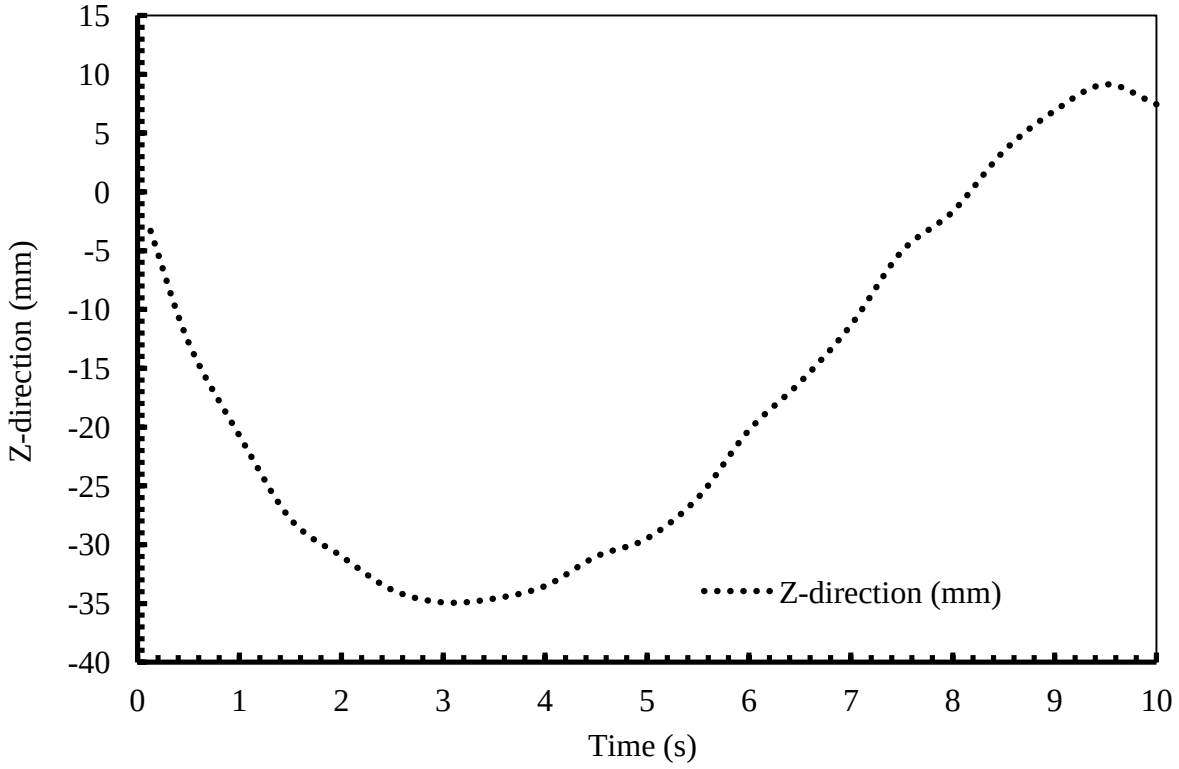

Figure 7-4 The Z-direction of a single bubble vs. time (s)

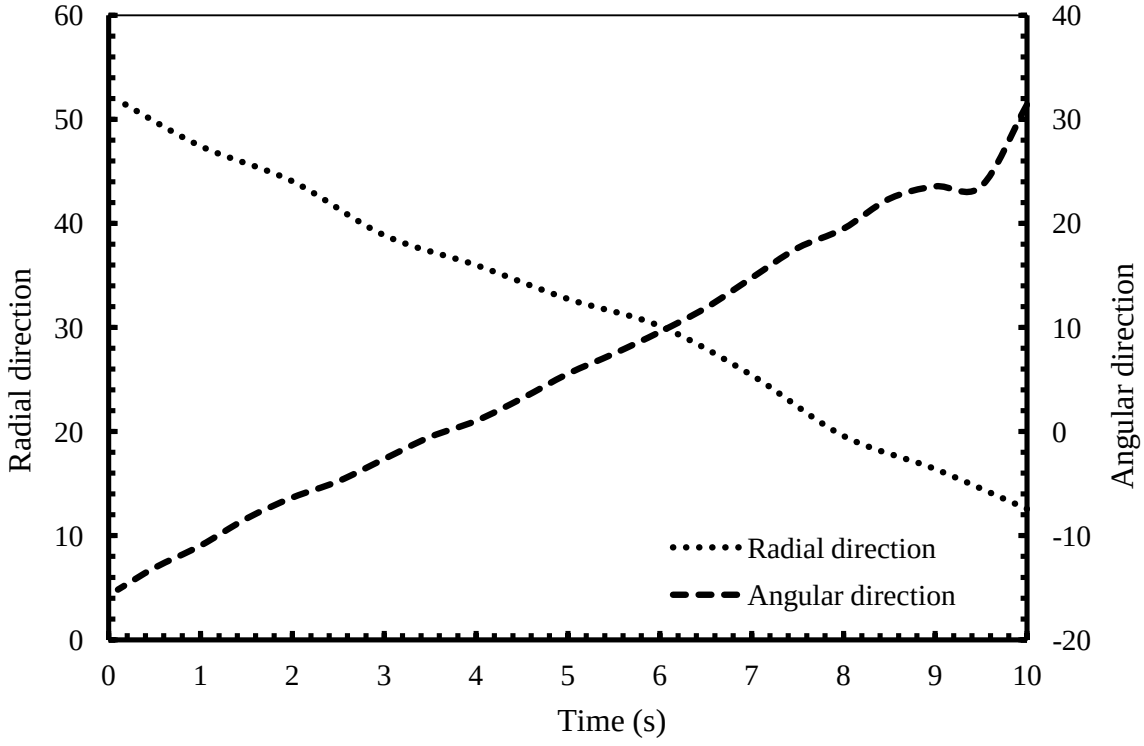

Figure 7-5 The radial and angular directions of a single bubble vs. time (s)

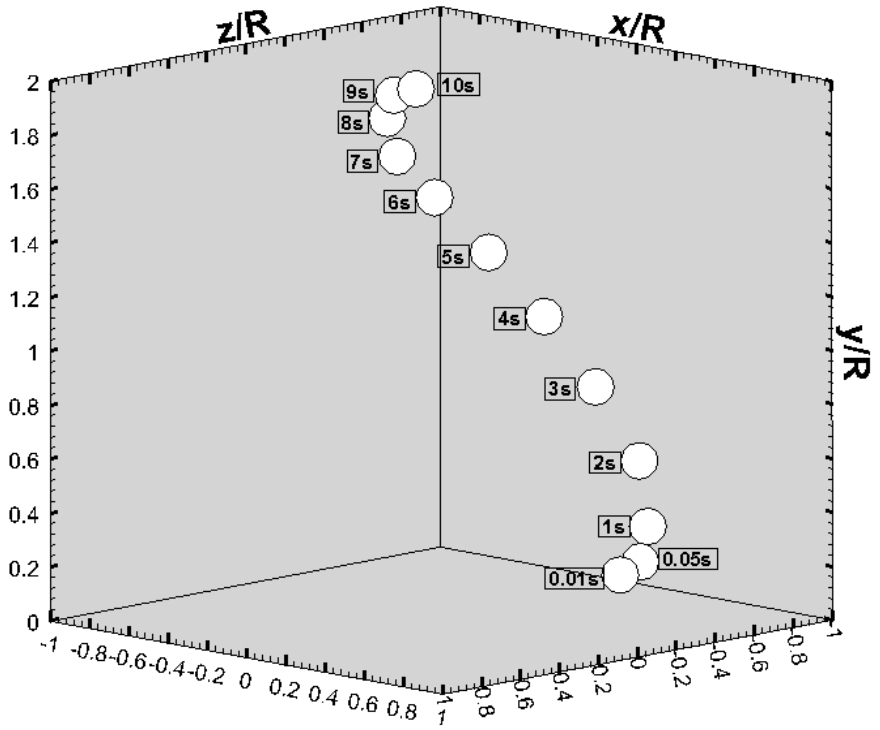

Figure 7-6 A non-dimensional numerical solution of a bubble dynamic when ω=0.5 rad/sec, d=10mm, V_{YGB} =35.8 mm/s

7.5 Impact of changing the angular velocity of the cylinder upon bubble dynamic and coalescence

The current set of results are from simulations carried out for two bubbles equal in diameter (10 mm each) located side by side at a distance of 10d from each other. Constant temperature gradient equal to 0.208 K/mm was prescribed for each simulation and the corresponding thermal Reynolds (Re_T) and Marangoni (Ma_T) numbers for all cases were set to 257 and 4188 respectively. The values of *Ta, Ro,* E_k were calculated and are reported in Table 7.3 using constant V_{YGB}=35.8 mm/s and r =50 mm.

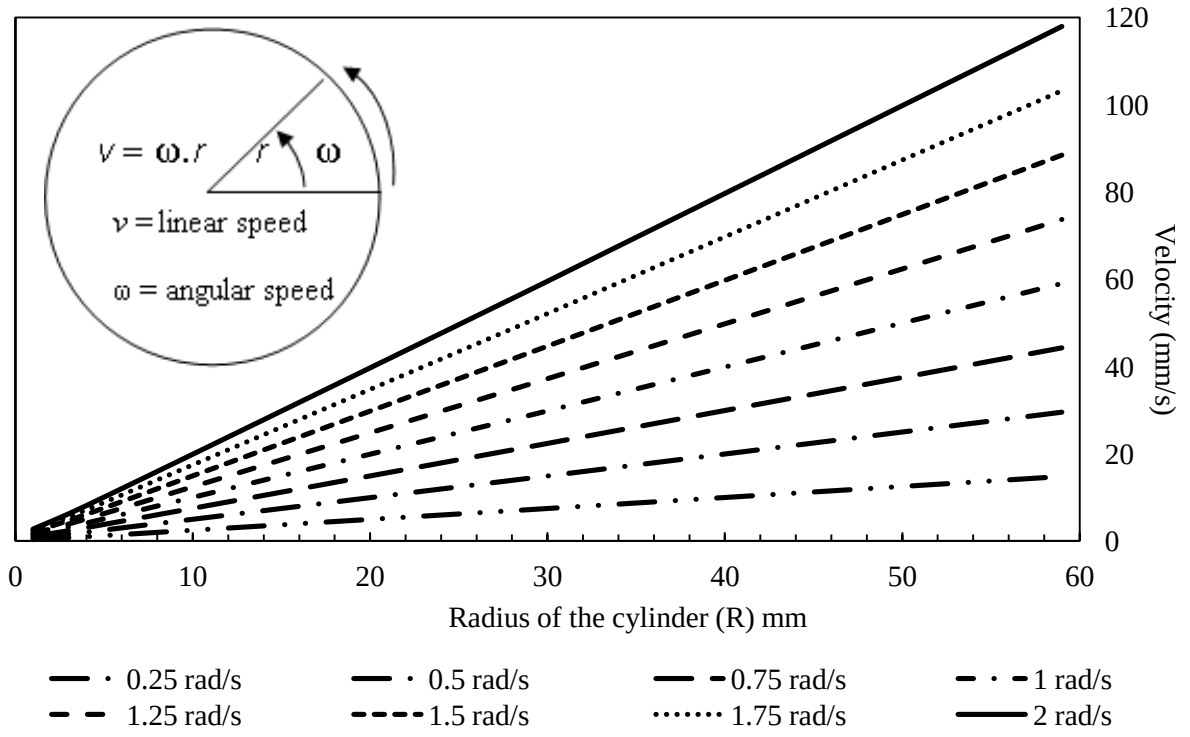

Figure 7-7 Tangential velocity along the radius for ω= (0.25 to 2 rad/sec)

Figure 7.7 shows the results of numerical simulations of eight different angular velocities. The degree to which the bubble diverged toward the axis of rotation depended on the angular velocity, ω, and distance (r) from the centre, as seen in Figures 7.8. In the case where Ro= 2.74, the bubbles developed into almost perfect spherical shapes and rose separately with slight diversion at the top of the cylinder towards the axis of rotation but no merger occurred.

Table 7-3 Non-dimensional numbers used in the calculation of (R=50 mm) and constant (V_{YGB}=35.8 mm/s)

ω (rad/s)	Ta	Re_T	Ma_T	Ro	E_k
0.25	411.5	257	4188	2.74	0.00243
0.50	822.9	257	4188	1.37	0.00122
0.60	987.5	257	4188	1.14	0.00101
0.75	1234	257	4188	0.91	0.00081
1.00	1645	257	4188	0.68	0.00061
1.25	2057	257	4188	0.55	0.00049
1.50	2468	257	4188	0.46	0.00041
1.75	2880	257	4188	0.39	0.00034
2.00	3291	257	4188	0.34	0.00030

As the angular velocity of the cylinder increased to 0.5 rad/sec, (Ro=1.37), the bubble divergence increased toward the axis of rotation and the effects of the Coriolis forces on the bubbles trajectory can be observed. However, the thermocapillary force still dominated the bubble dynamics, as seen in figures 7.8a-b. These figures show that at this angular speed and beyond, the oscillating regime appears and the bubble moves from the left to the right of the axis of rotation before reaching the top of the cylinder.

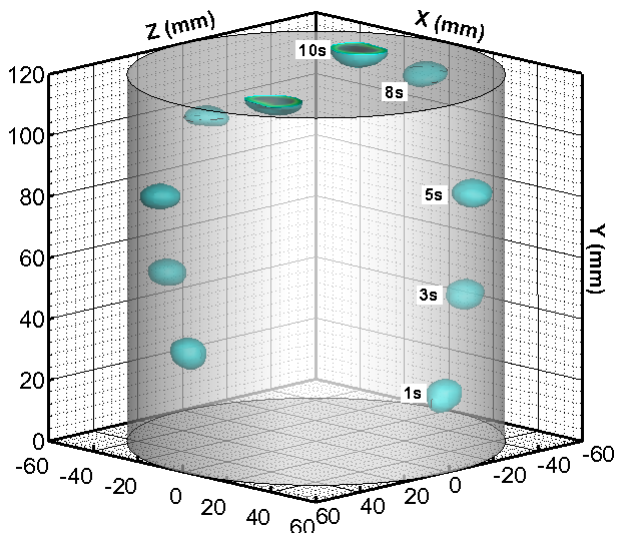

Figure7.8a ω= 0.25 rad/sec and Ro=2.74

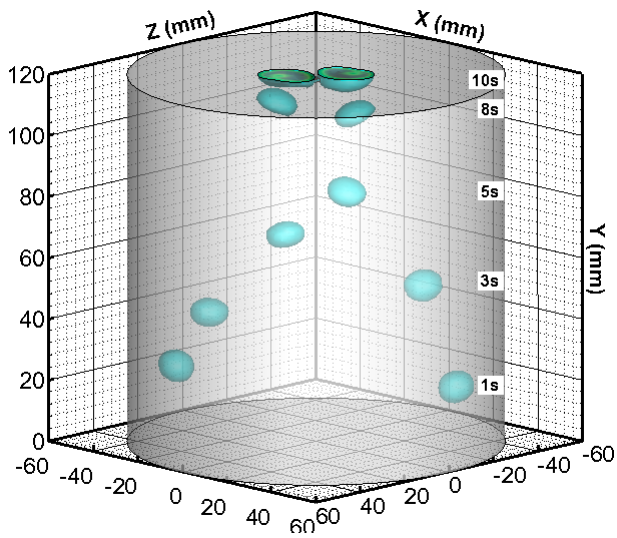

Figure7.8b ω= 0.5 rad/sec and Ro=1.37

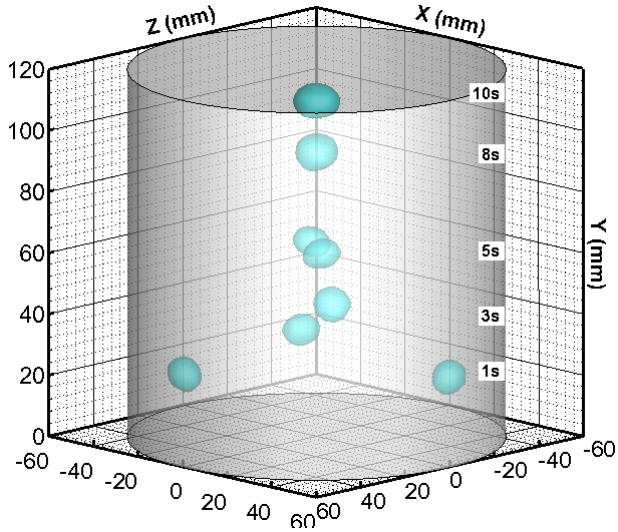

Figure7.8c ω= 0.75 rad/sec and Ro=0.91

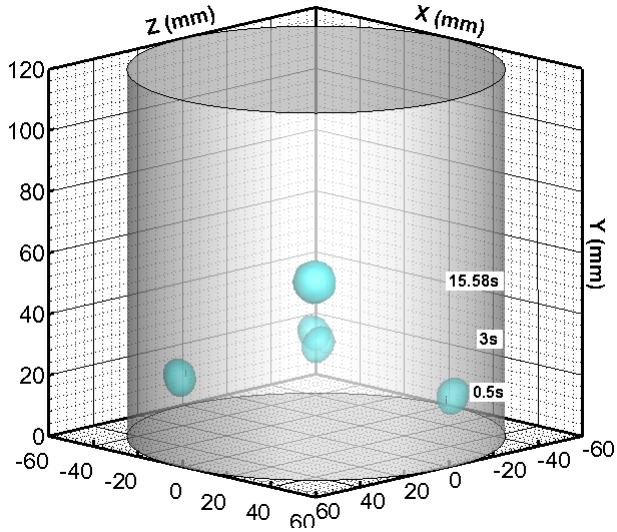

Figure7.8d ω= 1 rad/sec and Ro=0.68

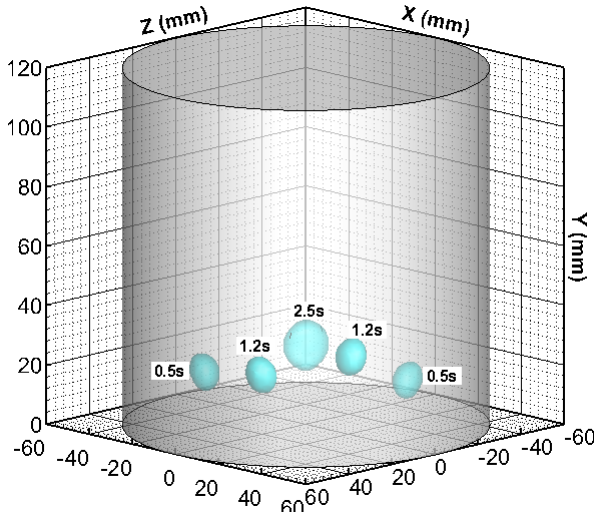

Figure7.8e ω= 1.25 rad/sec and Ro=0.55

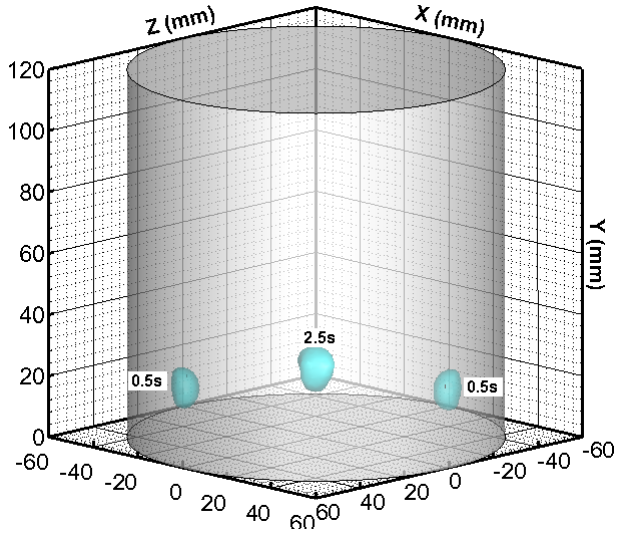

Figure7.8f 1 ω= 1.5 rad/sec and Ro=0.46

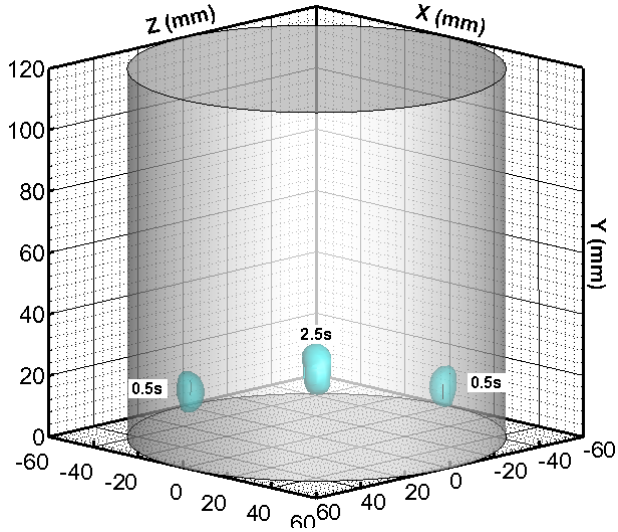

Figure7.8g ω= 01.75 rad/sec and Ro=0.39

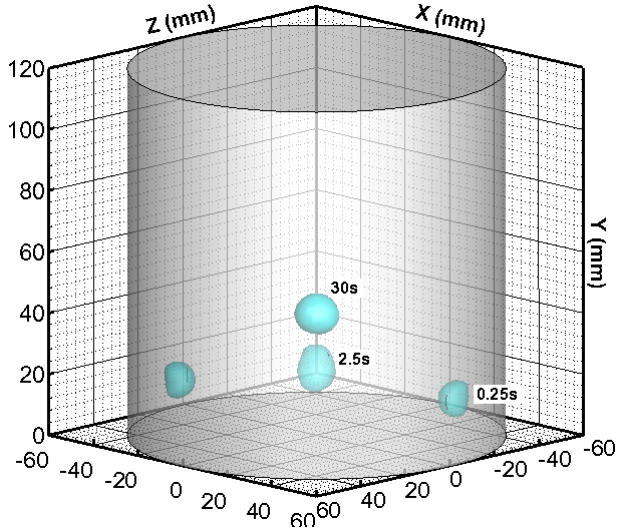

Figure7.8h ω= 2 rad/sec and Ro=0.34

Figure 7-8(a-h) The migration sequence of two bubbles with diameters d=10mm and ∇T = 0.208 K/mm at eight different angular speeds.

The majority of the bubble divergence caused by the Coriolis forces can be observed by increasing ω to 0.75 rad/sec at Ro <1.37, which resulted in a large divergence of the bubbles toward the axis of rotation with a small effect in the direction of the warmer region. Increasing the rotation rate to 1 rad/sec and beyond leads to a further divergence which is accompanied by a decrease in the magnitude of the Coriolis force. Overall the bubble divergence remains unchanged as angular velocity ω is further increased and Ro number is further decreased as seen in figures 7.8d to 7.8h. In the simulations it was observed that for Rossby number (Ro) >1.0 the bubble motion was mainly guided by thermocapillary force. However, at smaller Rossby numbers (Ro < 1), the flow was rotationally dominated and behaved quite differently. Such low Rossby numbers indicate that rotation is significant to the dynamics of the bubble.

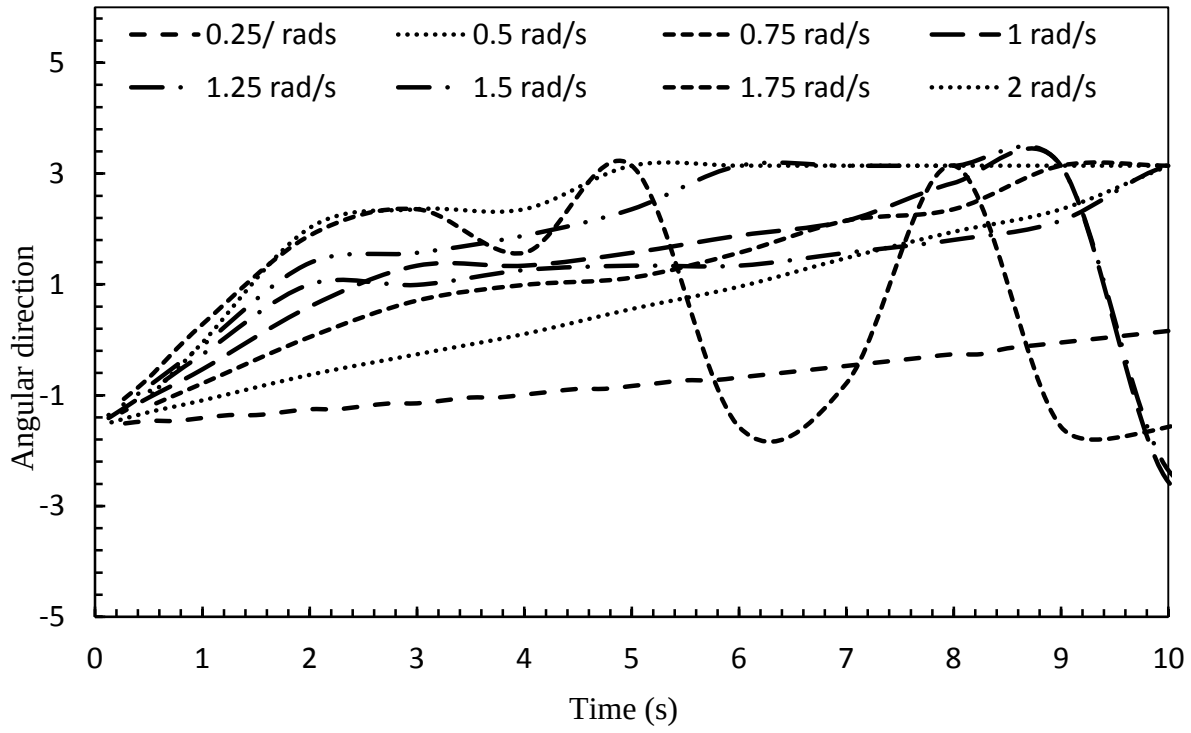

Figure 7-9 Plot of the angular direction of each angular velocity vs. time(s)

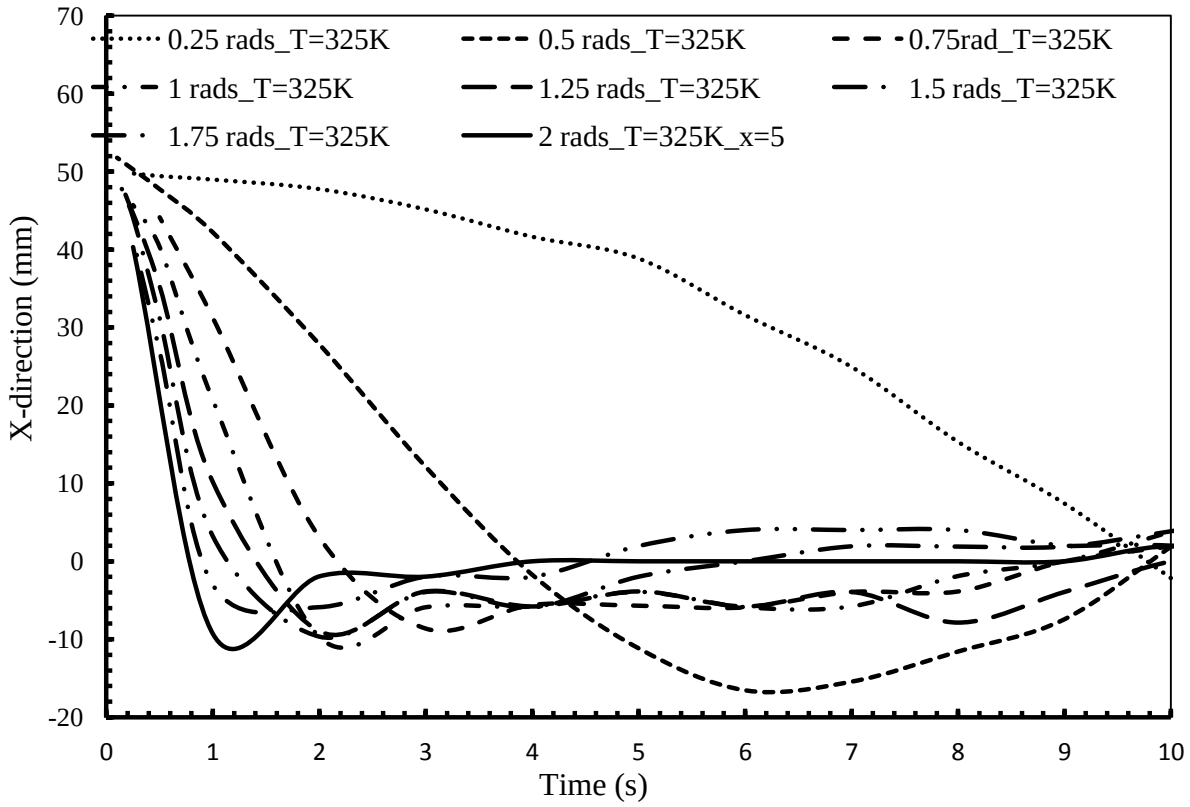

Figure 7-10 Plot of the bubble spiral in the X-coordinate for the eight cases vs. time (s)

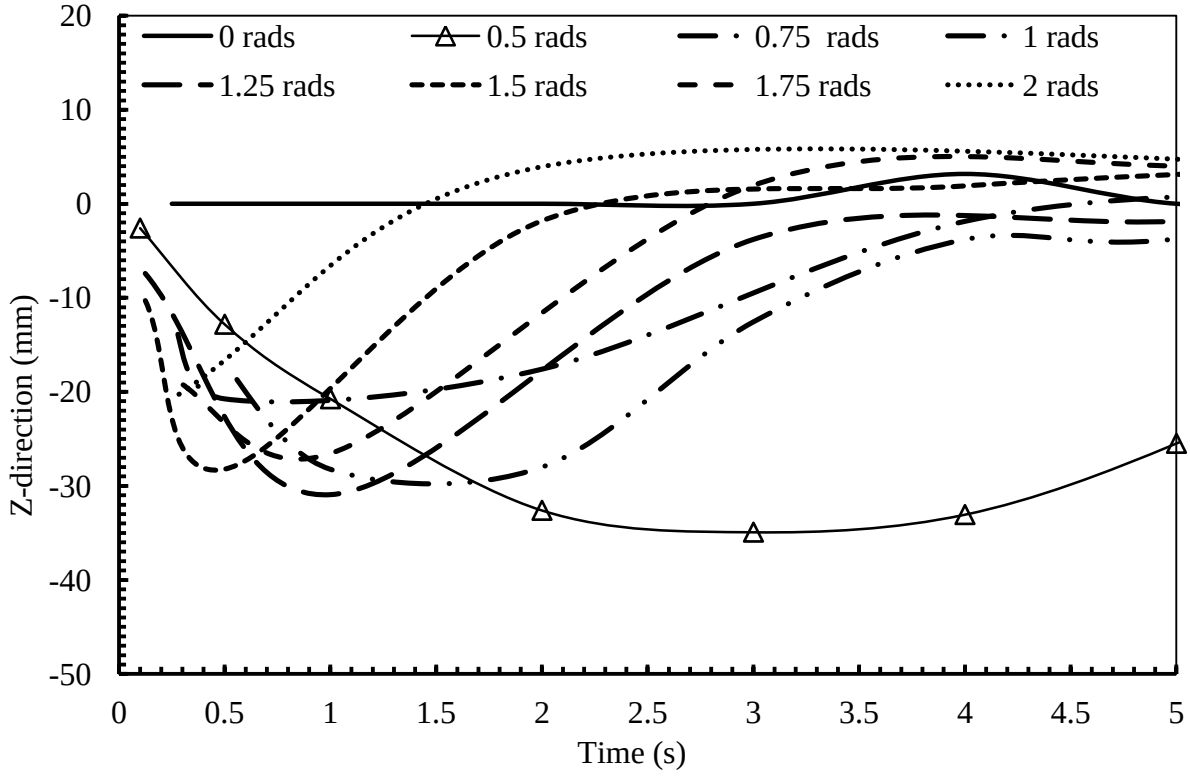

Figure 7-11 Bubble displacement (mm) from the releasing position (at Z=0 mm) toward the axis of rotation and the hotter side vs. time (s)

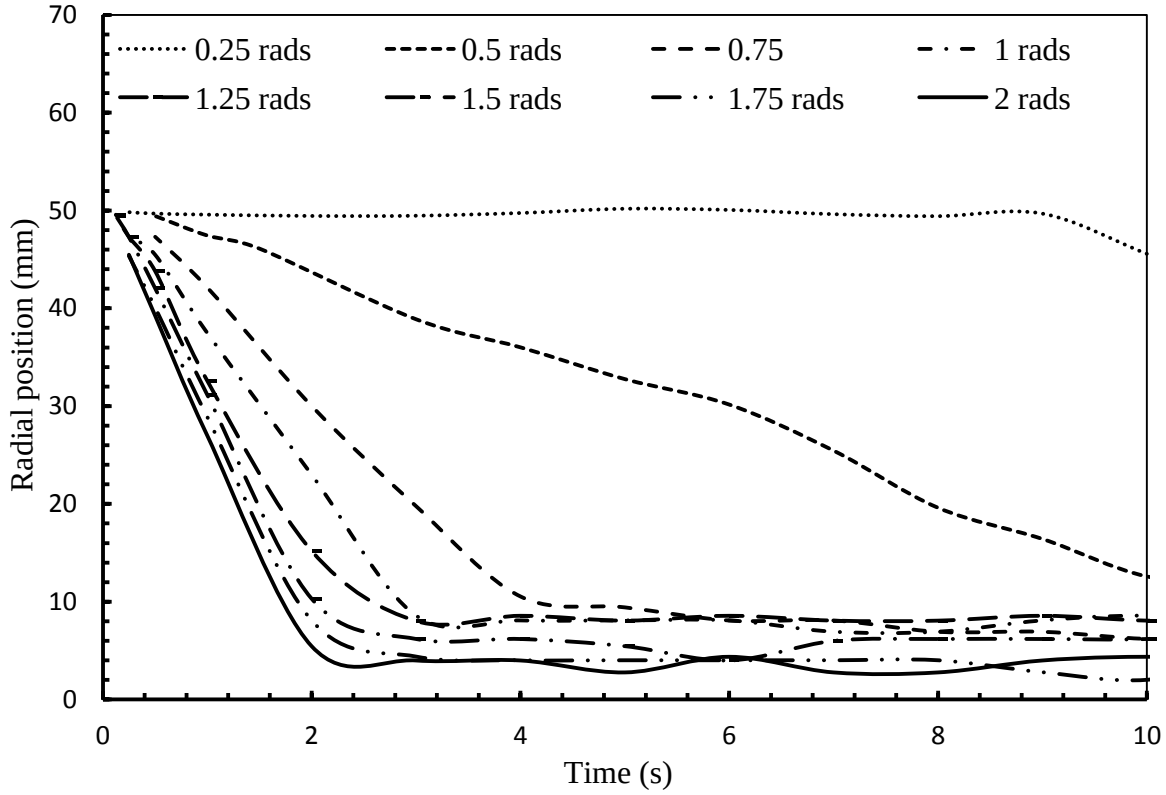

Figure 7-12 Plot of the radial bubble trajectory for the eight cases vs. time (s)

Although centrifugal forces can develop a merging process in a group of bubbles, they can also cause a major reduction in the bubble velocity towards the hotter side. This is seen in figure from 7.9 to 7.13, which shows that the reduction in the bubble velocity toward the hotter side becomes considerable as ω increase beyond 0.5 rad/sec.

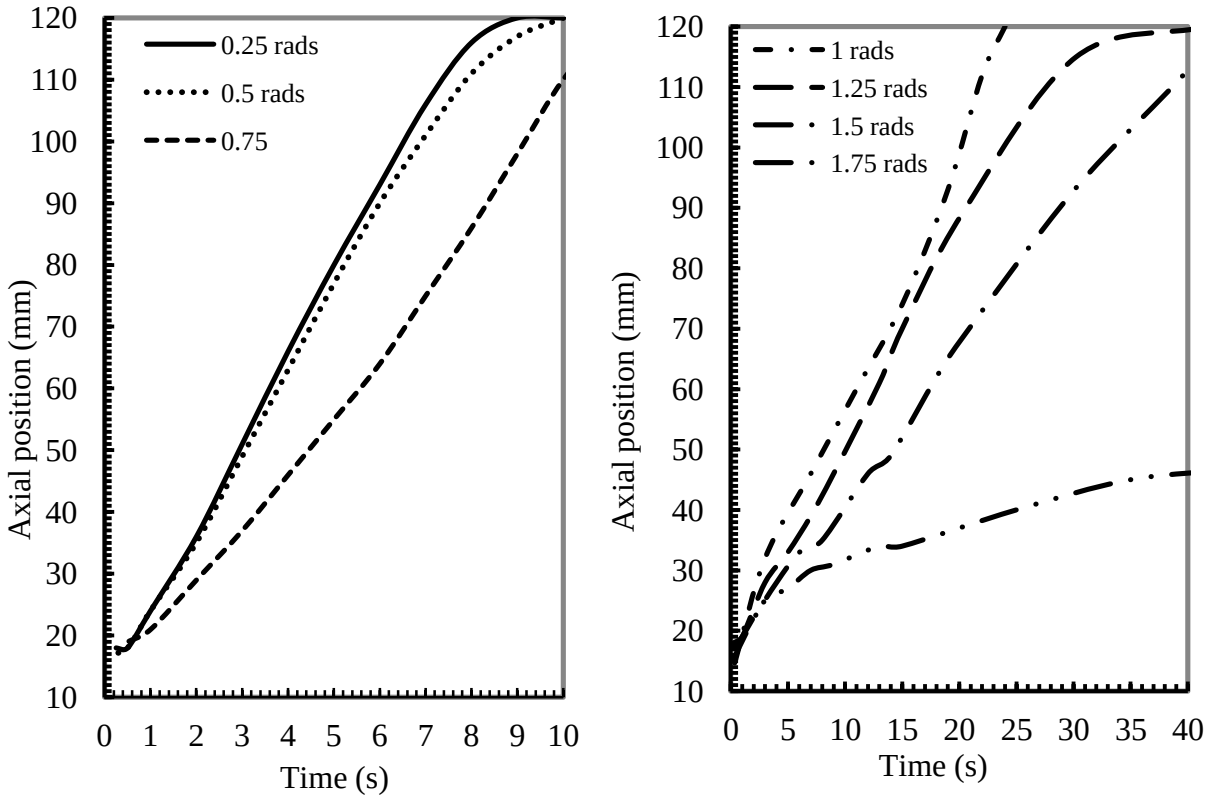

Figure 7-13 Bubble displacement (cm) from the releasing position (3 cm from the axis of rotation) toward the axis of rotation and the warmer side (Marangoni).

7.6 Impact of changing the temperature gradient of the host liquid upon bubble dynamic and coalescence

Several series of simulations were performed with the cylinder size and liquid properties that were used in the previous sections to investigate the impact of changing the temperature gradient of the host liquid upon thermocapillary flow and coalescence of four bubbles. The four bubbles of equal diameter were located at a distance of 50 mm from the axis of rotation and 90 mm apart from each other in the angular direction. The temperature at the lower surface was kept constant at 300K for all cases, while the temperature at the top of the cylinder varied between 310 to 330 K giving a temperature gradient between 0.0833 K/mm to 0.25 K/mm. The corresponding thermocapillary Reynolds, Marangoni numbers and the resultant YYGB and Rossby number (Ro) differ with temperature, see table 7.4 for details.

Table 7-4 Non-dimensional numbers used in the calculation of (R=50 mm and ω=0.5 & 0.6 rad/sec) at different temperature gradients

∇T(K/mm)	V_{CFD}	Re_T	Ma_T	Ro (0.5 Rad/s)	Ro (0.6 rad/s)
0.083	0.014	102.8	1675	0.57	0.48
0.125	0.022	154.3	2512	0.86	0.72
0.167	0.028	205.7	3350	1.15	0.96
0.208	0.036	257.2	4188	1.4	1.2
0.250	0.043	308.6	5025	1.72	1.4

The left column in figure 7.14a-e represent the trajectory of the four bubbles subjected to a constant rotational speed of 0.5 rad/sec with varying thermal gradients between 0.0833 to 0.25K. The results show that with low rotational speeds, increasing the temperature gradient can help to control the bubble trajectories and their merging inside the cylinder.

This is because the greater the thermal gradient experienced by the bubbles, the greater the thermocapillary force exerted on the bubbles by the fluid. Results for a constant rotational speed of 0.6 rad/sec are shown in the right column of figure 7.15a-e. The corresponding thermocapillary Reynolds, Marangoni, and Rossby numbers and the resultant Y_{YGB} for 0.5 and 0.6 rad/s angular velocities are giving in table 7.4. In these figures at a constant angular velocity, the temperature is seen to advance the motion of the bubbles towards the centre of the cylinder. At low angular speeds, once the bubble reaches the middle of the cylinder, it is pushed further into the centre due to an increase in the temperature gradient. Both the rotational cases show that as the Ro increases, the bubbles move more consistently and their trajectory and agglomeration are dominated by the temperature gradient. In the earlier sections, it was proven that the bubble migration velocity varies linearly with the temperature gradient. Here, in the case of low rotational speeds, increasing thermal gradient causes the bubbles to move further in the radial and axial directions. This ascent due to Marangoni flow causes the bubbles to be pushed further towards the centre of the cylinder.

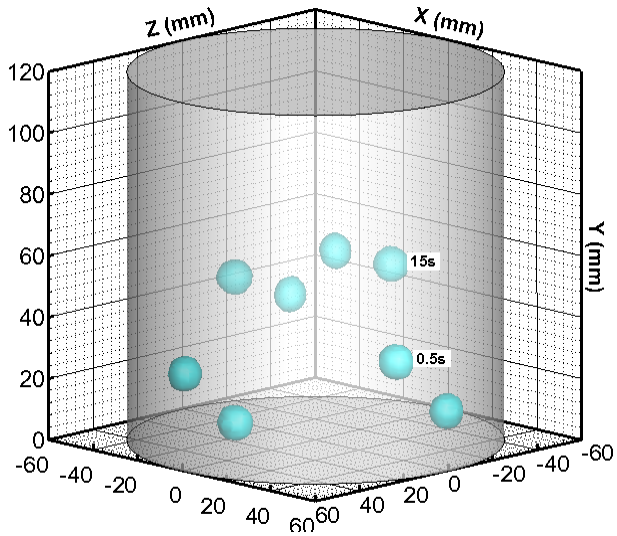

Figure7.14a Migration sequence of four bubbles when ∇T =0.083 K/mm and Ro=0.57 at ω=0.5rad/s

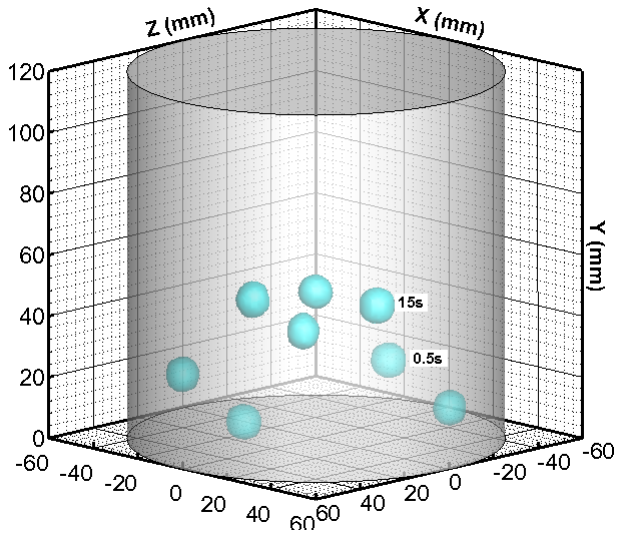

Figure7.15a Migration sequence of four bubbles when ∇T =0.083 K/mm and Ro=0.48 at ω=0.6rad/s

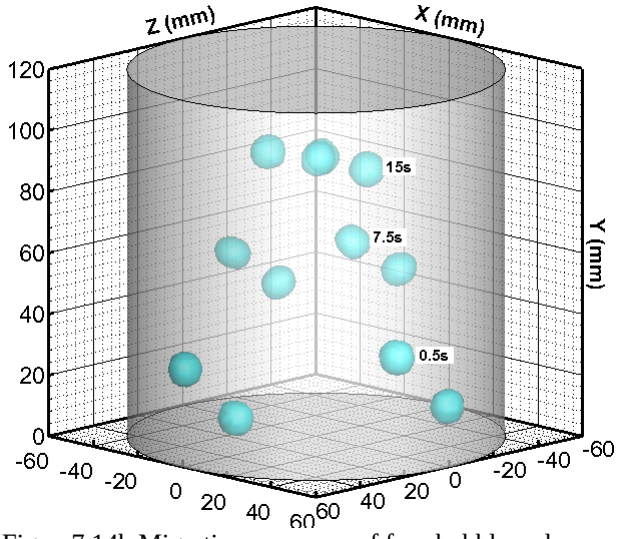

Figure7.14b Migration sequence of four bubbles when T=0.125K/mm, and Ro=0.86 at ω=0.5rad/s

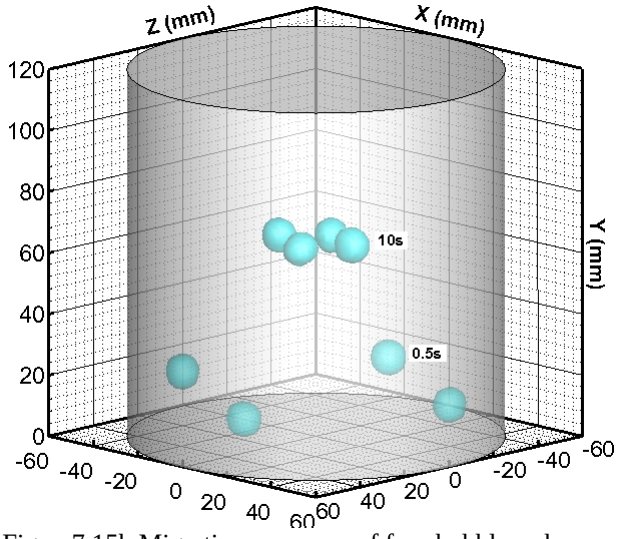

Figure7.15b Migration sequence of four bubbles when T=0.125 K/mm, and Ro=0.72 at ω=0.6rad/s

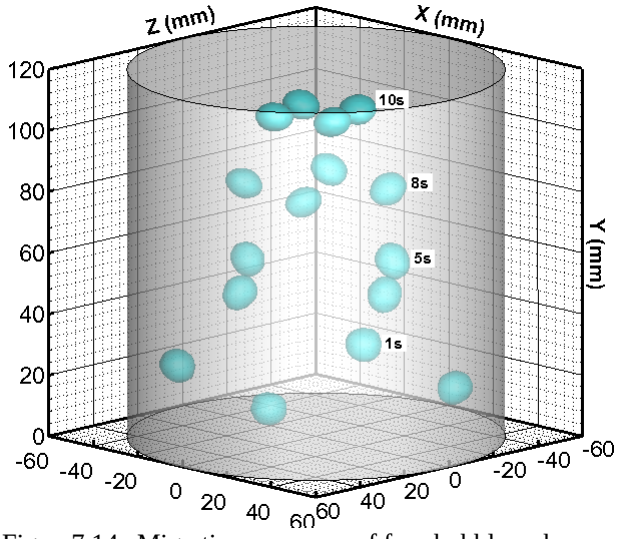

Figure7.14c Migration sequence of four bubbles when T=0.167 K/mm, and Ro=1.15 at ω=0.5rad/s

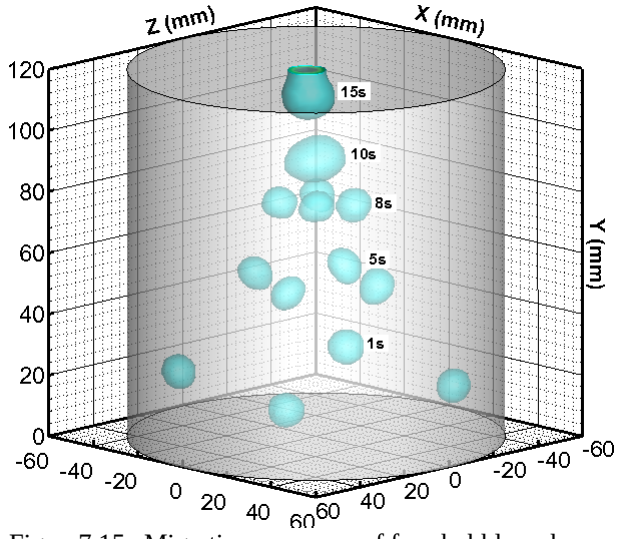

Figure7.15c Migration sequence of four bubbles when T=0.167 K/mm, and Ro=0.96 at ω=0.6rad/s

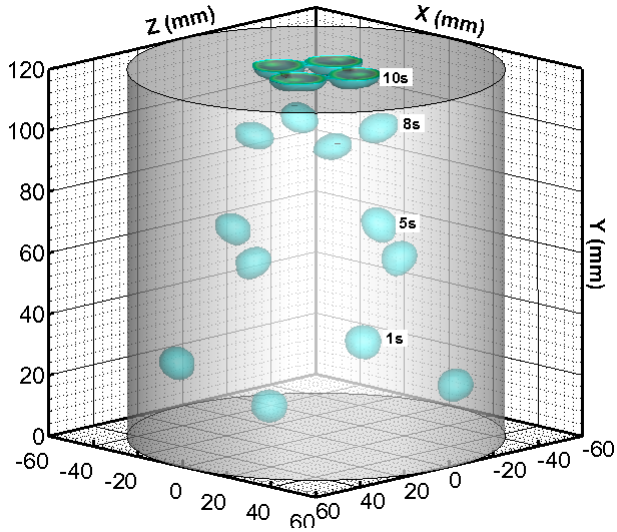

Fiture 7.14d migration sequence of four bubbles when T=0.208 K/mm, and Ro=1.4 at ω=0.5rad/s

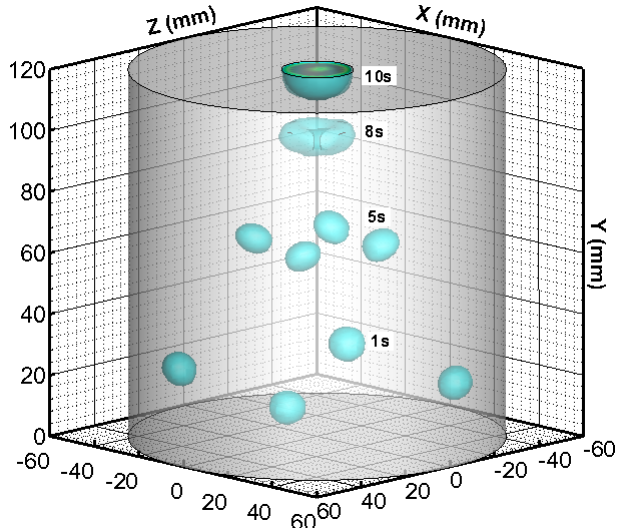

Figure7.15d Migration sequence of four bubbles when T=0.208 K/mm, and Ro=1.2 at ω=0.6rad/s

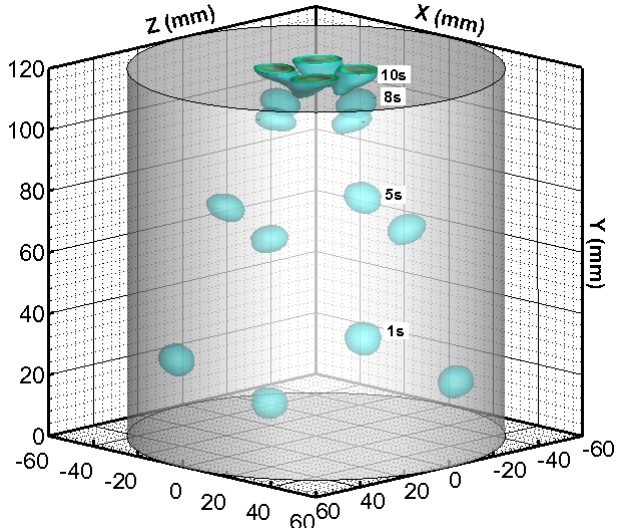

Figure 7.14e migration sequence of four bubbles when T=0.25 K/mm, and Ro=1.72 at ω=0.5rad/s

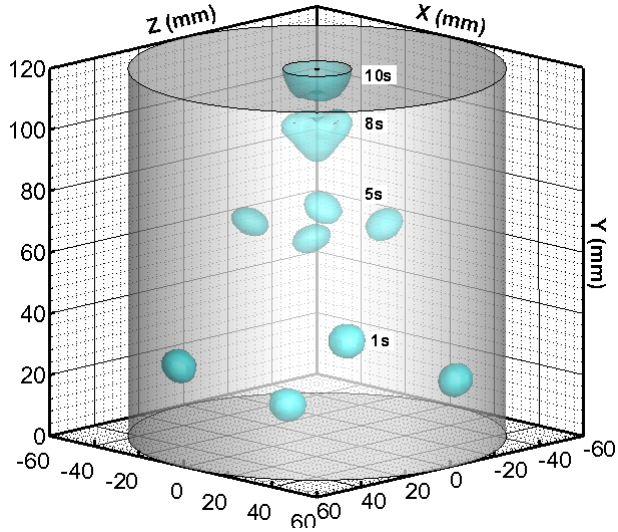

Figure7.15e Migration sequence of four bubbles when T=0.25 K/mm, and Ro=1.4at ω=0.6rad/s

Figure 7-14 and Figure 7-15 Comparison between ω = 0.5 rad/s and ω = 0.6 rad/sat five different temperatuer gradient

7.7 Coagulation of bubbles at varying distances from the axis of rotation

Different parameters have been changed in order to study different scenarios of bubble dynamics and coalescence in a rotating cylinder under zero-gravity conditions. In this section, simulations were carried out to investigate in detail the effect of bubble placement from the centre of the cylinder, as well as the impact of the position of the bubbles in relation to each other on the collision and agglomeration of a group of bubbles.

7.7.1 Single bubbles located at five different distances from the centre of a cylinder

The position of a collection of bubbles from the axis of rotation may have a major effect on their diverging and merging. In order to discover the effect of bubble distance from the centre of the cylinder, more than 40 fully three-dimensional cases for five different positions have been studied in this section, in order to identify the relationship between the distance and the diverging level, time, and merging process for eight rotational speeds.

Bubbles with a diameter of 10 mm were placed axially at a distance of one and a half times the diameter of the bubble from the lower surface of the cylinder (cooler region), and at X=10 to 50 mm in increments of 10 mm for each case in the radial direction. The size of the computational domain and the fluid parameters were kept the same as in the previous section. After steady state condition was achieved, the bubbles were patched against a constant temperature gradient of 0.208 K/mm and against each rotational speed from 0.25 to 2 rad/sec in increments of 0.25 rad/sec. Each Figure from 7.16to 7.23 presents the comparison of the five bubble positions at different angular speeds. The Ro numbers vary from each model to the next due to changes in radial position and (ω), as seen in each plot. Thermal Reynolds and Marangoni numbers were kept constant for all simulations at 257 and 4188 respectively. The Rossby number (Ro), assumed as ω=0.25 rad/sec for the five positions shown in Figure7.16, was between 2.87 and 14.3. The plot shows no oscillating regime for any Rossby numbers in this range, which confirm the previous results obtained in this chapter. In the next Figure 7.17, related to ω=0.5 rad/sec, the spiral regime appears for the first time when a single bubble was placed at a distance of between 40 and 50 mm from the Y- axis, which is equivalent to Rossby numbers of 1.4-1.8 respectively. For ω=0.75 rad/sec in Figure7.18, the bubbles spiral around the Y-axis after 2 seconds and show similar behaviour with a slight difference in time, as shown in Figures 7.18 to7.23. As the angular rotational rate was increased, the bubble(s) reached the Y-axis in a shorter time. The results show that the

maximum looping around the Y-axis occurs at x=-16.6 when ω=0.5 rad/sec and the bubble is in a position of 50 mm from the axis. For the same bubble position and for ω=2 rad/sec, the looping was shorter and the bubble tends to move faster toward the Y-axis. This indicates that at a higher angular speed, the bubble tends to settle on the axis of rotation. These calculations can also be used to estimate the typical time required for the bubble to reach the axis.

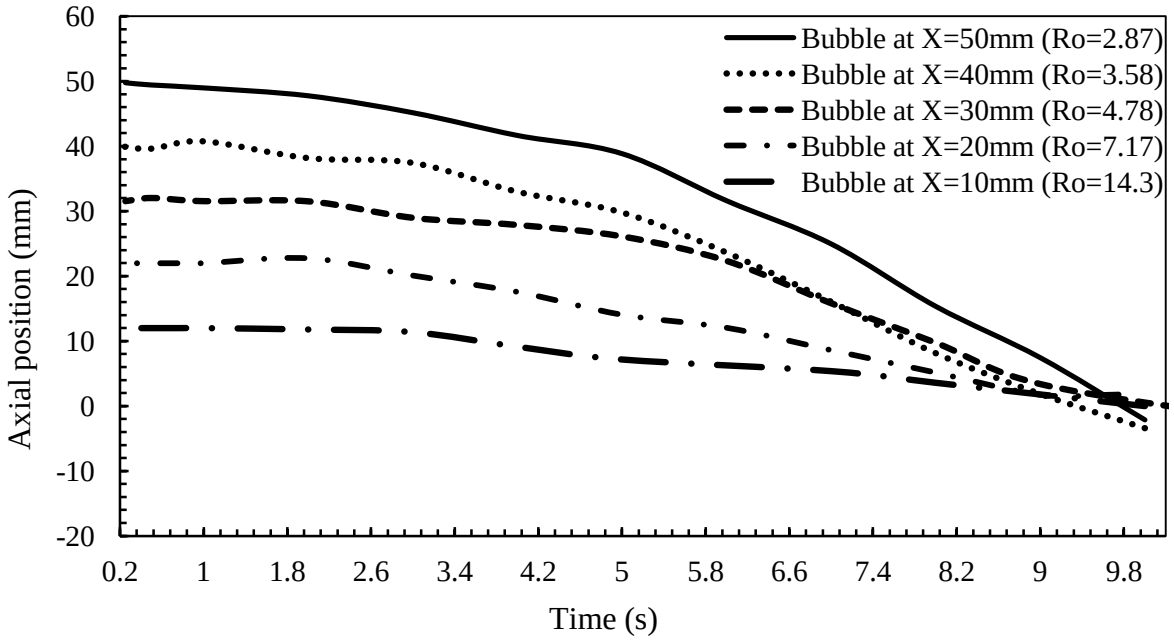

Figure 7-16 Computed results of the bubble released from the five positions (ω=0.25 rad/sec)

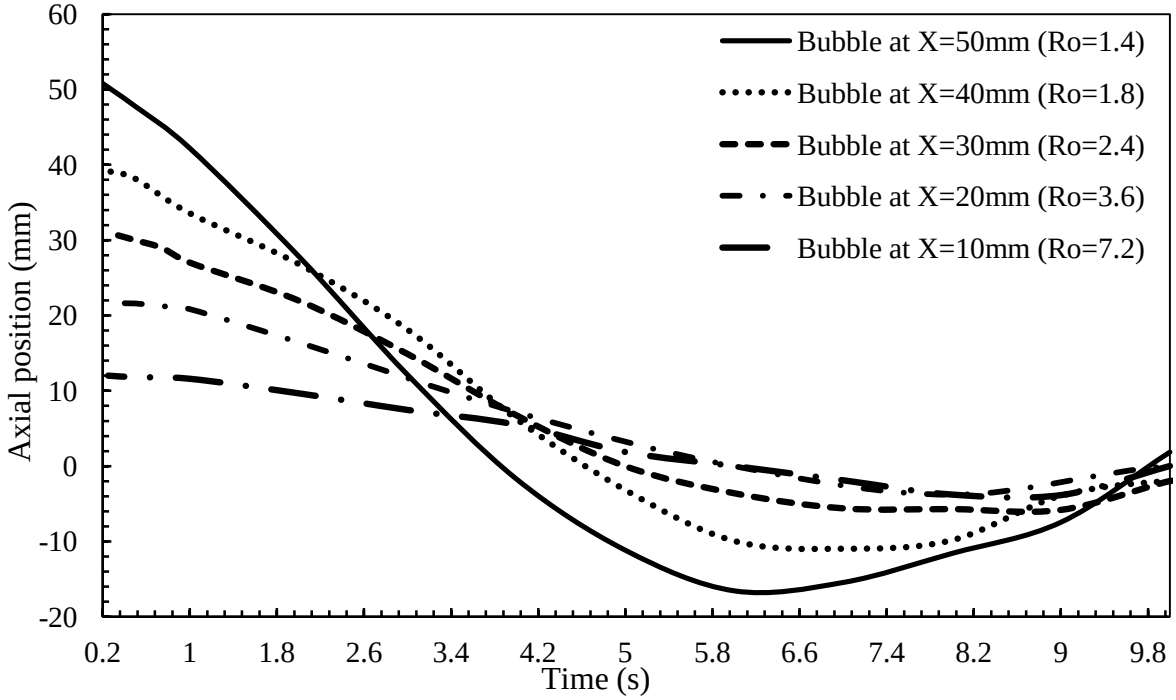

Figure 7-17 Computed results of the bubble released from the five positions (ω=0.5 rad/sec)

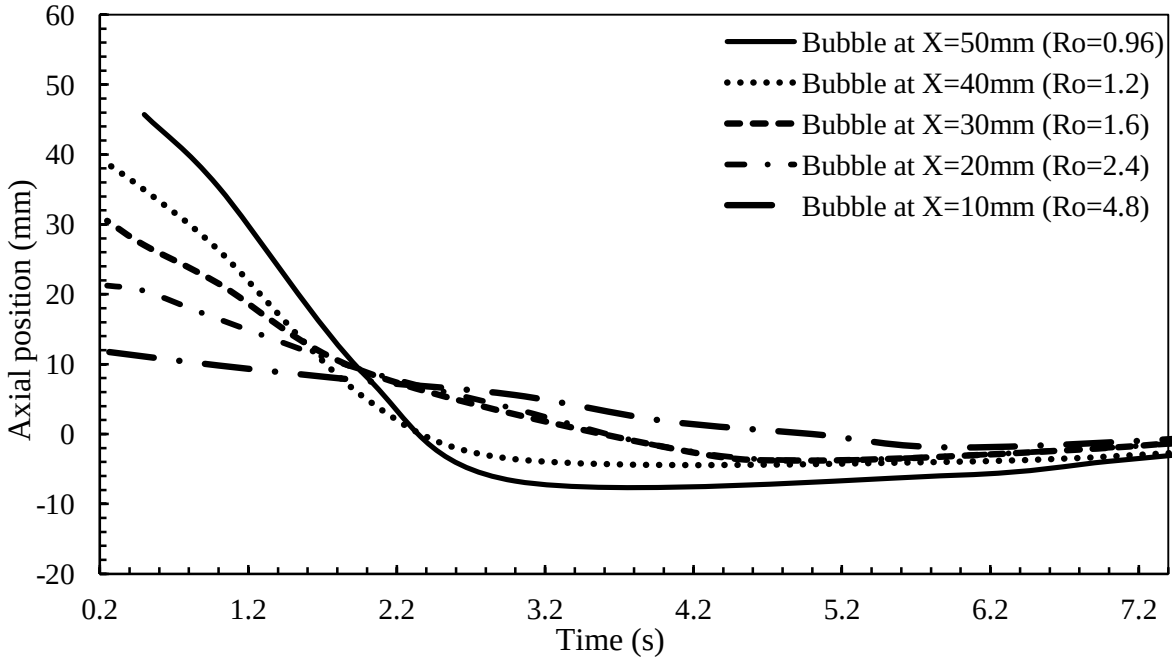

Figure 7-18 Computed results of the bubble released from the five positions (ω=0.75 rad/sec)

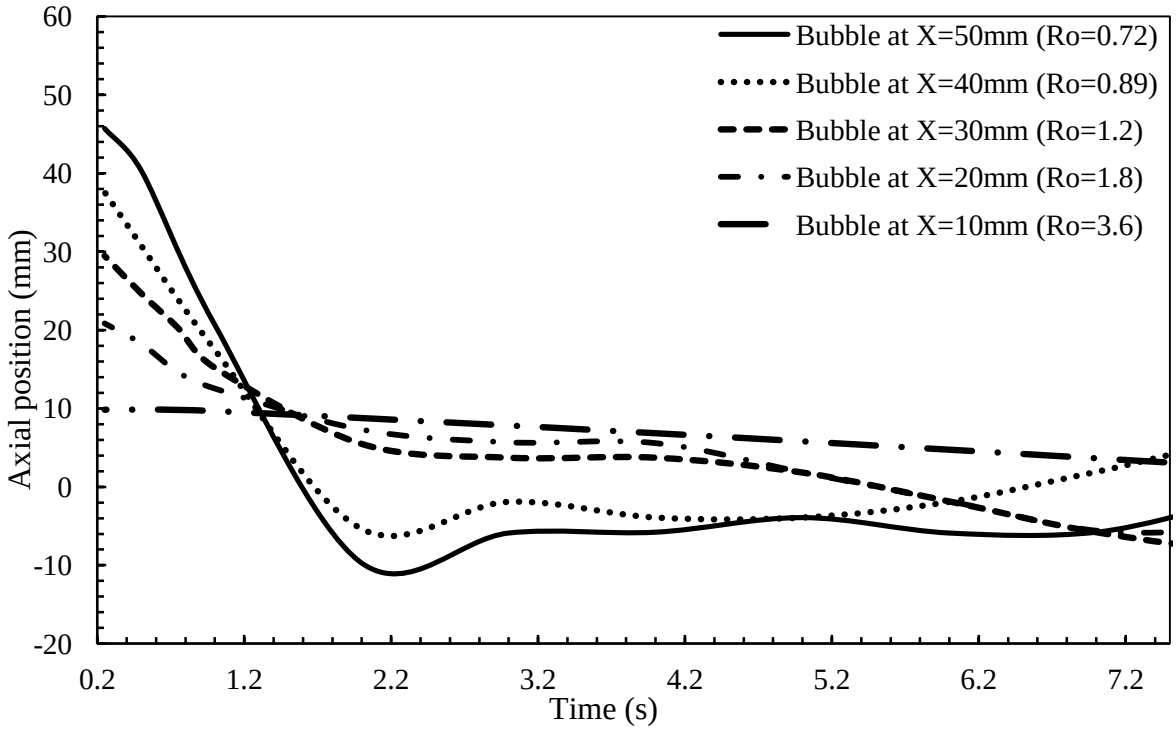

Figure 7-19 Computed results of the bubble released from the five positions (ω=1 rad/sec)

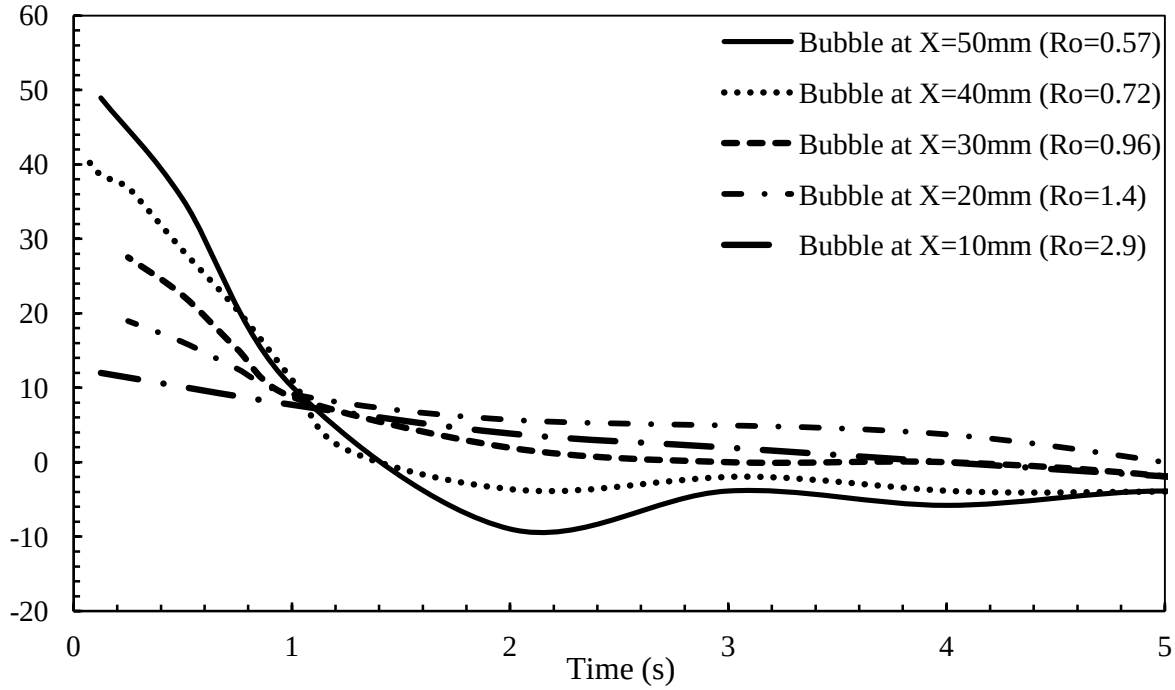

Figure 7-20 Computed results of the bubble released from the five positions (ω=1.25 rad/sec)

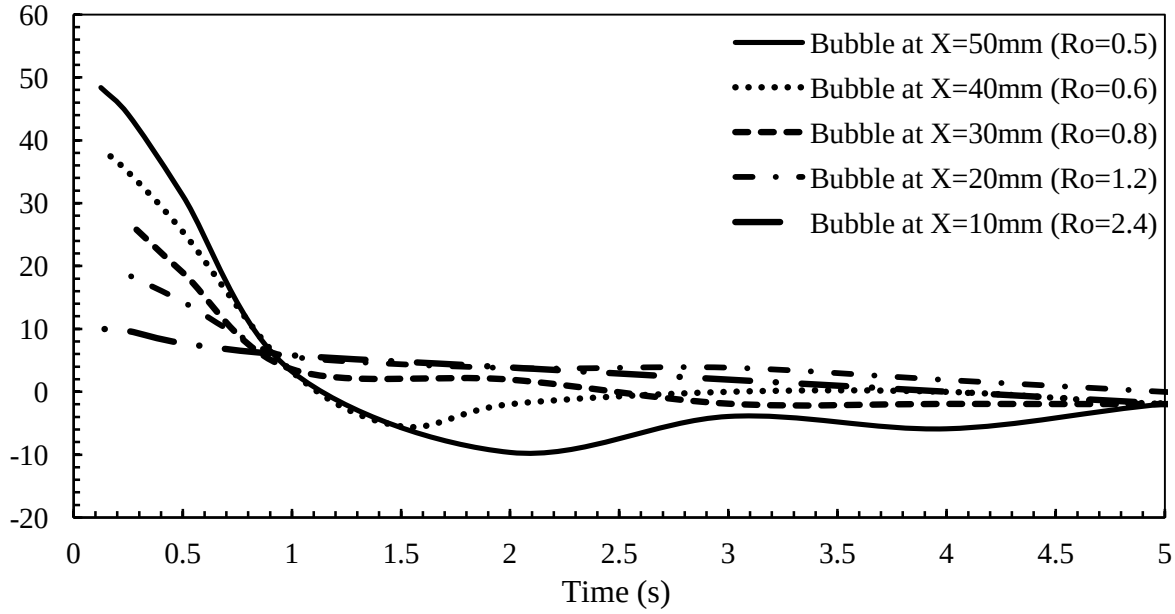

Figure 7-21 Computed results of the bubble released from the five positions (ω=1.5 rad/sec)

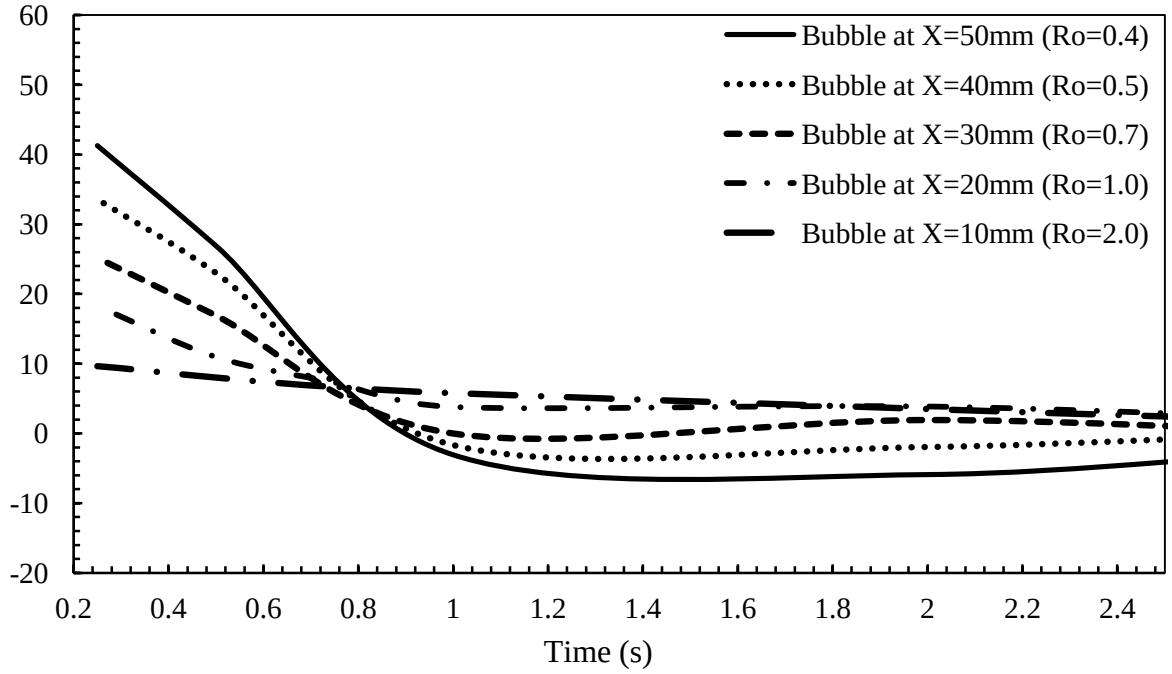

Figure 7-22 Computed results of the bubble released from the five positions (ω=1.75 rad/sec)

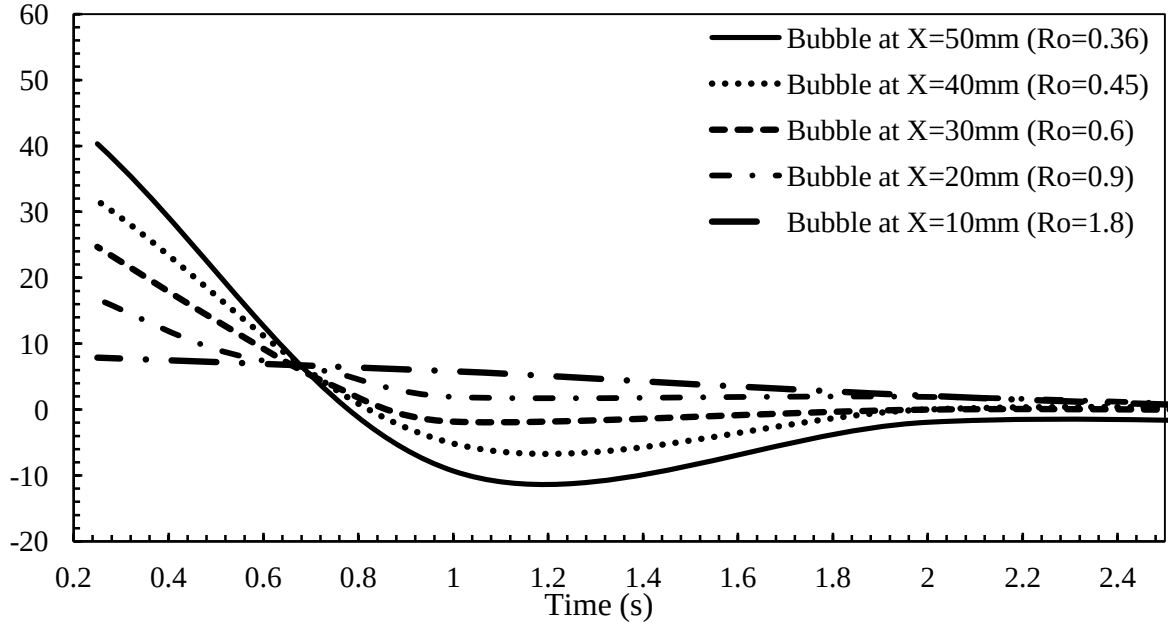

Figure 7-23 Computed results of the bubble released from the five positions (ω=2 rad/sec)

7.7.2 Multiple bubbles located side by side along the radial plane

Nine bubbles with a diameter of 10 mm were placed axially at a distance of one and a half times the diameter of the bubble from the lower surface of the cylinder (cooler region). The cylinder height and diameter measured 120 mm x120 mm, rotating at 0.5 rad/sec in the first calculation and 0.6 rad/sec in the second calculation. The chosen liquid had a Prandtl number of 16.28. The first group of bubbles contained 4 bubbles located at 2d from the bubble in the centre, and the second group contained the same number of bubbles located at 4d from the centre on the X-Z planes. In this section, two rotational speeds (ω=0.5 rads/sec and 0.6 rads/sec) were applied to the cylinder to observe the behaviour of 9 bubbles. The results show that for the first angular speed (0.5 rad/sec) the inner four bubbles (first row) collide and agglomerate with the bubble in the centre of the cylinder in a time of 6 seconds, while the outer group of bubbles (second row) rotate around the axis of rotation. The higher centrifugal force, as seen in the second case for ω=0.6 rad/sec, caused the bubbles to agglomerate in a shorter time and more closely to the lower surface as seen in figures 7.24 and 7.25 .

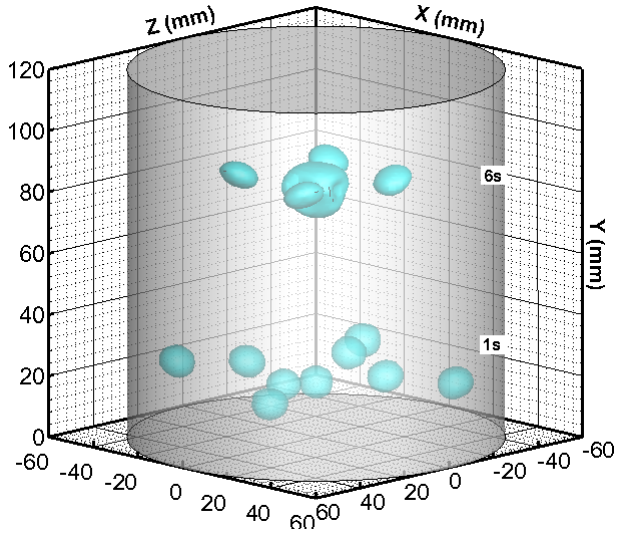

Figure 7-24 Two migrating time for nine bubbles located side by side (ω=0.5 rad/sec)

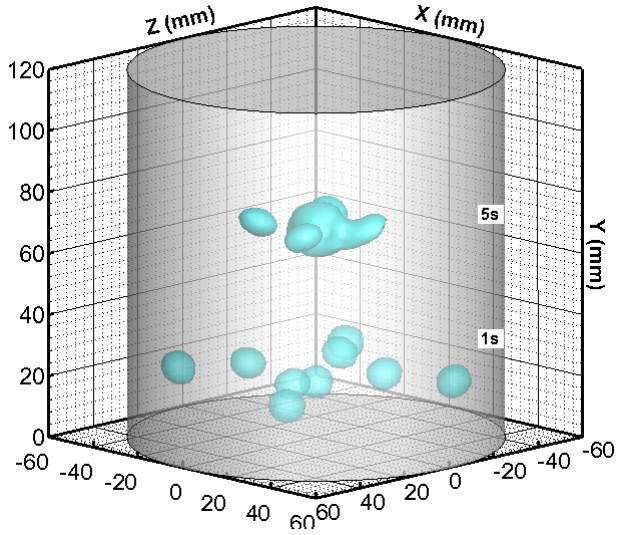

Figure 7-25 Two migrating time for nine bubbles located side by side (ω=0.6 rad/sec)

7.7.3 Group of bubbles located above the second row

In order to further investigate the effect of bubble position and angular speed on the bubbles' dynamics and agglomeration, a simulation of two groups of bubbles placed above each other is carried out in this section. The two groups consisted of eight bubbles of equal diameter (10 mm) located at a distance of 50 mm from the axis of rotation and 90 mm apart from each other in the angular direction. The first group, containing four bubbles, was placed axially at a distance of one and a half times the diameter of a bubble from the lower surface and the second group at a position of 1.5d from the first group on the axial direction. The size of the computational domain and the fluid parameters were kept the same as in previous sections. Upon steady state condition being reached, the bubbles were patched against a temperature gradient equal to 0.208 K/mm and a rotational speed of 0.5and 0.6 rad/sec for the first and second simulations respectively. A comparison of the results of the two different simulations is presented in Figures 7.26a-c and 7.27a-c. Figures 7.26a-c for ω=0.5 rad/sec show the same results as the previous section for a singular, pair, and group of bubbles under the same conditions. The two groups migrate in a straight line to the upper surface of the cylinder without intersecting. In Figures 7.26a-c for ω=0.6 rad/sec, the merging process of the two group took place just before they reached the top of the cylinder. The results show that large numbers of bubbles could be compounded inside the cylinder to form a larger bubble. The behaviour of the bubbles in both simulations is also similar to the results from the same conditions studied in previous sections. By comparing the migration time between the two simulations, we find that the bubbles with higher angular velocity (0.6 rad/sec) reached the surface faster. However, for the same simulation conditions, velocities higher than 0.6 rad/sec will tend to increase the bubble migration time. The results obtained from this section can explain the angular velocity required to merge bubbles inside the cylinder without reducing their migration speed.

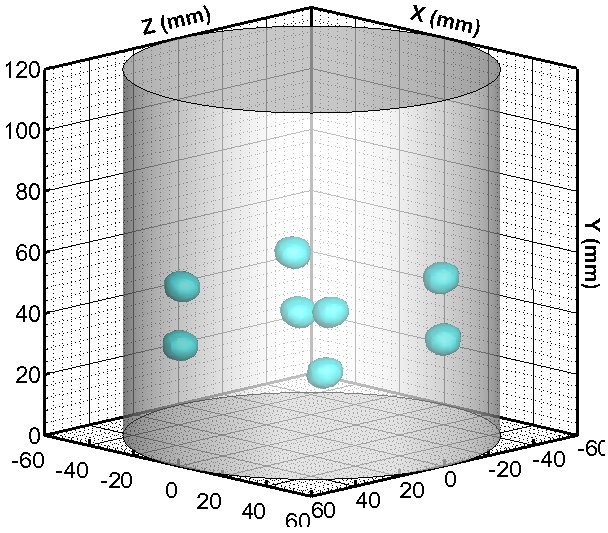

Figure7.26a Migration time=2 s

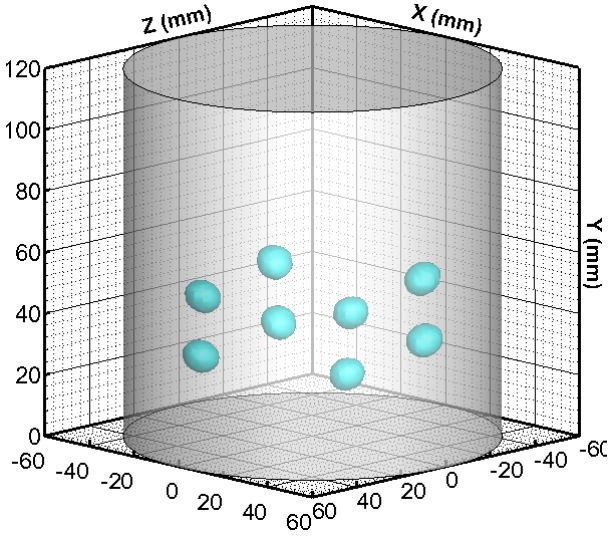

Figure7.27a Migration time=2 s

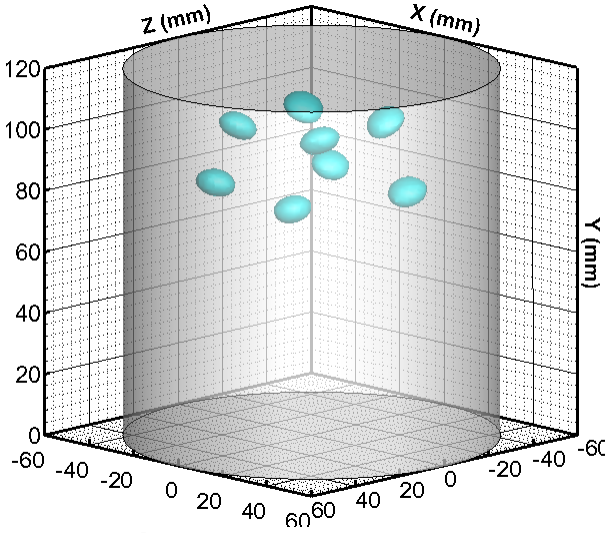

Figure7.26b Migration time=6 s

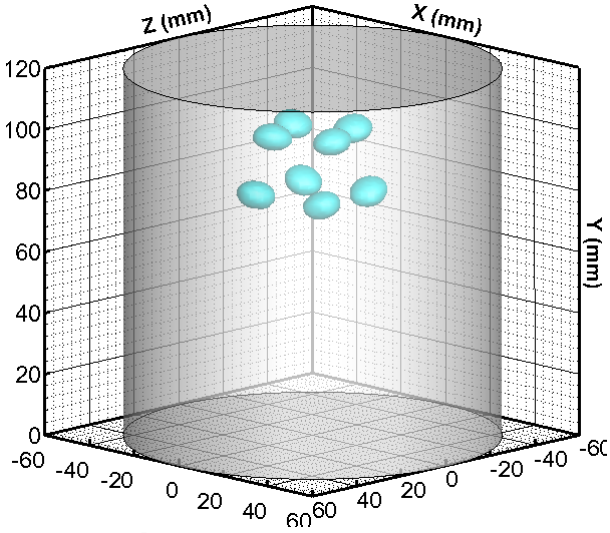

Figure7.27b Migration time=6 s

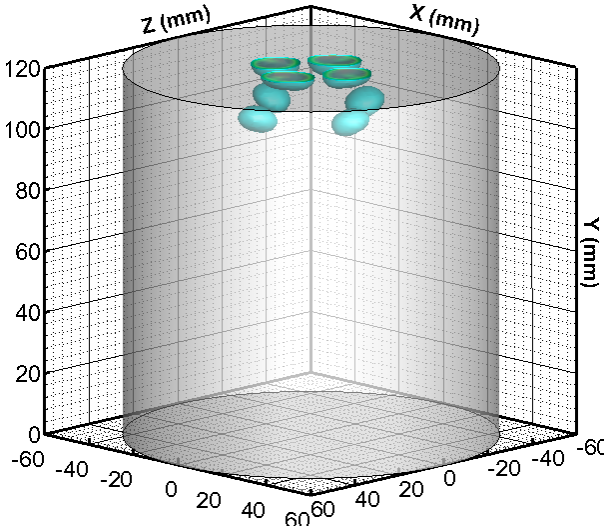

Figure7.26c Migration time=8 s

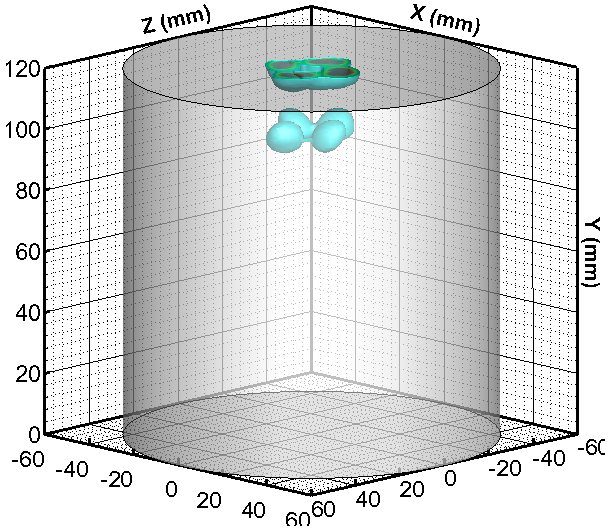

Figure7.27c Migration time=8 s

Figure 7-26a-c The interaction of eight bubbles at a selected time for ω=0.5 rad/s

Figure 7-27a-c The interaction of eight bubbles at a selected time for ω=0.6 rad/s

7.8 Coagulation of bubbles of various sizes

The results presented in Figures 7.28a-c and 7.29a-c show a comparison of two cylinders each containing 4 bubbles of equal diameter located at a distance of 50 mm from the axis of rotation and 90 mm apart from each other in the angular direction. The cylinder measured 120 mm in diameter and rotated at an angular velocity of 0.5 rad/sec, filled with a liquid with a Prandtl number of 16.28. The temperature was 300 K at the lower surface for all cases and 325 K at the upper surface of the cylinder. For given conditions, the temperature gradient measured 0.0208 K/mm and thermocapillary Reynolds and Marangoni numbers were 257 and 4188 respectively. The computed results in this section compare two bubble diameters migrating under the same conditions. The two bubble diameters were 10 and 11mm for the first and second simulation respectively. The bubbles were placed axially at a distance of one and a half times the diameter of the bubble from the bottom of the cylinder (cooler region). In the time sequence shown in Figures 7.28a-c, no merging process was observed for bubbles with a size of 10 mm and all four bubbles reached the top wall without coalescing. On the other hand, the merging occurred at the top of the cylinder and at the time (t)=8s for the bubbles with diameter equal to 11 mm, as seen in the time sequence in Figure7.29a-c. These two figures show the possibility of controlling bubble agglomeration by adjusting the angular velocity.

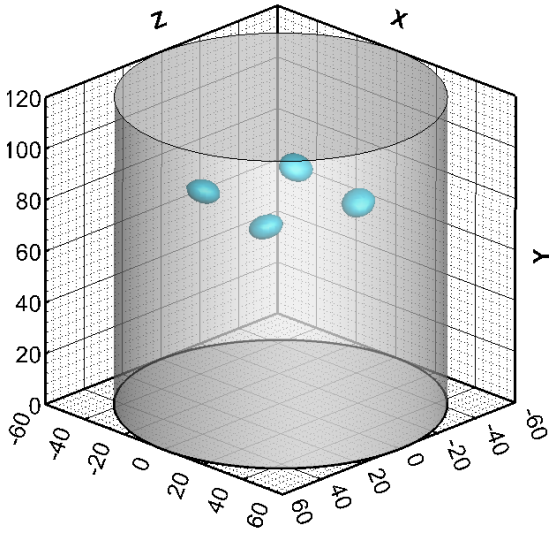

Figure7.28c Migration time= 6 s

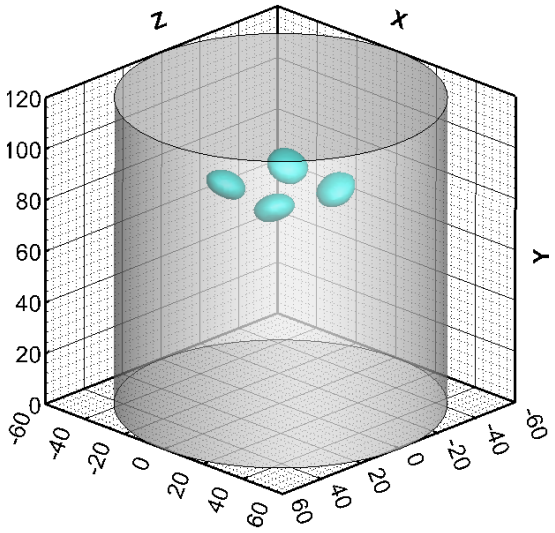

Figure7.29c Migration time= 6 s

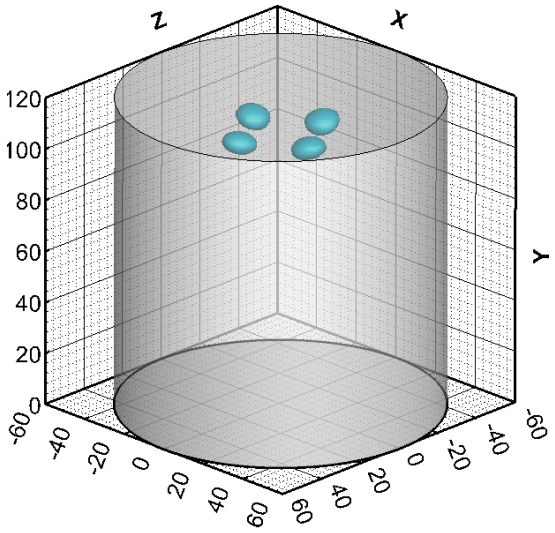

Figure7.28c Migration time= 8 s

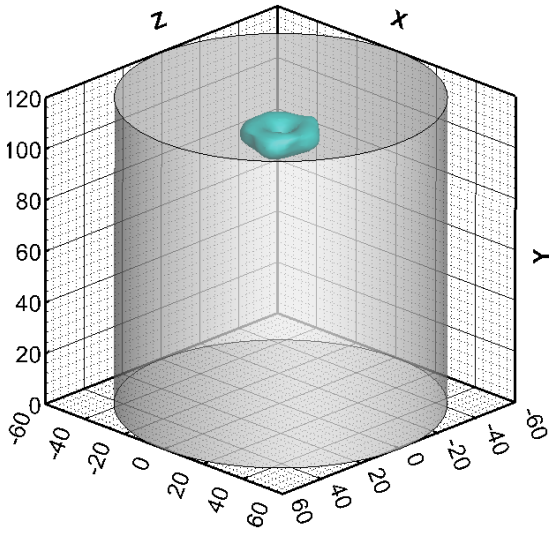

Figure7.29c Migration time= 8 s

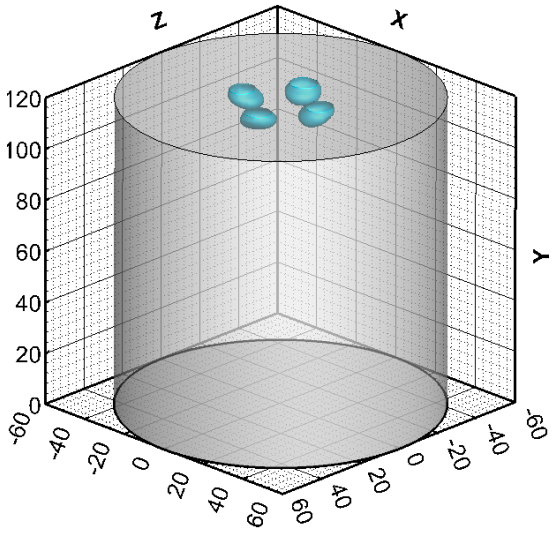

Figure7.28c Migration time= 9 s

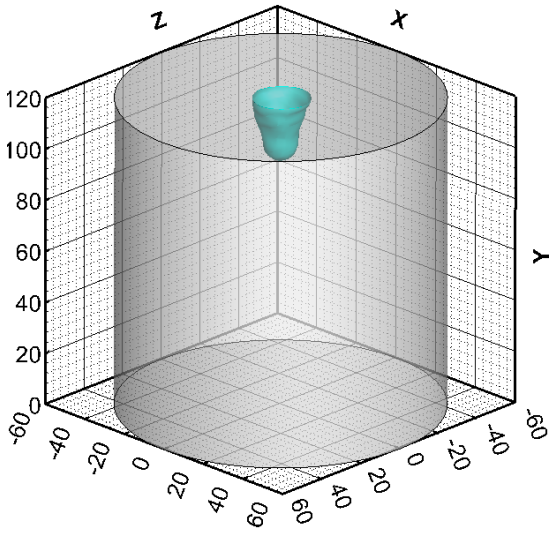

Figure7.29c Migration time=9 s

Figure 7-28a-c Bubble diameter=10 mm

Figure 7-29a-c Bubble diameter=11 mm

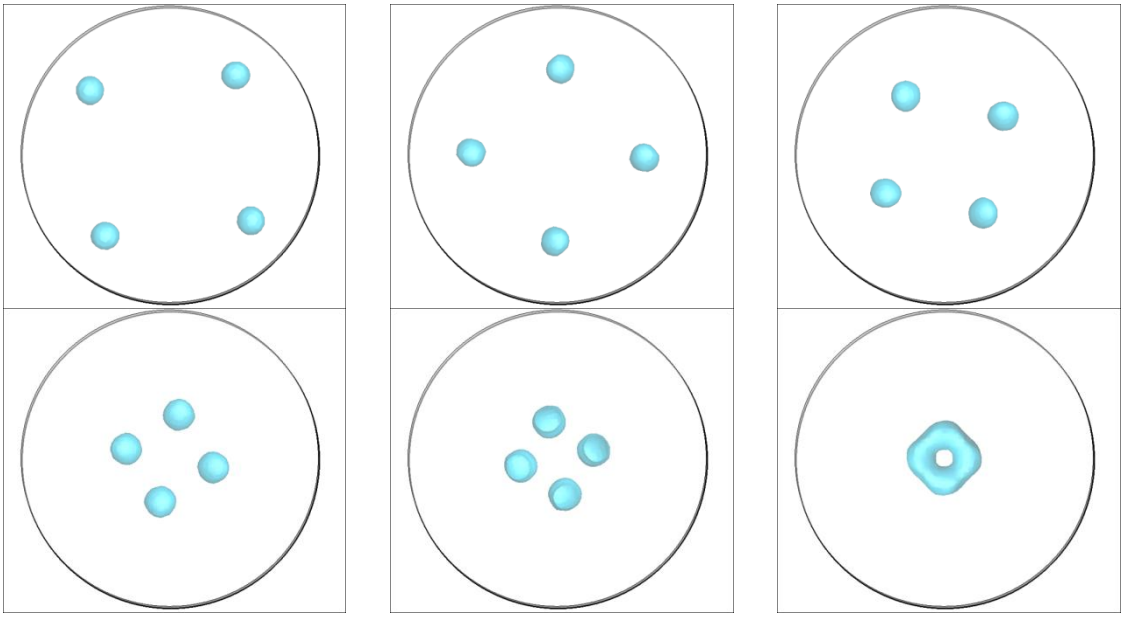

Figure 7-30 Top view of the migration and agglomeration of four bubbles with diameter =11 mm

7.8.1 Simulation of heterogeneous bubble sizes in a single cylinder

Finally, in order to further confirm that the merging process is affected by the diameter of the bubbles involved, a simulation of four different bubble sizes were carried out in a single cylinder at the same time. The diameters of the bubbles measured 9, 10, 11 and 12 mm and the bubbles were located at a distance of 50 mm from the axis of rotation and 90 mm apart from each other in the angular direction. The bubbles were placed axially at a distance of one and a half times the diameter of the bubble from the base of the cylinder (cooler region). The size of the computational domain and the fluid parameters were kept the same as in the previous sections of the study, and the bubbles were patched after obtaining the steady state condition against a constant temperature gradient of 0.208 K/mm and a rotational velocity of 0.5 rad/sec. The bubble dynamics in Figures 7.31a-b are similar to those of the bubbles with equal diameters and the same flow conditions. The results show that the bubbles migrate with equal space between them towards the centre and the hotter side of the cylinder, while maintaining a steady state velocity. The plots in Figures 7.32 and 7.33 show that bubbles with a larger diameter reached the axis of ration and the warmer side faster than those with smaller

diameters. On the other hand, the bubbles with smaller diameters exhibited a taller helix than the other bubbles in Figure7.34.

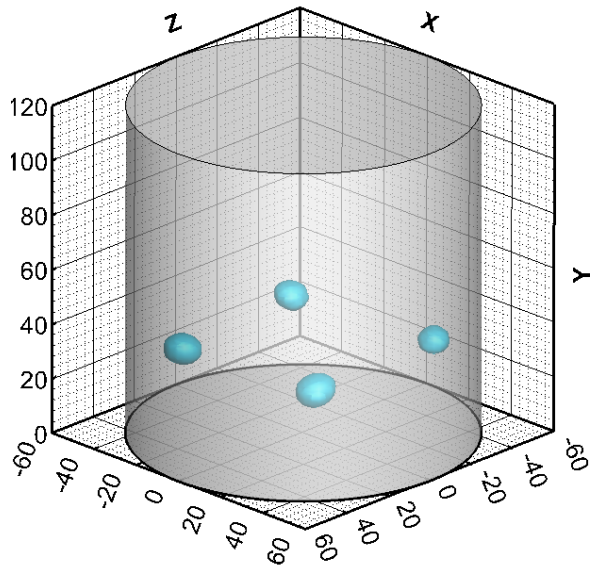

Figure 7-31a Time step=2 s

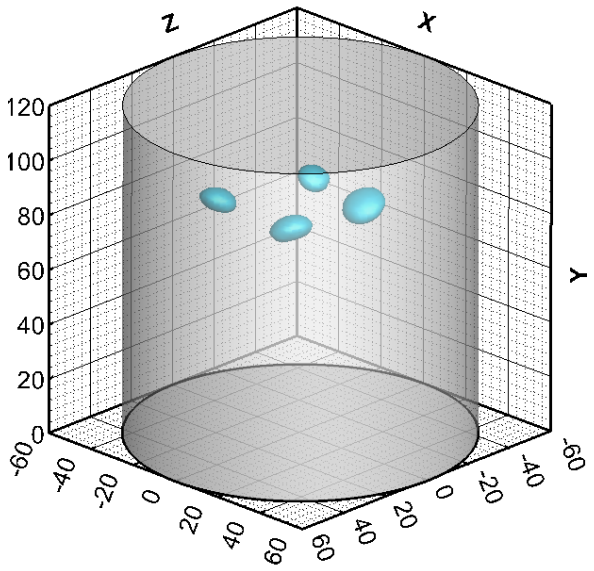

Figure 7-31b Tme step=6 s

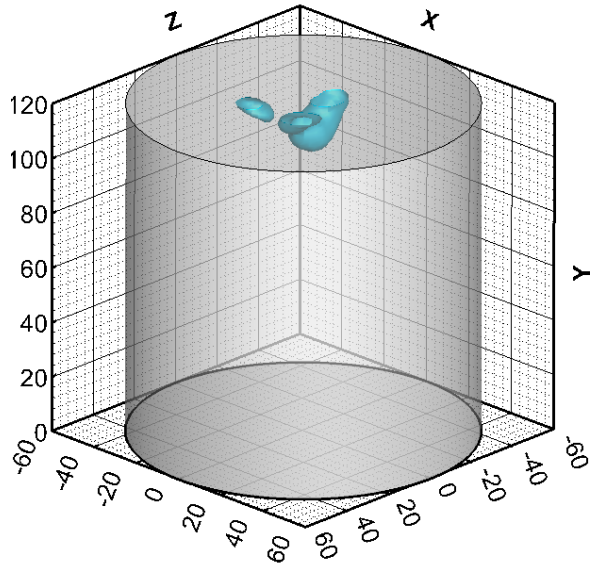

Figure 7-31c Time step=10 s

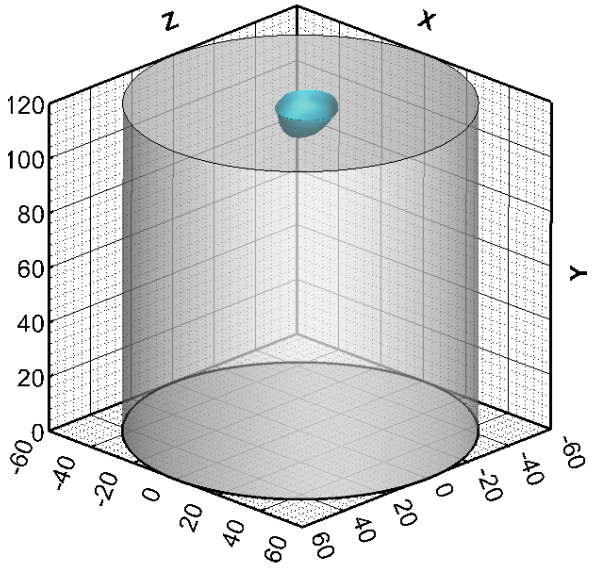

Figure 7-31d Time step=14 s

Figure 7-31a-d Four snap-shot in time showing heterogeneous bubbles moving toward the warmer region

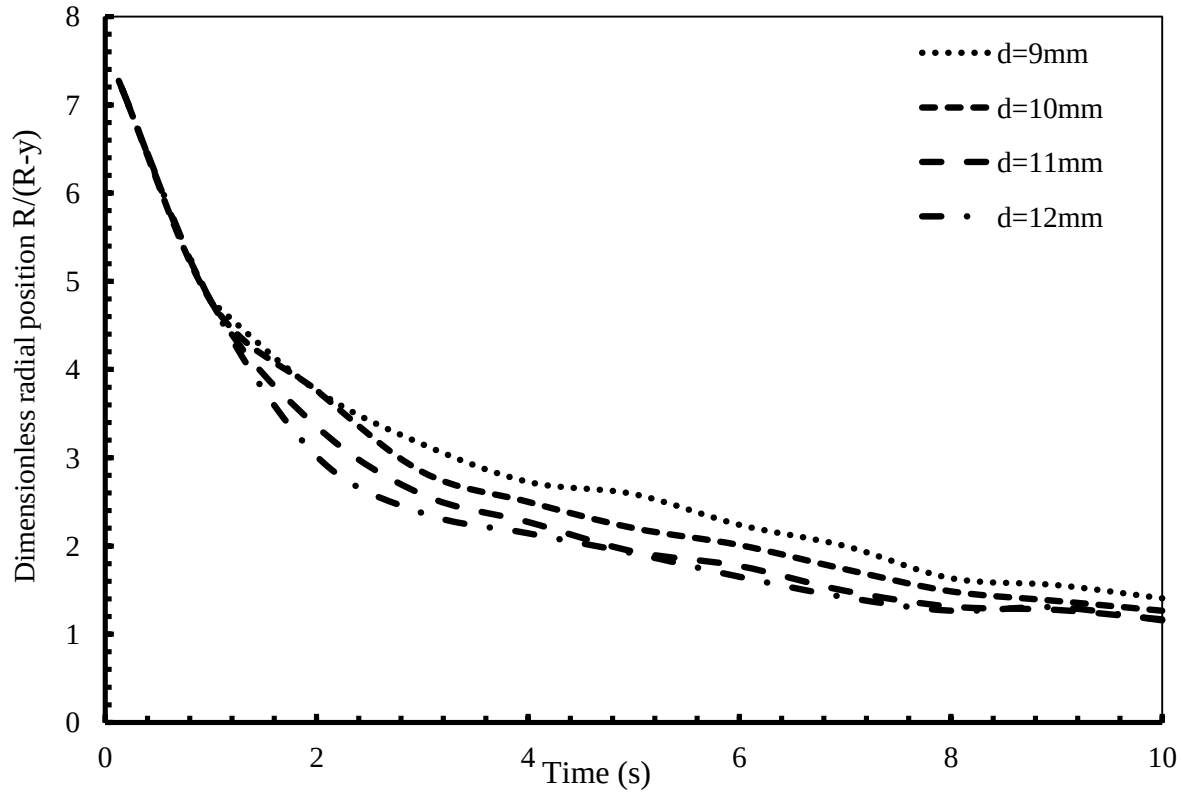

Figure 7-32 Dimensionless radial position for the four heterogeneous diameters versus time (s)

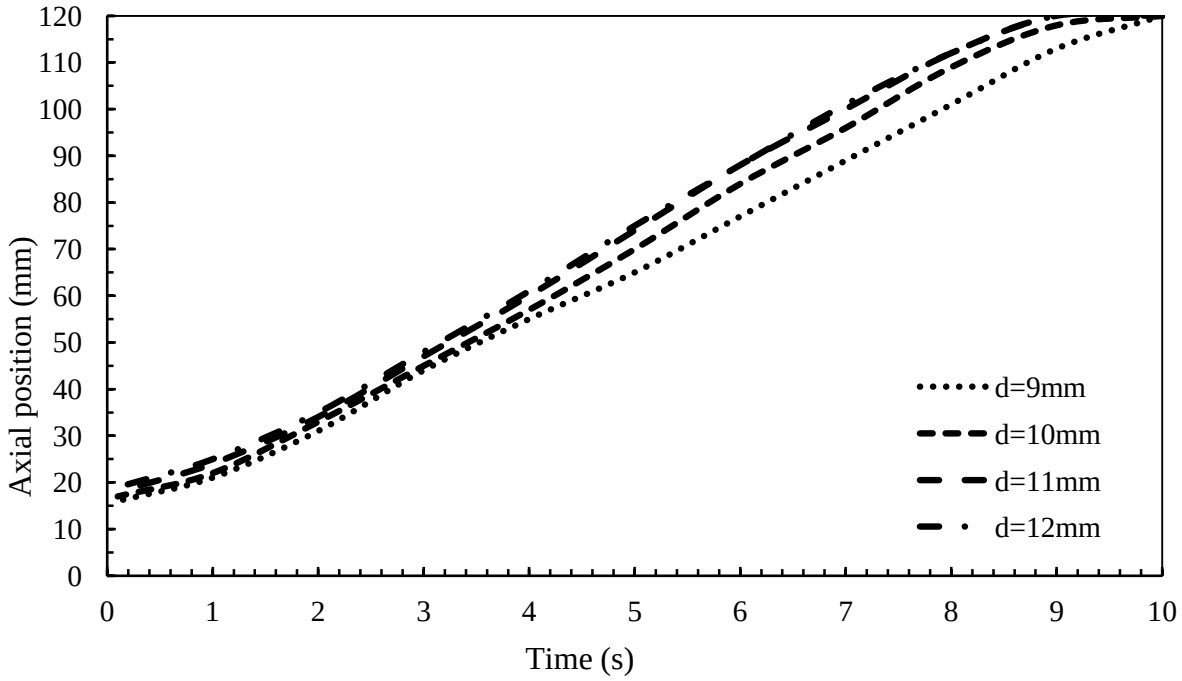

Figure 7-33 Displacement of the four bubbles towards the warmer region

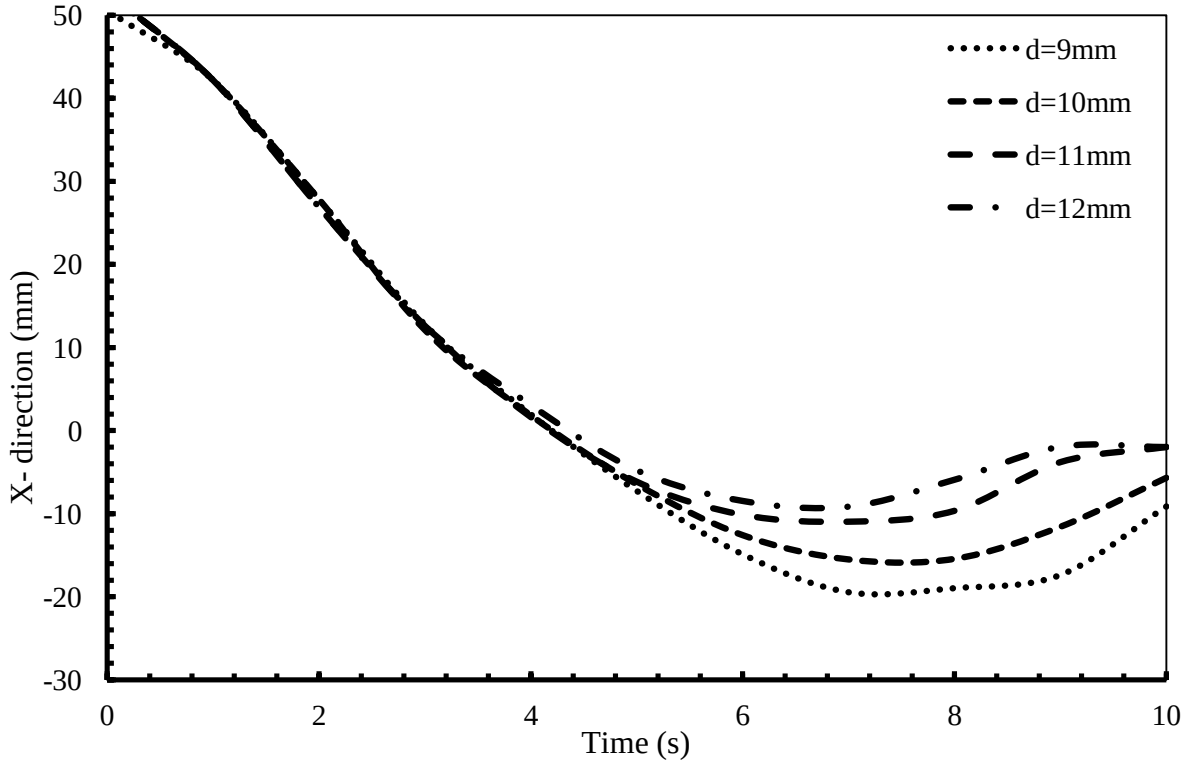

Figure 7-34 Plot of bubble motion around the axis of rotation

The final configuration can be explained by the fact that in order to simulate the merging process between bubbles, we apply angular velocity to the cylinder containing bubbles. This rotational rate forces the bubbles to move closer to the axis of rotation, leading to coalescence. For similar conditions and fluid properties given in this chapter, at a small angular velocity of $\omega = 0.5$ rads^{-1}, the gas bubbles tend to merge in the upper area of the cylinder. However, as the angular velocities increase ($\omega = 0.6$ rad/sec), the coalescence shifts, occurring in the lower part of the cylinder. This implies that controlling the bubble coalescence and manipulation is possible by controlling the rotational rate of the cylinder, which was illustrated by figures and plots throughout this chapter. In order to describe a bubble rising in a rotating cylinder under the effect of surface tension gradient in zero gravity, the ratio of inertia force to Coriolis force is given by the dimensionless Rossby number:

$$Ro = \frac{V_{YGB}}{R\omega} = \frac{V_{YGB}}{V_{\omega}}$$

where V_{YGB} is the thermocapillary bubble velocity in zero gravity, which can be calculated from Eq.2-1 and V_{ω} is the rotational or angular velocity given as $V_{\omega} = \omega R$. From the results of this report, one can see that if the Rossby number is larger than 1.0, i.e. if the angular velocity is slower than the thermocapillary bubble velocity, the bubble deflection towards the axis of rotation is small, due to minimal rotational effects. On the other hand, for Rossby numbers of less than 1.0, the bubble motion is significantly affected by the rotation rate, and the amount of deflection (in relation to the size of the cylinder) increases further towards the axis of rotation. This suggests that the Coriolis forces have minimal contribution to the agglomeration of the bubbles when the Rossby number is substantially greater than one. On the other hand a bubble's trajectory and coalescence will be significantly affected when the Rossby number is much less than unity:

$$\text{Rossby number } (Ro) = \frac{inertial}{Coriolis} \approx 1 \Rightarrow \text{Coriolis dominant}$$

7.9 Conclusion

The results for motion of a singular and multiple bubbles incorporating thermocapillary forces in a rotating liquid in a zero-gravity environment have been presented for the first time. When the Rossby number ≥ 1, the effects of rotation are important. Furthermore, the deflection of the gas bubble motion increases towards the axis of rotation with a decrease in the Rossby number (Ro). On the other hand for a stationary cylinder, the thermocapillary migration of two bubbles was found to move in a linear fashion. This shows that the coalescence rates could be improved by operating the cylinder at lower mechanical rotation rates. As can be seen from the results, centrifugal and Coriolis forces are an example of external phenomena that may be used to control bubble agglomeration in zero gravity. Furthermore rotation can play an important role in the dynamics and collision of bubbles in zero-gravity conditions. Different flow patterns such as thermocapillary bubble migration, stream function, and thermal gradients were observed for the 2-D and 3-D models under the effect of zero gravity. It was found that the flow pattern transitions appeared as a result of the temperature gradient and the angular velocity rates. Since zero gravity is difficult to achieve in a laboratory setting, one can demonstrate the relevant phenomena using numerical simulations. It also allows one to study sensitivity effects regarding different parameters. It may be concluded that VOF is a robust numerical method for the simulation of gas-liquid two-phase flows with high-density ratios. With computer simulations proving their worth as a valuable tool to study the complex problems under the conditions of zero gravity, and from the results of this chapter one can assess the credentials of modelling to simulate realistic 3-D Marangoni cases.

Chapter 8 : Bubble Population Balance Modelling in Normal and Zero Gravity

8.1 Introduction

The size distribution of the bubbles plays a critical role in mass transfer and reactions that may occur between the any two phases. Detailed knowledge about the bubble-bubble interaction is of great importance for improving bubble contact and increasing efficiency of the bubble column. The operation of bubble-bubble interaction in bubble column reactors is affected by different operating parameters such as initial boundary conditions of the two phases (gas and liquid) as well as outside forces such as column rotation, vibration, pulsation...etc. Hence resolving the bubble size distribution is an important task in the CFD analysis of bubble column reactors. Population balances is the most frequently used modelling tool to investigate the large size distribution of the dispersed gas bubble and accounting for the break-up and coalescence effects in bubble column flows. An extensive review of the application of population balances to particulate systems in engineering is given by Ramkrishna (2000). Bubbles usually flow in a large number of groups and all the data of previous calculations have been carried out for single and a small group of bubbles using the VOF model. Bubble population balance equation (BPBE) in the Euler–Euler computational fluid dynamics (CFD) representation is used to assess the effect of inlet gas velocity on the bubble collision and agglomeration. The implemented population balance models (PBM) will also be used to perform 2D axisymmetric simulations of air bubbles flow in a rotational column to investigate the possibility of using a rotating cylinder for bubble population modelling under both normal and zero gravity. The implemented population balance models (PBM) in a CFD Eulerian-Eulerian model of air-water bubble column flows will be validated with the experimental data of Degaleesan et al. (2001) and the population balance simulations performed by Chen et al. (2005). The validated PBM code will also be subjected to grid

dependency checks before the final set of calculations. The investigation of air bubbles flow under zero gravity will be carried out based on the details of the bubble-bubble interaction for rotating cylinders given by the previous calculations (results presented in the last few chapters).

8.2 Numerical Methodology

The discrete method was developed by Hounslow et al. (1988) , Litster et al. (1995), and Ramkrishna (2000). It is based on representing the continuous particle size distribution (PSD) in terms of a set of discrete size classes or bins. In the current solver Population Balance Modelling Equations (PBE) are written in terms of volume fraction of particle size *i*:

$$\frac{\partial}{\partial t}(\rho_s \alpha_i) + \nabla.(\rho_s u_i \alpha_i) + \frac{\partial}{\partial V}\left(\frac{G_v \rho_s \alpha_i}{V}\right) = \rho_s V_i (B_{ag,i} - D_{ag,i} + B_{br,i} - D_{br,i}) + 0^i \rho_s V_0 \dot{n}_0 \quad 8\text{-}1$$

where ρ_s is the density of the secondary phase and α_s is the volume fraction of particle size *i*, defined as

$\alpha_i = N_i V_i$ (*i*=0, 1 ...N-1)

where

$$N_i(t) = \int_{V_i}^{V_{i+1}} n(V,t)dV \quad 8\text{-}2$$

and V_i is the volume of the particle size i. For the simulations, a fraction of α called f_i is introduced as the solution variable. This fraction is defined as

$$f_i = \frac{\alpha_i}{\alpha} \quad 8\text{-}3$$

where α is the total volume fraction of the secondary phase. The nucleation rate $\dot{n}_0$ appears in the discretized equation for the volume fraction of the smallest size V_0. The notation 0^i signifies that this particular term ($\rho_s V_0 \dot{n}_0$) appears in Equation 8-1 only in the for the

smallest particle size. The growth rate in Equation (8.1) is discretized as follows (PBM-Manual, 2011)

$$\frac{\partial}{\partial V}\left(\frac{G_v \rho_s \alpha_i}{V}\right) = \rho_s V_i \left[\left(\frac{G_{v,i-1} N_{i-1}}{V_i - V_{i-1}}\right) - \right]\left(\frac{G_{v,i} N_i}{V_{i+1} - V_i}\right) \quad 8\text{-}4$$

The volume coordinate is discretized as $V_{i-1}/V_i = 2^q$ where q=1, 2,...and is referred to as the "ratio factor". The particle birth and death rates are defined as follows:

$$B_{ag,i} = \sum_{k=1}^{N}\sum_{j=1}^{N} a_{kj} N_k N_j \chi_{kj} \xi_{kj} \quad 8\text{-}5$$

$$D_{ag,i} = \sum_{j=1}^{N} a_{kj} N_i N_j \quad 8\text{-}6$$

$$B_{br,i} = \sum_{j=i+1}^{N} g(V_j) N_j \beta(Vi/Vj) \quad 8\text{-}7$$

$$D_{br,i} = g(V_i) N_i \quad 8\text{-}8$$

here $a_{kj} = a(V_i, V_j)$ and $\xi_{kj} = 1$ for $V_i < V_{ag} < V_{i+1}$ where $i < N-1$, otherwise =0

V_{ag} is the particle volume resulting from the aggregation of particles κ and j, and is defined as

$$V_{ag} = [\chi_{\kappa j} V_i + (1 - \chi_{\kappa j}) V_{i+1}] \quad 8\text{-}9$$

where

$$\chi_{\kappa j} = \frac{V_{ag} - V_{i+1}}{V_i - V_{i+1}} \quad 8\text{-}10$$

If V_{ag} is greater than or equal to the largest particle size V_N, then the contribution to class $N-1$ is

$$\chi_{\kappa j} = \frac{V_{ag}}{V_N} \quad 8\text{-}11$$

Note that there is no breakage for the smallest particle class, (Ansys-Fluent, 2011). The readers are encouraged to refer to the Population Balance Model Manual (2006) for a

comprehensive overview of the FLUENT population balance model and its application in solving multiphase flows involving a secondary phase with a size distribution.

8.3 Computational settings and validation of the PBM model

The first part of this work is to combine a coalescence and break-up model with a complete flow numerical simulation under normal gravity. The flow equations are solved using a population balance approach coupled with the Eulerian multiphase model. The population balance module is provided as an add-on with the standard FLUENT solver. A two-phase air-water bubble column with a height of 200 cm and diameter of 14.5 cm is used for the simulations. The geometry and operating conditions are all based on the air-water experimental system of Degaleesan et al. (2001), which have been validated by simulations from Chen et al. (2005) and Law and Battaglia (2013). The initial diameter of the injected air bubbles is 0.4 cm as specified by (Degaleesan et al., 2001). In accordance with Hounslow et al. (1988), the prescribed bubble classes are chosen in such a way that the bubble volume (or mass) in class *i + 1* is twice the volume (or mass) of the antecedent class below *i*:

$$v_{i+1} = n.v_i \qquad 8\text{-}12$$

where i refers to the bubbles size group and *n=2, i.e.* classes were assigned such that the volume of class *i+1* is twice the volume of the antecedent class *i*, ($v_{i+1} = 2v_i$). For the purpose of PBM validation, six bubble sizes from 0.159 to 1.62 cm in diameter are considered as shown in table 8.1, and bubble size of only the 3th class i.e. 0.4 cm enter the column; these setting as all consistent with thoses of Degaleesan et al. (2001).

Table 8-1 Assigned bubble sizes of *n=2* for the population balance simulation

Class index	1	2	3	4	5	6
Bubble diameter(cm)	0.159	0.252	0.400	0.636	1.00	1.62

The properties for air and water used in the simulation were taken from (Ansys-Fluent, 2011), see table 8.2.

Table 8-2 Physical properties of the two fluids (water/air) employed in the simulation			
Properties	Unit	Water	Air
Density (ρ)	kg/m^3	998.2	1.225
Viscosity (μ)	kg/m-s	0.001003	1.79e-5
Surface tension	N/m	0.075	

The air bubble is injected into a 14 cm diameter bubble column filled with 98 cm of water through an inlet at the bottom with a constant velocity of 9.6 cm/s, as shown in figure 8.1. The geometry is modelled as two-dimensional axisymmetric to reduce the computational time.

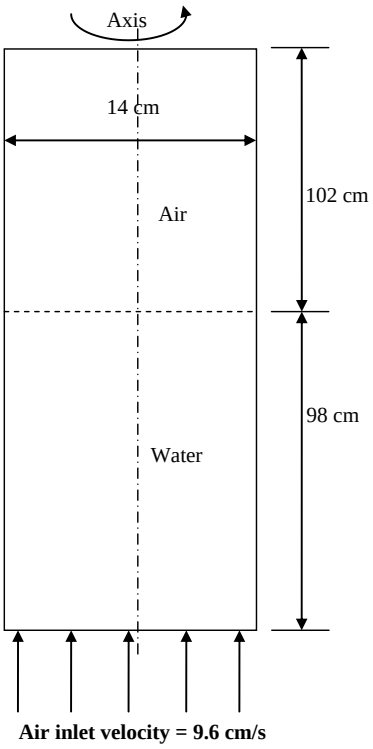

Figure 8-1 Problem Schematic for normal gravity flow

The coalescence and breakage models proposed by Luo and Luo-Svendsen are considered in the simulations to account for breakage and agglomeration mechanism, whereas the model of Schiller and Naumann has been employed for the drag coefficient calculation. The settings given in table 8.3 are used to compare the Fluent computations with the experimental data of Degaleesan et al. (2001). All these settings are used for all computational runs except for zero gravity conditions where laminar flow is consider.

Table 8-3 Physical properties of the two fluids (water/air) employed in the simulation

Category	**Description**	**Input**
Numerical solver	Segregated implicit unsteady first order	
Solution algorithm	Solving algorithm scheme	Phase Coupled SIMPLE
	Convergence Criteria	0.001
Turbulence modeling	Standard κ- ε model	
	Standard wall function	
	Mixture	
Multiphase model	Eulerian	
	Specified operational density and gravity-zero gravity	
Drag coefficient model	Schiller- Naumann	
Discretization scheme	Momentum	First order
	Turbulent viscosity	First order
	Turbulent dissipation rate	First order
Population Balance Model	Discrete method	Six different bubble sizes
	Aggregation Kernel	Luo model
	Breakage Kernel	Luo model
Under Relaxation Factors	Pressure	0.3
	Density	0.6

	Body-forces	0.6
	Momentum	0.2
	Volume Fraction	0.2
	Turbulent kinetic energy	0.8
	Turbulent dissipation rate	0.8
	Turbulent viscosity	0.6
	air Bin	0.8
Initial Conditions	Reference pressure	101325 [Pa]
	Turbulent kinetic energy	0.1
	Turbulent dissipation rate	0.25
Boundary condition	Rotating <-> Stationary grid	Interface
	Outer walls	No-slip wall
	Body	No-slip wall

For the present work, time-dependent simulations were run with time step of 0.01 s until a steady flow was established with acceptable mass balance for all fluid phases as shown in figures (8.2 to 8.4).

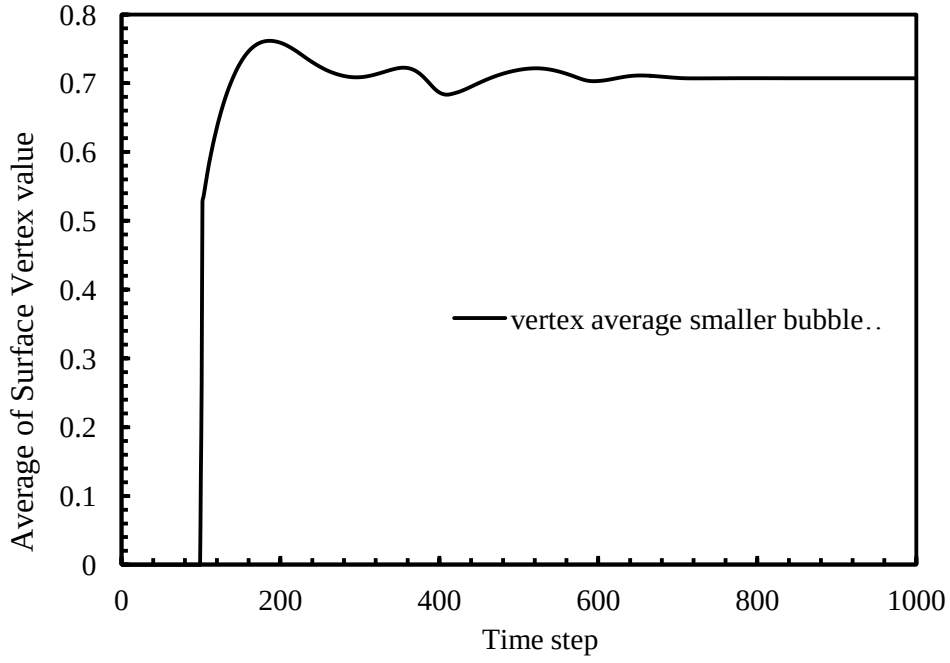

Figure 8-2 Monitoring of smaller bubble size

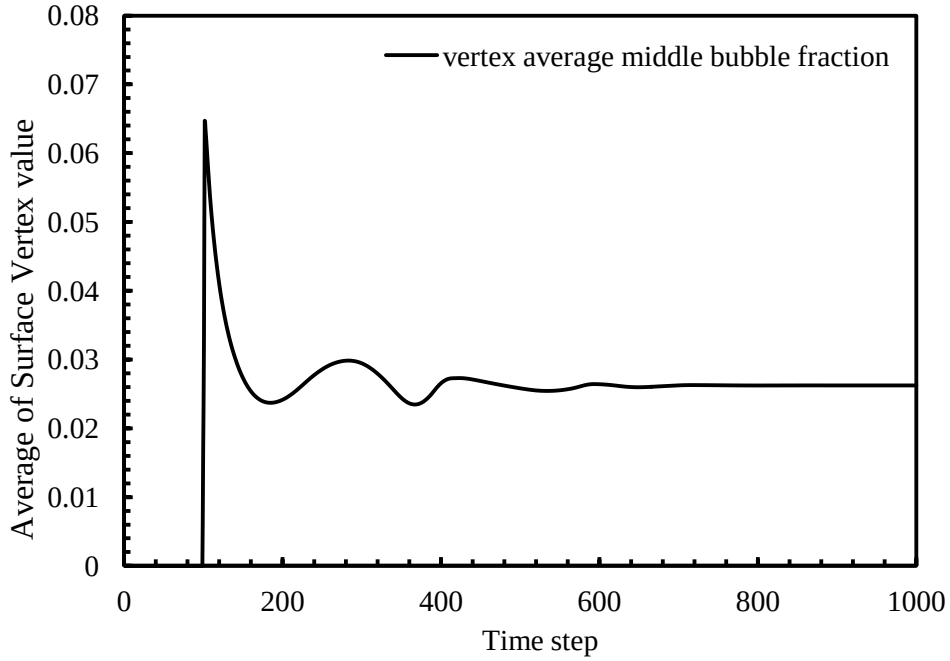

Figure 8-3 Monitoring of medium bubble size

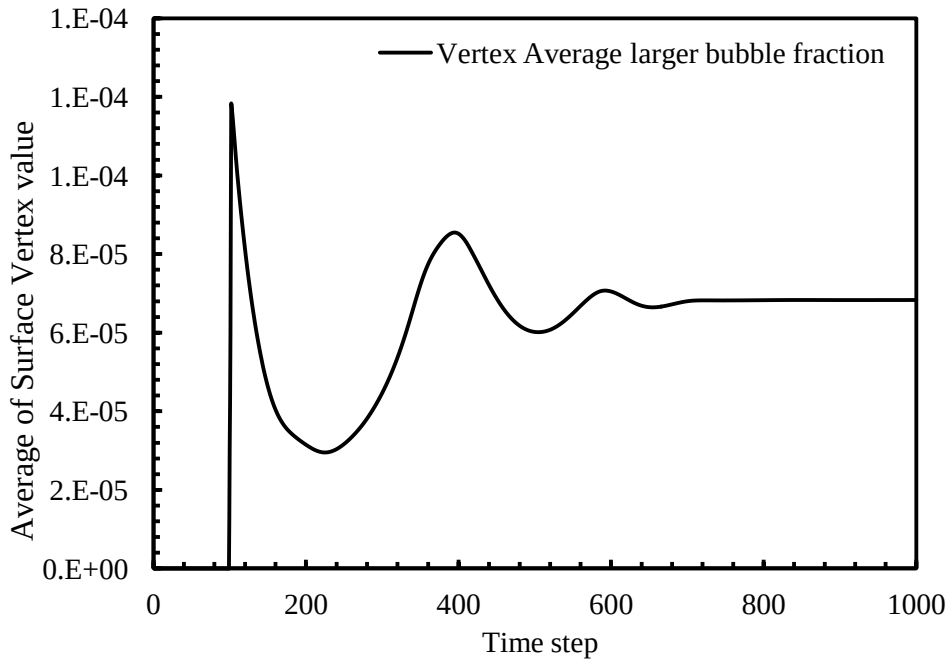

Figure 8-4 Monitoring of larger bubble size

Comparisons between the present results for six bubble sizes with previous experimental and numerical results at an air inlet velocity of 9.6 cm/s show acceptable agreements (see Figure 8.5). In fact, the results of axial water velocity agrees better with the predictions of Law and Battaglia (2013) and Chen et al. (2005) for six different bubble sizes. On the other hand in Figure 8.6 average axial liquid velocity predictions are shown to have little effect by varying column heights for a fixed inlet velocity of 9.6 cm/s.

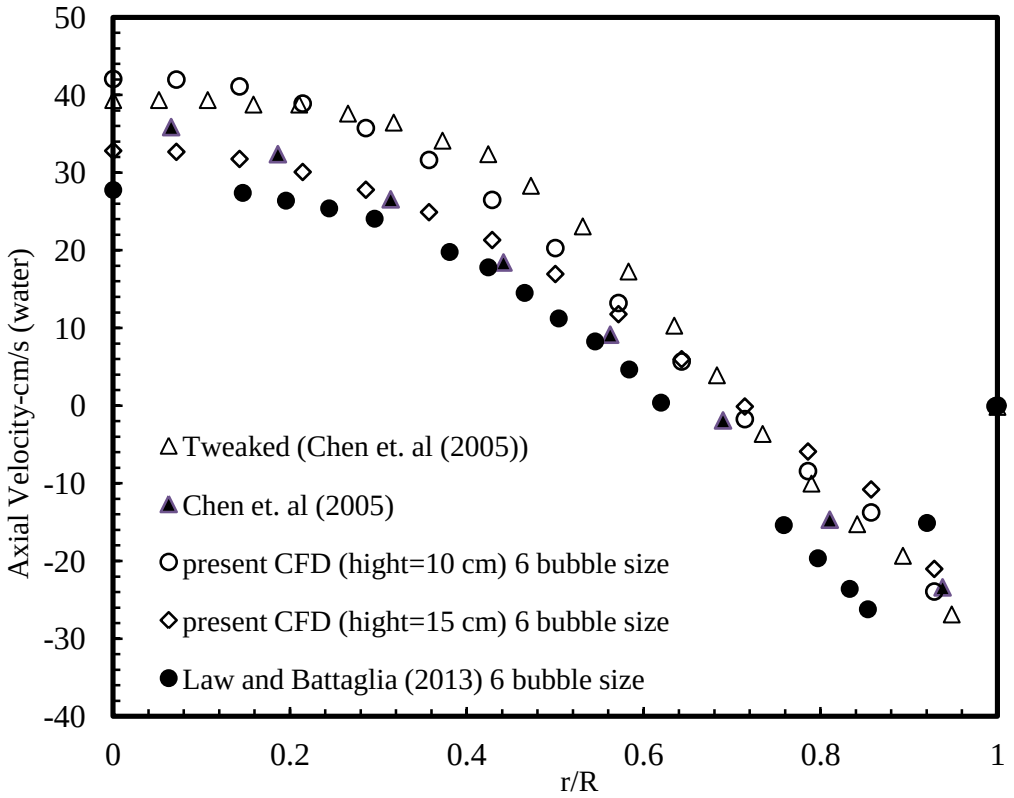

Figure 8-5 Comparison and validation of 2d axis of average axial liquid velocity predictions at 10, and 15 cm heights with experiments at 9.6 cm/s superficial gas velocity.

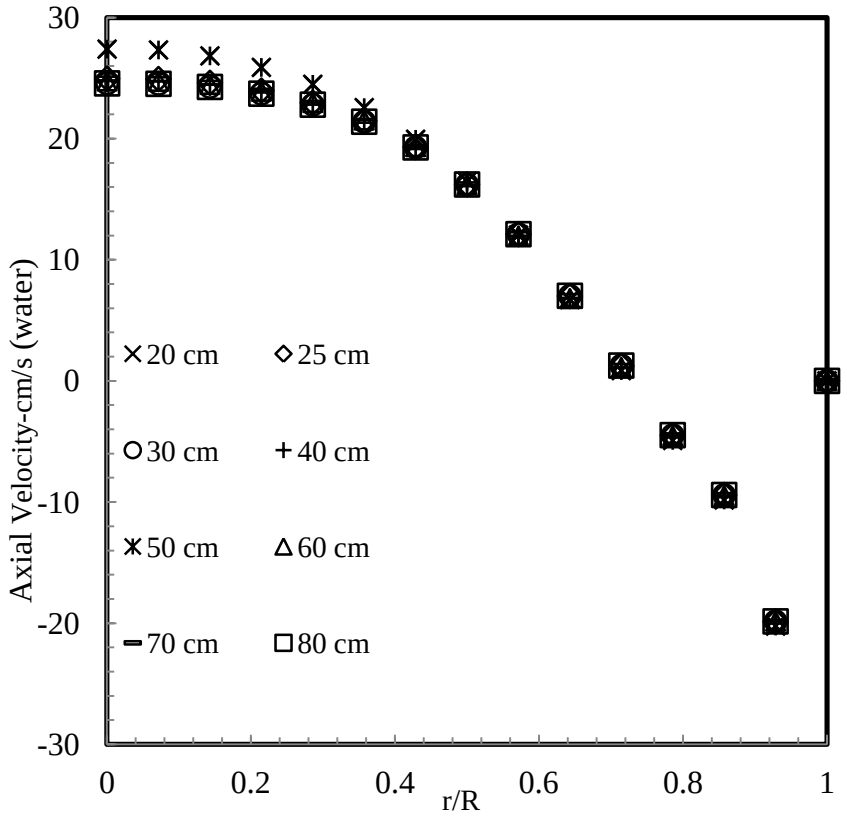

Figure 8-6 Calculated average axial liquid velocity predictions from 20 to 80 cm heights of column at 9.6 cm/s superficial gas velocity

8.4 Grid-Size Dependency

Further validation of the present PBM model was achieved by performing a series of refining grid densities using Gambit (2005) software. Grid independence was achieved by increasing the grid cells whilst plotting the convergence of certain parameters of interest, such as the radial profile of the axial velocity (cm/s) for water at a specific height. This was to ensure that the results remained independent of the grid size. It is very important to know which grid will produce the desired effect with the least computational cost. In this study, four different refined grid densities have been created for meshing the 2d axisymmetric cylinder with a structured grid approach. These cells number and figures are listed in table 8.4 and showed in figure 8.7. Based on these results, the use of 4800 cells seems to be adequate to capture key features of flow inside the bubble column. Therefore, 4800 cells were used in all the subsequent simulations.

Table 8-4 Grid sensitivity check for a the 2D axis models of air-water PBM

Grid	(Δx,Δy)	Number of cells
(1)	0.55,0.55	4004
(2)	0.5,0.5	4800
(3)	0.45,0.45	5772
(4)	0.40,0.40	7500

The final domain is 2d axisymmetric where the mesh is rectangular, structured and uniform with the control volumes being 0.5×0.5 cm^2 in size.

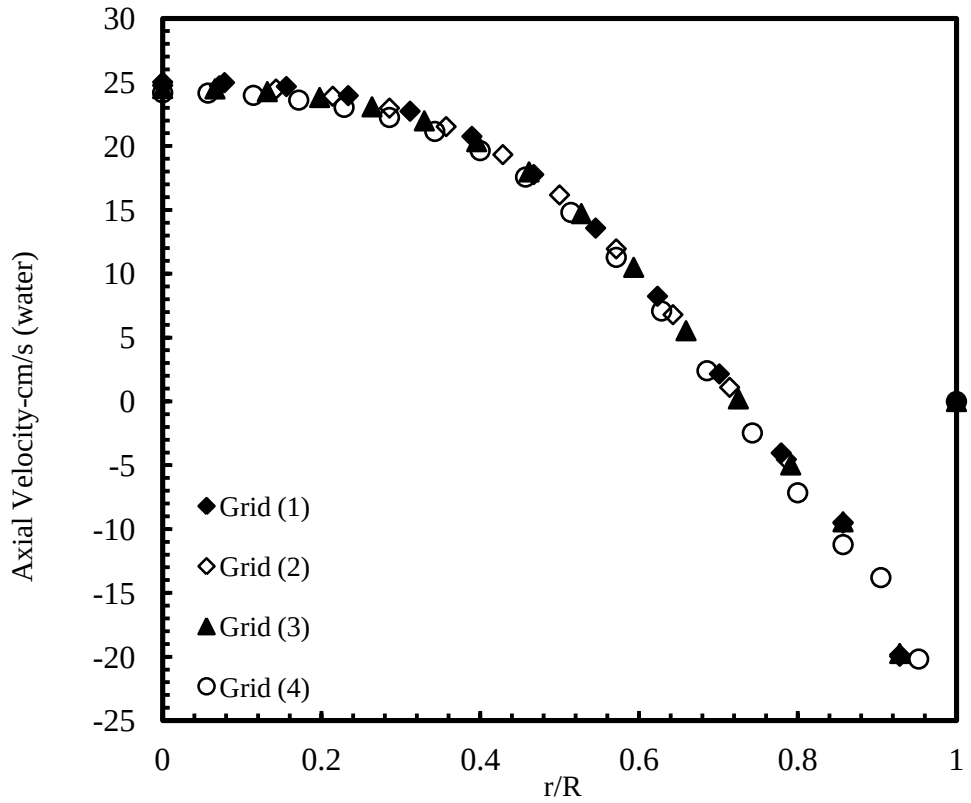

Figure 8-7 Grid sensitivity check for four different grid size

8.5 Influence of changing air inlet velocity open bubble breakup and coalescence in normal gravity

After validating the PBM model with the bubble column experiments of Degaleesan et al. (2001) and numerical simulations of Chen et al.(2005) and Law and Battaglia (2013), 2D simulations are performed for different bubble inlet velocities (varying from 2 to 9.6). This is

done not only to study the influence of changing air inlet velocity on bubble breakup and coalescence in normal gravity but also to understand and predict air inlet velocity effect on the particle size distribution. For the current simulations, similar boundary conditions to the validation cases have been used apart from a different air inlet velocity. Figure 8.8 presents the density distribution as a function of particle sizes at 2, 4, 6, 8, and 9.6 cm/s air inlet velocities. From the comparisons between figures 8.9a-f, it is clear that there is a reduction in the initial bubble size inlet (which was 0.4 cm). Furthermore with varying air inlet velocities there is an increment in the number density of larger (right) and smaller (left) bubble sizes, which shows the bubble coalescence and breakup, respectively. As the air inlet speed is increased, bubbles undergo coalescence which results in a sharper (low variance) bell shaped distribution.

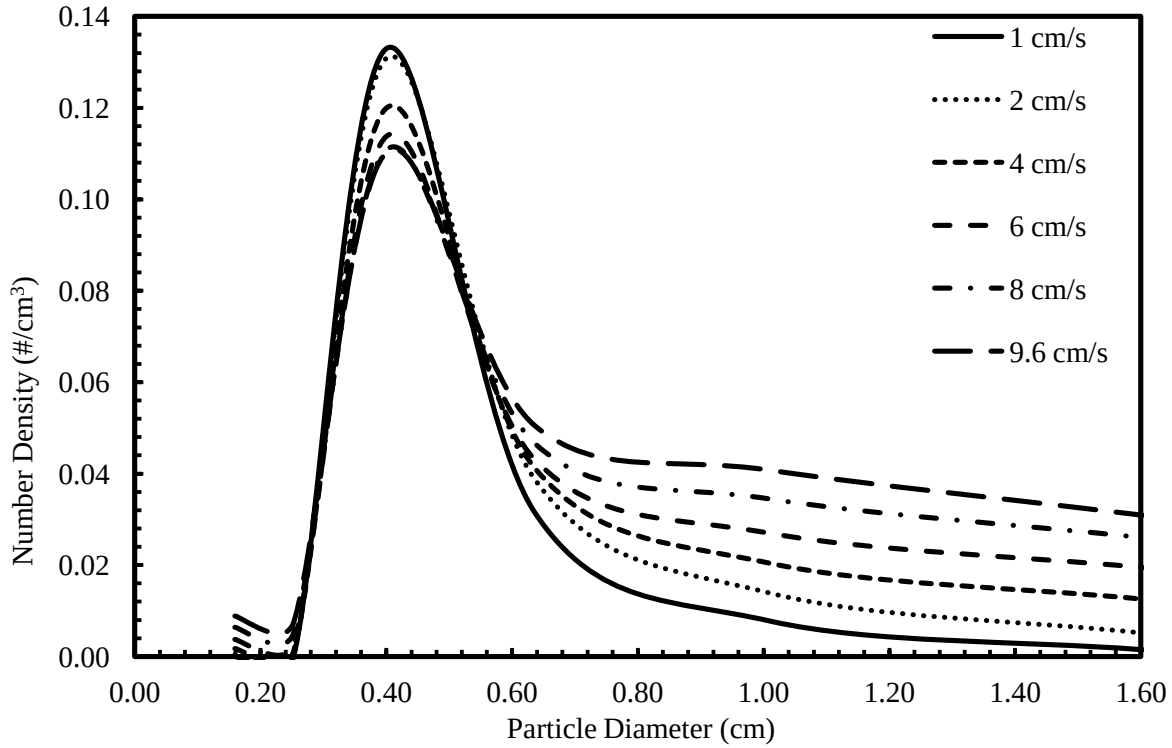

Figure 8-8 Bubble Number density for different air inlet velocities

Figures 8.9a to 8.9f compare number density (#/cm^3) for air diameter of 0.4 cm at different inlet velocities. These figures show an increase in smaller and larger bubble with an

increasing inlet air velocity, even though all simulations were started with the initial particles size equal to 0.4 cm and a constant growth rate. This is evident from the dominant number density of 0.4 cm peak histogram in all figures.

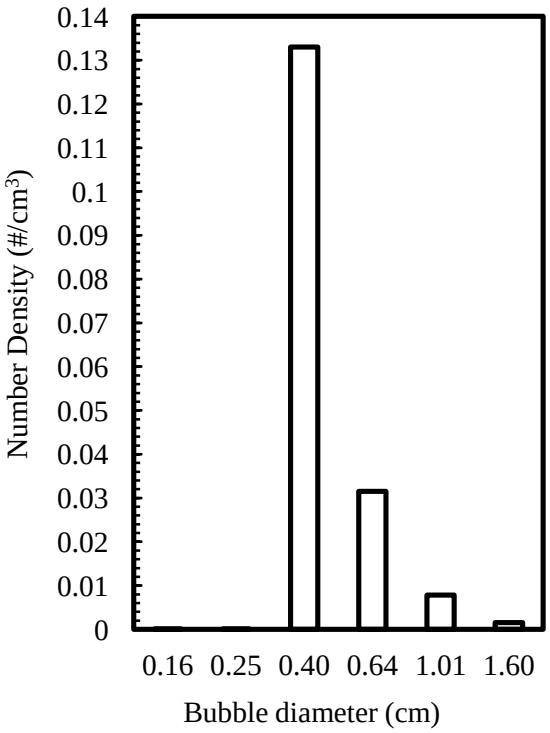

(a) Inlet gas velocity = 1 cm/s

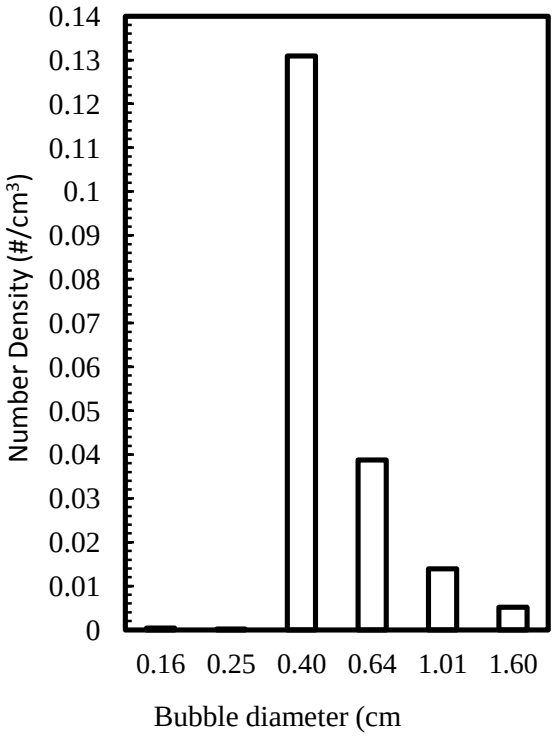

(b)Inlet gas velocity = 2 cm/s

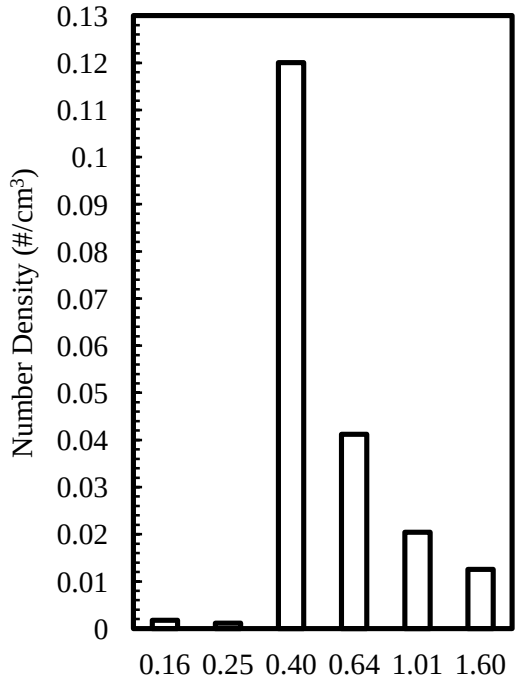

(c) Inlet gas velocity = 4 cm/s

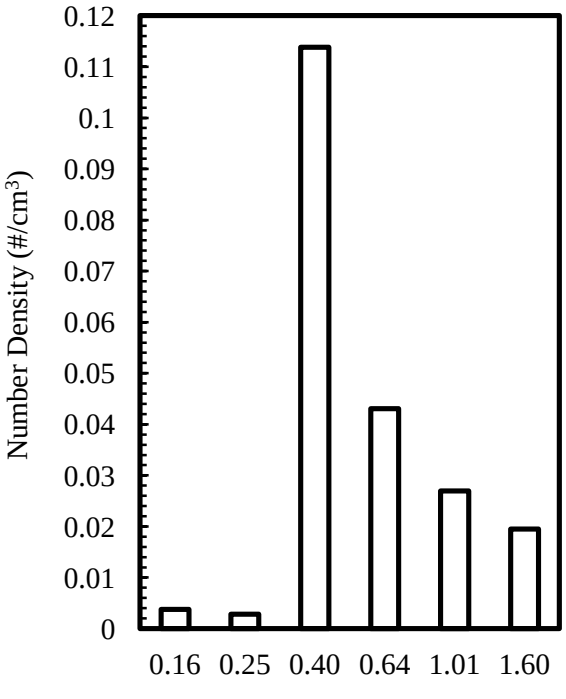

(d) Inlet gas velocity = 6 cm/s

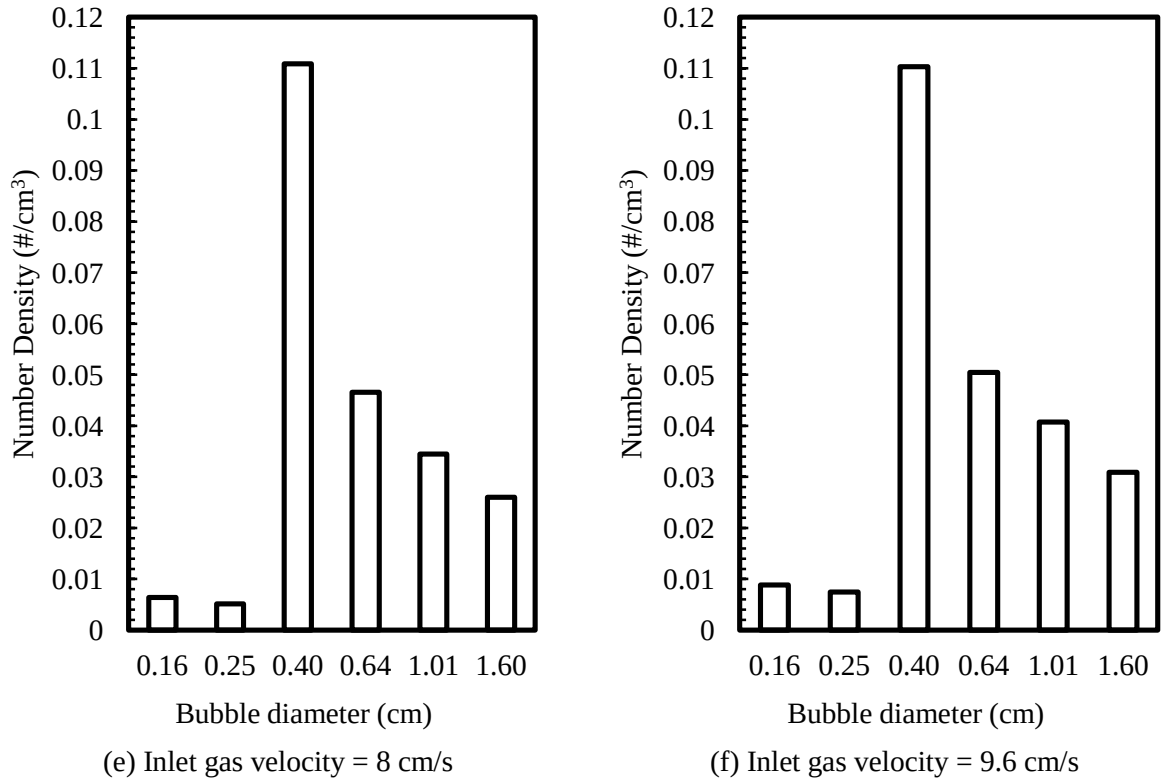

(e) Inlet gas velocity = 8 cm/s (f) Inlet gas velocity = 9.6 cm/s

Figure 8-9 Surface Averaged Number Density Distribution Histogram

All simulations show that bubbles with a range of sizes are formed in the bubble column. This model considers that several bubble groups with different diameters *di* can be represented by an equivalent phase with the Sauter mean diameter dg; a single bubble breaking into a large and a small bubble. Figure 8.10 shows reduction of the bubble size distribution with increasing velocity along the axis for Sauter mean diameter. In this figure it is clear the decrease is from inlet to outlet. Figure 8.11 shows air fraction flow development with increasing inlet velocity along the radial direction. The contour of figure 8.11 is clarified in figure 8.12.

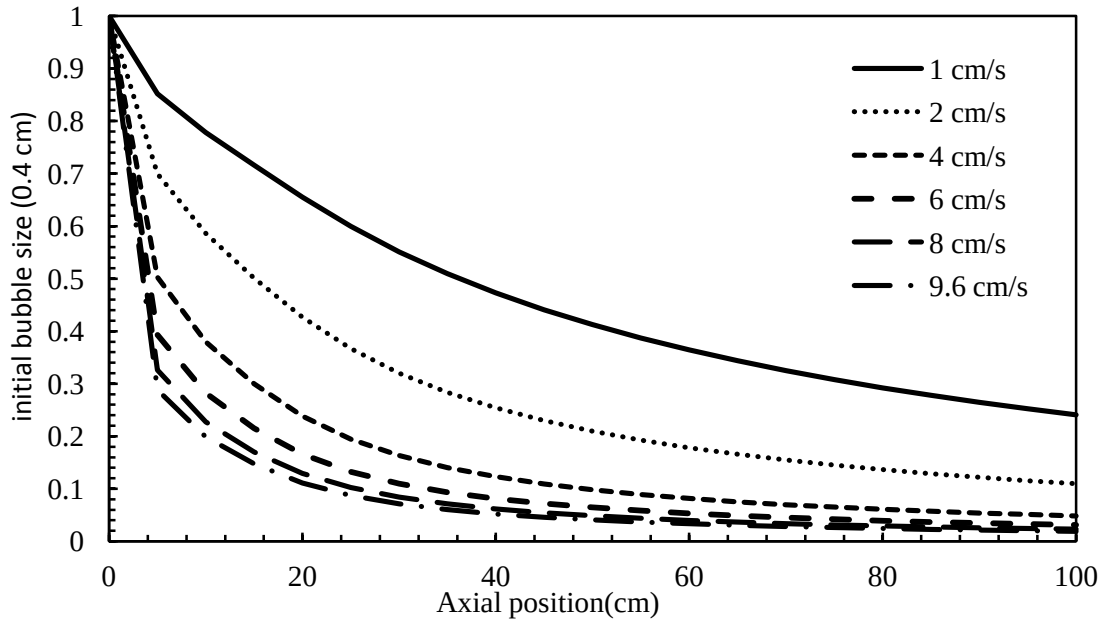

Figure 8-10 Distribution of bubble size along the axis for initial bubble size

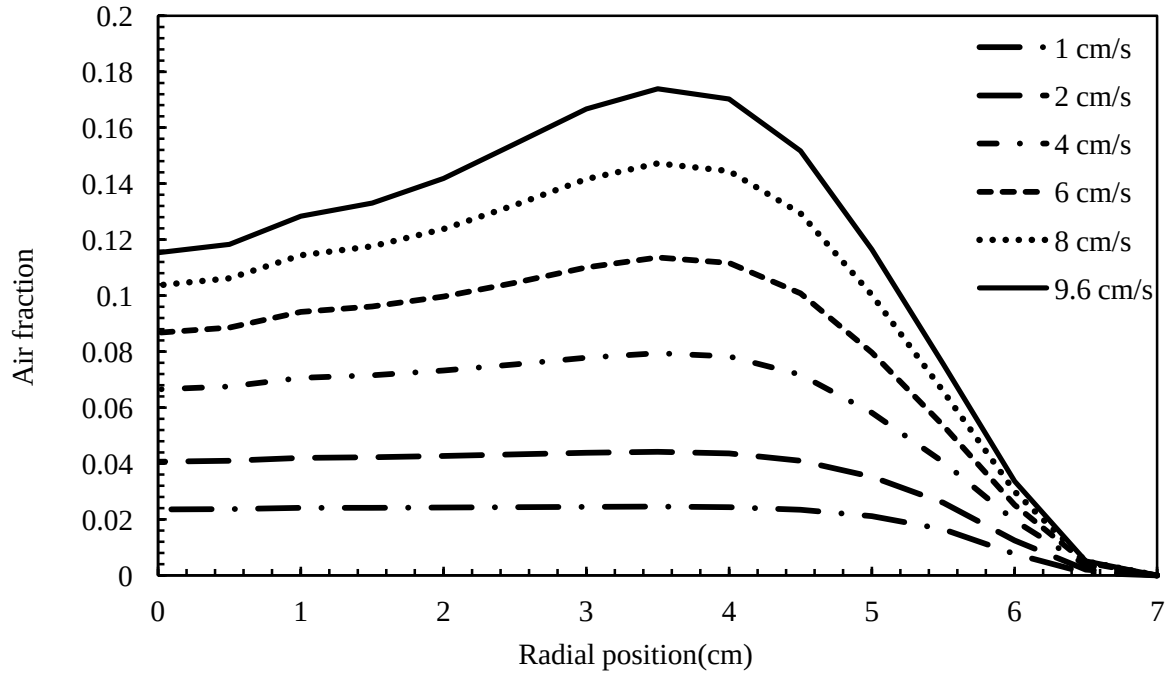

Figure 8-11 Air volume fraction for each velocity at 40 cm height of the bubble column

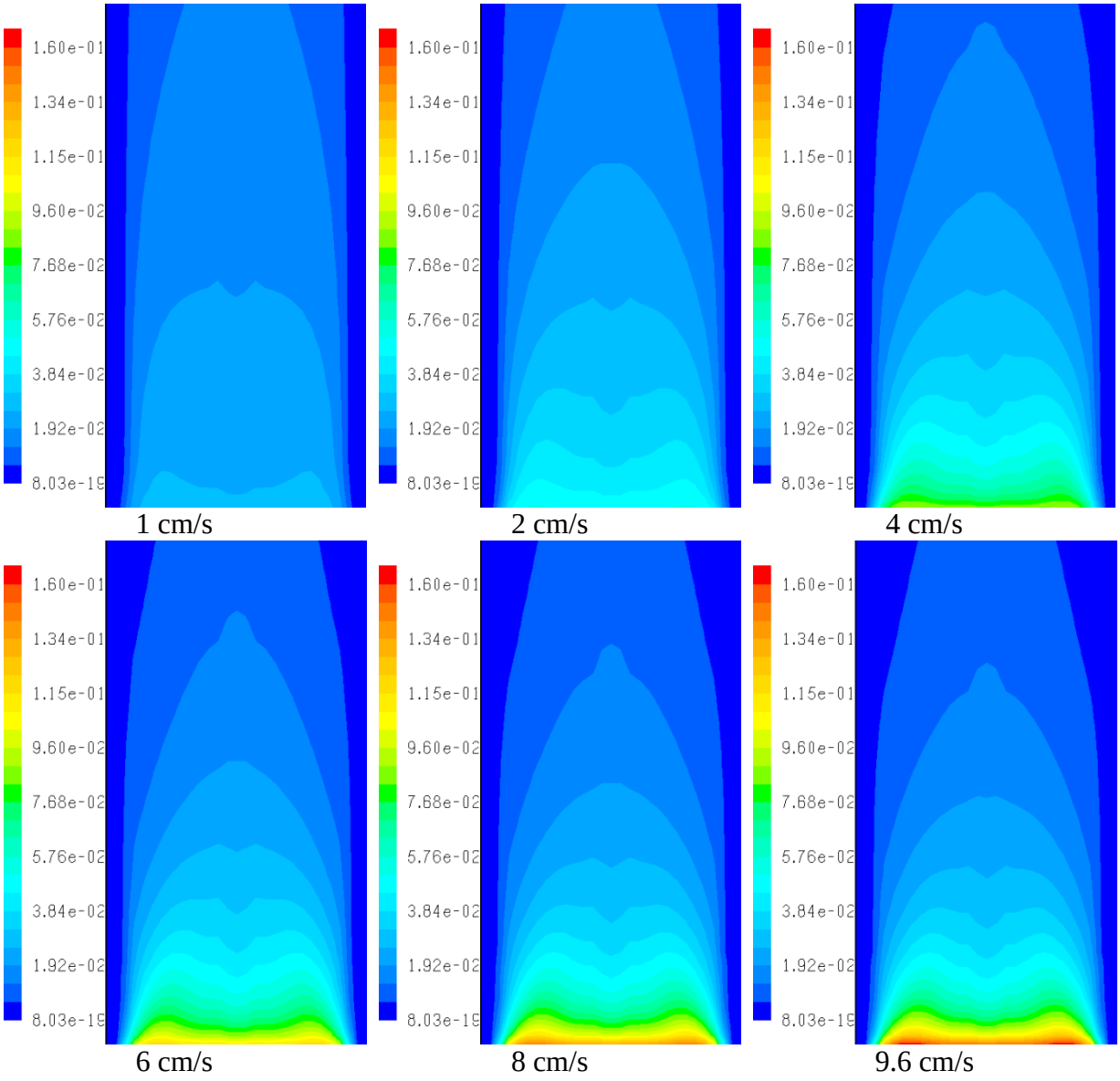

Figure 8-12 Contours of air fraction for different inlet velocity

It is observed that as the air inlet speed is increased, bubbles undergo coalescence which results in a sharper (low variance) bell shaped distribution. With increasing frequency, the peak of the bell curve shifts towards the right indicating larger mean bubble diameters as observed from figures 8.12 and 8.13

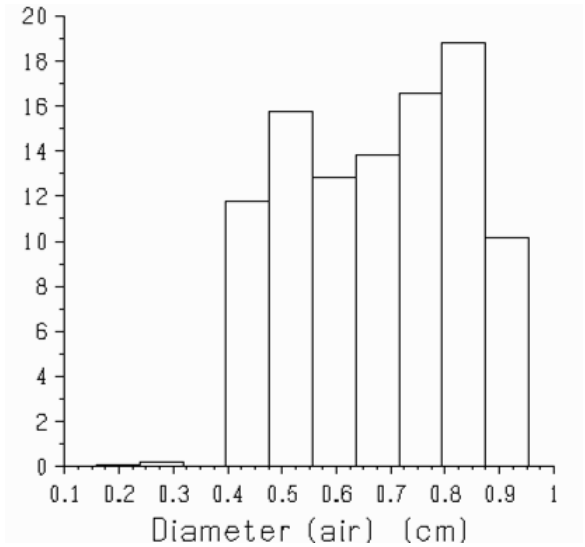

(a) Inlet gas velocity = 1 cm/s

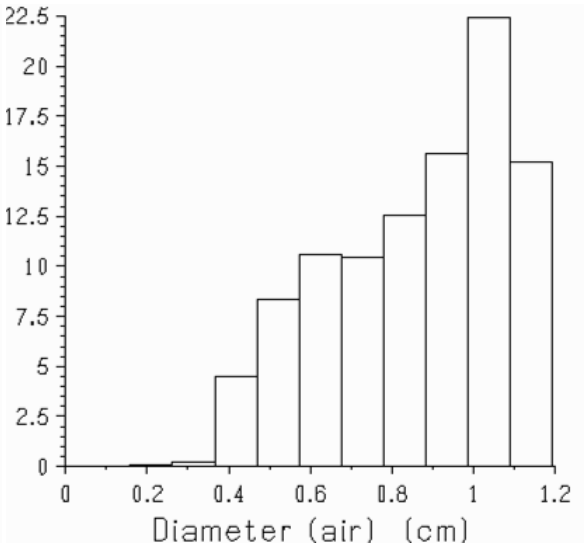

(b) Inlet gas velocity = 2 cm/s

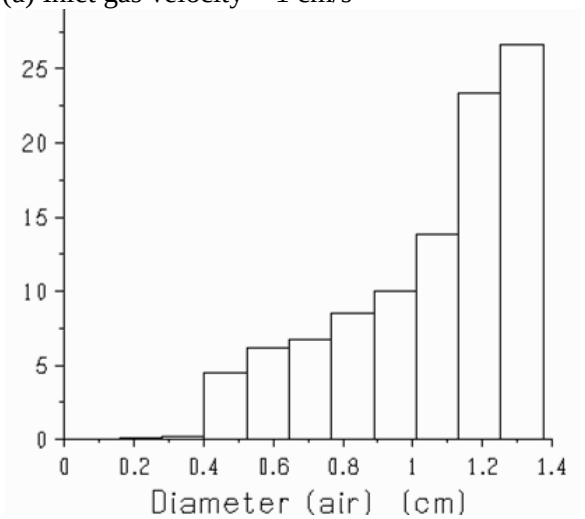

(c) Inlet gas velocity = 4s cm/s

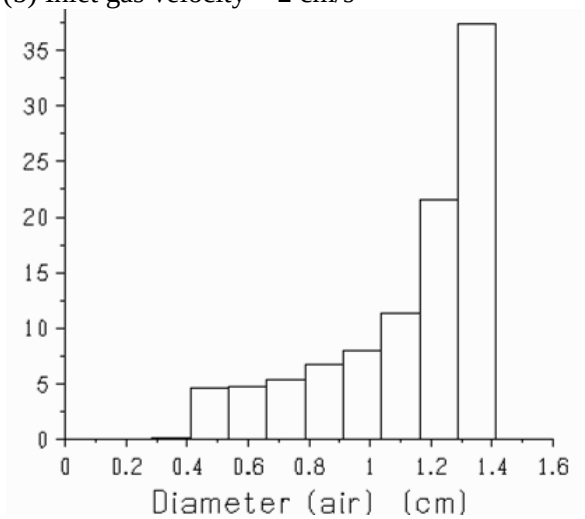

(d) Inlet gas velocity = 6 cm/s

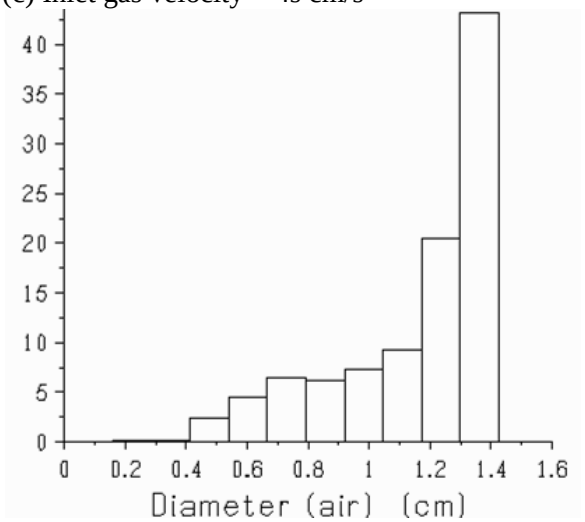

(e) Inlet gas velocity = 8 cm/s

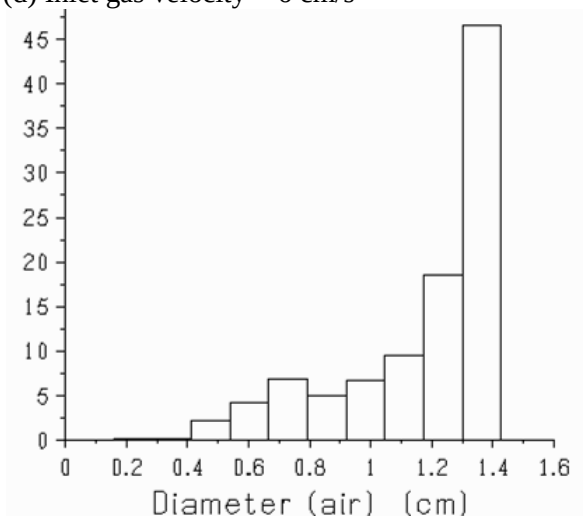

(f) Inlet gas velocity = 9.6 cm/s

Figure 8-13 Histogram of Sauter Diameter Distribution

8.6 Bubble breakup and coalescence undergoing forced rotation in normal gravity

The next logical step was to perform simulations for bubble breakup and coalescence using a forced rotation under normal gravity. For this case the column was rotated with a fixed angular velocity and air was injected from the bottom at 0.02 m/s. Calculations of the PBE for air entering from the bottom of the column were initiated after obtaining the steady state condition for each rotational speed using similar geometry and boundary condition as that of the previous simulations. (Figure 8.1, tables 8.1, 8.2).

The current simulations comprise of column rotational angular speeds of 0.5, 1.0, 1.5 and 2 rad/s. It is observed that the bubble breakup and coalesce due to turbulence and which is caused directly by the injected air inside the liquid column. The coalescence and breakage models proposed by Luo and Luo-Svendsen were considered in the simulations, and the model of Schiller and Naumann (1935) was employed for the drag coefficient calculation. For the present work, time-dependent simulations were run with a time step of 0.01 s until the steady state was established with acceptable mass balance for all fluid phases.

Figure 8.14 show development of the parabolic shape around the centreline of the column due to centrifugal force effect. The obtained figure is for different rotational speeds for air phase. The profiles are along the radial direction at a distance of 40 cm from the inlet. Results also indicate that rotation could help in moving the gas phase following a parabolic shape. Rotation also helps in reducing the turbulence dissipation coming from the wall.

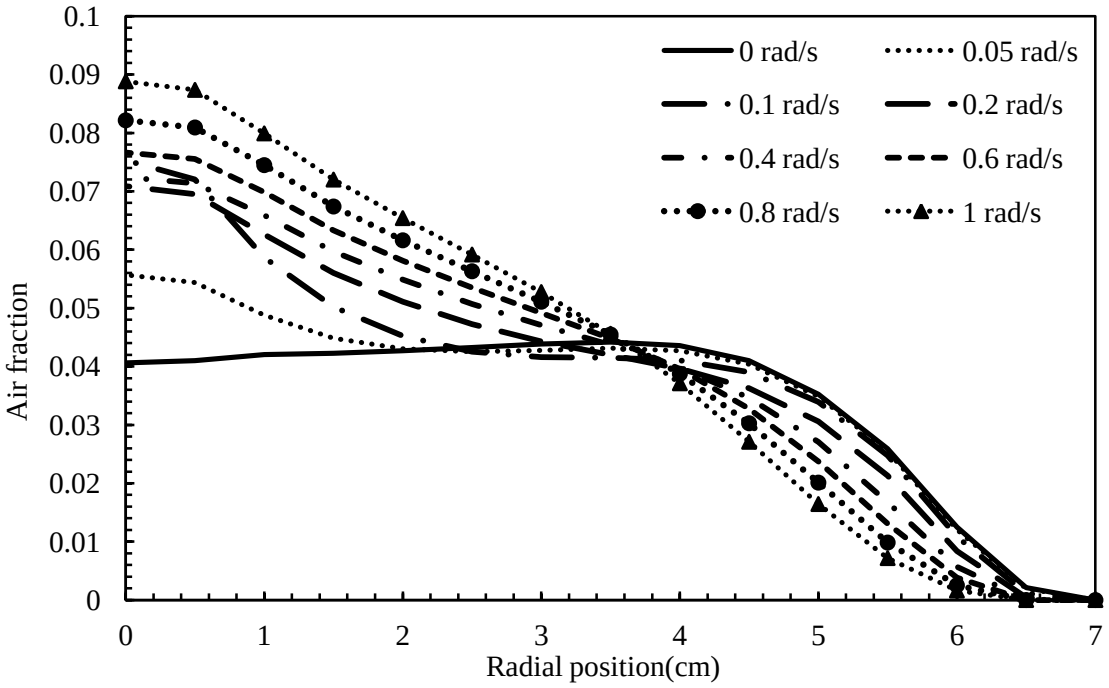

Figure 8-14 Air inlet velocity profile entering with 2 cm/s at 40 cm height of the bubble column.

The effect of rotation on the mean bubble size was quantified by measuring the fraction of the initial bubble size at various angular speeds. Figure 8.15 shows a decrease in the initial bubble diameter with increasing rotational speeds, where the initial bubble diameter is plotted along the axial direction showing a decrease from the inlet to the outlet. Figure 8.15 shows evolution of Sauter mean bubble diameter with respect to the height at constant air inlet velocity and rotational speed. It is also noted from the simulations that the mean bubble diameter decreases with increasing height, ultimately reaching an equilibrium size. By changing the rotational speed one changes the energy dissipation rate. For these analyses the representative bubble size was deduced from the bubble size distribution by calculating the Sauter mean diameter.

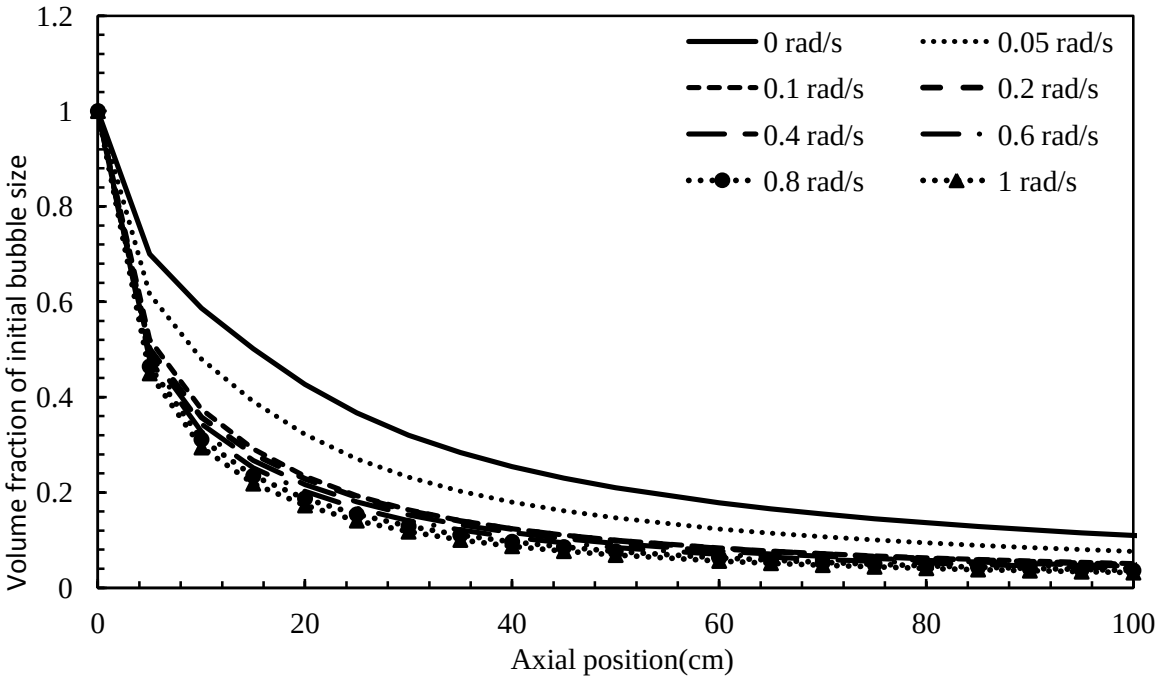

Figure 8-15 Distribution of bubble size along the axis of rotation for air initial bubble size at 2 cm/s

Figure 8.16 illustrates the effect of angular velocity on the bubble distribution. At low rotational speeds, the bubble bell shape of the number density is high. It is observed that rotation provides a radial force input to the system leading to an even narrower size distribution and a smaller number density as compared to the non-rotational case. As the rotational speed is further increased, the peak of the bell curve becomes smaller.

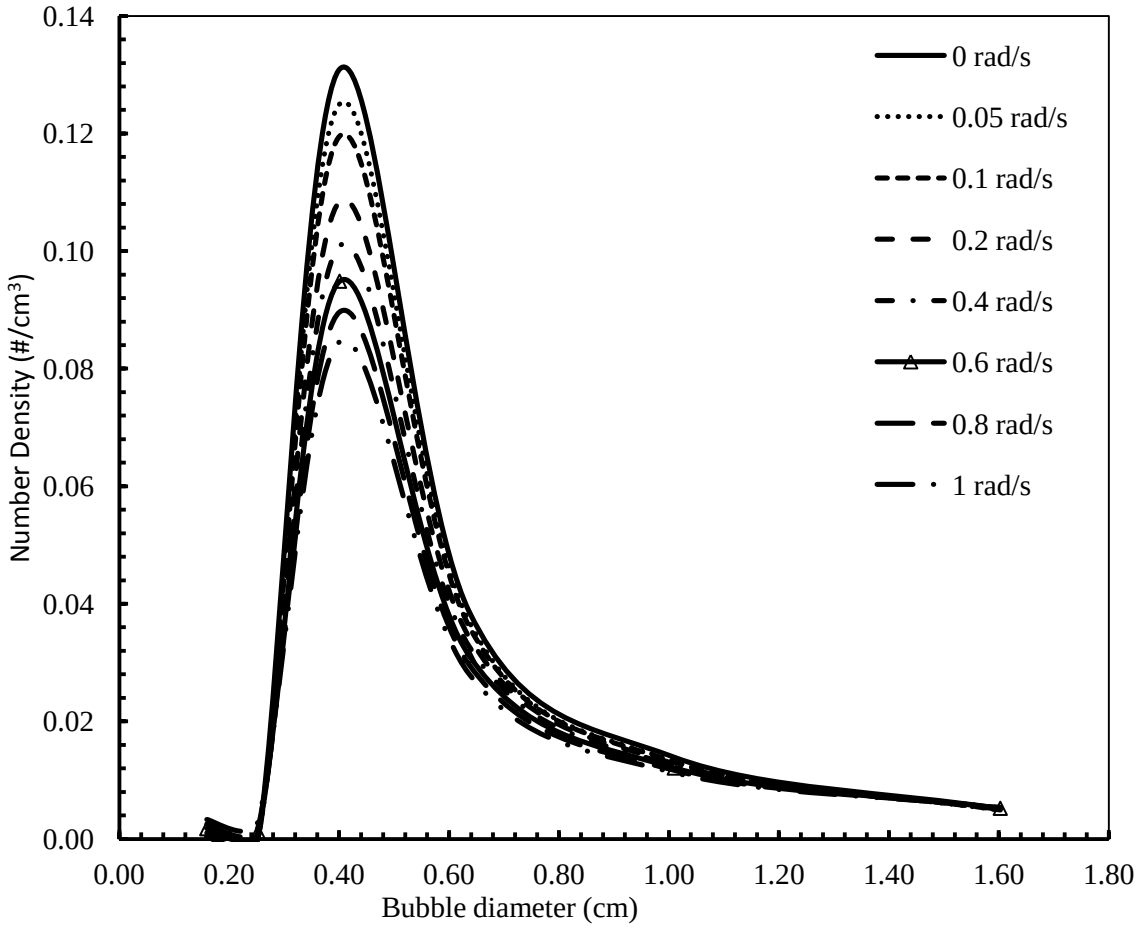

Figure 8-16 Effect of angular velocity on bubble distribution

Figures 8.17a to 8.17h show an increasing in the small bubbles (size less than the initial bubble diameter i.e. 0.4 cm). On the other hand the initial diameter bubbles and larger one remain mostly unchanged. The creation of smaller sized bubbles (less than 0.4 cm diameter) could be due to eddies creating by rotation.

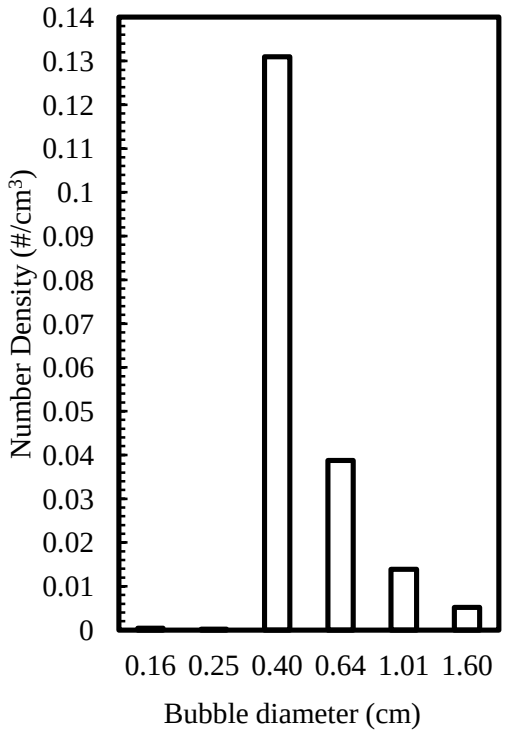

(a) Inlet gas velocity = 0 rad/s

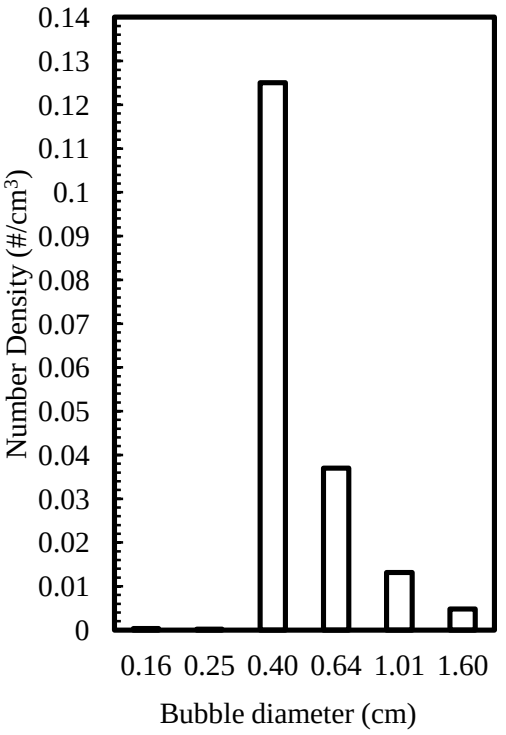

(b) Inlet gas velocity = 0.05 rads/s

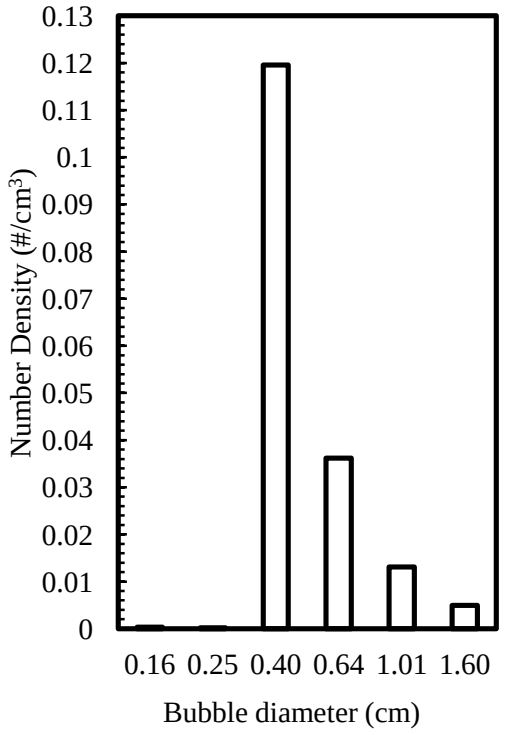

(c) Inlet gas velocity = 0.1 rad/s

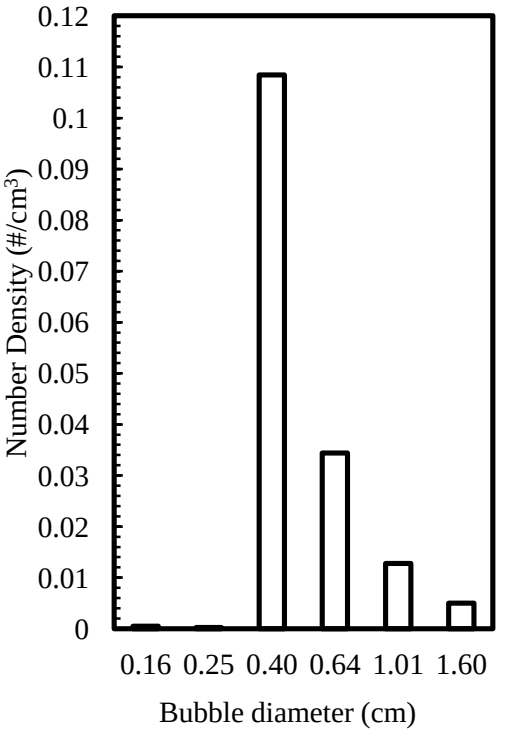

(d)Inlet gas velocity = 0.2 rad/s

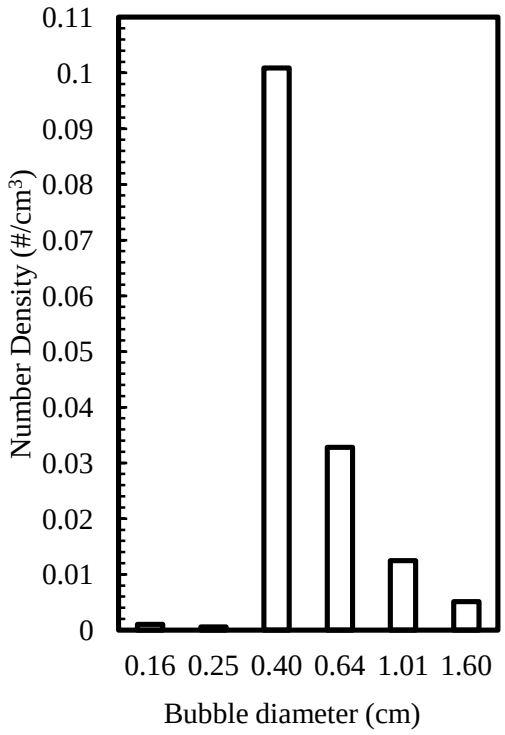

(e) Inlet gas velocity = 0.4 rad/s

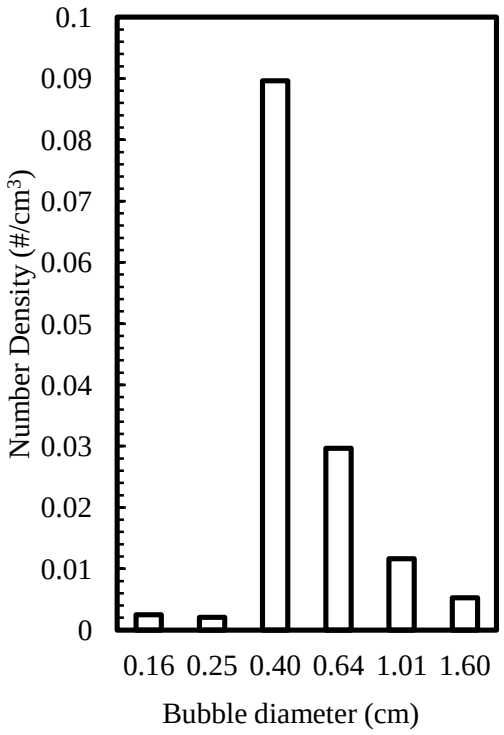

(f) Inlet gas velocity = 0.6 rad/s

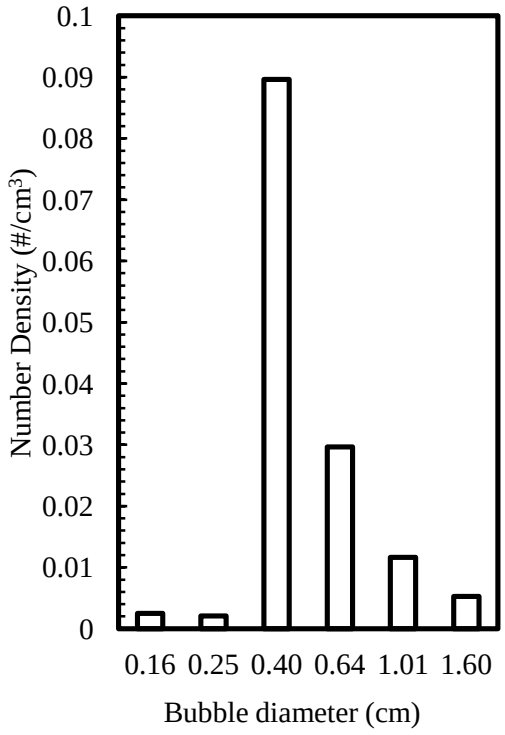

(g) Inlet gas velocity = 0.8 rad/s

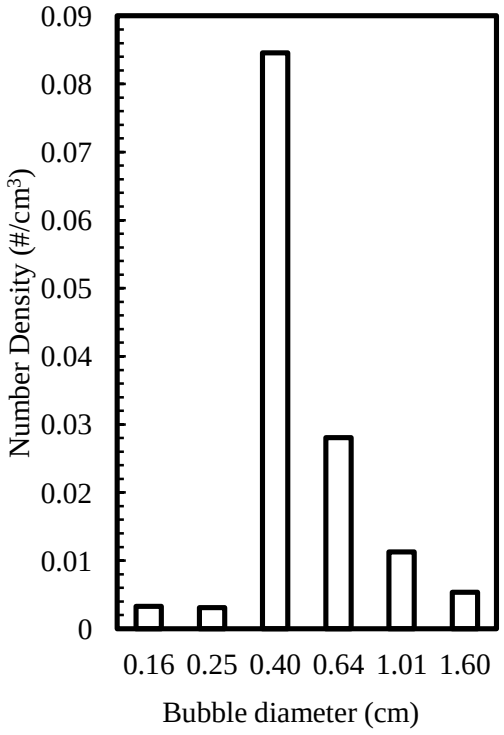

(h) Inlet gas velocity = 1 rad/s

Figure 8-17 Surface Averaged Number Density Distribution Histogram

Figure 8.18 shows comparisons of bubble diameter for different rotational speeds. With an increase in the angular velocity, a noticeable reduction on the larger bubble diameter is also observed; the larger bubbles (0.4 to 1 cm diameter ones). Thus it is concluded that at higher angular speeds more uniform air particles become to form.

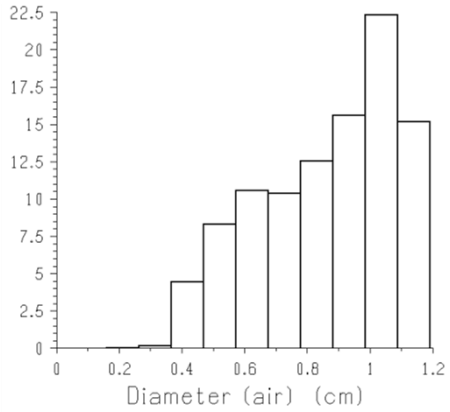

(a) angular speed = 0 rad/s

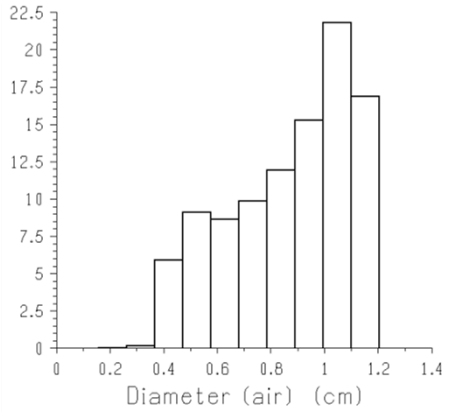

(b) angular speed = 0.05 rad/s

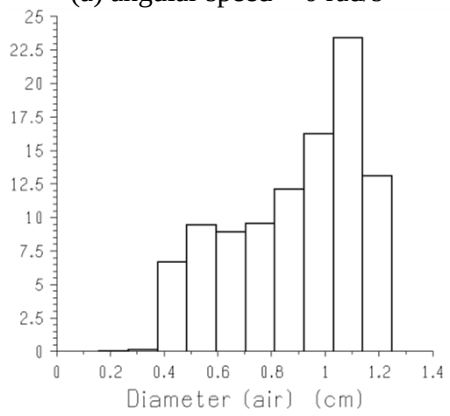

(c) angular speed = 0.1 rad/s

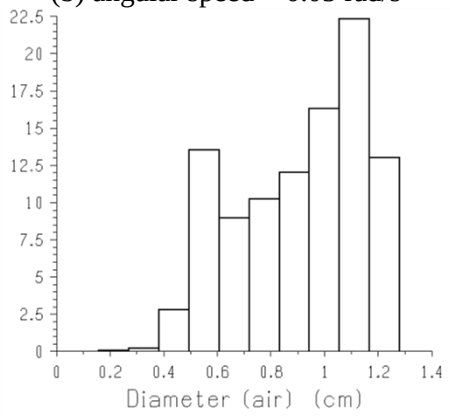

(d) angular speed = 0.2 rad/s

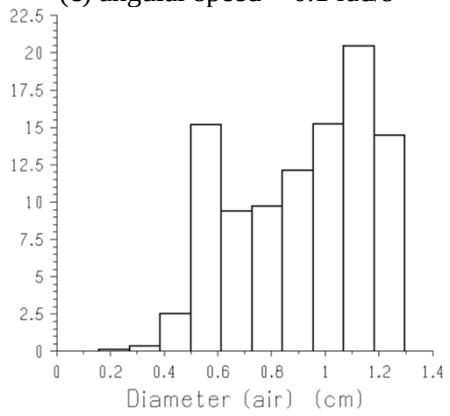

(e) angular speed = 0.4 rad/s

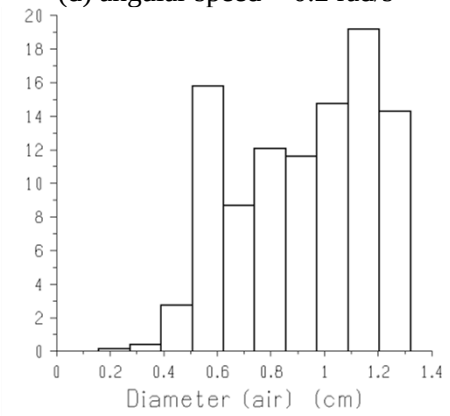

(f) angular speed = 0.6 rad/s

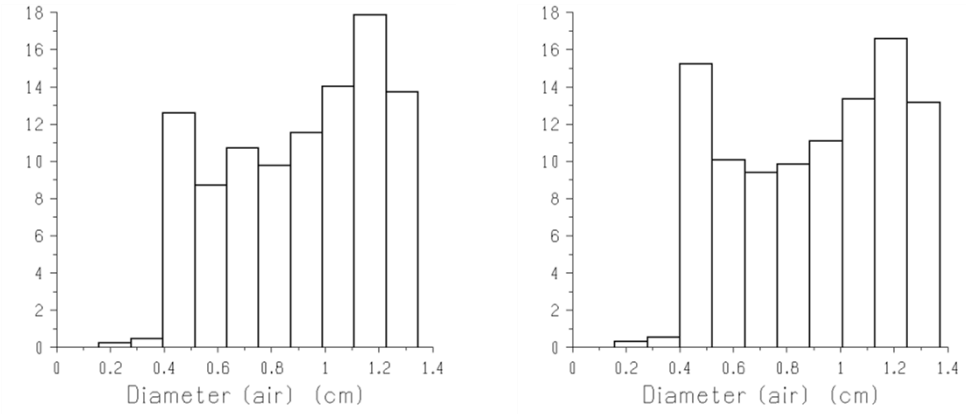

(g) angular speed = 0.8 rad/s (h) angular speed = 1 rad/s

Figure 8-18 Histogram of Sauter Diameter Distribution with increasing rotational speeds.

8.7 Bubble coalescence undergoing forced rotation in zero gravity

Coalescence undergoing rotational force holds the key to control the bubble aggregation as seen in the earlier chapters. To date, the understanding of the low gravity bubbles coalescence behaviour is limited mainly due to the unresolved physical mechanisms that lead to coalescence; the lack of information because of the difficulties in obtaining experimental result in microgravity, especially for a rotating column. There has been no study investigating bubble size distribution under both rotation and zero gravity condition; the work presented in this section fills this gap. It is widely accepted that bubble break up contributes to changes in the bubble size distribution but this is considered to be negligible for small bubbles and for Marangoni flow (zero buoyancy force). In this study a purely coalescing mechanism for bubble growth will be considered and the extent to which coalescence occurs is discussed. A rotating bubble column with varying rotational speeds of 0.25, 0.5, 0.75 and 1 rad/s about its axis of symmetry is considered. Figure 8.19 shows the schematic representation of the air-water bubble column of diameter of 120 mm and height of 120 mm. The properties for air and water used in the simulation were taken from (Ansys-Fluent, 2011), see table 8.2. The geometry consists of air with a constant speed of 1 cm/s flowing through a 30 mm inlet from the bottom of the water column. The inlet velocity was chosen to be close to the velocity of

gases in zero gravity (thermocapillary migration speed). The geometry was modelled as two-dimensional axisymmetric to reduce the computational time. Part of the upper surface (top wall) of the domain was set to pressure outlet; the rest of top and bottom walls were defined as no-slip solid walls (see fig.8.19 for details).

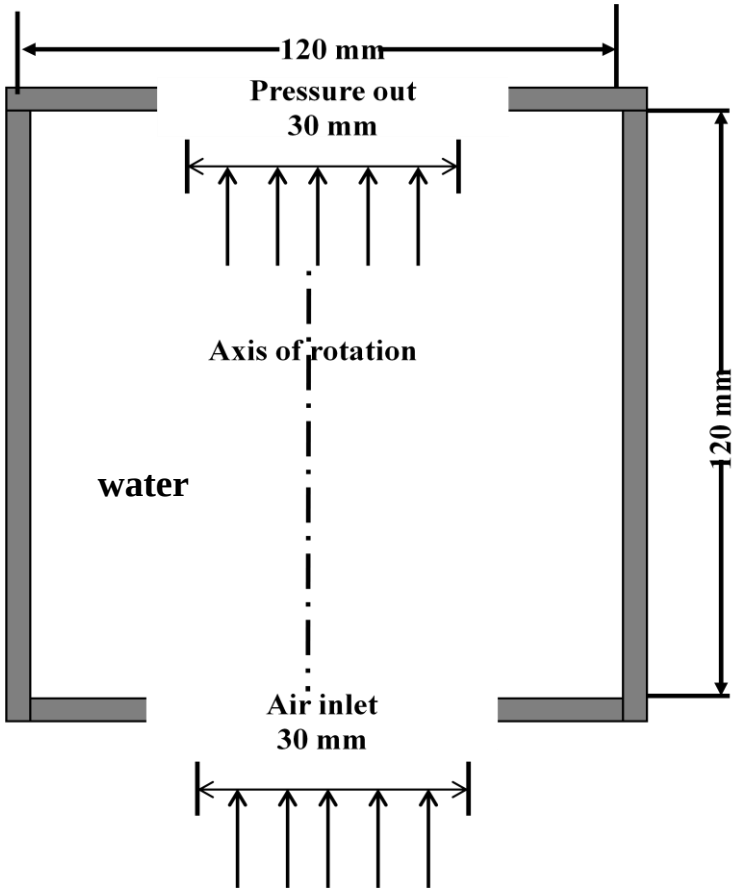

Figure 8-19 Problem Schematic for zero gravity flow

8.7.1 The aggregation kernel for Laminar Flow (model 1)

Coalescence occurs instantaneously after two particles collide forming a new sphere. Particle collision and coagulation leads to a reduction in total number concentration. However, the total particle volume remains unchanged. The coalescence rate can be expressed as the product of collision frequency and coalescence probability. The collection kernels used for the population balance modelling are complex and have not yet been benchmarked for zero gravity environments. A number of applicable kernel models for the determination of bubble coalescence in thermocapillary flow and two coalescence kernel suggested by number of authors for small bubbles diameter and laminar shear collision mechanisms will be implemented in this investigation.

The aggregation kernel $a_{kj} = a(V_i, V_j)$ has units of m^3/s, and is expressed as a product of the collision frequency of particles of volume *Vi* and *Vj*. The coalescence efficiency is the probability of particles of volume *Vi* coalescing with particles of volume *Vj*, where the two bubbles have diameters *di* and *dj*, respectively. In this study, the coalescence (model 1) is written as:

$$a_{kj} = K\frac{\pi}{4}(d_i + d_j)^2 \frac{du}{dx} \qquad 8\text{-}13$$

where $a_{kj} = a(V_i, V_j)$,with the unit of "volume per time (mm^3/sec)" depends on the sizes of the colliding particles and boundary condition of the flow field. When V_i and V_j collide, a new particle with volume of V_k is formed. In the present work all small bubbles collision frequency and efficiency are lumped into a single constant, K which depends on the intrinsic diameters *di* and *dj* of the two bubbles. The collection kernel (model 1) has been suggested by a number of authors (for example Everson (1971), and Argyriou et al. (1993)), where the

relative velocity $\frac{du}{dx}$ of the two colliding bubbles is assumed to be constant. It can be remarked that such a factorisation of the collection kernel is possible only if the characteristic time of the collision process is large compared with the time scale of coalescence (Everson et al., 1993).

8.7.2 The aggregation kernel for Laminar Shear Flow (model 2):

Particles in a uniform, laminar shear flow collide because of their relative motion. In modelling the particle motion in laminar shear flow its motion is assumed to be rectilinear. For this case the collision frequency function a_{kj} for coagulation is given by Friedlander (2000) reads as:

$$a_{kj} = \frac{4}{3}(d_i + d_j)^3 \frac{du}{dx} \qquad 8\text{-}14$$

where $\frac{du}{dx}$ is velocity gradient in the direction *x* normal to the streamline.

Simulations are performed to study the influence of changing the column rotational speed open bubble coalescence in zero gravity where air is entring from the bottom of the rotating column.

8.8 Results and discussions

In this section, we present a thorough study of the effect of rotational speed on bubble size distribution using two coalescence kernels for laminar flow. The study begins by investigating the dependency of aggregation kernel (1). Classes were assigned such that *n=4*, i.e. the volume of class *i+1* is four times the volume of the previous class *i*, ($v_{i+1} = n.vi$). A six different bubble size group used for the PBM simulations of the bubble column is shown in table 8.5

Table 8-5 Assigned bubble sizes of n=4 for the population balance simulation						
Class index	1	2	3	4	5	6
Bubble diameter(mm)	1	2.52	6.34	16.0	40.3	101.6

In figure 8.20, the inlet gas velocity was set equal to 1cm/ s (approximately close to the thermocapillary migration speed of same bubble size diameter). A 2-D rotating fluidized bed has an angular velocity of 0.5 rad/s. Under the current operating conditions a quasi-steady state was reached after 30-40 s of real-time simulations. Both kernels (1 & 2) were implemented in the CFD using UDFs.

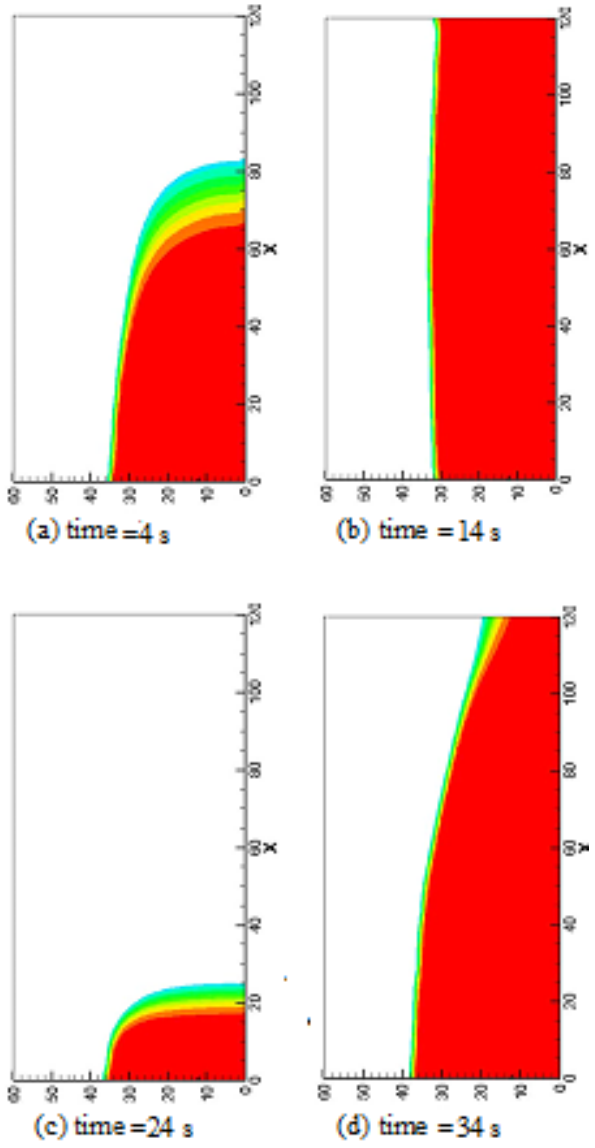

Figure 8-20 Air phase (1 cm/s) development inside a rotating column (ω=0.5 rad/s)

A typical percentage of bubble diameter columns for the same case and time step is shown in Figure 8.21, which show a coalescing mechanism for bubble growth during the flow until it reaches the steady state condition i.e. after 34 s.

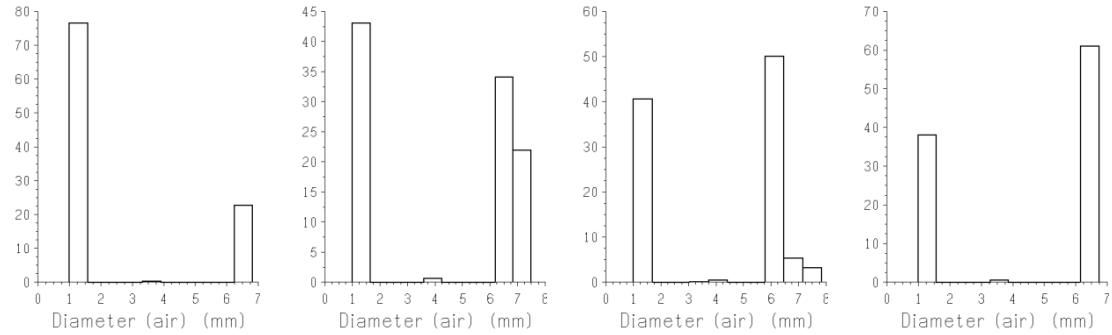

4 s 14 s 24 s 34 s

Figure 8-21 Percentage distribution of bubble diameter in a rotating column (ω=0.5 rad/s) and air flowing at 1cm/s in zero gravity

A typical number density of bubble size inside the rotating column is shown in Figure 8.22. It should be noted that the ND is a function of coalescence process only.

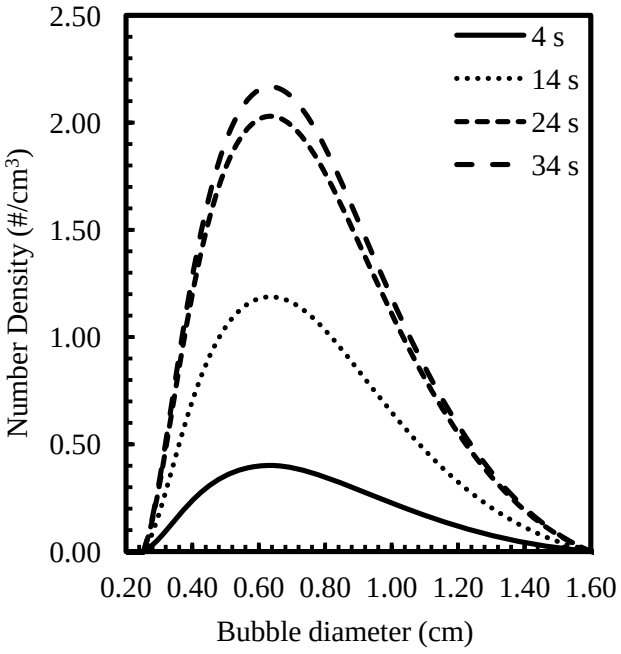

Figure 8-22 Number density for ω=0.5 rad/s

The simulation results shown in figures 8.23 are presented for four different rotating speeds (0, 0.25, 0.5, 0.75, 1rad/s) at a fixed air inlet velocity equal to 1 cm/s. In figure 8.23 it is

observed that for 1 rad/s at t=20 s, the column was in a complete fluidization state unlike at lower rotational speeds. These figures reveal that there is an influence of the rotational speed on the migration of air phase. i e. rotating the column not only causes bubble collision but also accelerates the speed of moving bubbles throughout the column.

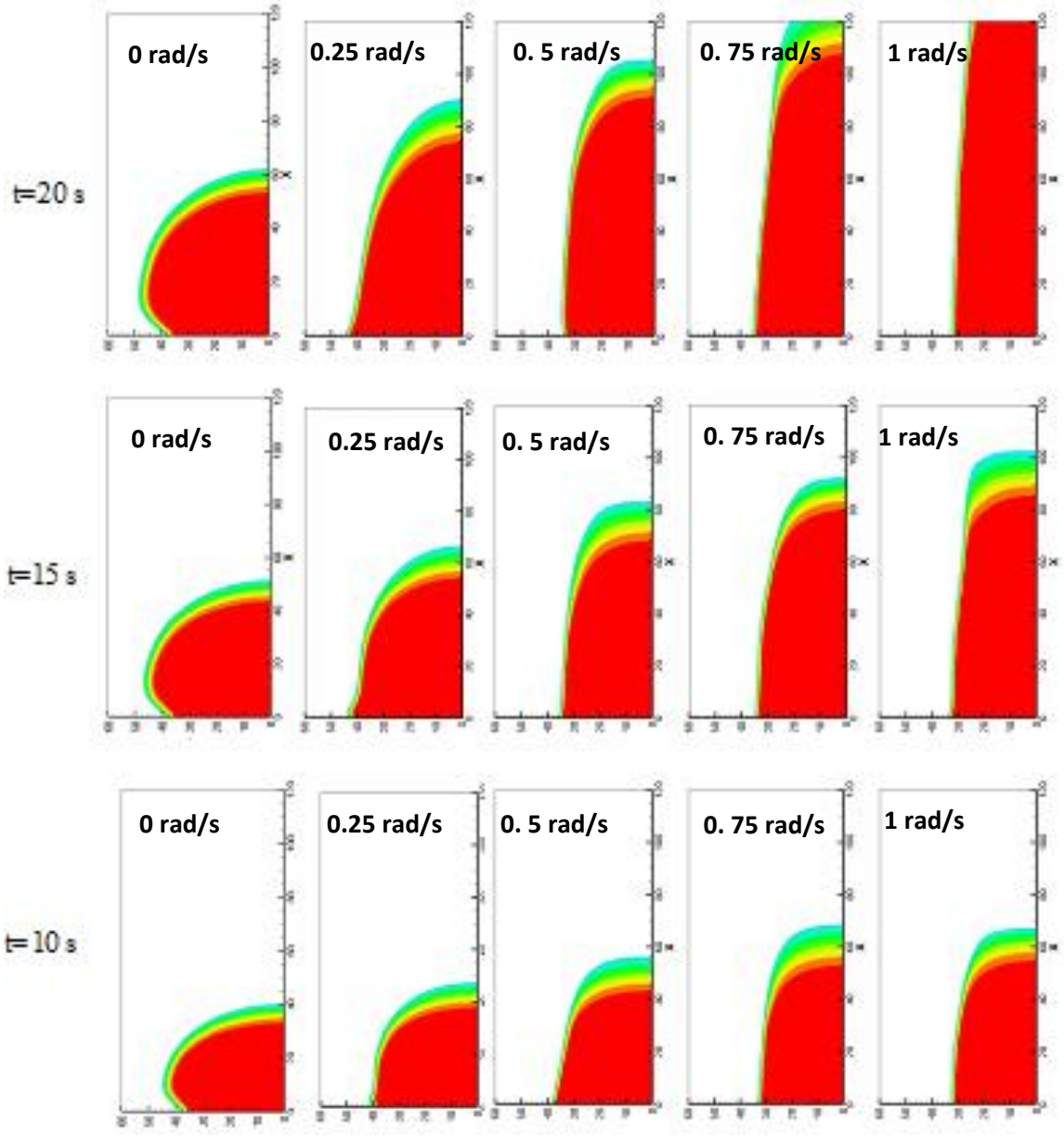

Figure 8-23 Transient development of air flow at 1 cm/s at different angular speed in zero gravity

A typical bubble number density columns is shown in Figure 8.24. It should be noted that the number density is a function of axial position in the column owing to the coalescence process.

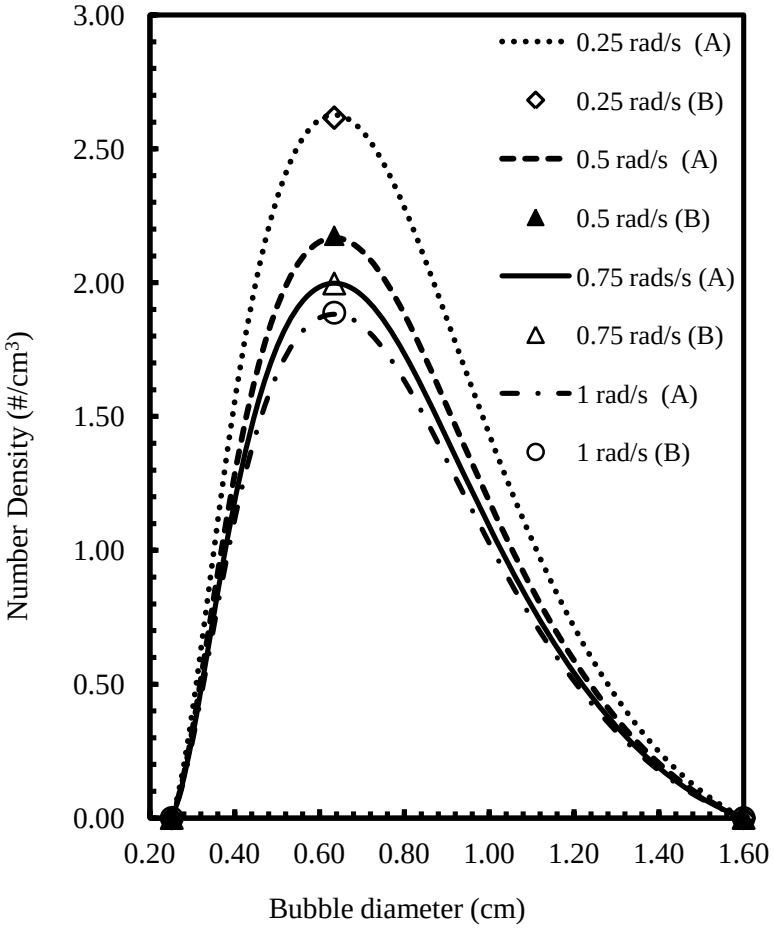

Figure 8-24 Comparison between the two kernels model for air inlet =1 cm/s

Another study has been done to investigate the size of bubble due to change in the *n* classes. The new value is assigned such that the volume of class *i+1* is twice the volume of the previous class *i*, ($v_{i+1} = 2v_i$). As mentioned earlier the determination of bubble size is based upon the bubble volume interval where index *i* refers to the bubble size group. Comparison of the bubble number density for air entering the column at 1 cm/s is presented in Table 8.6 and figures 8.25 for bubble sizes of *n*=2 and 4.

Table 8-6 Assigned bubble sizes of n=2 and 4 for the population balance simulation						
n	Bubble diameter(mm)					
2	1	1.59	2.52	4	6.35	10.08
4	1	2.52	6.34	16.0	40.3	101.6

Comparisons between figures show the difference in the bubbles size diameter with similar number density behaviour. Figure 8.25 shows that the PBM results are comparable with each other for different bubble size groups. Furthermore, the profiles collapse to the same with increasing bubble size groups.

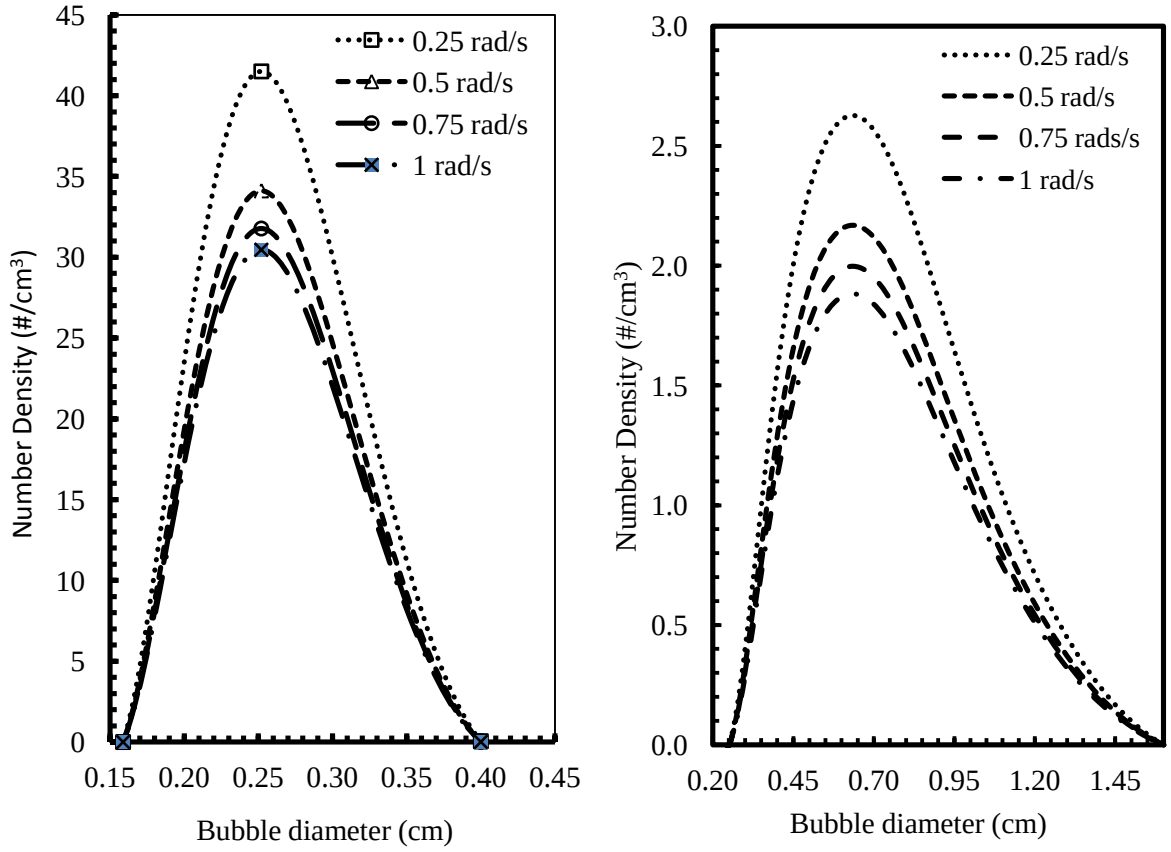

Figure 8-25 Number density for bubble sizes of n =2 (left) and n =4 (right).

Finally the bubble size distribution was measured at four different air superficial velocities of 1, 2, 3, and 4 cm/s and rotational speed was set constant at 1 rad/s. The simulations results in figure 8.25 for *n=2* show increase in number density with increase in air inlet velocity.

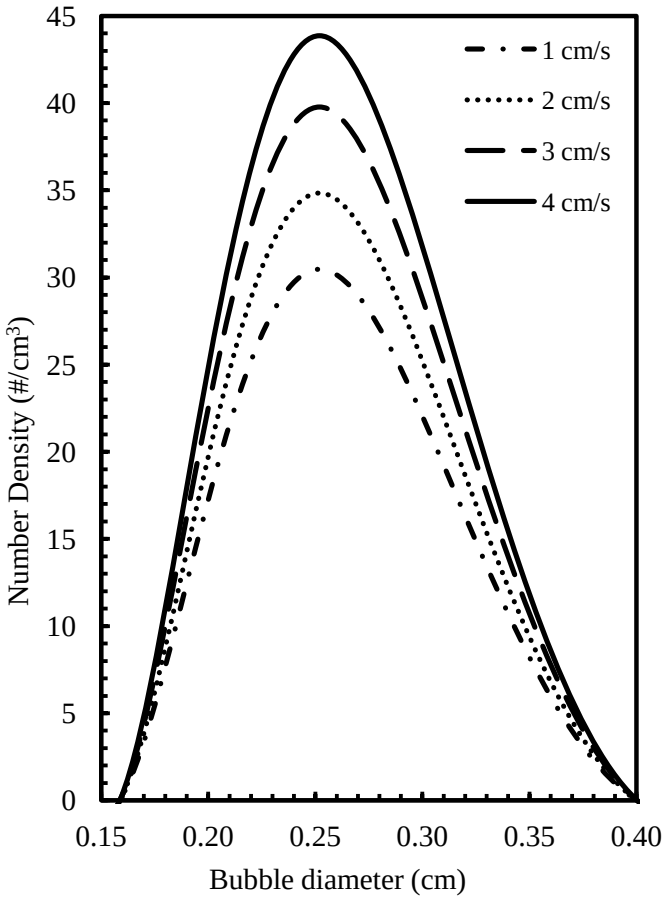

Figure 8-26 Number density for different air inlet velocity

This shows that the bubble diameter depends on gas hole velocity through the inlet. Histogram in figures 8.26 & 8.27 show the effect of inlet velocity on the air bubble diameter. As the gas flow rate is increased, the initial diameter decreases and bubble agglomeration increases.

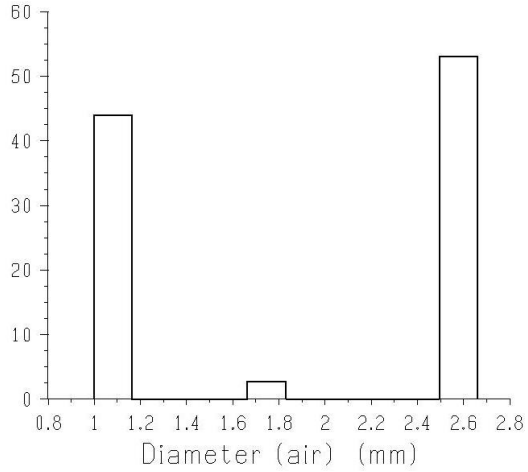

Air inlet velocity =1 cm/s

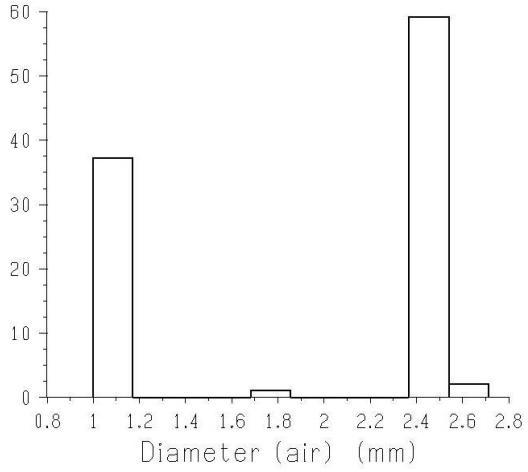

Air inlet velocity =2 cm/s

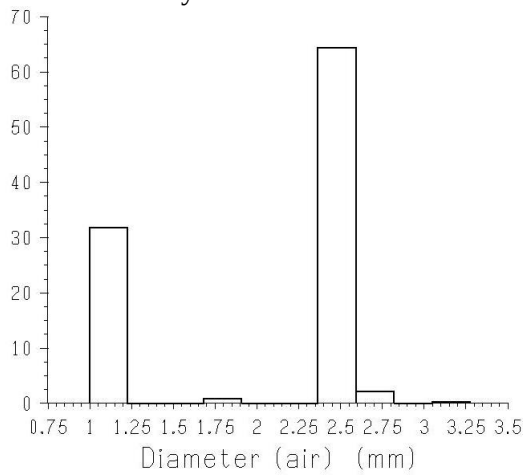

Air inlet velocity =3 cm/s

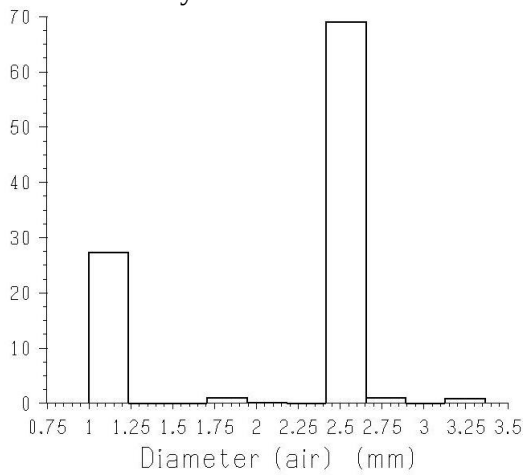

Air inlet velocity =4 cm/s

Figure 8-27 Effect of different air inlet velocity on the bubble size distribution

8.9 Conclusions

Euler–Euler simulations of gas–liquid flow in a bubble column have been coupled with a study of population balance. Bubbles have been distributed into 6 diameter classes. For each of them coalescence and break-up phenomena has been taken into account under normal gravity. For zero gravity condition coalescence only case was considered. The most important conclusion from these numerical results is that the centrifugal force is responsible for the bubble motion towards the axis of rotation shifting them away from the wall. The population balance under rotational effect for turbulence and in normal gravity is different than that for zero gravity and laminar. Two kernel models show no difference on the obtained data as rotation is dominant factor. In future a constant value for Kernel in zero gravity could be obtained and assigned for population balance modelling. Increasing the air flow rate shows an increase in the coalescence rate with a decrease in the inlet bubble diameter. Rotation changes the flow profile from turbulence to laminar under normal gravity, whereas it helps in accelerating the speed of bubble motion throughout the column under zero gravity. From the work of this thesis it can safely be concluded that Computational Fluid Dynamics (CFD) can be used as a reliable tool to gain more knowledge and a detailed understanding of the flow physics; especially for the hydrodynamics of bubble column under zero gravity conditions.

Chapter 9 Conclusions

Two axisymmetric and three-dimensional VOF simulations of two-phase (gas/liquid) transient flow were performed using a multiphase flow algorithm based on the finite-volume method. The current results show conclusive existence of Marangoni bubble/droplet flow phenomena in a zero-gravity environment. The present CFD results show that different temperature gradients lead to different droplet migration velocities, and it was proven that bubble migration velocity varies linearly with the temperature gradient for the given conditions. This phenomenon is expected due to an increase or decrease in the movement source - in this case, temperature difference. This study shows that, generally speaking, as Ma_T increases, the scaled velocity of a single bubble/droplet decreases and steadily approaches its asymptotic value. At the beginning of this research study, the terminal velocity of a single bubble was calculated and an expression for predicting the scaled velocity of a bubble has been derived based on the data obtained in the present numerical study for Marangoni numbers up to 10,721. An expression for predicting the scaled velocity of a Fluorinert droplet migrating in oil has also been presented for Ma ranging from 24.05 to 2771. The interactions of two droplets in thermocapillary motion have also been studied and compared with the results obtained for the isolated droplet. The results have shown that the leading droplet will not move faster than if it were isolated, as the trailing droplet has no influence on the velocity of the leading droplet. In addition, the trailing droplet translates more slowly than the isolated droplet, due to the thermal wake of the leading droplet. Moreover, the results indicate that as $Ma_T \rightarrow 0$, the trailing droplet will move at the same velocity as the isolated droplet. This research study has also covered the thermocapillary flow and interaction of a single and multiple bubbles in a three-dimensional domain. The results show that the trailing bubble migrates more slowly than the isolated bubble, due to the disturbed temperature caused by the leading bubble. The interaction and disturbance

increases as the gap between the two vertically aligned bubbles decreases, and vice versa. Other fundamental aspects of bubbles placed side by side were also presented, which included the size distribution of smaller bubbles and their agglomeration to form a larger bubble. The results show that collision and agglomeration could occur at a higher level if larger bubbles were used. No bubbles broke in any of the cases observed and agglomeration only occurred during thermocapillary migration for a given range of thermal Reynolds and Marangoni numbers. The results of the motion of a singular and multiple bubbles incorporating thermocapillary forces in a rotating liquid in a zero-gravity environment have been presented for the first time. When the Rossby number is 1, the effects of rotation are significant. Furthermore, the deflection of the gas bubble motion increases towards the axis of rotation with a decrease in the Rossby number (Ro). On the other hand, for a stationary cylinder, the thermocapillary migration of two bubbles was found to move in a linear fashion. This shows that the coalescence rates could be improved by operating the cylinder at lower mechanical rotation rates. It was also found that CFD predictions with the VOF model agreed better with the experimental data, due to the fact that it is based on the Geo-Reconstruct algorithm. The VOF model with the UDF were examined properly and results show that the surface tension coefficient was well coded, suggesting that it is an appropriate choice to solve thermocapillary problems.

Finally, two axisymmetric dimensional Eulerian/Eulerian simulations of two-phase (gas/liquid) transient flow were performed using a multiphase flow algorithm based on the finite-volume method to simulate bubble population balance modelling for both stationary and rotating columns in normal and zero gravity. Quantitative agreements between the experimental data and simulations are obtained for the averaged axial liquid velocity profiles. An important conclusion from these numerical results is that the centrifugal force is pulling

the bubbles towards the axis of rotation and shifts them away from the wall. Rotation could accelerate the moving bubbles throughout the column in zero-gravity conditions.

Recommendations and future works

Most experiments in microgravity have constraints such as time limitations; computer simulations, on the other hand, are not restricted to such constraints where any arbitrary geometry can be simulated. Thus, numerical simulations prove to be a valuable tool to study such complex problems under the conditions of zero and reduced gravity. A wider range of parameters as well as deeper physical explanations should be included in future work, such as a distance between the two droplets and the influence upon their interaction. The droplet behaviour is different from that of the bubble in thermocapillary flow, and more attention should be given to this topic in subsequent research studies. Since zero gravity is difficult to achieve in a laboratory setting, one can demonstrate the relevant phenomena using numerical simulations. It also allows one to study the effects of the sensitivity of different parameters. With computer simulations proving their worth as a valuable tool to study the complex problems under the conditions of zero gravity, and from the results of this thesis, one can assess the credentials of modelling to simulate realistic 3D Marangoni cases. Nonetheless, the numerical simulation facility on hand nowadays should encourage researchers to make use of high density grids and complex three-dimensional models to obtain results of the highest possible accuracy.

No previous similar work was used to compare the obtained results; this could be used in future in order to validate newer results. Mainly, there seems to be a need for further investigations on multiphase flow in zero gravity.

As stated in Chapter 3, FLUENT does not offer particle interaction simulation unless UDF is used. As a next step, this model could be upgraded with UDFs in which different aspects of particle collection can be depicted. For example, with UDF, a complete picture of the particle

behaviour in zero gravity could be established and the collective efficiency of a bubble and droplet agglomeration could be predicted. In future, many processes can be modelled to study different scenarios, such as the effects of pulsation, vibration, and surfactant on the behaviour of bubbles and droplets in zero gravity.

AKHTAR, A., PAREEK, V. & TADÉ, M. 2007. CFD simulations for continuous flow of bubbles through gas-liquid columns: application of VOF method. *Chemical Product and Process Modeling,* 2,.
ALHENDAL, Y. & TURAN, A. 2012. Volume-of-Fluid (VOF) Simulations of Marangoni Bubbles Motion in Zero Gravity. *In:* PETROVA, R. (ed.) *Finite Volume Method - Powerful Means of Engineering Design.* 2012-04 ed.: InTech.
ALHENDAL, Y., TURAN, A. & ALY, W. I. A. 2010. VOF simulation of marangoni flow of gas bubbles in 2D-axisymmetric column. *Procedia Computer Science,* 1**,** 673-680.
ANNAMALAI, P., SHANKAR, N., COLE, R. & SUBRAMANIAN, R. S. 1982. Bubble migration inside a liquid drop in a space laboratory. *Applied Scientific Research,* 38**,** 179-186.
ANSYS-FLUENT 2011. Users Guide.
ARGYRIOU, D. T., LIST, H. L. & SHINNAR, R. 1971. Bubble growth by coalescence in gas fluidized beds. *AIChE Journal,* 17**,** 122-130.
ARLABOSSE, P., LOCK, N., MEDALE, M. & JAEGER, M. 1999. Numerical investigation of thermocapillary flow around a bubble. *Physics of fluids,* 11**,** 18-29.
BALASUBRAMANIAM, R., LACY, C. E., WONIAK, G. & SUBRAMANIAN, R. S. 1996. Thermocapillary migration of bubbles and drops at moderate values of the Marangoni number in reduced gravity. *Physics of fluids,* 8**,** 872-880.
BALASUBRAMANIAM, R. & LAVERY, J. E. 1989. NUMERICAL SIMULATION OF THERMOCAPILLARY BUBBLE MIGRATION UNDER MICROGRAVITY FOR LARGE REYNOLDS AND MARANGONI NUMBERS. *Numerical Heat Transfer, Part A: Applications,* 16**,** 175-187.
BALASUBRAMANIAM, R. & SUBRAMANIAN, R. S. 2000. The migration of a drop in a uniform temperature gradient at large Marangoni numbers. *Physics of fluids,* 12**,** 733-743.
BATCHELOR, G. K. 2000 An Introduction to Fluid Dynamics. *Cambridge University Press, 2001*.
BHAGA, D. & WEBER, M. E. 1981. Bubbles in viscous liquids: shapes, wakes and velocities. *Journal of Fluid Mechanics,* 105**,** 61-85.
BOZZANO, G. & DENTE, M. 2009. SINGLE BUBBLE AND DROP MOTION MODELING. *AIDIC*.
BRACKBILL, J. U., KOTHE, D. B. & ZEMACH, C. 1992. A continuum method for modeling surface tension. *Journal of Computational Physics,* 100**,** 335-354.
BUSH, J. W. M., STONE, H. A. & BLOXHAM, J. 1995. Axial drop motion in rotating fluids. *Journal of Fluid Mechanics,* 282**,** 247-278.
CHEN, P., SANYAL, J. & DUDUKOVIĆ, M. P. 2005. Numerical simulation of bubble columns flows: effect of different breakup and coalescence closures. *Chemical Engineering Science,* 60**,** 1085-1101.
COOK, M. & BEHNIA, M. 2001. Bubble motion during inclined intermittent flow. *International Journal of Heat and Fluid Flow,* 22**,** 543-551.
CUI, H., HU, L., DUAN, L., KANG, Q. & HU, W. 2008. Space experimental investigation on thermocapillary migration of bubbles. *Science in China Series G: Physics, Mechanics and Astronomy,* 51**,** 894-904.
DEGALEESAN, S., DUDUKOVIC, M. & PAN, Y. 2001. Experimental study of gas-induced liquid-flow structures in bubble columns. *AIChE Journal,* 47**,** 1913-1931.
DETZEL, C. J., THORSON, M. R., VAN WIE, B. J. & IVORY, C. F. 2009. A study of the Coriolis effect on the fluid flow profile in a centrifugal bioreactor. *Biotechnology Progress,* 25**,** 1025-1034.
EDWARD L. PAUL, VICTOR A. ATIEMO-OBENG & KRESTA, S. M. 2004. Handbook of Industrial Mixing: Science and Practice.
ESSEMIANI, K., DUCOM, G., CABASSUD, C. & LINÉ, A. 2001. Spherical cap bubbles in a flat sheet nanofiltration module: experiments and numerical simulation. *Chemical Engineering Science,* 56**,** 6321-6327.
EVERSON, R. C., EYRE, D., O'CONNOR, C. T. & TUCKER, J. P. 1993. Measurement and analysis of small bubble size distributions. *Chemical Engineering Science,* 48**,** 3399-3403.
FRIEDLANDER, S. K. 2000. Smoke Dust and Haze. *Oxford*
University Press, New York, second edition.

GAMBIT 2005. User's Manual to GAMBIT *Fluent Inc*.
GUPTA, A. & KUMAR, R. 2007. Three-dimensional turbulent swirling flow in a cylinder: Experiments and computations. *International Journal of Heat and Fluid Flow,* 28**,** 249-261.
HADLAND, P. H., BALASUBRAMANIAM, R., WOZNIAK, G. & SUBRAMANIAN, R. S. 1999. Thermocapillary migration of bubbles and drops at moderate to large Marangoni number and moderate Reynolds number in reduced gravity. *Experiments in fluids,* 26**,** 240-248.
HARDY, S. C. 1979. The motion of bubbles in a vertical temperature gradient. *Journal of Colloid and Interface Science,* 69**,** 157-162.
HERRMANN, J. M., LOPEZ, P., BRADY & RAESSI, M. 2008. Thermocapillary. motion of deformable drops and bubbles. *Proceedings of the 2008 Summer Program***,** pp. 155-170.
HIRT, C. W. & NICHOLS, B. D. 1981. Volume of fluid (VOF) method for the dynamics of free boundaries. *Journal of Computational Physics,* 39**,** 201-225.
HOUNSLOW, M. J., RYALL, R. L. & MARSHALL, V. R. 1988. A discretized population balance for nucleation, growth, and aggregation. *AIChE Journal,* 34**,** 1821-1832.
J, H. 2002. A review of The Motion of Bubbles and Drops in Reduced Gravity by R Shankar and R. Subramanian (2001). .
KANG, D. H., AHN, Y.-C., OH, B. D. & KIM, M. H. 2004. Advanced electromagnetic flowmetry for slug flow: numerical signal prediction and calibration. *International Journal of Multiphase Flow,* 30**,** 585-614.
KANG, Q., CUI, H. L., HU, L. & DUAN, L. 2008. On-board Experimental Study of Bubble Thermocapillary Migration in a Recoverable Satellite. *Microgravity Science and Technology,* 20**,** 67-71.
KANG, Q., CUI, H. L., HU, L., DUAN, L. & HU, W. R. 2007. Experimental investigation on bubble coalescence under nonuniform temperature distribution in reduced gravity. *Journal of Colloid and Interface Science,* 310**,** 546-549.
KAWAJI, M., DEJESUS, J. M. & TUDOSE, G. 1997. Investigation of flow structures in vertical slug flow. *Nuclear Engineering and Design,* 175**,** 37-48.
KRISHNA, R. & VAN BATEN, J. M. 1999. Rise characteristics of gas bubbles in a 2D rectangular column: VOF simulations vs experiments. *International Communications in Heat and Mass Transfer,* 26**,** 965-974.
KUHLMANN, H. C. 1999. Thermocapillary convection in models of crystal growth. *springer Tracts in Modern Physics, 152,* Springer-Verlag, Berlin, Heidelberg**,** 83-89.
LAW, D. & BATTAGLIA, F. 2013. Numerical Simulations for Hydrodynamics of Air-Water External Loop Airlift Reactor Flows With Bubble Break-Up and Coalescence Effects. *Journal of Fluids Engineering,* 135**,** 081302-081302.
LEONARD, B. P. & MOKHTARI, S. 1990. Ultra-sharp non-oscillatory convection schemes for high speed steady multidimensional flow *NASA TM 1-2568 (ICOMP-90-12), NASA Lewis Research Center*.
LISTER, J. D., SMIT, D. J. & HOUNSLOW, M. J. 1995. Adjustable discretized population balance for growth and aggregation. *AIChE Journal,* 41**,** 591-603.
LÖRSTAD, D., FRANCOIS, M., SHYY, W. & FUCHS, L. 2004. Assessment of volume of fluid and immersed boundary methods for droplet computations. *International Journal for Numerical Methods in Fluids,* 46**,** 109-125.
MA, X. 1999. NUMERICAL SIMULATION OF THERMOCAPILLARY DROP MOTION WITH INTERNAL CIRCULATION. *Numerical Heat Transfer, Part A: Applications,* 35**,** 291-309.
MARSHALL, E. M. & BAKKER, A. 2003. COMPUTATIONAL FLUID MIXING.
MERRITT, R. M. & SHANKAR SUBRAMANIAN, R. 1988. The migration of isolated gas bubbles in a vertical temperature gradient. *Journal of Colloid and Interface Science,* 125**,** 333-339.
MEYYAPPAN, M., WILCOX, W. R. & SUBRAMANIAN, R. S. 1983. The slow axisymmetric motion of two bubbles in a thermal gradient. *Journal of Colloid and Interface Science,* 94**,** 243-257.

NAS 1995. Computational investigation of thermocapillary migration of bubbles and drops in zero gravity. *Ph.D. Dissertation*.
NAS, S. & TRYGGVASON, G. 1993. Computational investigation of the thermal migration of bubbles and drops. *175 Fluid Mechanics Phenomena in Microgravity*, 71–83
NAS, S. & TRYGGVASON, G. 2003. Thermocapillary interaction of two bubbles or drops. *International Journal of Multiphase Flow,* 29, 1117-1135.
OSTRACH, S. 1982. Low-gravity flows. *Ann. Rev*, 313–345.
PBM-MANUAL 2006. Population Balance
Module Manual.
PBM-MANUAL 2011. Population Balance
Module Manual.
RAMKRISHNA, D. 2000. Population Balances: Theory and Applications to Particulate Systems in Engineering. . *Academic Press, San Diego, CA,* .
RANADE, V. V. 2002. Computational Flow Modeling for Chemical Reactor Engineering. *Academic Press, New York (2002*.
ROACHE, P. J. 1998. Verification and Validation in Computational Science and Engineering.
SATRAPE, J. 1992. Interactions and collisions of bubbles in thermocapillary motion. *Physics of fluids,* 4, 18.
SCHILLER, L. & NAUMANN, Z. 1935. A Drag Coefficient Correlation. *Z. Ver. Deutsch. Ing.*, 77,318.
SHANKAR, N. & SHANKAR SUBRAMANIAN, R. 1988. The stokes motion of a gas bubble due to interfacial tension gradients at low to moderate Marangoni numbers. *Journal of Colloid and Interface Science,* 123, 512-522.
SOBRINO, C., ACOSTA-IBORRA, A., SANTANA, D. & DE VEGA, M. 2009. Bubble characteristics in a bubbling fluidized bed with a rotating distributor. *International Journal of Multiphase Flow,* 35, 970-976.
SUBRAMANIAN, K., PASCHKE, S., REPKE, J. & WOZNY, G. 2009. Drag force modelling in CFD simulation to gain insight of packed columns. *AIDIC Conference Series,,* 09, 299-308.
SUBRAMANIAN, R. & BALASUBRAMANIAN, R. 2010. The motion of bubbles and drops in reduced gravity. *Cambridge University Press, 2001*.
SUBRAMANIAN, R. S. 1981. Slow migration of a gas bubble in a thermal gradient. *AIChE Journal,* 27, 646-654.
SUBRAMANIAN, R. S. & COLE, R. 1979. Experiment Requirements and Implementation Plan (ERIP) for "Physical Phenomena in Containerless Glass *Experiment MPS 77F010, NASA Marshall Space Flight Center,* Document 77FR010.
SUN, R. & HU, W. R. 2003. Planar thermocapillary migration of two bubbles in microgravity environment. *Physics of fluids,* 15, 3015-3027.
SZYMCZYK, J. & SIEKMANN, J. 1988. NUMERICAL CALCULATION OF THE THERMOCAPILLARY MOTION OF A BUBBLE UNDER MICROGRAVITY. *Chemical Engineering Communications,* 69, 129-147.
TAHA, T. & CUI, Z. F. 2006. CFD modelling of slug flow in vertical tubes. *Chemical Engineering Science,* 61, 676-687.
THOMPSON, R. L., DEWITT, K. J. & LABUS, T. L. 1980. MARANGONI BUBBLE MOTION PHENOMENON IN ZERO GRAVITY. *Chemical Engineering Communications,* 5, 299-314.
TOMIYAMA, A., SOU, A., MINAGAWA, H. & SAKAGUCHI, T. 1993. Numerical Analysis of a Single Bubble by VOF Method. *JSME International Journal Series B,* 36, 51-56.
TREUNER, M., GALINDO, V., GERBETH, G., LANGBEIN, D. & RATH, H. J. 1996. Thermocapillary Bubble Migration at High Reynolds and Marangoni Numbers under Low Gravity. *Journal of Colloid and Interface Science,* 179, 114-127.
UDF-MANUAL 2011. User-Defined Functions *Manual*.
UHLMANN, D. R. 1981. Glass Processing in a Microgravity Environment. *MRS Online Proceedings Library,* 9, null-null.

VAN DOORMAAL, J. P. & RAITHBY, G. D. 1984. ENHANCEMENTS OF THE SIMPLE METHOD FOR PREDICTING INCOMPRESSIBLE FLUID FLOWS. *Numerical Heat Transfer,* 7**,** 147-163.

VAN LEER, B. 1979. Towards the ultimate conservative difference scheme. V. A second-order sequel to Godunov's method. *Journal of Computational Physics,* 32**,** 101-136.

WÖLK, G., DREYER, M. & RATH, H. J. 2000. Flow patterns in small diameter vertical non-circular channels. *International Journal of Multiphase Flow,* 26**,** 1037-1061.

WOZNIAK, G., BALASUBRAMANIAM, R., HADLAND, P. & SUBRAMANIAN, R. 2001. Temperature fields in a liquid due to the thermocapillary motion of bubbles and drops. *Experiments in fluids,* 31**,** 84-89.

XIE, J.-C., LIN, H., ZHANG, P., LIU, F. & HU, W.-R. 2005. Experimental investigation on thermocapillary drop migration at large Marangoni number in reduced gravity. *Journal of Colloid and Interface Science,* 285**,** 737-743.

XIE, J. C., LIN, H., HAN, J. H., DONG, X. Q., HU, W. R., HIRATA, A. & SAKURAI, M. 1998. Experimental investigation on Marangoni drop migrations using drop shaft facility. *International Journal of Heat and Mass Transfer,* 41**,** 2077-2081.

XIE, J. C., LIN, H., HAN, J. H. & HU, W. R. 1996. Drop migration of middle Reynolds number in a vertical temperature gradient. *Microgravity Science and Technology,* 9**,** 95-99.

YAMAGUCHI, T., IGUCHI, M. & UEMURA, T. 2004. Behavior of a small single bubble rising in a rotating flow field. *Experimental Mechanics,* 44**,** 533-540.

YIN, Z.-H., CHANG, L., HU, W.-R. & GAO, P. 2011. Thermocapillary migration and interaction of two nondeformable drops. *Applied Mathematics and Mechanics,* 32**,** 811-824.

YOUNG, N. O., GOLDSTEIN, J. S. & BLOCK, M. J. 1959. The motion of bubbles in a vertical temperature gradient. *Journal of Fluid Mechanics,* 6**,** 350-356.

YOUNGS, D. L. 1982. Time-dependent multi-material flow with large fluid distortion. *Numerical Methods for Fluid Dynamics,* Academic Press**,** 273–285.

Publications In Peer-Reviewed:

Journal Papers

Yousuf Alhendal, Ali Turan, Peter Hollingsworth. Thermocapillary Simulation of Single Bubble Dynamics in Zero-Gravity. Acta Astronautica. 2013 April.

Conference Papers

Alhendal, Y.; Turan, A.; Aly, W.I.A.. VOF simulation of marangoni flow of gas bubbles in 2D-axisymmetric column. Procedia Computer Science, Volume 1, Issue 1, May 2010, Pages 673-680.

Alhendal Y, Turan A. Numerical Investigation Regarding the Influence of 3-D Marangoni Flow on Bubble Behaviour in a Rotating Cylinder. Chemical Engineering Transactions. 2011 April; 24: 1381-1386

Book Chapters

Yousuf Alhendal, Ali Turan. Volume-of-Fluid (VOF) Simulations of Marangoni Bubbles Motion in Zero Gravity, Finite Volume Method. Finite Volume Method. CROATIA, INTEC.2012.

Journal Paper Under Revision

Yousuf Alhendal, Ali Turan Thermocapillary Bubble Flow and Coalescence in a Rotating Cylinder: 3D study. Chemical Engineering Communications

To be submitted:

1-Yousuf Alhendal, Ali Turan., Thermocapillary migration of an isolated droplet in zero gravity, The International Journal of Multiphase Flow

2-Yousuf Alhendal, Ali Turan., Interactions and collisions of bubbles in thermocapillary motion 3D Study., Particulate Science and Technology

3- Yousuf Alhendal, Ali Turan., Thermocapillary bubble dynamics in a 2D axis swirl domain

ELSEVIER

Procedia Computer Science

Volume 1, Issue 1, May 2010, Pages 673–680

ICCS 2010

International Conference on Computational Science, ICCS 2010

VOF simulation of marangoni flow of gas bubbles in 2D-axisymmetric column

Y. Alhendal[a], A. Turan[a], Wael I.A. Aly[b]

[a] School of Mechanical, Aerospace and Civil Engineering, University of Manchester, UK

[b] Department of Refrigeration and Air Conditioning Technology, Faculty of Industrial Education, Helwan Univ Cairo, Egypt

Abstract

The migration of gas bubbles immersed in a liquid under the action of temperature gradi tension (Marangoni flow) in zero gravity environment is numerically investigated for different (Marangoni, Reynolds, and Prandtl numbers). The full Navier–Stokes equations as well equation for temperature gradient are solved by a volume of fluid (VOF) method/Finite Volu the surface tension force is modeled by a continuum surface force (CSF) model. The beh migrating toward the hotter side by the action of surface tension using the flow relations betwe (leading and trailing bubble), and the trajectories and the velocities of the different bubble microgravity environment have been investigated numerically. It has been verified that the ca are in good agreement with available experimental and numerical results. It is also concluded able to simulate two-phase flow under zero gravity conditions.

Keywords

Marangoni flow; Zerogravity; Bubbles; VOF

References

[1] N.O. Young, J.S. Goldstein, M.J. Block

CHEMICAL ENGINEERING TRANSACTIONS Volume 24, 2011
Editor Sauro Pierucci
 ISBN 978-88-95608-15-0 ISSN 1974-9791
DOI: 10.3303/CET1124231

Numerical Investigation Regarding the Influence of 3-D Marangoni Flow on Bubble Behaviour in a Rotating Cylinder

Yousuf Alhendal*, Ali Turan

School of Mechanical, Aerospace and Civil Engineering, University of Manchester, UK.
Hendalyes@hotmail.com

The migration of gas bubbles immersed in a liquid under the action of a temperature gradient and surface tension (Marangoni flow) in a zero gravity environment is numerically investigated for different Ma, Re, and Pr (Marangoni, Reynolds, and Prandtl numbers). The full Navier–Stokes equations as well as the energy equation for temperature gradients are solved incorporating a volume of fluid (VOF). Finite Volume method, and the surface tension force is modeled by a continuum surface force (CSF). The axisymmetric model is further extended for a 3-D geometry to investigate the case of a rotating cylinder to enhance bubble merging behavior in a Marangoni flow. It has been verified that the calculated results are in agreement with available experimental and numerical results. Rotational force can effect the enhancement of bubble migration and contact between the bubbles in microgravity. It is also concluded that the VOF is able to simulate two-phase flow under microgravity conditions.

1. Introduction

In zero gravity, the Marangoni effect will dominate the system as the main driving force in the determination of the gas bubble movement due to the varying liquid surface tension in a temperature gradient. Bubble dynamics has become a very important study area for fundamental research and applications in a reduced gravity environment, such as space material science, chemical engineering, space-based containerless processing of materials e.g., glass is believed to have the potential of producing very pure materials, Uhlmann (1982), and thermocapillary migration may provide mechanisms to remove bubbles from the melt. Control of vapor bubbles forming in both the fuel systems of liquid-rockets (Nas and Tryggvason, 2003) and the cooling system of space habitats may be achievable using thermocapillary migration. Experiments under normal and microgravity conditions are too costly as well as being complicated, Bozzano (2009), and hence, numerical simulations become an important tool in research studies of two-phase flows under a microgravity environment. It is uneasy to get complete information about the behavior of bubble in space and a CFD study has been undertaken by many researchers to compare and analyze their experimental results, Treuner et al. (1996). The shape and the area of the varying interface are very complex and a simulation study is required, Subramanian et al. (2009). Therefore, it is necessary to carry out appropriate numerical simulations for the behavior of bubble in microgravity.

Please cite this article as: Alhendal Y. and Turan A., 2011, Numerical investigation regarding the influence of 3-d marangoni flow on bubble behaviour in a rotating cylinder, Chemical Engineering Transactions, 24, 1381-1386
DOI: 10.3303/CET1124231

10

Volume-of-Fluid (VOF) Simulations of Marangoni Bubbles Motion in Zero Gravity

Yousuf Alhendal and Ali Turan
The University of Manchester
United Kingdom

1. Introduction

This chapter deals with two-phase flows, i.e. systems of different fluid phases such as gas and liquid. A typical example of a two-phase flow is a motion of a particle (bubble or droplet) in a stagnant fluid (liquid or gas). In many branches of engineering it is important to be able to describe the motion of gas bubbles in a liquid (Krishna & Baten, 1999). In multiphase flow, the simultaneous flow strongly depends on the gravity force. However, in zero gravity conditions, buoyancy effects are negligible and as an alternative, three different methods were found to make the bubbles or drops move in zero gravity. They are electrocapillary, solutalcapillary and thermocapillary motion.

When a temperature gradient exists on the interface, the surface tension varies along the interface, resulting in bulk fluid motion, called thermocapillary (Marangoni) flow. In normal gravity this thermocapillary flow tends to be weighed down by buoyancy driven flow. However, for small geometry and/or zero gravity environments, this is not the case and thermocapillary is dominant and it could become an important driving force.

Bubbles suspended in a fluid with a temperature gradient will move toward the hot region due to thermocapillary forces. Surface tension generally decreases with increasing temperature and the non-uniform surface tension at the fluid interface leads to shear stresses that act on the outer fluid by viscous forces, thus inducing a motion of the fluid particle (a bubble or a drop) in the direction of the thermal gradient. In space, where buoyancy forces are negligible, thermocapillary forces can be dominant and can lead to both desirable and undesirable motion of fluid particles.

Particle dynamics has become a very important study area for fundamental research and applications in a zero gravity environment, such as space material science, chemical engineering, space-based containerless processing of materials e.g., glass is believed to have the potential of producing very pure materials, (Uhlmann, 1982), and thermocapillary migration may provide mechanisms to remove bubbles from the melt. Control of vapor bubbles forming in both the fuel systems of liquid-rockets (Ostrach, 1982) and the cooling system of space habitats may be achievable using thermocapillary migration. Thermocapillary migration may also lead to accumulation of gas bubbles on the hot surface of heat exchangers and reducing their efficiency. Ostrach (1982) studied various types of fluid flows that could occur under low-gravity conditions and pointed out that Marangoni convection is one of the important flows. In practical applications, it is frequently necessary

Contents lists available at SciVerse ScienceDirect

Acta Astronautica

journal homepage: www.elsevier.com/locate/actaastro

Thermocapillary simulation of single bubble dynamics in zero gravity

Yousuf Alhendal *, Ali Turan, Peter Hollingsworth

School of Mechanical, Aerospace and Civil Engineering, the University of Manchester, George Begg Building, Sackville St Manchester, M13 9PL, UK

ARTICLE INFO

Article history:
Received 7 June 2012
Received in revised form
8 March 2013
Accepted 17 March 2013
Available online 26 March 2013

Keywords:
Bubble
Two-phase
Zero-gravity
Thermocapillary
Surface Tension gradient
VOF-Ansys

ABSTRACT

The lack of significant buoyancy effects in zero gravity co transfer in a stagnant liquid. In this paper bubble m analysed and presented numerically using a comp approach. The governing continuum conservation eq solved using the commercial software package Ansys-Fl (VOF) method is used to track the liquid/gas interfa simulation results are in reasonable agreement with t tions, the VOF algorithm is found to be a valuable tool fo liquid interaction. The flow is driven via Marangoni influ difference which in turn drives the bubble from the c thermal Reynolds (Re_T) and Marangoni numbers (Ma_T simulations, specifically Re_T=13–658 and Ma_T=214– indicate that the inherent velocity of bubbles decreases v number, a result that is line with the results of previou 2008) [1]. An expression for predicting the scaled vel based on the data obtained in the present numerical simulations are also performed to compare and e dimensional simulations.

1. Introduction

In zero gravity conditions, buoyancy effects are negligible for bubble and drop transport, leading to alternative methods of transport including electrocapillary, solutalcapillary and thermocapillary modes. Bubbles suspended in a fluid with a temperature gradient will move towards the hot region due to thermocapillary forces. Surface tension generally decreases with increasing temperature and the non-uniform surface tension at the fluid interface leads to shear stresses that act on thermal gradient. In microgra negligible, thermocapillary fo lead to both desirable and particles. An understanding c in zero gravity conditions is microgravity experiments suc space station. In addition, such the future design of thermo-fl might be employed in comp able literature of the zero gra